universität
wien

DISSERTATION

Titel der Dissertation

Simulations of Quantum Spin Chains with Translationally Invariant Matrix Product States

Verfasser

Dipl. Ing. Bogdan Corneliu Pirvu

angestrebter akademischer Grad

Doktor der Naturwissenschaften (Dr. rer. nat.)

Wien, 2012

Studienkennzahl laut Studienblatt: A 091 411

Dissertationsgebiet laut Studienblatt: Physik

Betreuer: Univ.-Prof. Dr. Frank Verstraete

In memory of my beloved grandfather.

Contents

Zusammenfassung **9**

Abstract **11**

Acknowledgments **13**

Introduction **15**

1 Matrix Product Operator Representations **21**

1.1 Introduction . . . 22

1.2 Matrix Product Operator descriptions of exponentials . . . 22

1.2.1 Construction . . . 22

1.2.2 Algorithms . . . 26

1.3 Matrix Product Operator descriptions of Hamiltonians with long-range interactions . . . 27

1.3.1 Construction . . . 27

1.4 Conclusion . . . 29

1.5 Appendix A: Optimal cut of the MPS bond dimension during imaginary time evolution . . . 30

1.5.1 Imaginary time evolution for the infinite chain . . . 30

1.5.2 Optimal bond dimension cut for TI MPS . . . 31

1.6 Appendix B: Imaginary time evolution for the Bilinear-Biquadratic spin-1 chain 35

1.6.1 MPO representation for $e^{\epsilon X\otimes X}$ . . . 35

1.6.2 MPO representation for $e^{\epsilon Z\otimes Z}$ . . . 37

1.6.3 MPO representation for $e^{-\epsilon Y\otimes Y}$ . . . 37

1.6.4 MPO representation for $e^{\epsilon X^2\otimes X^2}$, $e^{\epsilon Y^2\otimes Y^2}$ and $e^{\epsilon Z^2\otimes Z^2}$ . . . 38

1.6.5 MPO representation for $e^{\epsilon XZ\otimes XZ}$ and $e^{\epsilon ZX\otimes ZX}$ . . . 39

1.6.6 MPO representation for $e^{-\epsilon XY\otimes XY}$, $e^{-\epsilon YX\otimes YX}$, $e^{-\epsilon ZY\otimes ZY}$ and $e^{-\epsilon YZ\otimes YZ}$ 39

1.7 Appendix C: Imaginary time evolution for the spin-$1/2$ Heisenberg ladder . . . 41

1.7.1 MPO representation for $e^{\epsilon H_X}$ and $e^{\epsilon H_Z}$ . . . 43

1.7.2 MPO representation for $e^{-\epsilon H_Y}$ 45
1.8 Appendix D: Approximation of functions as sums of exponentials 47

2 Translationally Invariant MPS Simulations of PBC chains 49
2.1 Introduction 50
2.2 Overview 52
2.3 The algorithm 54
2.4 Numerical results 59
2.4.1 Critical systems 59
2.4.2 Observables - energy and correlation functions 61
2.4.3 Non-critical systems 65
2.5 Conclusions and outlook 67
2.6 Appendix 67
2.6.1 Computation of $H_{eff}(\mathbf{A})$ 67
2.6.2 Computation of $N_{eff}(\mathbf{A})$ 72

3 Finite Size Scaling versus Finite Entanglement Scaling 73
3.1 Introduction 74
3.2 Numerical results 78
3.2.1 Two different regimes for MPS simulations 79
3.2.2 The transition between the two regimes 80
3.2.3 Minimal D for faithful simulations 87
3.2.4 Thermodynamic limit of the transition 87
3.2.5 The scaling function 88
3.3 Conclusions 90
3.4 Appendix A: Effective correlation length 91
3.4.1 Analytical results 91
3.4.2 Numerical results 92
3.5 Appendix B: Detailed treatment of the thermodynamic limit of the transition . . 94
3.5.1 Scaling of $\lambda_i(k, N)$ 102
3.6 Appendix C: Comparison to other PBC MPS algorithms 104

4 Determining dispersion relations of PBC chains 107
4.1 Introduction 108
4.2 Overview 109
4.3 The algorithm 110
4.3.1 Overall scaling of the computational cost 113
4.4 Numerical results 115
4.4.1 Quantum Ising model 115
4.4.2 Heisenberg model 123

4.4.3 Bilinear-Biquadratic spin-1 chain 129
4.5 Conclusions and Outlook 131

Conclusions and Outlook **133**

Bibliography **135**

A Analytical solution of the Quantum Ising model with PBC **141**
A.1 Jordan-Wigner transformation 142
A.2 Bogoliubov transformation - Diagonalization of a general quadratic form in Fermi operators 144
A.3 Bogoliubov transformation - Applied 147
A.3.1 Diagonalization of $\mathcal{H}_{odd}$ - Jordan-Wigner boundary conditions 148
A.3.2 Diagonalization of $\mathcal{H}_{even}$ 149
A.3.3 The parity anomaly 150

Lebenslauf **153**

Zusammenfassung

Gegenstand der vorliegenden Arbeit ist die Entwicklung und Analyse neuer effizienter Algorithmen zur Simulation stark gekoppelter Quantenspinketten. Unsere Methode beruht auf einer bestimmten Klasse von Testzuständen, die sich in den letzten Jahren als besonders geeignet für Variationsrechnungen in diesem Bereich herausgestellt hat, der Klasse der sogenannten Matrix-Produkt-Zuständen (MPS). Aufgrund ihrer Struktur kann man MPS sehr gut dazu verwenden, um Zustände mit endlicher Verschränkung darzustellen. Daher sind MPS dafür prädestiniert um nicht-kritische Systeme akkurat zu simulieren. Bei Quantenphasenübergängen divergiert die Verschränkung des Grundzustands logarithmisch mit der Systemgröße, sodass am quantenkritischen Punkt die Präzision von MPS Simulationen erheblich sinkt. Nichtsdestotrotz wird im Folgenden gezeigt, dass sogar kritische Systeme mittels MPS präzise simuliert werden können wenn man sie im Rahmen einer geeigneten Skalenanalyse behandelt. Wir werden uns in dieser Arbeit auf translationsinvariante (TI) Systeme konzentrieren und uns diese Eigenschaft zugute machen, indem wir translationsinvariante MPS als Grundlage unserer Algorithmen verwenden werden. Verglichen mit Algorithmen, die nicht-translationsinvariante MPS verwenden, ist unsere Methode um einen Faktor proportional zur Größe des Systems schneller. Zunächst behandeln wir unendliche Ketten mit offenen Randbedingungen (OBC) und stellen einen Algorithmus vor, der basierend auf TI MPS den Grundzustand des Systems mittels Imaginärzeitentwicklung bestimmt. Die Hauptidee bei diesem Zugang besteht darin den Imaginärzeitentwicklungsoperator durch eine Trotter-Zerlegung derart zu approximieren, dass jeder Faktor als translationsinvarianter Matrix-Produkt-Operator (MPO) dargestellt werden kann. Diese Methode wird angewendet um die Quanten-Ising und Heisenberg Spin-1/2 Modelle zu untersuchen, die als Paradebeispiele für stark wechselwirkende Spinketten in allen Kapiteln dieser Arbeit ausführlich behandelt werden. In Folge werden sowohl einige bislang nicht publizierte Ergebnisse für den Imaginärzeitentwicklungs-MPO des Bilinear-Biquadratischen Modells und der Heisenberg Spin-1/2 Leiter als auch ein Beweis dafür vorgestellt, dass der entscheidende Schritt im MPO-Algorithmus nach gewissen Kriterien optimal ist. In weiterer Folge wird ein Algorithmus für die Approximation des Grundzustandes endlicher Ketten mit periodischen Randbedingungen (PBC) eingeführt. Wie im OBC Fall wird wieder ein translationsinvarianter Ansatz verwendet, um den Rechenaufwand der Simulation zu reduzieren. Es wird gezeigt, dass für kritische Systeme mit PBC, in Vergleich zu Systemen mit OBC, der Rechenaufwand einen zusätzlichen Faktor beinhaltet. Es folgt eine ausführliche Analyse der Ergebnisse von Simulationen einiger kritischer Systeme mit PBC. Diese Analyse zeigt die Entstehung unterschiedlicher Bereiche in MPS Simulationen: den “Finite-Size Scaling” (FSS) und den “Finite-Entanglement Scaling” (FSS) Bereich. Im Rahmen dieser Untersuchung zeigt sich, um kritische Systeme wahrheitsgetreu simulieren zu können, müssen die MPS derart gewählt werden,

dass sie sich im FSS Bereich befinden. Schließlich wird ein Algorithmus für die Approximation angeregter Zustände von Quantenspinketten mit PBC vorgestellt, der als Grundlage einen translationsinvarianten MPS Ansatz für Impulseigenzustände verwendet. Ein Vergleich der Ergebnisse unserer Simulationen mit den analytischen Lösungen bestätigt, dass besonders Einteilchenzustände mit diesem Ansatz sehr gut approximert werden können. Im Appendix wird die analytische Lösung für die Berechnung des gesamten Spektrums des Quanten-Ising Modells mit PBC vorgestellt. Obwohl diese Lösung schon länger bekannt ist, führen wir in unserer Darstellung einige Aspekte an, die wir in der Fachliteratur nicht finden konnten.

Abstract

This thesis is mainly concerned with the development and analysis of new efficient algorithms for the simulation of strongly correlated quantum spin chains. To this end we are using a special class of variational states that has received increased attention recently: Matrix Product States (MPS). MPS are particularly well suited to represent states with a finite amount of entanglement thus they can be used to simulate non-critical systems with very good accuracy. When a system undergoes a quantum phase transition the entanglement entropy diverges logarithmically with the system size thus the precision of MPS simulations suffers at a quantum critical point. Nevertheless we are able to show that by applying the correct scaling analysis, MPS can also be used to simulate critical systems faithfully. We focus here on translationally invariant systems and exploit this property by using translationally invariant MPS in our algorithms. Compared with algorithms that use non-translationally invariant MPS, this approach yields a computational speed-up proportional to the size of the system. We start by developing an algorithm for obtaining the ground state of infinite chains with open boundary conditions (OBC) by means of imaginary time evolution. The main idea here is to approximate the imaginary time evolution operator using a Trotter expansion in such a way that every factor can be represented by a translationally invariant Matrix Product Operator (MPO). We apply this method to the Quantum Ising model and to the Heisenberg spin-1/2 chain, which are the main two paradigmatic models studied thoroughly throughout the entire thesis. We then continue by presenting some unpublished results regarding the MPO for the imaginary time evolution operator of the Bilinear-Biquadratic model and of the Heisenberg spin-1/2 ladder. Furthermore we give an unpublished proof of the fact that the crucial step in the MPO based algorithm is in some sense optimal. We then proceed with an algorithm for the computation of ground states of finite chains with periodic boundary conditions (PBC) that again exploits translational invariance in order to reduce the computational cost. We show that in the case of critical systems, the scaling of the computational cost of faithful PBC simulations contains an additional factor in comparison to that of OBC simulations. Next we provide an in-depth analysis of a large number of simulations of critical systems with PBC that shows the emergence of different regimes for MPS simulations: the finite size scaling (FSS) regime and the finite entanglement scaling (FES) regime. It turns out that in order to faithfully simulate critical systems, one must choose the MPS in such a way that it is always in the FSS regime. Finally we present an algorithm for the approximation of excited states of quantum spin chains with PBC that is based on a translationally invariant MPS ansatz with well defined momentum. A comparison of the obtained numerical results with the available analytical solutions confirms that this ansatz is particularly well suited for the approximation of one-particle states. In the appendix of this thesis we give a detailed analytical derivation of the spectrum of the Quantum Ising model with PBC. While

this derivation has been known for several decades we believe it has some pedagogical value since we emphasize several aspects that we have not found in any other previous publications.

Acknowledgments

I would like to thank my supervisor Prof. Frank Verstraete for his support and encouragement during my graduate studies. Due to his enthusiasm for quantum physics and other fields like information theory or complexity theory I have had the the unique opportunity to work in an inspiring interdisciplinary environment and learn many interesting things outside the main scope of my research.

I would like to thank Prof. Markus Arndt for organizing and supporting the CoQuS doctoral program which provided a very stimulating environment as well as the opportunity to share knowledge and interact scientifically with my fellow graduate students. I owe special thanks to Prof. Guifre Vidal and Prof. Maciej Lewenstein for their generous hospitality during my visits to their groups. Furthermore I would like to thank everybody I have had the chance to collaborate with for the inspiring and fruitful discussions that led to the results presented in this thesis.

I would also like to thank all my colleagues from the University of Vienna for the pleasant time we spent together during the last several years. Special thanks go to my family and friends for their encouragement during this time.

I gratefully acknowledge the generous support by the FWF doctoral program Complex Quantum Systems (W1210), the ERC grant QUERG, and the FWF SFB projects FoQuS and ViCoM.

Introduction

In the last decades the development of numerical simulations for strongly correlated systems has received plenty of attention in the condensed matter community. For such systems mean field methods fail due to strong interactions and one has to take into account the full electronic many-body problem. This problem, i.e. solving the Schrödinger equation of the system, is not tractable except for very small systems . However, for certain values of the parameters of the system, it is possible to obtain good approximations of the original problem via relatively simple effective Hamiltonians that can be considered to be equivalent to the original ones. The famous Hubbard or Heisenberg Hamiltonians emerge in this way. These are models for quantum systems (fermions or bosons for the Hubbard, spins attached to a site for the Heisenberg model) on discrete lattices. If the local Hilbert space dimension is finite like in the case of spin models or fermionic models, any finite-size lattice will yield a finite dimension of the global Hilbert space of the quantum system[1]. The Hamiltonian of such a system is then a finite-size matrix that is obtained by projecting the original Hamiltonian onto a suitably chosen basis of the reduced effective Hilbert space. All one has to do then is to diagonalize a Hamiltonian which is much simpler than the original one. Solving this may seem an easy task for any numerical library. The only limitation is the amount of memory available and the amount of time one is willing to wait for the result[2]. However, since the effective Hilbert space dimension is growing exponentially with the system size, very soon the Hamiltonian matrix will be too big to fit into any imaginable memory. Note that brute-force diagonalization can be done nowadays on a normal PC for systems with roughly up to 20 particles[3]. Hence the big challenge is to come up with methods that overcome the problem of the exponentially growing Hilbert space.

The big breakthrough in this direction was made by Kenneth Wilson in his seminal paper [1] on the Numerical Renormalization Group (NRG). In that work Wilson applies previously developed ideas about the Renormalization Group Theory numerically to the Kondo problem. Inspired by these ideas, the next step towards efficient simulation of strongly correlated systems was done by Steve White in 1992 [2]. His Density Matrix Renormalization Group (DMRG) combines some of Wilson's NRG ideas with concepts from Quantum Information Theory (QIT), like the entanglement amount of a certain state, in order to numerically approximate ground states of spin chains. Today, DMRG and related methods, like the ones presented in this thesis, are along with Monte Carlo methods (only for bosonic systems) the most accurate algorithms available for the investigation of strongly correlated systems.

---

[1] Finite-dimensional effective Hamiltonians for bosonic systems can also be easily obtained if one defines a finite filling factor. This approach is equivalent to fixing the chemical potential of the system.

[2] Note that for sparse matrix diagonalization there exist very efficient iterative algorithms like the Lanczos algorithm.

[3] Assuming a local Hilbert space dimension $d = 2$, i.e. either spin-1/2 particles or fermions.

In 1995 Rommer and Östlund [3] realized the equivalence between a previously known variational class of states going under the name of *Matrix Product States* (MPS) and DMRG. At that time MPS and similar ideas had been already known for roughly 8 years in the community dealing with exactly solvable systems. The MPS concept has its roots in the seminal papers of Affleck, Kennedy, Lieb and Tasaki [4, 5], where the authors show that a so-called *Valence Bond State* (VBS) is the exact ground state of what is today known as the AKLT-model, a special instance of the Bilinear-Biquadratic spin-1 chain. In 1992 Fannes, Nachtergaele and Werner came up with the *Finitely Correlated States* (FCS) as a generalization of the VBS [6]. Even though FCS were introduced as exact ground states, the authors of [6] realized that they could in principle also be used as variational states for non-exactly solvable models. The name Matrix Product State was encountered for the first time in another seminal paper by Klümper, Schadschneider and Zittartz [7]. In that work the authors show that the ground state of a certain class of spin-1 quantum antiferromagnetic chains has a very special structure which can be expressed in terms of matrix products. The MPS as introduced by Klümper and coworkers are a straightforward generalization of VBS and FCS. It is interesting to notice that for some 8 years the two fields of specially structured ground states for exactly solvable models (VBS, FCS, MPS) and the numerical renormalization methods were developing in parallel without noticing how much they have in common. It was only in 1995 that Rommer and Östlund opened in their seminal work [3] the door to what was about to become a very fruitful cross-fertilization between mathematical physics (condensed matter theory) and numerical physics (renormalization group methods). Some years later tools from quantum information theory (entanglement theory in many-qubit systems) were introduced into the MPS realm when the role of entanglement in quantum phase transitions of strongly correlated systems started to be increasingly investigated and understood [8, 9, 10, 11].

Since then there has been an explosion in this field leading to a much better understanding of strongly correlated systems via MPS and their generalizations. One particularly important generalization was due to Verstraete and Cirac in their 2004 paper [12] where the MPS concept is extended to higher dimensional lattices. In that work the authors introduce a new class of states called *Projected Entangled Pair States* (PEPS) which can be arbitrarily adapted to the actual geometry of the model under consideration. Another important contribution was made by Vidal in 2006 [13]. In that work the linear MPS entanglement structure is generalized to accommodate for a tree-like structure. States generated by Vidal's *Multiscale Entanglement Renormalization Ansatz* MERA can accommodate for long-range entanglement in a very natural way. This class of states turns out to be particularly useful in the context of critical systems where the fixed point of an entanglement renormalization procedure is such a MERA state with identical tensors on all levels of the entanglement tree.

This thesis is the result of our efforts towards the development of new algorithms for the simulation of one-dimensional strongly correlated systems with MPS. Our algorithms are designed to improve existing ones both in terms of the achievable precision and in terms of the required computational cost. As a side-product we obtain some deeper insights into the MPS concept itself. For instance we observe how the finite correlation length of MPS impacts simulations of critical systems. This will teach us how MPS simulations must be performed if one wants to properly capture global properties of critical systems. Furthermore we observe how a special MPS based ansatz for the approximation of excitations is particularly well suited to simulate single-particle states and how it gradually becomes less and less precise if one is moving towards many-particle states with increasing momentum. The results presented in this thesis can be transferred to other directions of similar research like the recently introduced *continuous MPS* (cMPS) [14] in one-dimensional systems.

Regarding the computational efficiency, the most relevant parameter for the scaling of the computational cost of MPS-algorithms is the so-called virtual bond dimension D. D gives an upper bound[1] for the maximal amount of entanglement that a MPS can contain. Another important parameter that affects the computational cost in the case of finite chains is the system size N. We are able to eliminate N from most of the algorithms by using exclusively translationally invariant (TI) MPS ansätze for the simulation of translationally invariant systems. However we must emphasize that even with the use of TI MPS it is not possible to eliminate the factor N (or relics thereof) from all algorithms. Improving the D and N scaling of the computational cost in simulations of translationally invariant systems will be one of the main goals in this thesis.

Outline and Summary of the results

Chapter 1: In this chapter we show how to obtain exact Matrix Product Operator (MPO) representations of exponentials of certain operators that often appear as the building blocks of common spin Hamiltonians. These MPO can be used in order to approximate the imaginary or real time evolution operator for these systems. We then present an algorithm based on imaginary time evolution of MPS that converges towards the ground state of the system. The core of the algorithm is the so-called ”bond dimension cut” procedure which we show to be optimal in a certain sense. We present results obtained for the Quantum Ising and the spin-$1/2$ Heisenberg chain. The precision of the ground state energy turns out to scale polynomially in the bond dimension of the used MPS. A feature that proves to be very useful from the computational point of view is the fact that our MPO matrices are real and symmetric. This property yields our algorithm very robust and efficient[1]. In a further step we then present a method for obtaining Matrix Product Operator representations of Hamiltonians with long-range interactions. For exponentially decaying interactions, we are able to obtain the exact MPO, while for polynomially decaying interactions we show how they can be approximated by sums of exponentials, which in turn can be exactly represented as MPO. In the appendix of this chapter we present previously unpublished results for a real and symmetric MPO representation of the imaginary time evolution operator for the spin-1 Bilinear-Biquadratic chain and for the spin-1/2 Heisenberg ladder.

---

[1] Actually D is the Schmidt number for a bipartite cut between two sites of the system.

Chapter 2: In this chapter we introduce a new gradient-based algorithm for the simulation of translationally invariant quantum spin chains with periodic boundary conditions (PBC). The reason why systems with periodic boundary conditions are very interesting to investigate, is the fact that they approach the thermodynamic limit much faster than systems with open boundary conditions. It turns out that the gradient of the energy of MPS with PBC can be nicely expressed as a sum of open tensor networks that can be more or less efficiently contracted. Depending on the chain length N and on the correlation length ξ of the system[2], the computational cost scales between $O(nD^3)+O(mD^3)$ and $O(n^2D^3)+O(nmD^3)$, where n and m are parameters depending on the size of the system and on the amount of correlations (entanglement) of the ground state. In order to avoid getting stuck in local minima, we must use as a starting point for the gradient search a MPS that is reasonably close to the one that minimizes the energy. It turns out that the MPS obtained in Chapter 1 via imaginary time evolution of the infinite chain for the same model is ideally suited for this purpose. In this way the numerical results obtained in Chapter 2 are built on top of the ones obtained in Chapter 1, since the usage of any other starting MPS yields suboptimal results.

Conceptually, the main finding of Chapter 2 is that in the case of critical systems with PBC, MPS simulations are much more complex than previously assumed (e.g. in [15]). We show how this complexity can be accounted for and we present a method of how to scan the parameter plane $\{n, m\}$ in order to find the optimal pair beyond which the MPS ground state energy can not be further reduced. On top of this we find strong hints towards the presence of two different regimes in MPS simulations of critical systems. The transition between these regimes is then extensively studied in Chapter 3.

Chapter 3: In this chapter we make heavily use of the algorithm developed in Chapter 2 in order to study MPS simulations of critical spin chains with PBC. Our analysis reveals the existence of two different regimes for MPS simulations: the *Finite Size Scaling* (FSS) regime and the *Finite Entanglement Scaling* (FES) regime. The two regimes are separated by the so-called *critical line* where the induced correlation length is equal to the system size, i.e. $\xi_D = N$. The FES regime is defined by $\xi_D < N$; the FSS regime is defined by $\xi_D > N$; thus MPS simulations in the FSS regime are much more expensive from a computational point of view. We show that global properties[1] of critical chains are only faithfully captured in the FSS regime, while for local properties[2] it is enough to run the simulation in the FES regime. Furthermore we show how to precisely detect the transition from the FES to the FSS regime, in order to optimize the cost necessary for the computation of global properties of the ground state. Additionally we give strong evidence for the persistence of the transition between the two regimes in the thermodynamic limit[3]. This finding is very important since it shows that in order to do a proper scaling analysis of global properties, one has to ensure that all simulations are performed in the FSS regime. If one is merely interested in the scaling analysis of local observables like the energy, it is enough to remain in the FES regime, which allows for a considerable computational speed-up. In the appendix of this chapter, we give an alternative derivation of the result of Pollmann et al. [16] relating the bond dimension of the MPS to the effective correlation length ξ_D, as well as a detailed comparison between older PBC algorithms [17, 15] and the one presented in Chapter 2.

---

[1] The scaling of the computational cost is with $O(D^3)$ not better than in other algorithms, however the fact the the MPS transfer matrix is real and symmetric reduces the constant factor in front of D^3 considerably.

[2] In this context we must differentiate between the genuine correlation length of the Hamiltonian ξ_H and the correlation length induced by MPS with finite bond dimension D, ξ_D. Generally speaking, the relevant correlation length for MPS simulations is always the smaller one. For critical Hamiltonians with diverging ξ_H, the relevant correlation length is always $\xi = \xi_D$, while for non-critical systems, it is given by $\xi = \min(\xi_H, \xi_D)$.

Chapter 4: In this chapter we present an algorithm for the approximation of the low-energy spectrum of translationally invariant Hamiltonians with PBC. The main idea here is to use the TI ground state MPS obtained in chapter 2 as the backbone of an ansatz for states with well defined momentum. We use these states in order to project the Hamiltonian onto subspaces with fixed momentum and then we solve an eigenvalue problem in order to obtain the full low-energy spectrum of states with that momentum. In this way we obtain surprisingly accurate results for the lower branches of excitations of several different models. In the case of the Quantum Ising model we observe certain strange looking jumps in the precision of the energy of different branches. A careful study of the analytical solution and subsequent comparison with the simulations reveals that the jumps occur between states with different numbers of quasi-particles. The states that are best approximated are one-particle states, which makes perfectly sense since our ansatz is reminiscent of one-particle Bloch states. For the Quantum Ising model, our results show how a certain ambiguity that appears in the exact solution can be fixed by demanding the quasi-particle excitations to have positive energy[4]. Furthermore we compare our results obtained for several other models with previous work and we show that our algorithm performs better in almost all cases.

---

[1] E.g. overlap with the exact ground state or long-range correlation functions.

[2] E.g. the energy density of the MPS.

[3] We are able to show this only for the Quantum Ising model. For the Heisenberg model we are not able to do the same as the required precision of the MPS simulations is not achievable on present-day computers.

[4] In principle one could choose the quasi-particle energy to be negative, which would correspond to hole-excitations.

Appendix A: We conclude the thesis with a very detailed derivation of the exact spectrum for the Quantum Ising model with PBC. Even though the raw outline of the derivation was previously known [18], we point out some details that we could not find in the literature. The most important thing to notice is that for $g < 1$ there exists an ambiguity in the definition of the Bogoliubov modes which may lead to a flip of the sign of the parity operator. The numerical results from Chapter 4 however raise this ambiguity by showing that in this region of the phase diagram there exist no one-particle states, which then constrains the quasi-particle definition to the physical one.

Chapter 1

Matrix Product Operator Representations

Synopsis:

We show how to construct relevant families of matrix product operators in one dimension. Those form the building blocks for the numerical simulation methods based on matrix product states. In particular, we construct translationally invariant matrix product operators suitable for time evolution, and show how such descriptions are possible for Hamiltonians with long-range interactions. We show how those tools can be exploited for constructing new algorithms for simulating quantum spin systems.

Based on:
B. Pirvu, V. Murg, J.I. Cirac and F. Verstraete,
New J. Phys. **12**, 025012 (2010)

Changes compared to published version: parts not directly connected to the rest of the thesis removed, main text adapted, relevant unpublished calculations appended (Appendix A, B and C).

1.1 Introduction

The study of strongly correlated quantum systems is currently receiving a lot of attention. To a large extent, this is due to the formidable progress that has been made in creating such systems under controlled laboratory conditions such as in optical lattices and ion traps. From the theoretical point of view, major new insights have been obtained into characterizing the nature of the wavefunctions associated to those strongly correlated systems. The concept of matrix product states and their generalizations plays a central role in those new insights, as it provides a sound foundation and justification for the success of numerical renormalization group methods and especially of DMRG [2, 19]. Those insights have led to the development of new algorithms for simulating quantum spin systems; most notable are the algorithms for simulating time evolution [10, 20, 21, 22] and the ones generalizing DMRG to higher dimensions [12].

In this work, we are concerned with the efficient construction of so-called matrix product operators (MPO), the basic building blocks for those novel algorithms. MPO were introduced in the paper [22, 23] and form the operator analogue of matrix product states. We will show how to construct translationally invariant MPOs in one dimension that approximate real or imaginary time evolution; in contrast to the TEBD/DMRG algorithms [20, 21], the translational symmetry is not broken in the Trotter step. This generalizes the constructions reported in [24]. Second, we construct MPO descriptions for general Hamiltonians with decaying long-range interactions. This is very interesting in the light of simulating quantum spin systems with long-range interactions.

Similar work for constructing MPO representations of Hamiltonians has independently been reported in [25, 26]. Reference [26] gives a very nice presentation of matrix product operators from the point of view of DMRG, and also contains results on how to write spin chain Hamiltonians using MPO. Reference [25] explores the connection between matrix product operators and Markov processes in depth, and also contains some results on generalizations to higher dimensions. In reference [27], an algorithm is devised to simulate quantum spin chains with long-range interactions in the thermodynamic limit; it also contains similar results as reported here on the approximation of power law decaying interactions by sums of exponentials.

1.2 Matrix Product Operator descriptions of exponentials

1.2.1 Construction

Let us first start with a simple example: suppose we want to simulate the real or imaginary time evolution under the Quantum Ising Hamiltonian

$$H_{IS} = -\sum_i \sigma_i^z \sigma_{i+1}^z - B \sum_i \sigma_i^x \tag{1.1}$$

where only nearest neighbour interactions are considered; only the one-dimensional case will be considered. As usual, this evolution can be approximated using a Trotter expansion, but we want to do this in such a way that the translational invariance is not broken. To this end we split the Hamiltonian in two parts containing only terms commuting among eachother as follows: $H_{IS} = H_z + H_x$. H_z contains all terms with the σ^z operators and H_x the ones with the σ^x. The first order Trotter expansion [1] of the imaginary time evolution operator with respect to this decomposition reads $\exp(-\epsilon H_{IS}) = \exp(-\epsilon H_x)\exp(-\epsilon H_z)$. Of course $\exp(-\epsilon H_x)$ has a trivial MPO description as it is a product of strictly local operators.

Let us show now that $\exp(-\epsilon H_z)$ has a very simple and elegant MPO description that is translationally invariant. In the following we will use whenever possible for the Pauli matrices the shorter notation: $X := \sigma^x$, $Y := \sigma^y$ $Z := \sigma^z$. Since $Z^2 = \mathbb{1}$ we have

$$\begin{aligned} e^{\epsilon Z\otimes Z} &= \mathbb{1}_{4\times 4} + \epsilon Z\otimes Z + \frac{\epsilon^2}{2!}\mathbb{1}\otimes\mathbb{1} + \frac{\epsilon^3}{3!}Z\otimes Z + \frac{\epsilon^4}{4!}\mathbb{1}\otimes\mathbb{1} + \dots \\ &= \cosh(\epsilon)\mathbb{1}\otimes\mathbb{1} + \sinh(\epsilon) Z\otimes Z \\ = \underbrace{\begin{pmatrix}\sqrt{\cosh(\epsilon)} & 0\end{pmatrix}}_{\langle B_0|} &\begin{pmatrix}\sqrt{\cosh(\epsilon)} \\ 0\end{pmatrix} \underbrace{\mathbb{1}\otimes\mathbb{1}}_{O_0\otimes O_0} + \underbrace{\begin{pmatrix}0 & \sqrt{\sinh(\epsilon)}\end{pmatrix}}_{\langle B_1|} \begin{pmatrix}0 \\ \sqrt{\sinh(\epsilon)}\end{pmatrix} \underbrace{Z\otimes Z}_{O_1\otimes O_1} \end{aligned} \tag{1.2}$$

Thus $e^{\epsilon Z\otimes Z}$ can be expressed in terms of the incomplete local matrix basis $\{O_0, O_1\}$ where $O_0 = \mathbb{1}$ and $O_1 = Z$ (or $O_\alpha = Z^\alpha$) as

$$e^{\epsilon Z\otimes Z} = \sum_{\alpha=0}^{1} \langle B_\alpha | B_\alpha\rangle\, O_\alpha \otimes O_\alpha \,. \tag{1.3}$$

For the next step we will assume that our system has periodic boundary conditions (PBC) since this assumption will allow us to write $\exp(\epsilon H_z)$ as a translationally invariant MPO. Explicitly it reads

$$\begin{aligned} e^{\epsilon\sum_i Z_i Z_{i+1}} &= \prod_{i=1}^{N_{PBC}} \left[e^{\epsilon Z\otimes Z}\right]_{i,i+1} \\ &= \sum_{\alpha_1,\alpha_2,\dots,\alpha_N} \left[\, \langle B_{\alpha_1}|B_{\alpha_1}\rangle \langle B_{\alpha_2}|B_{\alpha_2}\rangle \dots \langle B_{\alpha_N}|B_{\alpha_N}\rangle \,\right] \\ &\qquad O_{\alpha_1}O_{\alpha_N} \otimes O_{\alpha_1}O_{\alpha_2} \otimes O_{\alpha_2}O_{\alpha_3} \otimes \dots \otimes O_{\alpha_{N-1}}O_{\alpha_N} \,. \end{aligned} \tag{1.4}$$

Note however that due to $\langle B_\alpha|B_\beta\rangle \propto \delta_{\alpha\beta}$ we can introduce further summation indices as

---

[1] The Trotter error is very big when using the first order Trotter decomposition. In practical simulations we use second or higher order, however for illustration purposes the first order is enough.

$$
\begin{aligned}
e^{\epsilon \sum_i Z_i Z_{i+1}} &= \prod_{i=1}^{N_{PBC}} \left[e^{\epsilon Z \otimes Z} \right]_{i,i+1} \\
&= \sum_{\substack{\alpha_1,\alpha_2,\ldots,\alpha_N \\ \beta_1,\beta_2,\ldots,\beta_N}} \Big[\langle B_{\alpha_1} | B_{\beta_1} \rangle \langle B_{\alpha_2} | B_{\beta_2} \rangle \ldots \langle B_{\alpha_N} | B_{\beta_N} \rangle \Big] O_{\alpha_1} O_{\beta_N} \otimes O_{\beta_1} O_{\alpha_2} \otimes \cdots \otimes O_{\beta_{N-1}} O_{\alpha_N} \\
&= \sum_{\substack{\alpha_1,\alpha_2,\ldots,\alpha_N \\ \beta_1,\beta_2,\ldots,\beta_N}} \mathrm{Tr}\Big[|B_{\beta_N}\rangle \langle B_{\alpha_1} | B_{\beta_1} \rangle \ldots |B_{\beta_{N-1}}\rangle \langle B_{\alpha_N}| \Big] O_{\alpha_1} O_{\beta_N} \otimes O_{\beta_1} O_{\alpha_2} \otimes \cdots \otimes O_{\beta_{N-1}} O_{\alpha_N} \, .
\end{aligned} \tag{1.5}
$$

The expression above is precisely of the form of a Matrix Product Operator (MPO) with PBC, i.e.

$$
e^{\epsilon \sum_i Z_i Z_{i+1}} = \sum_{\gamma_1,\gamma_2,\ldots,\gamma_N} \mathrm{Tr}\Big[C_{\gamma_1} C_{\gamma_2} \ldots C_{\gamma_N} \Big] \Omega_{\gamma_1} \otimes \Omega_{\gamma_2} \otimes \cdots \otimes \Omega_{\gamma_N} \tag{1.6}
$$

if we manage to merge the pairs of indices $\{\beta_i, \alpha_{i+1}\}$ into a single index γ_i. In (1.6) the $\{\Omega_\gamma\}$ represent a basis for $d \times d$ Hermitian matrices which must not be necessarily complete. d stands for the physical dimension of the spins (i.e. $d = 2$ in the case of spin-$1/2$). The $D \times D$ matrices C_γ are MPO matrices with arbitrary virtual bond dimension D.

The merging we mentioned above can be easily done. First we notice that even though there are four possible combinations of $O_\beta O_\alpha$ since $\alpha, \beta \in \{0, 1\}$, most of them yield the same result, leaving us with only two distinct one-site operators:

$$
\begin{aligned}
\Omega_0 &= \mathbb{1} = O_0 O_0 = O_1 O_1 \\
\Omega_1 &= Z = O_0 O_1 = O_1 O_0
\end{aligned} \tag{1.7}
$$

The matrix coefficients of the Ω_γ read then:

$$
\begin{aligned}
C_0 &= \begin{pmatrix} \cosh(\epsilon) & 0 \\ 0 & \sinh(\epsilon) \end{pmatrix} = |B_0\rangle \langle B_0| + |B_1\rangle \langle B_1| \\
C_1 &= \begin{pmatrix} 0 & \sqrt{\sinh(\epsilon)\cosh(\epsilon)} \\ \sqrt{\sinh(\epsilon)\cosh(\epsilon)} & 0 \end{pmatrix} = |B_0\rangle \langle B_1| + |B_1\rangle \langle B_0| \quad .
\end{aligned} \tag{1.8}
$$

We have therefore proven that $\exp(-\epsilon H_z) = \exp\left(\epsilon \sum_i Z_i Z_{i+1}\right)$ has a very efficient matrix product description with the matrices C_γ. A big advantage of this precise MPO formulation is that it is symmetric; the spectral properties of the associated transfer operator are hence well behaved, which is important if used in algorithms with periodic boundary conditions [28, 29].

From numerical considerations, it is useful if the matrices/tensors occurring in the MPO description are real and symmetric. There are some tricks of how to achieve this in case the previously described method does not automatically yield such MPO. Consider for example the Heisenberg antiferromagnetic Hamiltonian

$$H_{HB} = \frac{1}{4}\sum_{i=1}^{N}(\sigma_i^x\sigma_{i+1}^x + \sigma_i^y\sigma_{i+1}^y + \sigma_i^z\sigma_{i+1}^z) = \frac{1}{4}(H_x + H_y + H_z) \ . \tag{1.9}$$

The operator $\exp(-\epsilon H_{HB})$ can be decomposed in Trotter steps consisting of H_x, H_y, H_z, and every Trotter term involves operators of the form $\exp(-\epsilon H_x)$. As we saw in the previous section, the associated matrices involve terms like $\sqrt{\sinh(-\epsilon)}$, which becomes complex when $\epsilon > 0$. What we can do however is a change of basis on every second site (this obviously only works for bipartite lattices), where we rotate the spins with the unitary operator $Y = \sigma^y$; this maps $X_{2n} \to -X_{2n}, Y_{2n} \to Y_{2n}, Z_{2n} \to -Z_{2n}$. On the level of the Hamiltonian, this flips the sign of the H_x and H_z interactions, for which the associated operators $\exp(+\epsilon H_x)$ have indeed real and symmetric MPO descriptions. The problem seems to remain however with the operator $\exp(-\epsilon H_y)$. This can however easily be cured by defining the real antisymmetric matrix $\tilde{Y} := iY$ for which $\tilde{H}_y = -H_y$ when we replace all operators Y by $\tilde{Y}$. Next, $\exp(+\epsilon\tilde{H}_y)$ can again be expressed as a MPO; however, we have to be careful as $\tilde{Y}\cdot\tilde{Y} = -\mathbb{1}$ as opposed to $+\mathbb{1}$. Explicitly the derivation goes along the same lines like before

$$\begin{aligned} e^{-\epsilon Y\otimes Y} &= \mathbb{1}_{9\times 9} - \epsilon Y\otimes Y + \frac{\epsilon^2}{2!}\mathbb{1}\otimes\mathbb{1} - \frac{\epsilon^3}{3!}Y\otimes Y + \frac{\epsilon^4}{4!}\mathbb{1}\otimes\mathbb{1} - \dots \\ &= \cosh(\epsilon)\mathbb{1}\otimes\mathbb{1} - \sinh(\epsilon)Y\otimes Y \\ = \underbrace{\begin{pmatrix}\sqrt{\cosh(\epsilon)} & 0\end{pmatrix}}_{\langle B_0|} &\begin{pmatrix}\sqrt{\cosh(\epsilon)}\\ 0\end{pmatrix}\underbrace{\mathbb{1}\otimes\mathbb{1}}_{O_0\otimes O_0} + \underbrace{\begin{pmatrix}0 & \sqrt{\sinh(\epsilon)}\end{pmatrix}}_{\langle B_1|}\begin{pmatrix}0\\ \sqrt{\sinh(\epsilon)}\end{pmatrix}\underbrace{iY\otimes iY}_{O_1\otimes O_1} \end{aligned} \tag{1.10}$$

Following the same steps that led from 1.5 to 1.7 we define the operators Ω_γ as

$$\begin{aligned} \Omega_0 &= \mathbb{1} = O_0O_0 = -O_1O_1 \\ \Omega_1 &= iY = O_0O_1 = O_1O_0 =: \tilde{Y} \ . \end{aligned} \tag{1.11}$$

Note that we have inserted a minus sign in front of the O_1O_1 term which must be accounted for in the matrices C_γ accordingly

$$\begin{aligned} C_0 &= \begin{pmatrix}\cosh(\epsilon) & 0\\ 0 & -\sinh(\epsilon)\end{pmatrix} = |B_0\rangle\langle B_0| - |B_1\rangle\langle B_1| \\ C_1 &= \begin{pmatrix}0 & \sqrt{\sinh(\epsilon)\cosh(\epsilon)}\\ \sqrt{\sinh(\epsilon)\cosh(\epsilon)} & 0\end{pmatrix} = |B_0\rangle\langle B_1| + |B_1\rangle\langle B_0| \ . \end{aligned} \tag{1.12}$$

Together with the fact the $\tilde{Y}$ is real we have thus indeed obtained a MPO which is real and symmetric.

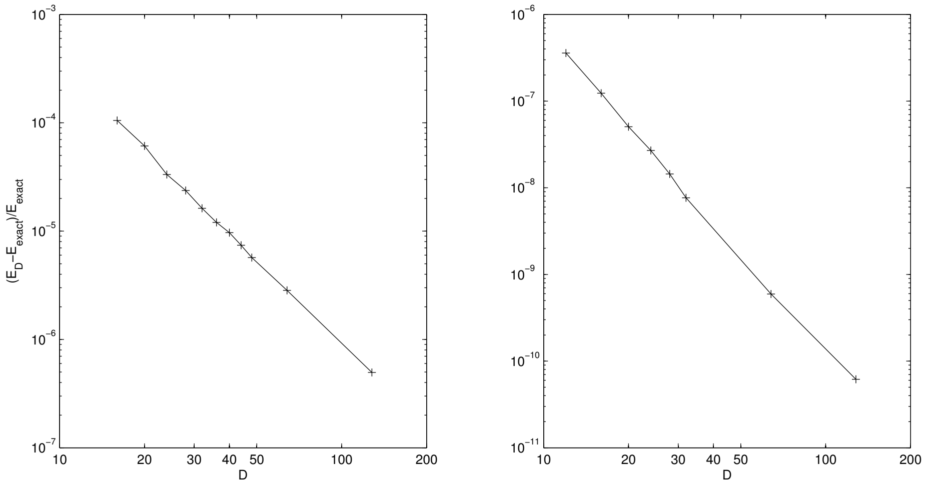

Figure 1.1: Dependence of the precision $(E_D - E_{exact})/|E_{exact}|$ on the bond dimension D for the Heisenberg antiferromagnetic spin chain (left) and the critical Ising chain in a transverse field (right)

1.2.2 Algorithms

It is now obvious how to turn those MPO-descriptions to our advantage for constructing new algorithms for the simulation of quantum spin chains.

Let us first consider the case of imaginary time evolution, where the goal is to evolve a state in imaginary time such as to simulate a thermal (finite β) or ground state ($\beta \to \infty$). Obviously, we will use the Trotterization described in the previous section. The big advantage there is that the translational invariance is never broken, and furthermore that the matrices involved in the MPS description of the MPO are real and symmetric. In particular, that means that, if we start with a translationally invariant MPS with real symmetric MPS description, then it will stay like that during the whole course of the evolution. This has a dramatic effect on the numerical conditioning and stability of the algorithm.

The algorithm for time evolution is now as follows: given a translationally invariant MPS with matrices $\{A_\alpha\}$ with bond dimension D and MPO with matrices $\{C_\alpha\}$, $\{\Omega_\alpha\}$ of dimension D', we want to find a way of representing cutting the bond dimension of the MPS $\{\bar{A}_\alpha\}$ given by

$$\bar{A}_\alpha = \sum_{\beta\gamma} A_\beta \otimes C_\gamma \, \langle\alpha|X_\gamma|\beta\rangle \tag{1.13}$$

in an optimal way. This can easily be done as follows: calculate the leading eigenvector $|\lambda_1\rangle$ of the transfer operator $E = \sum_\alpha \bar{A}_\alpha \otimes \bar{A}_\alpha$ (note that E is symmetric and as such this is a very well conditioned problem). Rewriting $|\lambda_1\rangle$ as a $DD' \times DD'$ positive semidefinite matrix ρ with $\mathrm{vec}(\rho) := |\lambda_1\rangle$, we can easily calculate its eigenvalue decomposition $\rho = U\Sigma U^\dagger$. We now define the projector/isometry P as the rectangular matrix consisting of the first D rows of

U, and act with this P on the matrices $\bar{A}_\alpha$. The updated matrices A_α are therefore obtained by $A_\alpha = P^\dagger \bar{A}_\alpha P$ which is obviously still symmetric and real. Clearly, all those steps have to be done in such a way as to exploit the sparse nature of the problem, such as done in DMRG, which leads to a complexity that scales like D^3. Also, if the eigenvalues that are thrown away are not small enough, we can always increase the bond dimension.

The big advantage of this procedure is that it is extremely well conditioned and very efficient to implement. This allows to go to very large bond dimensions. Notably, as compared to the original formulation of the iTEBD algorithm [30], we do not have to take inverses at any time (because the gauge degrees of freedom are trivial as they consist of unitary matrices), and furthermore it works equally well if the MPO is very far from the identity operator.

We have tested those new algorithms on the critical Ising and Heisenberg spin chain models, and obtained results that are consistent with what we expected. In particular, for the Heisenberg antiferromagnetic spin chain, we obtain a precision of $(E_{D=64} - E_{exact})/|E_{exact}| = 2.83 \cdot 10^{-6}$ with very modest calculations. In the case of the critical Ising chain in a transverse field, we get $(E_{D=64} - E_{exact})/|E_{exact}| = 1.10 \cdot 10^{-9}$. The dependence of the precision on the bond dimension D can be gathered from figure 1.1. Note that the precision follows a power law in the bond dimension, a fact which we will analyze further in chapter 3.

1.3 Matrix Product Operator descriptions of Hamiltonians with long-range interactions

1.3.1 Construction

Let us next investigate how to represent Hamiltonians with long-range interactions of the form

$$H = \sum_{ij} f(i-j) \cdot Z_i Z_j \tag{1.14}$$

with $f(i-j)$ some decaying function. The first question to ask is whether it is still possible to find an exact MPO description of $\exp(-\epsilon H)$. It can easily be seen that this is not possible if the function $f(x)$ does not vanish at some finite distance: otherwise, the action of $\exp(-\epsilon H)$ on a MPS could increase the Schmidt number over any cut with an arbitrary large amount, and hence no finite MPO description is possible. This is the reason why the transfer matrix approach in classical 1-D spin systems breaks down for such long-range interactions.

So let's be less ambitious and try to find a MPO description of the Hamiltonian itself. This is interesting for several reasons: first, this is useful in constructing algorithms for time evolution using iterative methods like Lanczos, and second, it allows to calculate quantities like $\langle\psi|H^2|\psi\rangle$ efficiently.

As a start, let us consider a general 1-D spin 1/2 Hamiltonian with nearest neighbour interactions. If the Hamiltonian is translationally and reflection invariant, then there always exists a basis such that the Hamiltonian can be written as

$$H = \sum_{\alpha,i} \mu_\alpha \sigma_i^\alpha \otimes \sigma_{i+1}^\alpha + \sum_j \hat{O}_j \tag{1.15}$$

where $\hat{O}$ can be any one-qubit operator. Similarly to the construction of MPS descriptions of the W-state [31], a MPO can be constructed to represent this H by making use of nilpotent matrices:

$$\begin{aligned}
&H = \sum_{i_1 i_2 \ldots} \left(v_l^T C_{i_1} C_{i_2} \ldots C_{i_N} v_r\right) \Omega_{i_1} \otimes \Omega_{i_2} \otimes \ldots \otimes \Omega_{i_N} \\
&\Omega_0 = \mathbb{1} \qquad \Omega_1 = \sigma^x \qquad \Omega_2 = \sigma_y \qquad \Omega_3 = \sigma_z \qquad \Omega_4 = \hat{O} \\
&v_l = |0\rangle \qquad v_r = |4\rangle \\
&C_0 = |0\rangle\langle 0| + |4\rangle\langle 4| \\
&C_1 = |0\rangle\langle 1| + \mu_1 |1\rangle\langle 4| \qquad C_2 = |0\rangle\langle 2| + \mu_2 |2\rangle\langle 4| \qquad C_3 = |0\rangle\langle 3| + \mu_3 |3\rangle\langle 4| \\
&C_4 = |0\rangle\langle 4|
\end{aligned} \tag{1.16}$$

The simplest way of deriving this is to think about the Hamiltonian as a Markov process with 5 possible symbols (remember that MPS can be constructed using Markov processes), such that a symbol $\Omega_1, \Omega_2, \Omega_3$ is always followed by itself and then all zeros Ω_0, and Ω_4 by all zeros. As such, one can easily prove that $D = 5$ is optimal in this case because this is the operator Schmidt number of the Hamiltonian when splitting it into two pieces. Note that if only Ising interactions would have been considered, then $D = 3$ would have been sufficient and we could have chosen

$$C_0 = |0\rangle\langle 0| + |2\rangle\langle 2| \qquad C_1 = |0\rangle\langle 1| + \mu_1 |1\rangle\langle 2| \quad . \tag{1.17}$$

Note that there is no need for C_2, C_3, C_4 in that case.

It is obvious how to generalize this description to the case of exponentially decaying interactions. By adding diagonal terms to C_0

$$B_0 = |0\rangle\langle 0| + \lambda_x |1\rangle\langle 1| + \lambda_y |2\rangle\langle 2| + \lambda_z |3\rangle\langle 3| + |4\rangle\langle 4| \tag{1.18}$$

we can immediately check that that the corresponding Hamiltonian / MPO is given by

$$H = \sum_{\alpha, i<j} \mu_\alpha \lambda_\alpha^{i-j} \cdot \sigma_i^\alpha \otimes \sigma_j^\alpha + \sum_j \hat{O}^j \tag{1.19}$$

which is a spin chain with exponentially decaying interactions.

Unfortunately, it is impossible to get exact MPO descriptions when the interactions are decaying following a power law. However, inverse polynomials can pretty well be approximated by sums of exponentials (this is the reason why DMRG is able to reproduce the correlations in critical models pretty well). Hamiltonians with power law decay of correlations can therefore be well approximated by sums of MPO's, which is itself a MPO. Actually, very few exponentials are needed to get a good approximation, even at large distances. The problem of finding the optimal weights $\{x_i\}$ and $\{\lambda_1\}$ for such an approximation problem for a general function $f(k)$, i.e.

$$\min_{x_i,\lambda_i} \sum_{k=1}^{N} |f(k) - \sum_{i=1}^{n} x_i \lambda_i^k| \ , \tag{1.20}$$

is not completely trivial. In the appendix, we present a simple method that solves this optimization problem for general $f(k)$ and a given number of exponentials n and a number of sites $N > n$ (the method works for any functions, and returns complex exponents in the case of oscillating functions as should be). If we choose power law decay with power 3, N=1000 and n=10 then the above cost function is 10^{-5} (the maximal difference between the function and the approximated one is $5 \cdot 10^{-8}$). This maximal difference falls to $3 \cdot 10^{-6}$ for power 2 and $3 \cdot 10^{-4}$ for power 1.

In conclusion, we found the exact MPO description for Hamiltonians with exponentially decaying interactions. Hamiltonians with power law decay can be approximated very well using sums of such MPO. The matrix product operators obtained for the description of Hamiltonians are of a very different form than the ones obtained by taking the exponential. The main difference is that the corresponding transfer matrices will always contain a Jordan block structure, and one has to be careful in dealing with such situations when considering the thermodynamic limit. A further investigation of MPO for systems with long-range interactions can be found in [32].

1.4 Conclusion

In conclusion, we constructed several examples of interesting families of matrix product operators in one dimension. Those descriptions turn out to be very valuable for constructing stable and scalable algorithms for simulating quantum spin systems. In the appendices we have given detailed derivations of the MPOs for the imaginary time evolution operators of the Bilinear-Biquadratic spin-1 chain and of the spin-$1/2$ Heisenberg ladder. Furthermore we presented a proof for the fact that the bond dimension cut we use in the imaginary time evolution algorithm is optimal in a certain sense.

1.5 Appendix A: Optimal cut of the MPS bond dimension during imaginary time evolution

1.5.1 Imaginary time evolution for the infinite chain

The imaginary time evolution of a typical random state converges exponentially fast to the ground state manifold of the respective system. For TI systems in the thermodynamic limit, if there is a TI-MPO representation of the time evolution operator available, the algorithm to find the ground state has been presented in section 1.2.2. Here we give the proof of why the bond dimension cutting method presented there is indeed optimal in a certain sense.

The TI MPS representation of a given state with N sites and PBC has the usual form

$$|\psi\rangle = \sum_{i_1,i_2,\dots i_N} \mathrm{Tr}(A_{i_1}A_{i_2}\dots A_{i_N})\, |i_1\rangle \otimes |i_2\rangle \otimes \dots \otimes |i_N\rangle \quad . \tag{1.21}$$

At the beginning of the algorithm this is just a random state with identical matrices A_i at every site. For an arbitrary TI MPO-representation of the imaginary time evolution operator

$$\exp\left(-\tau H\right) \approx \sum_{k_1,k_2,\dots k_N} \mathrm{Tr}(C_{k_1}C_{k_2}\dots C_{k_N})\Omega_{k_1} \otimes \Omega_{k_2} \otimes \dots \otimes \Omega_{k_N} \quad , \tag{1.22}$$

the MPS-matrices after the time evolution step are given by (see Eq. 1.13)

$$\bar{A}_i = \sum_{jk} A_j \otimes C_k \,\langle i|\Omega_k|j\rangle \quad . \tag{1.23}$$

For the sake of simplicity we have ommited in our notation the τ dependency in the MPO-matrices (actually $B_{k_i} = B_{k_i}(\tau)$) as well as the site index, since the matrices are equal on all sites ($A_{k_i} = A_k$, $B_{k_i} = B_k$).

Note that equality holds in (1.22) only if H can be expressed as a sum of commuting terms $H = \sum_\alpha H_\alpha$, $[H_\alpha, H_\beta] = 0$ and if for each $\exp\left(-\tau H_\alpha\right)$ there exists an exact MPO representation. If this is not the case, we must make a Suzuki-Trotter expansion of $\exp\left(-\tau H\right)$ in powers of τ and consider only the lowest order terms. This procedure introduces the so-called Trotter-error, which can be reduced by using higher order Suzuki-Trotter expansions and by dividing τ into a large number of very small $\delta\tau = \tau/M$ at the cost of applying $\exp\left(-\delta\tau\, H\right)$ many times

$$|GS\rangle = \lim_{M\to\infty} \left(e^{-\delta\tau\, H}\right)^M |\psi\rangle \quad . \tag{1.24}$$

In practice, due to finite numerical precision, convergence of the $|GS\rangle$ is reached after a finite number of steps M, which increases as we get closer to criticality.

Now, if the original A_i was of dimension D, $\bar{A}_i$ in (1.23) will have dimension $\bar{D} = cD$ where c is the MPO-matrix dimension. As we must repeat this step a large number of times, without any further measures the bond dimension would grow exponentially in M, making the computation very quickly unfeasible. The solution is to reduce the bond dimension $\bar{D}$ after every time evolution step back to the original one D in such a way that TI is preserved and we can perform the next step.

1.5.2 Optimal bond dimension cut for TI MPS

In this section we show how to reduce the bond dimension of a given infinite TI MPS $|\bar{\psi}\rangle$ optimally so that the newly obtained $|\psi\rangle$ minimizes the distance $\| \, |\bar{\psi}\rangle - |\psi\rangle \, \|$ to the original one and still can be represented by a TI MPS with the same symmetry properties. The proof holds only for hermitian MPS matrices $\bar{A}_i$, however it gives us a hint at how to deal with matrices that don't fulfill these requirements. We will elaborate more on this topic at the end of this section.

For the moment we assume that $\bar{A}_i$ have the required property which means that the *transfer matrix*

$$E = \sum_i \bar{A}_i \otimes \bar{A}_i^* \tag{1.25}$$

is also hermitian with conjugate left and right eigenvectors i.e. $E = \sum_j^{\bar{D}^2} \lambda_j \, |\lambda_j\rangle \, \langle\lambda_j|$. Similarly to the transfer matrix known from classical statistcal physics, it is the spectrum of (1.25) that governs the behavior of the system. Note however that in our case the transfer matrix appears only in expectation values and not in the computation of the partition function. The norm of a state $|\bar{\psi}\rangle$ with transfer matrix (1.25) and an infinite number of sites reads

$$\langle\bar{\psi}|\bar{\psi}\rangle = \lim_{N\to\infty} \mathrm{Tr}(E^N) = \lim_{N\to\infty} \sum_{j=1}^{D^2} \lambda_j^N \, \langle\lambda_j|\lambda_j\rangle = \lim_{N\to\infty} \left[\lambda_1^N + \sum_{j=2}^{D^2} \left(\frac{\lambda_j}{\lambda_1} \right)^N \right] \tag{1.26}$$

where λ_1 is the largest magnitude eigenvalue of (1.25). Therefore any $\lambda_1 \neq 1$ will yield the norm of $|\bar{\psi}\rangle$ either zero or infinite and thus ill defined. However, one can easily see that expectation values of operators acting on a finite number of sites $\langle\bar{\psi}|O_{i\ldots i+n}|\bar{\psi}\rangle \, / \, \langle\bar{\psi}|\bar{\psi}\rangle$ are well defined even for degenerate λ_1 due to the cancellation of an infinite power of λ_1 in the previous fraction. In the following we will assume that the largest eigenvalue is not degenerate, which yields for the norm $\langle\bar{\psi}|\bar{\psi}\rangle = \lambda_1^N$, from which we see that at each step of the algorithm we must renormalize the transfer matrix (1.25) such that $\lambda_1 = 1$ if we want to get a norm that is finite yet not zero in the $N \to \infty$ limit. With this in mind, the norm of such a state becomes

$$\langle\bar{\psi}|\bar{\psi}\rangle = \langle\lambda_1|\lambda_1\rangle = \mathrm{Tr}(\rho\rho^\dagger) = 1 \tag{1.27}$$

where $|\lambda_1\rangle$ is the eigenvector corresponding to the largest eigenvalue and where we have used the inverse of the vec() operation to define its *matrix form* ρ, $\mathrm{vec}(\rho) := |\lambda_1\rangle$.

Note that (1.25) acting on a vector $|\xi\rangle$ is equivalent to a CP-map acting on a matrix X with $\text{vec}(X) = |\xi\rangle$ by virtue of its Kraus operator representation $\mathcal{E}(X) = \sum_i \bar{A}_i X \bar{A}^\dagger$. For hermitian $\bar{A}_i$ one can easily check that the matrix form of eigenvectors corresponding to non-degenerate eigenvalues is also hermitian, thus (1.27) becomes $\langle\bar{\psi}|\bar{\psi}\rangle = \text{Tr}(\rho^2)$. Furthermore it is known that for CP-maps, the fixed point with the largest eigenvalue is always positive [33] which means that our ρ is also a positive matrix. Now the reason for our notation becomes obvious. Note however that ρ is no density matrix i.e. $\text{Tr}(\rho) \neq 1$. If this would be the case, (1.27) would imply that ρ is trivially proportional to $\mathbb{1}$.

Our method for the bond dimension cut under conservation of the MPS symmetry is to project the matrices $\bar{A}_i$ onto some subspace which should be chosen optimally. As we have seen, the central quantity in MPS computations is the transfer matrix E. It is the dimension of this matrix which we ultimately want to reduce. However, in order to achieve this, we must use the same projector P for all matrices $\bar{A}_i$. If we would use for every $\bar{A}_i$ a different P_i, the rank of the resulting $E = \sum_i P_i \bar{A}_i P_i \otimes P_i^* \bar{A}_i^* P_i^*$ would be arbitrary large and we would not be able to "cut" the superfluous dimensions. Thus our transformation will read

$$E = \sum_i P\bar{A}_i P \otimes P^* \bar{A}_i^* P^* = \sum_i (P \otimes P^*)(\bar{A}_i \otimes \bar{A}_i^*)(P \otimes P^*) \tag{1.28}$$

with $\text{rank}\,(E) = [\text{rank}\,(P)]^2$ if we assume that $(\bar{A}_i \otimes \bar{A}_i^*)$ has full rank. This means that the MPS $|\psi\rangle$ with reduced bond dimension reads

$$|\psi\rangle = \lim_{N\to\infty} \sum_{i_1,i_2,\dots i_N} \text{Tr}(A_{i_1} P A_{i_2} P \dots P A_{i_N} P)\, |i_1\rangle \otimes |i_2\rangle \otimes \cdots \otimes |i_N\rangle \quad . \tag{1.29}$$

It is quite clear that finding the optimal P in (1.29) is very hard. We will instead find the P that minimizes the distance from $|\bar{\psi}\rangle$ to a state where only one projector is inserted between two arbitrary sites, namely

$$|\psi\rangle = \lim_{N\to\infty} \sum_{i_1,i_2,\dots i_N} \text{Tr}(A_{i_1} A_{i_2} \dots A_{i_n} P' A_{i_{n+1}} \dots A_{i_N})\, |i_1\rangle \otimes |i_2\rangle \otimes \cdots \otimes |i_N\rangle \quad . \tag{1.30}$$

where n is arbitrary. Finding the optimal P' in (1.30) is possible and applying this P' in-between every two MPS matrices yields the desired TI MPS with reduced bond dimension. We have no proof that the optimal P' in (1.30) is equal to the one in (1.29), however there is strong evidence that this is true: *i)* applying two P' at positions in the MPS that are far enough from each other (say m sites) so that there are no correlations [1] between them (i.e. $E^m = |\lambda_1\rangle\langle\lambda_1|$) is obviously another MPS with periodicity m that minimizes the distance to $|\bar{\psi}\rangle$ under the constraint that the bond dimension is reduced at every m'th site to $\text{rank}(P)$. One could now imagine to introduce at every site between these two P' further projectors $P^{(i)}$ with

---

[1] More about the correlation length of TI MPS can be found in chapters 2 and 3.

$2 \leq i \leq m$ so that the bond dimension is reduced along the entire chain. However, since we are looking for a new TI MPS, it seems sensible to choose $P^{(i)} = P'$. *ii)* maybe even stronger evidence is the fact that in the simulations, using the optimal projector from (1.30) at every site along the chain, yields very accurate numerical results. Given these arguments we will not distinguish any more between the projectors in (1.30) and (1.29), denoting both of them by P in the following.

Using the conventions made so far in order to obtain the MPS for $|\psi\rangle$, the cost function to be minimized reads

$$\begin{aligned} \| \, |\bar{\psi}\rangle - |\psi\rangle \, \|^2 &= \langle\bar{\psi}|\bar{\psi}\rangle + \langle\psi|\psi\rangle - \langle\bar{\psi}|\psi\rangle - \langle\psi|\bar{\psi}\rangle \\ &= \mathrm{Tr}(\rho\rho) + \mathrm{Tr}(P\rho P\rho) - \mathrm{Tr}(P\rho\rho) - \mathrm{Tr}(\rho P\rho) \qquad (1.31) \\ &= \mathrm{Tr}\big[(\mathbb{1} - P)\rho(\mathbb{1} - P)\rho\big] \ . \end{aligned}$$

Defining $\tilde{P} := \mathbb{1} - P$, our new task is to find the $\tilde{P}$ that minimizes $\mathrm{Tr}(\tilde{P}\rho\tilde{P}\rho) = \mathrm{Tr}(\tilde{\rho}\tilde{\rho})$ with $\tilde{\rho} = \tilde{P}\rho\tilde{P}$. This turns out to be the projector onto the subspace spanned by the eigenvectors of ρ that correspond to the lowest magnitude eigenvalues. To see this write the matrix equation with respect to a basis in which $\tilde{\rho}$ has block diagonal form, with the lower block containing only zeros. Now we invoke the *interlacing eigenvalues theorem for bordered matrices* as stated in *Theorem 4.3.8* of [34] from which we obtain the set of inequalities $\lambda_1^{\rho} \leq \lambda_1^{\tilde{\rho}}, \lambda_2^{\rho} \leq \lambda_2^{\tilde{\rho}}, \ldots, \lambda_D^{\rho} \leq \lambda_D^{\tilde{\rho}}$. Note that here we reversed the order for the eigenvalue indexing, i.e. λ_1^{ρ} is the lowest one which, since $\rho > 0$, is also the one with lowest magnitude. Since our goal is to minimize $\mathrm{Tr}(\tilde{\rho}\tilde{\rho}) = \sum_i (\lambda_i^{\tilde{\rho}})^2$ the optimal projector $\tilde{P}$ is the one onto the subspace spanned by the eigenvectors of ρ corresponding to the lowest eigenvalues $\lambda_1^{\rho}, \ldots, \lambda_D^{\rho}$ [1]. Hence the initially searched P is the projector onto the largest eigenvalue subspace. Note that this P is exactly the one that maximizes $\langle\bar{\psi}|\psi\rangle$, thus in this specific context minimization of the distance between the original state and the one with reduced bond dimension is equivalent to maximization of their overlap.

We can use this result as a hint of how to deal with non-hermitian MPS or even with MPS with PBC. Promoting the maximization of the overlap $\langle\bar{\psi}|\psi\rangle$ to the leading principle in the search of the optimal bond dimension cut, yields in both cases satisfactory results when applied in numerical simulations. The overlap reads now $\mathrm{Tr}(M)$ with an arbitrary matrix M. The best rank D approximation to M is obtained by making a SVD and discarding the lowest magnitude eigenvalues. For hermitian M this is just the previously described procedure, however for arbitrary M the transformation is no simple projection any more. With $M = U\Sigma V^{\dagger} \approx \tilde{U}\tilde{\Sigma}\tilde{V}^{\dagger}$ the MPS matrices with reduced bond dimension read $A_i = \tilde{V}^{\dagger} A_i \tilde{U} \tilde{U}^{\dagger} \tilde{V}$.

Using this prescription for the imaginary time evolution of the OBC chain in the TL where the starting MPS matrices are non-hermitian (for real matrices non-symmetric) yields for the studied models the same results like the algorithm that starts with symmetric A_i. The matrices become during the algorithm more and more symmetric, which is basically due to the symmetry of the MPO representation of the time evolution operator.

---

[1] Note that this yields $\lambda_1^{\tilde{\rho}} = \lambda_1^{\rho}, \lambda_2^{\tilde{\rho}} = \lambda_2^{\rho}, \ldots, \lambda_D^{\tilde{\rho}} = \lambda_D^{\rho}$.

We have also implemented the imaginary time evolution of chains with PBC using this prescription. The obtained precision here was slightly worse than the one for the OBC chain. However, we have developed another method which is described in chapter 3 and which yields for a given amount of computational resources the best possible precision within the context of MPS.

1.6 Appendix B: Imaginary time evolution for the Bilinear-Biquadratic spin-1 chain

The original Hamiltonian reads

$$H = \sum_{i=1}^{N} \mathbf{S}_i \mathbf{S}_{i+1} - \beta (\mathbf{S}_i \mathbf{S}_{i+1})^2 \tag{1.32}$$

(see [35]). The one we are treating is $H' = U^\dagger H U$ where $U = \prod_{n=1}^{N/2} (e^{i\pi S_2})_{2n-1}$, i.e. a rotation on every second site. The rotation changes the sign of some terms such that the Trotter decomposition of the imaginary time evolution operator for H' can be expressed entirely in terms of real and symmetric MPO. We are working with the spin-1 representation of $SU(2)$, i.e. with the matrices

$$S_1 = X = \frac{1}{\sqrt{2}} \begin{pmatrix} 0 & 1 & 0 \\ 1 & 0 & 1 \\ 0 & 1 & 0 \end{pmatrix}, \quad S_2 = Y = \frac{1}{\sqrt{2}} \begin{pmatrix} 0 & -i & 0 \\ i & 0 & -i \\ 0 & i & 0 \end{pmatrix}, \quad S_3 = Z = \frac{1}{\sqrt{2}} \begin{pmatrix} 1 & 0 & 0 \\ 0 & 0 & 0 \\ 0 & 0 & -1 \end{pmatrix}. \tag{1.33}$$

The S_α fulfill of course the $SU(2)$ algebra (i.e. $[S_\alpha, S_\beta] = i\epsilon_{\alpha\beta\gamma} S_\gamma$) and the relation $S_\alpha^3 = S_\alpha$. This allows us to simplify the series expansions of exponentials occuring in the (imaginary) time evolution operator considerably.

1.6.1 MPO representation for $e^{\epsilon X \otimes X}$

Since $X^3 = X$ we have

$$\begin{aligned} e^{\epsilon X \otimes X} &= \mathbb{1}_{9\times 9} + \epsilon X \otimes X + \frac{\epsilon^2}{2!} X^2 \otimes X^2 + \frac{\epsilon^3}{3!} X \otimes X + \frac{\epsilon^4}{4!} X^2 \otimes X^2 + \dots \\ &= \mathbb{1} \otimes \mathbb{1} + \sinh(\epsilon) X \otimes X + \big[\cosh(\epsilon) - 1\big] X^2 \otimes X^2 \\ &= \underbrace{\begin{pmatrix} 1 & 0 & 0 \end{pmatrix}}_{\langle B_0|} \begin{pmatrix} 1 \\ 0 \\ 0 \end{pmatrix} \underbrace{\mathbb{1} \otimes \mathbb{1}}_{O_0 \otimes O_0} + \underbrace{\begin{pmatrix} 0 & \sqrt{\sinh(\epsilon)} & 0 \end{pmatrix}}_{\langle B_1|} \begin{pmatrix} 0 \\ \sqrt{\sinh(\epsilon)} \\ 0 \end{pmatrix} \underbrace{X \otimes X}_{O_1 \otimes O_1} \\ &\quad + \underbrace{\begin{pmatrix} 0 & 0 & \sqrt{\cosh(\epsilon) - 1} \end{pmatrix}}_{\langle B_2|} \begin{pmatrix} 0 \\ 0 \\ \sqrt{\cosh(\epsilon) - 1} \end{pmatrix} \underbrace{X^2 \otimes X^2}_{O_2 \otimes O_2} \end{aligned} \tag{1.34}$$

Thus $e^{\epsilon X \otimes X}$ can be expressed in terms of the incomplete local matrix basis $\{O_0, O_1, O_2\}$ where $O_0 = \mathbb{1}$, $O_1 = X$ and $O_2 = X^2$ (or $O_\alpha = X^\alpha$) as

$$e^{\epsilon X \otimes X} = \sum_{\alpha=0}^{2} \langle B_\alpha | B_\alpha \rangle \, O_\alpha \otimes O_\alpha \,. \tag{1.35}$$

The Trotterization of the time evolution operator contains string operators with periodic boundary conditions that can now be written as

$$
\begin{aligned}
e^{\epsilon \sum_i X_i X_{i+1}} &= \prod_{i=1}^{N_{PBC}} \left[e^{\epsilon X \otimes X}\right]_{i,i+1} \\
&= \sum_{\alpha_1,\alpha_2,\dots,\alpha_N} \big[\langle B_{\alpha_1} | B_{\alpha_1} \rangle \langle B_{\alpha_2} | B_{\alpha_2} \rangle \dots \langle B_{\alpha_N} | B_{\alpha_N} \rangle \big] \cdot \\
&\qquad O_{\alpha_1} O_{\alpha_N} \otimes O_{\alpha_1} O_{\alpha_2} \otimes O_{\alpha_2} O_{\alpha_3} \otimes \dots \otimes O_{\alpha_{N-1}} O_{\alpha_N} \,.
\end{aligned}
\tag{1.36}
$$

Note however that due to $\langle B_\alpha | B_\beta \rangle \propto \delta_{\alpha\beta}$ we can introduce further summation indices as

$$
\begin{aligned}
e^{\epsilon \sum_i X_i X_{i+1}} &= \prod_{i=1}^{N_{PBC}} \left[e^{\epsilon X \otimes X}\right]_{i,i+1} \\
&= \sum_{\substack{\alpha_1,\alpha_2,\dots,\alpha_N \\ \beta_1,\beta_2,\dots,\beta_N}} \Big[\langle B_{\alpha_1} | B_{\beta_1} \rangle \langle B_{\alpha_2} | B_{\beta_2} \rangle \dots \langle B_{\alpha_N} | B_{\beta_N} \rangle \Big] \cdot \\
&\qquad O_{\alpha_1} O_{\beta_N} \otimes O_{\beta_1} O_{\alpha_2} \otimes \dots \otimes O_{\beta_{N-1}} O_{\alpha_N} \\
&= \sum_{\substack{\alpha_1,\alpha_2,\dots,\alpha_N \\ \beta_1,\beta_2,\dots,\beta_N}} \mathrm{Tr}\Big[|B_{\beta_N}\rangle \langle B_{\alpha_1} | B_{\beta_1} \rangle \dots | B_{\beta_{N-1}} \rangle \langle B_{\alpha_N} | \Big] \cdot \\
&\qquad O_{\alpha_1} O_{\beta_N} \otimes O_{\beta_1} O_{\alpha_2} \otimes \dots \otimes O_{\beta_{N-1}} O_{\alpha_N} \,.
\end{aligned}
\tag{1.37}
$$

The expression above is precisely of the form of a Matrix Product Operator (MPO) with periodic boundary conditions (PBC), i.e.

$$
e^{\epsilon \sum_i X_i X_{i+1}} = \sum_{\gamma_1,\gamma_2,\dots,\gamma_N} \mathrm{Tr}\Big[C_{\gamma_1} C_{\gamma_2} \dots C_{\gamma_N} \Big] \Omega_{\gamma_1} \otimes \Omega_{\gamma_2} \otimes \dots \otimes \Omega_{\gamma_N} \tag{1.38}
$$

if we manage to merge the pairs of indices $\{\beta_i, \alpha_{i+1}\}$ into a single index γ_i. In (1.58) the $\{\Omega_\gamma\}$ represent a basis for $d \times d$ Hermitian matrices which must not be necessarily complete. d stands for the physical dimension of the spins (i.e. d=3 in the case of spin-1). The $D \times D$ matrices C_γ are MPO matrices with arbitrary virtual bond dimension D.

The merging we mentioned above can be easily done. First we notice that even though there are nine possible combinations of $O_\beta O_\alpha$ since $\alpha, \beta \in \{0, 1, 2\}$, most of them yield the same result leaving us with only three distinct one-site operators:

$$
\begin{aligned}
\Omega_0 &= \mathbb{1} &&= O_0 O_0 \\
\Omega_1 &= X &&= O_0 O_1 = O_1 O_0 = O_1 O_2 = O_2 O_1 \\
\Omega_2 &= X^2 &&= O_0 O_2 = O_2 O_0 = O_1 O_1 = O_2 O_2 \,.
\end{aligned}
\tag{1.39}
$$

The matrix coefficients of the Ω_γ read then:

$$\begin{aligned}
C_0 &= \begin{pmatrix} 1 & 0 & 0 \\ 0 & 0 & 0 \\ 0 & 0 & 0 \end{pmatrix} = |B_0\rangle\langle B_0| \\
C_1 &= \begin{pmatrix} 0 & \sqrt{\sinh(\epsilon)} & 0 \\ \sqrt{\sinh(\epsilon)} & 0 & \sqrt{\sinh(\epsilon)[\cosh(\epsilon)-1]} \\ 0 & \sqrt{\sinh(\epsilon)[\cosh(\epsilon)-1]} & 0 \end{pmatrix} \\
&= |B_0\rangle\langle B_1| + |B_1\rangle\langle B_0| + |B_1\rangle\langle B_2| + |B_2\rangle\langle B_1| \\
C_2 &= \begin{pmatrix} 0 & 0 & \sqrt{\cosh(\epsilon)-1} \\ 0 & \sinh(\epsilon) & 0 \\ \sqrt{\cosh(\epsilon)-1} & 0 & \cosh(\epsilon)-1 \end{pmatrix} \\
&= |B_0\rangle\langle B_2| + |B_2\rangle\langle B_0| + |B_1\rangle\langle B_1| + |B_2\rangle\langle B_2|
\end{aligned} \tag{1.40}$$

1.6.2 MPO representation for $e^{\epsilon Z\otimes Z}$

For $e^{\epsilon\sum_i Z_i Z_{i+1}}$ the situation is very similar. Following the same steps like above we arrive at the exact same expression (1.58) with the only difference that the basis matrices now read

$$\begin{aligned}
\Omega_0 &= \mathbb{1} &&= O_0O_0 \\
\Omega_1 &= Z &&= O_0O_1 = O_1O_0 = O_1O_2 = O_2O_1 \\
\Omega_2 &= Z^2 &&= O_0O_2 = O_2O_0 = O_1O_1 = O_2O_2\,.
\end{aligned} \tag{1.41}$$

The coefficients C_γ are the same like before.

1.6.3 MPO representation for $e^{-\epsilon Y\otimes Y}$

For $e^{-\epsilon\sum_i Y_i Y_{i+1}}$ the situation is slightly different. Due to the fact that we have the minus sign in the exponent, if we want to follow the same derivation like above, we have to absorb the minus sign into the spin operators, i.e. $e^{\epsilon\sum_i (iY_i)(iY_{i+1})}$. We get then

$$\begin{aligned}
\Omega_0 &= \mathbb{1} &&= O_0O_0 \\
\Omega_1 &= iY &&= O_0O_1 = O_1O_0 = O_1O_2 = O_2O_1 \\
\Omega_2 &= Y^2 &&= O_0O_2 = O_2O_0 = -O_1O_1 = O_2O_2\,.
\end{aligned} \tag{1.42}$$

Note the minus sign in front of O_1O_1. We can account for that by absorbing it into the corresponding entry in the matrix coefficient thereby getting

$$
\begin{aligned}
C_0 &= \begin{pmatrix} 1 & 0 & 0 \\ 0 & 0 & 0 \\ 0 & 0 & 0 \end{pmatrix} = |B_0\rangle\langle B_0| \\
C_1 &= \begin{pmatrix} 0 & \sqrt{\sinh(\epsilon)} & 0 \\ \sqrt{\sinh(\epsilon)} & 0 & \sqrt{\sinh(\epsilon)[\cosh(\epsilon)-1]} \\ 0 & \sqrt{\sinh(\epsilon)[\cosh(\epsilon)-1]} & 0 \end{pmatrix} \\
&= |B_0\rangle\langle B_1| + |B_1\rangle\langle B_0| + |B_1\rangle\langle B_2| + |B_2\rangle\langle B_1| \\
C_2 &= \begin{pmatrix} 0 & 0 & \sqrt{\cosh(\epsilon)-1} \\ 0 & -\sinh(\epsilon) & 0 \\ \sqrt{\cosh(\epsilon)-1} & 0 & \cosh(\epsilon)-1 \end{pmatrix} \\
&= |B_0\rangle\langle B_2| + |B_2\rangle\langle B_0| - |B_1\rangle\langle B_1| + |B_2\rangle\langle B_2| \; .
\end{aligned}
\tag{1.43}
$$

We see that miraculously the MPO for $e^{-\epsilon \sum_i Y_i Y_{i+1}}$ is again real and symmetric!

1.6.4 MPO representation for $e^{\epsilon X^2 \otimes X^2}$, $e^{\epsilon Y^2 \otimes Y^2}$ and $e^{\epsilon Z^2 \otimes Z^2}$

Since $S_\alpha^4 = S_\alpha^2$ we have

$$
\begin{aligned}
e^{\epsilon X^2 \otimes X^2} &= \mathbb{1}_{9\times 9} + \epsilon X^2 \otimes X^2 + \frac{\epsilon^2}{2!} X^2 \otimes X^2 + \cdots = \mathbb{1} \otimes \mathbb{1} + \big[e^\epsilon - 1\big] X^2 \otimes X^2 \\
&= \underbrace{\begin{pmatrix} 1 & 0 \end{pmatrix}}_{\langle B_0|} \begin{pmatrix} 1 \\ 0 \end{pmatrix} \underbrace{\mathbb{1} \otimes \mathbb{1}}_{O_0 \otimes O_0} + \underbrace{\begin{pmatrix} 0 & \sqrt{e^\epsilon - 1} \end{pmatrix}}_{\langle B_1|} \begin{pmatrix} 0 \\ \sqrt{e^\epsilon - 1} \end{pmatrix} \underbrace{X^2 \otimes X^2}_{O_1 \otimes O_1}
\end{aligned}
\tag{1.44}
$$

Following the same considerations like above we get for the Ω_γ

$$
\begin{aligned}
\Omega_0 &= \mathbb{1} \;\; = O_0 O_0 \\
\Omega_1 &= X^2 = O_0 O_1 = O_1 O_0 = O_1 O_1
\end{aligned}
\tag{1.45}
$$

which yields for the C_γ

$$
\begin{aligned}
C_0 &= \begin{pmatrix} 1 & 0 \\ 0 & 0 \end{pmatrix} = |B_0\rangle\langle B_0| \\
C_1 &= \begin{pmatrix} 0 & \sqrt{e^\epsilon - 1} \\ \sqrt{e^\epsilon - 1} & e^\epsilon - 1 \end{pmatrix} = |B_0\rangle\langle B_1| + |B_1\rangle\langle B_0| + |B_1\rangle\langle B_1| \; .
\end{aligned}
\tag{1.46}
$$

The MPO representation of $e^{\epsilon Y^2 \otimes Y^2}$ and $e^{\epsilon Z^2 \otimes Z^2}$ can be derived analogously with the only difference that in these cases $\Omega_1 = Y^2$ respectively $\Omega_1 = Z^2$.

1.6.5 MPO representation for $e^{\epsilon XZ\otimes XZ}$ and $e^{\epsilon ZX\otimes ZX}$

Since $XZXZ = 0$ we have

$$\begin{aligned} e^{\epsilon XZ\otimes XZ} &= \mathbb{1}_{9\times 9} + \epsilon XZ\otimes XZ \\ &= \underbrace{\begin{pmatrix} 1 & 0 \end{pmatrix}}_{\langle B_0|} \begin{pmatrix} 1 \\ 0 \end{pmatrix} \underbrace{\mathbb{1}\otimes\mathbb{1}}_{O_0\otimes O_0} + \underbrace{\begin{pmatrix} 0 & \sqrt{\epsilon} \end{pmatrix}}_{\langle B_1|} \begin{pmatrix} 0 \\ \sqrt{\epsilon} \end{pmatrix} \underbrace{XZ\otimes XZ}_{O_1\otimes O_1} \end{aligned} \tag{1.47}$$

Following the usual procedure we get for the Ω_γ

$$\begin{aligned} \Omega_0 &= \ \mathbb{1} \ \ = O_0O_0 \\ \Omega_1 &= XZ = O_0O_1 = O_1O_0 \\ \Omega_2 &= XZXZ = O_1O_1 = 0\,. \end{aligned} \tag{1.48}$$

Since $\Omega_2 = 0$ we need merely the matrices C_1 and C_2

$$\begin{aligned} C_0 &= \begin{pmatrix} 1 & 0 \\ 0 & 0 \end{pmatrix} = |B_0\rangle\langle B_0| \\ C_1 &= \begin{pmatrix} 0 & \sqrt{\epsilon} \\ \sqrt{\epsilon} & 0 \end{pmatrix} = |B_0\rangle\langle B_1| + |B_1\rangle\langle B_0|\ . \end{aligned} \tag{1.49}$$

The MPO representation of $e^{\epsilon ZX\otimes ZX}$ can be derived analogously but in this case $\Omega_1 = ZX$.

1.6.6 MPO representation for $e^{-\epsilon XY\otimes XY}$, $e^{-\epsilon YX\otimes YX}$, $e^{-\epsilon ZY\otimes ZY}$ and $e^{-\epsilon YZ\otimes YZ}$

Again due to $S_\alpha S_\beta S_\alpha S_\beta = \delta_{\alpha\beta} S_\alpha^2$ we get

$$\begin{aligned} e^{-\epsilon XY\otimes XY} &= \mathbb{1}_{9\times 9} - \epsilon XY\otimes XY \\ &= \underbrace{\begin{pmatrix} 1 & 0 \end{pmatrix}}_{\langle B_0|} \begin{pmatrix} 1 \\ 0 \end{pmatrix} \underbrace{\mathbb{1}\otimes\mathbb{1}}_{O_0\otimes O_0} + \underbrace{\begin{pmatrix} 0 & \sqrt{\epsilon} \end{pmatrix}}_{\langle B_1|} \begin{pmatrix} 0 \\ \sqrt{\epsilon} \end{pmatrix} \underbrace{iXY\otimes iXY}_{O_1\otimes O_1} \end{aligned} \tag{1.50}$$

Note that we have absorbed the minus sign into O_1 and in this way both $|B_a\rangle$ and O_1 are real! Following the usual procedure we get for the Ω_γ

$$\begin{aligned} \Omega_0 &= \ \mathbb{1} \ \ = O_0O_0 \\ \Omega_1 &= iXY = O_0O_1 = O_1O_0 \\ \Omega_2 &= -XYXY = O_1O_1 = 0\,. \end{aligned} \tag{1.51}$$

Again we need only the matrices C_1 and C_2

$$\begin{aligned} C_0 &= \begin{pmatrix} 1 & 0 \\ 0 & 0 \end{pmatrix} = |B_0\rangle\langle B_0| \\ C_1 &= \begin{pmatrix} 0 & \sqrt{\epsilon} \\ \sqrt{\epsilon} & 0 \end{pmatrix} = |B_0\rangle\langle B_1| + |B_1\rangle\langle B_0|\ . \end{aligned} \tag{1.52}$$

The MPO representations for $e^{-\epsilon YX \otimes YX}$, $e^{-\epsilon ZY \otimes ZY}$ and $e^{-\epsilon YZ \otimes YZ}$ are derived analogously with $\Omega_1 = iYX$, $\Omega_1 = iZY$ and $\Omega_1 = iYZ$ respectively.

1.7 Appendix C: Imaginary time evolution for the spin-$1/2$ Heisenberg ladder

The Hamiltonian reads

$$H = J_{\|} \sum_{i=1}^{N} (\mathbf{S}_i^{\uparrow}\mathbf{S}_{i+1}^{\uparrow} + \mathbf{S}_i^{\downarrow}\mathbf{S}_{i+1}^{\downarrow}) + J_{\perp} \sum_{i=1}^{N} \mathbf{S}_i^{\uparrow}\mathbf{S}_i^{\downarrow} \tag{1.53}$$

where the index i labels the rungs, the superscript $\uparrow$ denotes operators acting on the upper row and the superscript $\downarrow$ operators on the lower row (see Figure 1.2). In the following we will use $J_{\|} = J_{\perp} = 1$ for the sake of simplicity. Reintroducing variable coupling constants into all formulas can be easily done if needed. We are working with the spin-$1/2$ representation of $SU(2)$, i.e. with the spin operators

$$S_1 = \frac{1}{2}\sigma^x = \frac{1}{2}\begin{pmatrix} 0 & 1 \\ 1 & 0 \end{pmatrix}, \quad S_2 = \frac{1}{2}\sigma^y = \frac{1}{2}\begin{pmatrix} 0 & -i \\ i & 0 \end{pmatrix}, \quad S_3 = \frac{1}{2}\sigma^z = \frac{1}{2}\begin{pmatrix} 1 & 0 \\ 0 & -1 \end{pmatrix}. \tag{1.54}$$

We will use whenever possible for the Pauli matrices the following shorter notation: $X := \sigma^x$, $Y := \sigma^y$ $Z := \sigma^z$. The S_α fulfill of course the $SU(2)$ algebra (i.e. $[S_\alpha, S_\beta] = i\epsilon_{\alpha\beta\gamma}S_\gamma$) and while the σ^α themselves anticommute (i.e. $\{\sigma^\alpha, \sigma^\beta\} = \delta_{\alpha\beta}$). These relations will allow us to simplify the series expansions of exponentials occuring in the (imaginary) time evolution operator considerably.

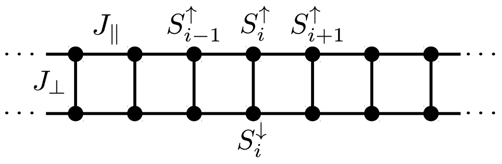

Figure 1.2: Spin ladder.

Let us first briefly recapitulate how the MPO representation of the imaginary time evolution operator for spin-$1/2$ systems is obtained [36]. Since $X^2 = \mathbb{1}$ we have

$$\begin{aligned} e^{\epsilon X \otimes X} &= \mathbb{1}_{4\times 4} + \epsilon X \otimes X + \frac{\epsilon^2}{2!}\mathbb{1}\otimes\mathbb{1} + \frac{\epsilon^3}{3!}X\otimes X + \frac{\epsilon^4}{4!}\mathbb{1}\otimes\mathbb{1} + \dots \\ &= \cosh(\epsilon)\mathbb{1}\otimes\mathbb{1} + \sinh(\epsilon)X\otimes X \\ = \underbrace{\begin{pmatrix} \sqrt{\cosh(\epsilon)} & 0 \end{pmatrix}}_{\langle B_0|} &\begin{pmatrix} \sqrt{\cosh(\epsilon)} \\ 0 \end{pmatrix} \underbrace{\mathbb{1}\otimes\mathbb{1}}_{O_0\otimes O_0} + \underbrace{\begin{pmatrix} 0 & \sqrt{\sinh(\epsilon)} \end{pmatrix}}_{\langle B_1|} \begin{pmatrix} 0 \\ \sqrt{\sinh(\epsilon)} \end{pmatrix} \underbrace{X\otimes X}_{O_1\otimes O_1} \end{aligned} \tag{1.55}$$

Following the usual procedure we get for the Ω_γ

$$\begin{aligned} \Omega_0 &= \mathbb{1} = O_0 O_0 = O_1 O_1 \\ \Omega_1 &= X = O_0 O_1 = O_1 O_0 \end{aligned} \tag{1.56}$$

and for the matrices C_γ

$$\begin{aligned} C_0 &= \begin{pmatrix} \cosh(\epsilon) & 0 \\ 0 & \sinh(\epsilon) \end{pmatrix} = |B_0\rangle\langle B_0| + |B_1\rangle\langle B_1| \\ C_1 &= \begin{pmatrix} 0 & \sqrt{\sinh(\epsilon)\cosh(\epsilon)} \\ \sqrt{\sinh(\epsilon)\cosh(\epsilon)} & 0 \end{pmatrix} = |B_0\rangle\langle B_1| + |B_1\rangle\langle B_0| \end{aligned} \tag{1.57}$$

such that the exponential then reads

$$e^{\epsilon \sum_i X_i X_{i+1}} = \sum_{\gamma_1, \gamma_2, \ldots, \gamma_N} \mathrm{Tr}\Big[C_{\gamma_1} C_{\gamma_2} \ldots C_{\gamma_N}\Big] \Omega_{\gamma_1} \otimes \Omega_{\gamma_2} \otimes \cdots \otimes \Omega_{\gamma_N} \,. \tag{1.58}$$

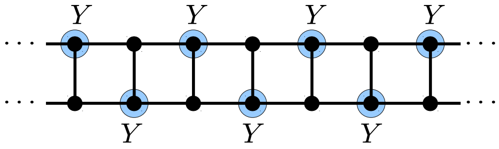

Figure 1.3: Pattern for the transformation $H \to H'$.

Now let us return to the spin ladder and separate the Hamiltonian into three parts such that all terms within each part commute with eachother

$$H = \frac{1}{4}(H_X + H_Y + H_Z) \,. \tag{1.59}$$

Each of the terms contains only the corresponding spin operator, i.e.

$$H_X = \sum_{i=1}^{N} X_i^\uparrow X_{i+1}^\uparrow + X_i^\downarrow X_{i+1}^\downarrow + X_i^\uparrow X_i^\downarrow \,. \tag{1.60}$$

It is clear that if we want the matrices C_γ to be real, we must have a positive exponent in the imaginary time evolution operator i.e. $e^{-\epsilon H}$ may not contain for instance factors like $e^{-\epsilon X \otimes X}$. In order to achieve this we apply on every second site the Y matrix as described in Figure 1.3. Explicitly we must use the operator

$$U = \prod_{i=1}^{N/2} Y_{2i-1}^\uparrow Y_{2i}^\downarrow = (Y \otimes \mathbb{1}) \otimes_1 (\mathbb{1} \otimes Y) \otimes_2 (Y \otimes \mathbb{1}) \otimes_3 \cdots \otimes_{N-1} (\mathbb{1} \otimes Y) \tag{1.61}$$

to obtain the transformed Hamiltonian

$$H' = U^\dagger H U \ = \frac{1}{4}(-H_X + H_Y - H_Z) \tag{1.62}$$

with H_α defined as in (1.60). Note that in (1.61) the $\otimes_i$ denote tensor products between the operators belonging to rungs i and $i+1$.

1.7.1 MPO representation for $e^{\epsilon H_X}$ and $e^{\epsilon H_Z}$

Let us first look at the MPO representation of the X terms in the imaginary time evolution operator for H'

$$\begin{aligned}
e^{\epsilon H_X} &= e^{\epsilon \sum_i (X_i^\uparrow X_{i+1}^\uparrow + X_i^\downarrow X_{i+1}^\downarrow + X_i^\uparrow X_i^\downarrow)} \\
&= \sum_{\gamma_1,\gamma_2,\ldots,\gamma_N} \mathrm{Tr}\Big[C_{\gamma_1} C_{\gamma_2} \ldots C_{\gamma_N}\Big] (\Omega_{\gamma_1} \otimes \mathbb{1}) \otimes_1 (\Omega_{\gamma_2} \otimes \mathbb{1}) \otimes_2 \cdots \otimes_{N-1} (\Omega_{\gamma_N} \otimes \mathbb{1}) \\
&\cdot \sum_{\gamma_1',\gamma_2',\ldots,\gamma_N'} \mathrm{Tr}\Big[C_{\gamma_1'} C_{\gamma_2'} \ldots C_{\gamma_N'}\Big] (\mathbb{1} \otimes \Omega_{\gamma_1'}) \otimes_1 (\mathbb{1} \otimes \Omega_{\gamma_2'}) \otimes_2 \cdots \otimes_{N-1} (\mathbb{1} \otimes \Omega_{\gamma_N'}) \\
&\cdot \ e^{\epsilon X \otimes X} \otimes_1 e^{\epsilon X \otimes X} \otimes_2 \cdots \otimes_{N-1} e^{\epsilon X \otimes X} \\
&= \sum_{\substack{\gamma_1,\gamma_2,\ldots,\gamma_N \\ \gamma_1',\gamma_2',\ldots,\gamma_N'}} \mathrm{Tr}\Big[(C_{\gamma_1} \otimes C_{\gamma_1'}) \cdot (C_{\gamma_2} \otimes C_{\gamma_2'}) \ldots (C_{\gamma_N} \otimes C_{\gamma_N'})\Big] \\
&\qquad \cdot (\Omega_{\gamma_1} \otimes \Omega_{\gamma_1'}) \otimes_1 \cdots \otimes_{N-1} (\Omega_{\gamma_N} \otimes \Omega_{\gamma_N'}) \\
&\qquad \cdot \Big\{ \big[\cosh(\epsilon)(\mathbb{1} \otimes \mathbb{1}) + \sinh(\epsilon)(X \otimes X)\big] \otimes_1 \ldots \\
&\qquad\quad \otimes_{N-1} \big[\cosh(\epsilon)(\mathbb{1} \otimes \mathbb{1}) + \sinh(\epsilon)(X \otimes X)\big] \Big\}
\end{aligned} \tag{1.63}$$

where we have used the identities $\mathrm{Tr}(A)\mathrm{Tr}(B) = \mathrm{Tr}(A \otimes B)$ and $\mathrm{Tr}(AB \otimes CD) = \mathrm{Tr}[(A \otimes C)(B \otimes D)]$. Since the Ω_γ and C_γ are simply given by (1.56) and (1.57) we can readily compute the action of the rung factors onto the row-MPO. With the following definitions for the rung operators

$$\begin{aligned}
\bar{\Omega}_0 &= \mathbb{1} \otimes \mathbb{1} \\
\bar{\Omega}_1 &= \mathbb{1} \otimes X \\
\bar{\Omega}_2 &= X \otimes \mathbb{1} \\
\bar{\Omega}_3 &= X \otimes X
\end{aligned} \tag{1.64}$$

we obtain for the action of the rung factors on operator "basis" $\{\Omega_\gamma \otimes \Omega_{\gamma'}\}$

$$
\begin{aligned}
\gamma=0,\gamma'=0 &\Rightarrow \big[\cosh(\epsilon)(\mathbb{1}\otimes\mathbb{1})+\sinh(\epsilon)(X\otimes X)\big]\cdot(\mathbb{1}\otimes\mathbb{1}) &&= \cosh(\epsilon)\bar{\Omega}_0+\sinh(\epsilon)\bar{\Omega}_3\\
\gamma=0,\gamma'=1 &\Rightarrow \big[\cosh(\epsilon)(\mathbb{1}\otimes\mathbb{1})+\sinh(\epsilon)(X\otimes X)\big]\cdot(\mathbb{1}\otimes X) &&= \cosh(\epsilon)\bar{\Omega}_1+\sinh(\epsilon)\bar{\Omega}_2\\
\gamma=1,\gamma'=0 &\Rightarrow \big[\cosh(\epsilon)(\mathbb{1}\otimes\mathbb{1})+\sinh(\epsilon)(X\otimes X)\big]\cdot(X\otimes\mathbb{1}) &&= \cosh(\epsilon)\bar{\Omega}_2+\sinh(\epsilon)\bar{\Omega}_1\\
\gamma=1,\gamma'=1 &\Rightarrow \big[\cosh(\epsilon)(\mathbb{1}\otimes\mathbb{1})+\sinh(\epsilon)(X\otimes X)\big]\cdot(X\otimes X) &&= \cosh(\epsilon)\bar{\Omega}_3+\sinh(\epsilon)\bar{\Omega}_0\,.
\end{aligned}
\tag{1.65}
$$

We obtain the rung matrix coefficients $\bar{C}_\gamma$ in the usual way by collecting all the prefactors correspondig to each $\bar{\Omega}_\gamma$, i.e.

$$
\begin{aligned}
\bar{C}_0 &= \cosh(\epsilon)(C_0\otimes C_0)+\sinh(\epsilon)(C_1\otimes C_1)\\
\bar{C}_1 &= \cosh(\epsilon)(C_0\otimes C_1)+\sinh(\epsilon)(C_1\otimes C_0)\\
\bar{C}_2 &= \sinh(\epsilon)(C_0\otimes C_1)+\cosh(\epsilon)(C_1\otimes C_0)\\
\bar{C}_3 &= \sinh(\epsilon)(C_0\otimes C_0)+\cosh(\epsilon)(C_1\otimes C_1)\,.
\end{aligned}
\tag{1.66}
$$

Explicitly they are

$$
\begin{aligned}
\bar{C}_0 &= \begin{pmatrix} \mathrm{ch}^3(\epsilon) & 0 & 0 & \mathrm{sh}^2(\epsilon)\mathrm{ch}(\epsilon)\\ 0 & \mathrm{sh}(\epsilon)\mathrm{ch}^2(\epsilon) & \mathrm{sh}^2(\epsilon)\mathrm{ch}(\epsilon) & 0\\ 0 & \mathrm{sh}^2(\epsilon)\mathrm{ch}(\epsilon) & \mathrm{sh}(\epsilon)\mathrm{ch}^2(\epsilon) & 0\\ \mathrm{sh}^2(\epsilon)\mathrm{ch}(\epsilon) & 0 & 0 & \mathrm{sh}^2(\epsilon)\mathrm{ch}(\epsilon) \end{pmatrix}\\
\bar{C}_1 &= \sqrt{\mathrm{sh}(\epsilon)\mathrm{ch}(\epsilon)}\cdot\begin{pmatrix} 0 & \mathrm{ch}^2(\epsilon) & \mathrm{sh}^2(\epsilon) & 0\\ \mathrm{ch}^2(\epsilon) & 0 & 0 & \mathrm{sh}^2(\epsilon)\\ \mathrm{sh}(\epsilon)\mathrm{ch}(\epsilon) & 0 & 0 & \mathrm{sh}(\epsilon)\mathrm{ch}(\epsilon)\\ 0 & \mathrm{sh}(\epsilon)\mathrm{ch}(\epsilon) & \mathrm{sh}(\epsilon)\mathrm{ch}(\epsilon) & 0 \end{pmatrix}\\
\bar{C}_2 &= \sqrt{\mathrm{sh}(\epsilon)\mathrm{ch}(\epsilon)}\cdot\begin{pmatrix} 0 & \mathrm{sh}(\epsilon)\mathrm{ch}(\epsilon) & \mathrm{sh}(\epsilon)\mathrm{ch}(\epsilon) & 0\\ \mathrm{sh}(\epsilon)\mathrm{ch}(\epsilon) & 0 & 0 & \mathrm{sh}(\epsilon)\mathrm{ch}(\epsilon)\\ \mathrm{ch}^2(\epsilon) & 0 & 0 & \mathrm{sh}^2(\epsilon)\\ 0 & \mathrm{ch}^2(\epsilon) & \mathrm{sh}^2(\epsilon) & 0 \end{pmatrix}\\
\bar{C}_3 &= \begin{pmatrix} \mathrm{sh}(\epsilon)\mathrm{ch}^2(\epsilon) & 0 & 0 & \mathrm{sh}(\epsilon)\mathrm{ch}^2(\epsilon)\\ 0 & \mathrm{sh}^2(\epsilon)\mathrm{ch}(\epsilon) & \mathrm{sh}(\epsilon)\mathrm{ch}^2(\epsilon) & 0\\ 0 & \mathrm{sh}(\epsilon)\mathrm{ch}^2(\epsilon) & \mathrm{sh}^2(\epsilon)\mathrm{ch}(\epsilon) & 0\\ \mathrm{sh}(\epsilon)\mathrm{ch}^2(\epsilon) & 0 & 0 & \mathrm{sh}^3(\epsilon) \end{pmatrix}\,.
\end{aligned}
\tag{1.67}
$$

Thus we obtain in the end an MPO with local matrices that act on rungs that reads

$$
e^{\epsilon H_X} = \sum_{\gamma_1,\gamma_2,\ldots,\gamma_N} \mathrm{Tr}\Big[\bar{C}_{\gamma_1}\bar{C}_{\gamma_2}\ldots\bar{C}_{\gamma_N}\Big]\bar{\Omega}_{\gamma_1}\otimes\bar{\Omega}_{\gamma_2}\otimes\cdots\otimes\bar{\Omega}_{\gamma_N} \tag{1.68}
$$

with $\bar{\Omega}_\gamma$ and $\bar{C}_\gamma$ as defined in (1.64) respectively in (1.68).

The MPO for $e^{\epsilon H_Z}$ can be computed analogously to contain the same $\bar{C}_\gamma$ (1.68). However the $\bar{\Omega}_\gamma$ now read

$$\begin{aligned}
\bar{\Omega}_0 &= \mathbb{1} \otimes \mathbb{1} \\
\bar{\Omega}_1 &= \mathbb{1} \otimes Z \\
\bar{\Omega}_2 &= Z \otimes \mathbb{1} \\
\bar{\Omega}_3 &= Z \otimes Z
\end{aligned} \tag{1.69}$$

1.7.2 MPO representation for $e^{-\epsilon H_Y}$

The derivation of the MPO for $e^{-\epsilon H_Y}$ is only slightly different than the one above. First of all the derivation of the MPO for the spin-1/2 chain reads now

$$\begin{aligned}
e^{-\epsilon Y \otimes Y} &= \mathbb{1}_{9\times 9} - \epsilon Y \otimes Y + \frac{\epsilon^2}{2!}\mathbb{1} \otimes \mathbb{1} - \frac{\epsilon^3}{3!} Y \otimes Y + \frac{\epsilon^4}{4!}\mathbb{1} \otimes \mathbb{1} - \dots \\
&= \cosh(\epsilon)\mathbb{1} \otimes \mathbb{1} - \sinh(\epsilon) Y \otimes Y \\
= \underbrace{\begin{pmatrix} \sqrt{\cosh(\epsilon)} & 0 \end{pmatrix}}_{\langle B_0|} &\begin{pmatrix} \sqrt{\cosh(\epsilon)} \\ 0 \end{pmatrix} \underbrace{\mathbb{1} \otimes \mathbb{1}}_{O_0 \otimes O_0} + \underbrace{\begin{pmatrix} 0 & \sqrt{\sinh(\epsilon)} \end{pmatrix}}_{\langle B_1|} \begin{pmatrix} 0 \\ \sqrt{\sinh(\epsilon)} \end{pmatrix} \underbrace{iY \otimes iY}_{O_1 \otimes O_1}
\end{aligned} \tag{1.70}$$

such that following [36] the operators Ω_γ are defined as

$$\begin{aligned}
\Omega_0 &= \mathbb{1} = O_0 O_0 = -O_1 O_1 \\
\Omega_1 &= iY = O_0 O_1 = O_1 O_0 =: \tilde{Y}
\end{aligned} \tag{1.71}$$

and the matrices C_γ as

$$\begin{aligned}
C_0 &= \begin{pmatrix} \cosh(\epsilon) & 0 \\ 0 & -\sinh(\epsilon) \end{pmatrix} = |B_0\rangle \langle B_0| - |B_1\rangle \langle B_1| \\
C_1 &= \begin{pmatrix} 0 & \sqrt{\sinh(\epsilon)\cosh(\epsilon)} \\ \sqrt{\sinh(\epsilon)\cosh(\epsilon)} & 0 \end{pmatrix} = |B_0\rangle \langle B_1| + |B_1\rangle \langle B_0| \,.
\end{aligned} \tag{1.72}$$

Following the same lines of reasoning as in 1.7.1 we get for the MPO representation of $e^{-\epsilon H_Y}$

$$\begin{aligned}
\bar{\Omega}_0 &= \mathbb{1} \otimes \mathbb{1} \\
\bar{\Omega}_1 &= \mathbb{1} \otimes \tilde{Y} \\
\bar{\Omega}_2 &= \tilde{Y} \otimes \mathbb{1} \\
\bar{\Omega}_3 &= \tilde{Y} \otimes \tilde{Y}
\end{aligned} \tag{1.73}$$

and

$$\begin{aligned}
\bar{C}_0 &= \quad \cosh(\epsilon)(C_0 \otimes C_0) + \sinh(\epsilon)(C_1 \otimes C_1) \\
\bar{C}_1 &= \quad \cosh(\epsilon)(C_0 \otimes C_1) - \sinh(\epsilon)(C_1 \otimes C_0) \\
\bar{C}_2 &= - \sinh(\epsilon)(C_0 \otimes C_1) + \cosh(\epsilon)(C_1 \otimes C_0) \\
\bar{C}_3 &= \quad \sinh(\epsilon)(C_0 \otimes C_0) + \cosh(\epsilon)(C_1 \otimes C_1)\,.
\end{aligned} \tag{1.74}$$

which is indeed real and symmetric as required.

1.8 Appendix D: Approximation of functions as sums of exponentials

In this appendix, we show how to solve the problem of approximating any function $f(k)$ as a sum of exponentials for $k = 1 \dots N$:

$$\min_{x_i,\lambda_i} \sum_{k=1}^{N} |f(k) - \sum_{i=1}^{n} x_i \lambda_i^k| \ . \tag{1.75}$$

First, construct the rectangular $N - n + 1 \times n$ matrix

$$\begin{aligned} F = & \begin{pmatrix} f(1) & f(2) & f(3) & \dots & f(n) \\ f(2) & f(3) & \dots & & f(n+1) \\ f(3) & \dots & & & \vdots \\ \vdots & & & & f(N-1) \\ f(N-n+1) & \dots & & f(N-1) & f(N) \end{pmatrix} \\ \simeq & \underbrace{\begin{pmatrix} \lambda_1^0 & \lambda_2^0 & \dots & \lambda_n^0 \\ \lambda_1^1 & \lambda_2^1 & \dots & \lambda_n^1 \\ \lambda_1^2 & \lambda_2^2 & \dots & \lambda_n^2 \\ \vdots & & & \vdots \\ \lambda_1^{N-n} & \lambda_2^{N-n} & \dots & \lambda_n^{N-n} \end{pmatrix}}_{W} \begin{pmatrix} x_1 & 0 & \dots & 0 \\ 0 & x_2 & & \vdots \\ \vdots & & \ddots & \\ 0 & \dots & & x_n \end{pmatrix} \begin{pmatrix} \lambda_1^1 & \lambda_1^2 & \dots & \lambda_1^n \\ \lambda_2^1 & \lambda_2^2 & \dots & \lambda_2^n \\ \vdots & & & \vdots \\ \lambda_n^1 & \lambda_n^2 & \dots & \lambda_n^n \end{pmatrix} \end{aligned} \tag{1.76}$$

Note that W is a Vandermonde matrix. We observe that F and W span the same space (note that N is typically much larger than n), such that there exists a $n \times n$ matrix Q s.t. $FQ \simeq W$. Define F_1 as the rectangular matrix which consists of the first $N - n$ rows of F and F_2 as the one with the last $N - n$ rows. Due to the Vandermonde structure of W, it must be approximately true that $F_1 Q \Lambda \simeq F_2 Q$ with Λ the diagonal matrix containing the exponents. Therefore, $\Lambda \simeq Q^{-1} F_1^{-\dagger} F_2 Q$ ($F_1^{-\dagger}$ denotes the pseudoinverse of F_1): the exponents $\{\lambda_i\}$ hence correspond to the eigenvalues of the matrix $F_1^{-\dagger} F_2$ which can be calculated very easily.

This method can be made more robust by making use of the so-called QR-decomposition. This can be done by first calculating the (economical) QR decomposition of $F = UV$ and by defining U_1 as the rectangular matrix which consists of the first $N - n$ rows and n columns of U and U_2 as the one with the last $N - n$ rows: there must again exist a Q such that $UQ \simeq W$. The exponents Λ can therefore easily be calculated as the eigenvalues of the matrix $U_1^{-\dagger} U_2$. The advantage of using the QR-decomposition is that the pseudoinverse of U_1 is much better conditioned than of F_1.

Once those exponents are found, a simple least squares algorithm can be used to find the corresponding weights $\{x_i\}$. It happens that this method is very efficient and reliable, even when oscillating functions are involved. A similar method is known in the field of signal processing under the name of Hankel singular value decomposition.

Chapter 2

Translationally Invariant MPS Simulations of PBC chains

Synopsis:

We present a matrix product state (MPS) algorithm to approximate ground states of translationally invariant systems with periodic boundary conditions. For a fixed value of the bond dimension D of the MPS, we discuss how to minimize the computational cost to obtain a seemingly optimal MPS approximation to the ground state. In a chain of N sites and correlation length ξ, the computational cost formally scales as $g(D, \xi/N)D^3$, where $g(D, \xi/N)$ is a nontrivial function. For $\xi \ll N$, this scaling reduces to D^3, independent of the system size N, making our algorithm N times faster than previous proposals. We apply the method to obtain MPS approximations for the ground states of the critical quantum Ising and Heisenberg spin-$1/2$ models as well as for the noncritical Heisenberg spin-1 model. In the critical case, for any chain length N, we find a model-dependent bond dimension $D(N)$ above which the polynomial decay of correlations is faithfully reproduced throughout the entire system.

Based on:
B. Pirvu, F. Verstraete and G.Vidal,
Phys. Rev. B **83**, 125104 (2011)

Changes compared to published version: minor corrections.

2.1 Introduction

Concepts of entanglement for many-body quantum systems have recently proven useful to devise new methods for the numerical simulation of quantum spin chains. It has been shown that the very successful density matrix renormalization method (DMRG) [2] can be rephrased as a variational method over the class of matrix product states (MPS) [35, 37, 11, 38]; this realization clarified the relatively poor performance of DMRG for systems with periodic boundary conditions (PBC), as MPS with open boundary conditions (OBC) do not have the right entanglement structure. It was shown in [11] how this could be cured by using a MPS with PBC. However, due to the cyclic structure of the underlying MPS, the computational cost of the simulation in terms of the MPS bond dimension D grew from $O(D^3)$ to $O(D^5)$. This was subsequently lowered to $O(D^3)$ in [39, 15].

An important motivation to study finite chains is that one can compute bulk properties of the system in the thermodynamic limit by extrapolating results obtained for increasingly large chains [40]. In this context, it is relevant whether OBC or PBC are considered. For a finite chain with OBC, local expectation values differ from those in thermodynamic limit due both to finite-size effects and to boundary effects, and larger chains need to be considered. In contrast, with PBC only finite-size effects are present. This makes the extrapolation to the thermodynamic more transparent and smaller systems need to be simulated. Another important advantage of PBC is that only in this case a finite chain can be translation invariant (TI) [1]. This is a crucial feature for the present work, where translation invariance is exploited in order to reduce the computational costs of simulating finite chains.

Pippan, White and Evertz [15] recently showed how to simulate spin chains with PBC with an MPS algorithm whose computational cost given in terms of D scales like $O(D^3)$. The intuition behind this scaling can be understood if one first considers systems with a correlation length ξ that is much shorter than the system size N. Let us choose a block of sites with size l such that $\xi > l$ (see figure 2.1a). In this case correlations between the left and the right ends of the block are mediated only through the sites inside the block. It is clear that the properties of this block are exactly the same as those of a block of equal length embeded in the bulk of a sufficiently large system with OBC. It is then not surprising that computing observables that are contained within the block has a cost proportional to D^3, as in the case of OBC. This is basically due to the fact that such calculations involve contracting a tensor network that has, as *uncorrelated* left and right boundary conditions, two *boundary vectors* with D^2 components [38]. Now imagine we are interested in the description of properties contained in a larger block such that $\xi > l > N - \xi$ (see figure 2.1b). This block is small enough for its ends to have correlations that are mediated via its own sites, yet large enough that correlations are also mediated via the sites outside the block, since now $N - l < \xi$. If these externally mediated correlations are relatively small, the situation is not very different from the previously described case where $l < N - \xi$. All we have to do is to replace the two uncorrelated *boundary vectors* with a low rank *boundary matrix* that contains the small amount of correlations. If the rank of the matrix is n, then the cost of this algorithm will be proportional to nD^3.

---

[1] TI can also be exploited for MPS simulations with OBC, but this requires addressing an infinite system [2, 41, 30, 42, 43, 36]. Notice that since the system size N is infinite from the start, there can not be finite-size or boundary corrections to the bulk properties of the system. However, in this case numerical results are contaminated by effects due to the finite bound dimension D of the MPS. Interestingly, one can apply ”finite-D” scaling techniques to extract accurate estimates of bulk properties [44, 45, 46, 16].

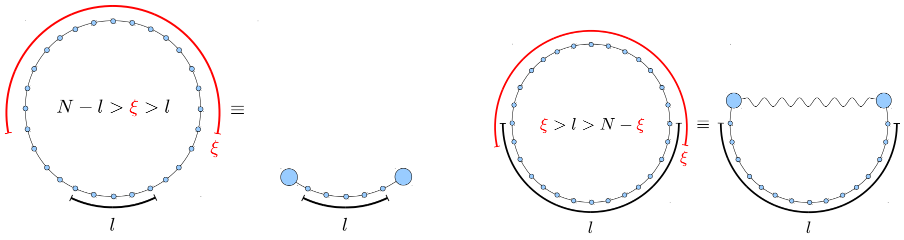

(a) Medium ξ, small l: equivalent to OBC environment.

(b) Medium ξ, medium l: equivalent to partially correlated OBC environment.

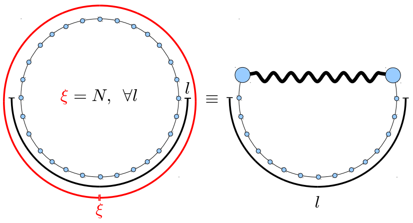

(c) Large ξ, any l: equivalent to fully correlated OBC environment.

Figure 2.1: (Color online). The properties of a block of size l within a PBC system can be equivalent to those of a block with same size in the bulk of an OBC system. Depending on l and the correlation length ξ, the left and right boundary conditions of the OBC system are more or less correlated.

We emphasize two important aspects of the computational cost of the algorithm in Ref. [15]. The *first* one is that the cost is also proportional to the system size N, due to the usual sweeping procedure that optimizes one site at each instant. We will show below how, in the case of a TI chain, one can basically get rid of this factor. It turns out that for chains where $\xi \ll N$ the cost will not depend on N at all. If $\xi \approx N$ on the other hand the cost will contain a factor that is smaller than N but is nevertheless an artifact thereof. The reduction of the computational cost is achieved by using a TI MPS, where the N tensors of the MPS are chosen to be identical. For all D, the precision of our results is comparable to that reported in Ref. [15]. This indicates that restricting the MPS ansatz to be TI does not lead to a loss of precision, while yielding a substantial reduction of the computational cost. The *second* one is the multiplicative factor n corresponding to the rank of the boundary matrix that transfers correlations between the ends of a block. In the case where the correlation length ξ is of the order of the system size N (see figure 2.1c), this factor may not be small. In a worst case scenario, where strong correlations between distant sites would force the boundary matrix to be full rank, i.e. $n = D^2$, the approach in Ref. [15] would not be better than the $O(D^5)$ algorithm of Ref. [11]. Thus for critical systems where $\xi \approx N$ it is a priori unclear what the overall scaling of the computational cost in D will be. However, in Ref. [15] it has been indicated that if D is not too large, the ground state energy of a critical spin chain obtained using a small constant n is satisfactory, in that its accuracy scales with D in a similar way as it would in an OBC chain of the same size.

Here we shall show how to exploit TI to obtain a faster algorithm that, for instance, does not scale with N when $\xi \ll N$. However, except for the case $\xi \ll N$, we still lack a precise characterization of how the cost scales as a function of D and N. We benchmark the present approach by addressing both critical (i.e. $\xi \approx N$) and non-critical (i.e. $\xi \ll N$) chains. An important observation is that in the case of critical systems the finite bond dimension D of the MPS introduces an effective correlation length $\xi_D \approx D^\kappa$ [44, 45, 46, 16] that depending on D can be much smaller than the actual one. This implies that as N grows, a larger bond dimension $D \approx N^{1/\kappa}$ needs to be considered if correlations between distant sites of the chain with PBC are to be properly captured Our numerical results are consistent with a complex scenario where the cost of simulations is dominated by the crossover between finite-N and finite-D corrections, as further discussed in [29].

The rest of the paper is structured as follows: we start by sketching the main idea of the approach in Sect. 2.2, followed by an in-depth presentation of the algorithm in Sect. 2.3. In Sect. 2.4 we present numerical results for the critical Quantum Ising and Heisenberg spin-$1/2$ models as well as for the non-critical Heisenberg spin-1 model. Finally Sect. 2.5 contains some conclusions.

2.2 Overview

This work is concerned with the approximation of ground states (GS) within the variational class of MPS with PBC defined in [11]. Since critical systems are arguably among the most challenging ones from a computational perspective, we will apply the approach to investigate critical spin chains (although non-critical chains can also be considered). An important restriction is that we only consider TI systems, which we will analyse with a TI MPS ansatz, namely an MPS where the tensors corresponding to different sites are all equal. The resulting variational class is a subclass of the one defined in [11]. The TI MPS with PBC reads

$$|\psi(A_i)\rangle = \sum_{i_1,\dots i_N=1}^{d} \mathrm{Tr}\big(A_{i_1} A_{i_2} \dots A_{i_N}\big) |i_1 i_2 \dots i_N\rangle \tag{2.1}$$

with identical matrices A_i at every site. The basis states are tensor products of the 1-site computational basis states i.e. $|i_1 i_2 \dots i_N\rangle = |i_1\rangle \otimes |i_2\rangle \otimes \dots \otimes |i_N\rangle$ where $|i\rangle \in \{|\uparrow\rangle, |\downarrow\rangle\}$ for a spin-$1/2$ chain. Note that for fixed i each A_i represents a matrix, thus the MPS is completely characterized by the three dimensional tensor ${A_i}^\alpha{}_\beta =: \mathbf{A}$. The components of $\mathbf{A}$ are then the variational parameters in our ansatz. Furthermore we would like to point out that we will mostly be interested in Hamiltonians that are real and reflection invariant; these symmetries can be implemented at the level of MPS by choosing the matrices A_i real and symmetric. This extra constraint does not seem to deteriorate the accuracy of the variational procedure.

Since our ansatz consists of N copies of the same tensor, the energy is not a quadratic expression in the variables defined by the tensors A_i; this implies that we cannot use the sweeping procedure described in [11] or any other procedure that lowers the energy by minimizing it for one site at a time. While this might seem a reason to be concerned at first, it will actually be the key to reducing computational costs.

The advantages of a TI MPS ansatz (with periodicity one or two) have already been exploited in the context of infinitely long chains [2, 41, 30, 42, 43, 36]. Refs. [2, 41, 42] used a TI MPS in the context of infinite system DMRG. In Ref. [30] instead, a (two-site periodic) MPS approximation to ground states was obtained by imaginary time evolution. Refs. [43, 36] discussed how to compute ground states with a one-site TI MPS when the imaginary time evolution operator can be well enough approximated by layers of one-site TI matrix product operators. An attempt to adapt that method to finite chains with PBC yielded results that are not as accurate as one might expect. This is basically due to the fact that the bond dimension truncation method used in [43, 36] can be shown to be optimal only for infinitely long chains. We have used a straightforward adaptation of that method for finite chains with PBC and the results are between one and a few orders of magnitude worse than the ones obtained by the gradient method described in the present work. Finally, we also point out that a TI MPS with PBC was already used in Ref. [39] together with Monte Carlo sampling techniques, with a formal cost $O(ND^3)$. In that case, the use of sampling techniques reduced the cost from $O(D^5)$ to $O(D^3)$, but at the same time enforced the multiplicative factor N, since a TI MPS does not represent a TI state once a given configuration is chosen during the sampling.

An obvious way to find the TI-MPS with minimal energy is a multidimensional minimization procedure that requires only evaluations of the function itself, such as the downhill simplex method [47]. When no further information about the function is available, this is indeed the method of choice. It is extremely robust but also extremely slow. However, if there is a feasible way to obtain more elaborate information such as the gradient or the Hessian, there are methods relying on these quantities that are clearly superior in what regards the speed of convergence and the required storage space.

In the following we will present an efficient algorithm to calculate the gradient of the energy $\nabla E(\mathbf{a})$ where the argument $\mathbf{a} = \mathrm{vec}(\mathbf{A})$ denotes the vector containing all entries of the MPS tensor $\mathbf{A}$. The result will then be used by a standard numerical library conjugate gradient algorithm to find a minimum of $E(\mathbf{a})$. We must emphasize that this minimum is by no means guaranteed to be the global one i.e. the optimal ground state approximation within the subspace defined by our special MPS ansatz. However, our numerical results seem to be slightly more accurate than previous results [15], while we have obtained a reduction in computational costs.

We will illustrate the accuracy of this approach by applying it to two exactly solvable models in order to give exact values for the numerical errors, and by applying it to a non-exactly solvable model that has been previously treated in the literature, in order to compare the precision of different approaches.

The computational cost will turn out to scale as $O(mnD^3) + O(n^2D^3)$ where D is the virtual bond dimension and m and n are some parameters to be specified below. Briefly speaking, the scaling can be understood as follows: first we approximate large powers of the MPS transfer matrix, whose exact definition will be given later in the text, within a reduced subspace of dimension n. Treating each of the n dimensions separately allows us to transform the contraction of a tensor network with PBC (which scales as $O(D^5)$) into n contractions of tensor networks with OBC (each of which scales as $O(D^3)$). As we will explain in more detail in the next section, the resulting tensor networks will still contain at most one portion represented by say m adjacent transfer matrices that is not connected to the already approximated one. If m is large, this second portion can again be approximated within a n-dimensional subspace thereby yielding the scaling $O(n^2D^3)$. If m is small, we are forced to contract the transfer matrices one after the other which gives the scaling $O(mnD^3)$.

2.3 The algorithm

Let us rearrange the MPS tensor components in a vector $\mathbf{a} = \mathrm{vec}(\mathbf{A})$ which allows us to write the energy as a function over the manifold of free parameters in the MPS

$$E(\mathbf{a}) = \frac{\langle\psi(\mathbf{a})|\, H\, |\psi(\mathbf{a})\rangle}{\langle\psi(\mathbf{a})|\psi(\mathbf{a})\rangle} \equiv \frac{\langle\psi(\mathbf{A})|\, H\, |\psi(\mathbf{A})\rangle}{\langle\psi(\mathbf{A})|\psi(\mathbf{A})\rangle} \quad . \tag{2.2}$$

Note that due to the constraints that the matrices are real and symmetric, the number of vector components in $\mathbf{a}$ has been reduced to $\frac{1}{2}dD(D+1)$. As we will treat only spin-1/2 chains (i.e. $d = 2$) in this work, the variational parameter manifold is actually $D(D+1)$-dimensional. Furthermore we will denote expectation values taken with respect to the MPS defined by the tensor $\mathbf{A}$ as $\langle O\rangle_{\mathbf{A}} := \langle\psi(\mathbf{A})|\, O\, |\psi(\mathbf{A})\rangle$.

Also note that (2.2) can have local extrema as opposed to $E(\Psi) = \langle\Psi|\, H\, |\Psi\rangle$ which is a convex quantity in the exponentially large Hilbert space. The MPS-parametrization restricts the full parameter space to a submanifold thus possibly generating local extrema where all derivatives in this subspace vanish. If one uses as a starting point of the conjugate gradient algorithm a random vector $\mathbf{a}_{rand}$, the search algorithm will typically get stuck in a local minimum. In order to avoid getting stuck in one of these, we will choose as a starting point a vector $\mathbf{a}_0$ of which we can be sure that it is close to the global minimum. This approach turns out to be very robust and fast. If we are interested in ground states of chains with very large N, the most natural choice for the starting vector is an MPS approximation of the GS of the same model in the thermodynamic limit. Note that this MPS must have exactly the same symmetry properties as our ansatz. It was shown in previous work [36] how to obtain this MPS and we will actually use the tensors computed there as starting points for the present algorithm. It is obvious why the MPS for the GS of the infinite chain is a good choice if one is interested in finite PBC-chains with $N \gg \xi_D$, where ξ_D is the correlation length induced by finite D. However, it turns out that this approach also works satisfactory for moderately large N. Of course, if there already is any PBC solution available, using that one as a starting point may provide a gain in convergence time, especially if the chain lengths are similar.

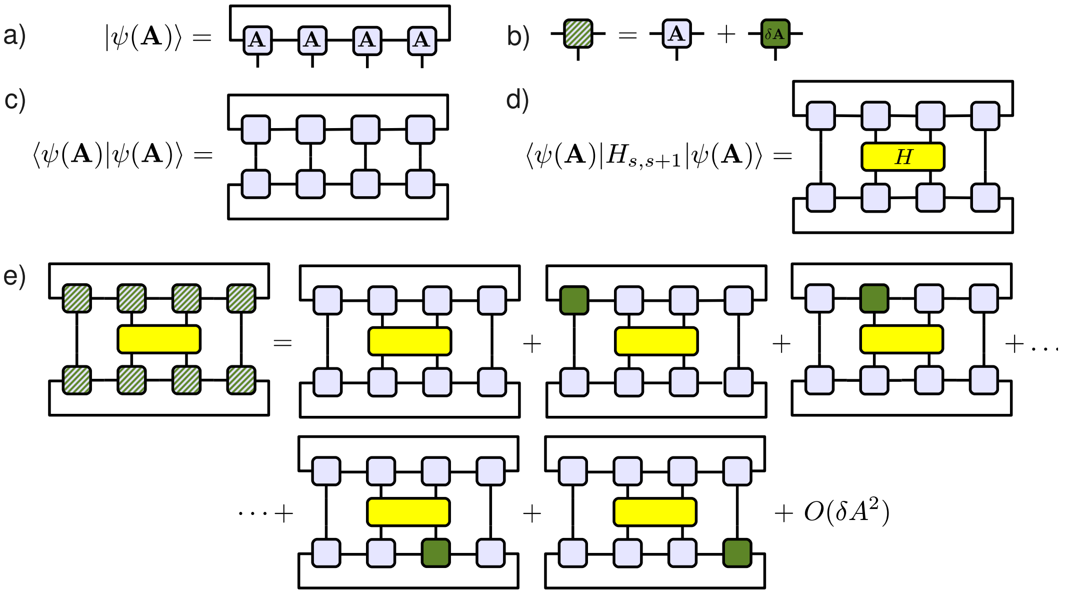
a)
$|\psi(\mathbf{A})\rangle =$
A
A
A
A
b)
$=$
A
$+$
δA
c)
$\langle\psi(\mathbf{A})|\psi(\mathbf{A})\rangle =$
d)
$\langle\psi(\mathbf{A})|H_{s,s+1}|\psi(\mathbf{A})\rangle =$
H
e)
$=$
$+$
$+$
$+\dots$
$\dots+$
$+$
$+\ O(\delta A^2)$

Figure 2.2: (Color online). (a) Graphical representation of the TI PBC MPS $|\psi(\mathbf{A})\rangle$ of a TI spin chain with 4 sites. Note the identical tensors $\mathbf{A}$ at each site. (b) Small perturbation $\delta\mathbf{A}$ is added to the to the MPS tensor $\mathbf{A}$. (c) Norm of a state $\langle\psi(\mathbf{A})|\psi(\mathbf{A})\rangle$. (d) Expectation value of a 2-site operator e.g. $\langle\psi(\mathbf{A})|H_{s,s+1}|\psi(\mathbf{A})\rangle$. (e) The expectation value is expanded in powers of $\delta\mathbf{A}$.

The gradient $\nabla E(\mathbf{a})$ reads explicitly

$$\nabla E(\mathbf{a}) = \frac{1}{\langle\psi(\mathbf{a})|\psi(\mathbf{a})\rangle}\nabla\left\langle\psi(\mathbf{a})\right| H \left|\psi(\mathbf{a})\right\rangle - \frac{\left\langle\psi(\mathbf{a})\right| H \left|\psi(\mathbf{a})\right\rangle}{\langle\psi(\mathbf{a})|\psi(\mathbf{a})\rangle^2}\nabla\left\langle\psi(\mathbf{a})|\psi(\mathbf{a})\right\rangle \quad . \tag{2.3}$$

It turns out that this quantity can be computed efficiently. First, since we assume a translationally invariant Hamiltonian with nearest neighbour interactions, we have

$$\langle H\rangle_{\mathbf{A}} = \langle H_{N,1}\rangle_{\mathbf{A}} + \sum_{s=1}^{N-1}\langle H_{s,s+1}\rangle_{\mathbf{A}} = N\langle H_{s,s+1}\rangle_{\mathbf{A}}.$$

Hence the first term in (2.3) is proportional to the gradient of the energy density $\rho_E(\mathbf{a}) = \langle H_{s,s+1}\rangle_{\mathbf{A}}$, $\forall s \in [1, N]$ (see figure 2.2d). Second, we can obtain gradients such as the ones occurring in (2.3) numerically at a given point $\mathbf{a}$ by expanding the differentiated quantity in powers of $\delta\mathbf{a}$ and computing the coefficient of the linear term. Thus the derivative in the first term is obtained via

$$\rho_E(\mathbf{a}+\delta\mathbf{a}) = \rho_E(\mathbf{a}) + \delta\mathbf{a}\big[\nabla_{\mathbf{a}'}\rho_E(\mathbf{a}')\big]_{\mathbf{a}'=\mathbf{a}} + O(\delta\mathbf{a}^2) \tag{2.4}$$

and the one in the second via

$$\langle\psi(\mathbf{a}+\delta\mathbf{a})|\psi(\mathbf{a}+\delta\mathbf{a})\rangle = \langle\psi(\mathbf{a})|\psi(\mathbf{a})\rangle + \delta\mathbf{a}\big[\nabla_{\mathbf{a}'}\langle\psi(\mathbf{a}')|\psi(\mathbf{a}')\rangle\big]_{\mathbf{a}'=\mathbf{a}} + O(\delta\mathbf{a}^2)\ . \tag{2.5}$$

Let us first consider (2.4). This can can be computed explicitly by taking a sum of completely contracted tensor networks (see figure 2.2e). Let $H_{eff}(\mathbf{A})$ denote the object that is obtained by removing the tensor $\delta\mathbf{A}$ from each term of $\rho_E(\mathbf{a}+\delta\mathbf{a})$ that is linear in $\delta\mathbf{a}$ (see figure 2.3). This is a tensor with three indices, that reshaped in vector form, yields the desired derivative $\nabla\rho_E(\mathbf{a}) = \text{vec}(H_{eff}(\mathbf{A}))$. The computational cost for the *exact* contraction of the tensor networks in $H_{eff}(\mathbf{A})$ scales as $O(ND^5)$ [11]. We will give below a prescription of how this can be improved to $O(mnD^3)+O(n^2D^3)$ by first making an ansatz for the approximation ot the exact result that depends on two integer parameters m and n. Subsequently we will show how to choose the smallest possible m and n such that no loss in precision occurs and why the scaling reduces to $O(mD^3)+O(nD^3)$ in the case of very long chains.

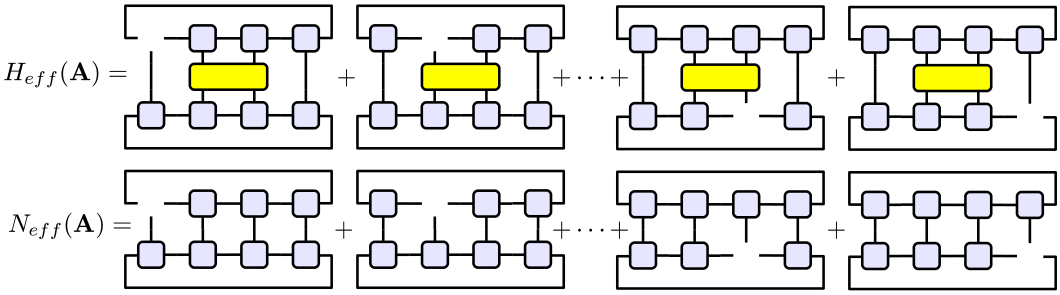

Figure 2.3: (Color online). Graphical representation of the tensor $H_{eff}(\mathbf{A})$ and $N_{eff}(\mathbf{A})$.

The other piece that is necessary for the computation of $\nabla E(\mathbf{a})$, is the derivative occurring in the second term of (2.3); this term can be obtained in a very similar way (see figure 2.3). We will use the notation $N_{eff}(\mathbf{A})$ for the object defined by $\nabla\langle\psi(\mathbf{a})|\psi(\mathbf{a})\rangle =: \text{vec}(N_{eff}(\mathbf{A}))$. Due to the simpler structure of the tensor network the computational cost here will scale as $O(nD^3)$ for arbitrary chains and as $O(D^3)$ for very long chains.

Now let us introduce the following convention for denoting incomplete tensor networks where merely one of the MPS tensors is missing: $\langle O\rangle_{\mathbf{A}}^{[s]}$ shall henceforth denote the expectation value of the operator O with respect to the TI MPS defined by the tensor $\mathbf{A}$, where one tensor $\mathbf{A}$ has been removed from $|\psi(\mathbf{A})\rangle$ at site s. Following this definition, the first term in the graphical representation of $H_{eff}(\mathbf{A})$ (see figure 2.3) reads $\langle H_{2,3}\rangle_{\mathbf{A}}^{[\overline{1}]}$. If a tensor has been removed from $\langle\psi(\mathbf{A})|$ at site s, we will denote this by underlining the site index, thus we write $\langle O\rangle_{\mathbf{A}}^{[\underline{s}]}$. Using this convention we can write $H_{eff}(\mathbf{A})$ as

$$H_{eff}(\mathbf{A}) = \sum_{s=1}^{N}\left(\langle H_{1,2}\rangle_{\mathbf{A}}^{[\overline{s}]} + \langle H_{1,2}\rangle_{\mathbf{A}}^{[\underline{s}]}\right) \ . \tag{2.6}$$

For real Hamiltonians and real MPS this reduces of course to

$$H_{eff}(\mathbf{A}) = 2\sum_{s=1}^{N}\langle H_{1,2}\rangle_{\mathbf{A}}^{[\overline{s}]} \ . \tag{2.7}$$

Similar considerations hold for $N_{eff}(\mathbf{A})$. Thus, using $\mathbb{1}$ to denote the identity operator, we can rewrite the gradient of the energy (2.3) as

$$\nabla E(\mathbf{a}) = \frac{N H_{eff}(\mathbf{A})}{\langle\psi(\mathbf{A})|\psi(\mathbf{A})\rangle} - \frac{N\rho_E(\mathbf{a})N_{eff}(\mathbf{A})}{\langle\psi(\mathbf{A})|\psi(\mathbf{A})\rangle^2} = 2N\sum_{s=1}^{N}\left(\frac{\langle H_{1,2}\rangle_{\mathbf{A}}^{[\overline{s}]}}{\langle\mathbb{1}\rangle_{\mathbf{A}}} - \frac{\langle H_{1,2}\rangle_{\mathbf{A}}\langle I\rangle_{\mathbf{A}}^{[\overline{s}]}}{\langle\mathbb{1}\rangle_{\mathbf{A}}^2}\right) \ . \tag{2.8}$$

Let us make a brief excursion to sketch how a gradient based procedure can be employed to find ground states of PBC chains if one is dealing with *complex* Hamiltonians and thereby *complex* MPS. One possibility is to use a gradient based algorithm that converges to a minimum of the real-valued function $E : \mathbb{C}^n \to \mathbb{R}$ within the complex manifold (n stands here for the number of independent complex parameters in the MPS). It can be shown that in this case one obtains the same expression (2.8) for the gradient of the energy albeit the individual terms are now complex valued vectors. However, since standard library routines for gradient based search cannot minimize over complex manifolds, let us mention the second possibility just for the sake of completeness. Due to $\mathbf{a} = \mathbf{x} + i\mathbf{y}$ with $\mathbf{x}, \mathbf{y} \in \mathbb{R}^n$, one can treat the energy as an analytic function over a real manifold with twice as many degrees of freedom, i.e. $E : \mathbb{R}^{2n} \to \mathbb{R}$. Similar considerations to the ones leading to (2.8) yield then for the gradient

$$\begin{aligned}
\nabla_{\mathbf{x}}E(\mathbf{x},\mathbf{y}) &= \ \ 2N\sum_{s=1}^{N}\left(\frac{\mathrm{Re}\langle H_{1,2}\rangle_{\mathbf{A}}^{[\overline{s}]}}{\langle\mathbb{1}\rangle_{\mathbf{A}}} - \frac{\langle H_{1,2}\rangle_{\mathbf{A}}\,\mathrm{Re}\langle I\rangle_{\mathbf{A}}^{[\overline{s}]}}{\langle\mathbb{1}\rangle_{\mathbf{A}}^2}\right) \\
\nabla_{\mathbf{y}}E(\mathbf{x},\mathbf{y}) &= -2N\sum_{s=1}^{N}\left(\frac{\mathrm{Im}\langle H_{1,2}\rangle_{\mathbf{A}}^{[\overline{s}]}}{\langle\mathbb{1}\rangle_{\mathbf{A}}} - \frac{\langle H_{1,2}\rangle_{\mathbf{A}}\,\mathrm{Im}\langle I\rangle_{\mathbf{A}}^{[\overline{s}]}}{\langle\mathbb{1}\rangle_{\mathbf{A}}^2}\right) \ .
\end{aligned} \tag{2.9}$$

Returning to *real* MPS, we still have to show how $H_{eff}(\mathbf{A})$ and $N_{eff}(\mathbf{A})$ can be computed efficiently. Since this is somewhat technical we will put the details into the appendix and give here only a brief overview of the algorithm. First note that for big chains (i.e. large N) tensor networks of the form shown in figure 2.3 will contain big powers of the transfer matrix

$$T = \sum_{i=1}^{d} A_i \otimes A_i \ . \tag{2.10}$$

The main idea is to exploit the fact that the eigenvalues of this $D^2 \times D^2$ transfer matrix usually decay rapidly enough s.t. we can approximate big powers thereof within a low-dimensional subspace spanned by its dominant eigenvectors. We will denote the dimension of this subspace by n. It is important however to realize that also small powers of T occur and that these may eventually require exact contraction. Let us denote the largest power of the transfer matrix that we contract exactly by m. As shown in the appendix, it turns out that in general it is possible to perform the contractions in such a way that the overall computational cost for $H_{eff}(\mathbf{A})$ scales like $O(mnD^3) + O(n^2D^3)$ and the one for $N_{eff}(\mathbf{A})$ like $O(nD^3)$. It is easy to see that the scalar expectation values in (2.3) can be obtained in an analogue yet simpler way. The fact that there are no vacant sites in the corresponding tensor networks enables us to use in that case a contraction method that is similar to the one used for $N_{eff}(\mathbf{A})$. Thus the computational cost for our algorithm scales as its most expensive part, namely as $O(mnD^3) + O(n^2D^3)$.

It is also not difficult to check that for very large chains (i.e. either when $N \gg \xi$ for non-critical systems or $N \gg \xi_D$ for critical ones, where ξ_D is the effective correlation length induced by finite D) this scaling can be improved. First note that as shown in the appendix, we have in every tensor network at least one portion of the chain expressed as a power of T that we approximate using its dominant eigenvectors. Now, for any bond dimension D there exists an N above which all approximated portions are long enough s.t. all eigenvalues except the largest one are suppressed by the very large exponent. In this case the overall scaling is $O(mD^3) + O(nD^3)$. Note that in the scaling for the "extremal-s" (appendix 2.6.1) terms we can not get rid of m because there will always be short portions between the $H_{1,2}$ and the vacant site, that must be contracted exactly. Similarly, for the "medium-s" terms (appendix 2.6.1) only the combinations of $\lambda_\alpha^m \lambda_\beta^m$ where both α and β are large will be negligible. Factors like $\lambda_1^m \lambda_\beta^m$ must usually always be taken into account. In any case, the ultimate check whether our approximations are justified must be done in the simulations, where one must verify if there exists an n beyond which our approximated ground state energy does not decrease.

We would like to compare our scaling of the computational cost to the one of [15] once again. Note that expressed in the terms used in this work, the scaling from Ref. [15] is $O(NnD^3)$. On one hand, as previously mentioned, our TI algorithm yields an improvement of one factor N. On the other hand there is an additional factor n that appears in our scaling. This is due to the fact that we compute the gradient of the energy explicitly. It is easy to see that the computational cost for the evaluation of the energy itself is $O(nD^3)$. However if we would restrict ourselves to evaluations of the energy only, we would have to use something like a downhill simplex method as the outer function that scans the MPS manifold for the energy minimum. In this case the outer function would call the energy evaluator a huge number of times, thereby yielding the overall cost much higher than one factor of n that we must pay when computing the gradient.

2.4 Numerical results

We have studied both critical and non-critical nearest neighbour interaction spin models. The first one is the Quantum Ising model for spins-$1/2$

$$H_{IS} = -\sum_{i=1}^{N} \sigma_i^z \sigma_{i+1}^z - g \sum_{i=1}^{N} \sigma_i^x \tag{2.11}$$

which we have simulated at its critical point $g = 1$. The periodic boundary conditions are implemented as usually by identifying σ_{N+1}^α with σ_1^α. The second one is the antiferromagnetic Heisenberg model

$$H_{HB} = \frac{1}{4} \sum_{i=1}^{N} (\sigma_i^x \sigma_{i+1}^x + \sigma_i^y \sigma_{i+1}^y + \sigma_i^z \sigma_{i+1}^z) \ . \tag{2.12}$$

This model is critical for spin-$1/2$ chains but non-critical for spin-1 chains. We have studied both cases. Note that (2.12) is not very well suited for the description with 1-site TI MPS due to its antiferromagnetic character. In order to cure this problem we apply in the case of the spin-$1/2$ chain a global unitary consisting of Pauli-σ^y matrices on each second site [1]. This leaves the spectrum unchanged and after we have found the 1-site TI MPS for the ground state, we can recover the one for the unchanged Hamiltonian by a new application of the global unitary. The resulting MPS is then of course 2-site TI. The rotated Heisenberg Hamiltonian reads

$$H_{HB} = \frac{1}{4} \sum_{i=1}^{N} (-\sigma_i^x \sigma_{i+1}^x + \sigma_i^y \sigma_{i+1}^y - \sigma_i^z \sigma_{i+1}^z) \ . \tag{2.13}$$

2.4.1 Critical systems

Let us illustrate the strategy for the scan of the parameter space spanned by $\{m, n\}$ on the basis of results obtained for small critical chains of 100 and 400 sites. Figure 2.4 and figure 2.5 show the relative precision $\Delta_{rel} E_0(m, n) = (E_0^{MPS}(m, n) - E_0^{exact})/|E_0^{exact}|$ of the MPS ground state energy compared to the exact solution as a function of the algorithm parameters m and n for the Quantum Ising respectively Heisenberg chain. The first observation is that there exist m_{max} and n_{max} s.t. for all $m \geq m_{max}$, $n \geq n_{max}$ the precision does not improve any more. In the featured plots the plateau $\mathcal{P}$ with minimal energy is reached within the plot range. The optimal point $\{m_{opt}, n_{opt}\}$ is then the point of $\mathcal{P}$ that minimizes the scaling of the computational cost $O(mnD^3) + O(n^2 D^3)$ i.e. $\{m_{opt}, n_{opt}\} = \min|_{\{m,n\} \in \mathcal{P}} (mn + n^2)$. Clearly, the optimal parameters m_{opt} and n_{opt} will be different for different models and different values of the chain length N and the MPS bond dimension D.

---

[1] For the spin-1 chain we must apply the operator $M = \exp(i\pi\sigma^y)$ on every second site in order to obtain the same effect.

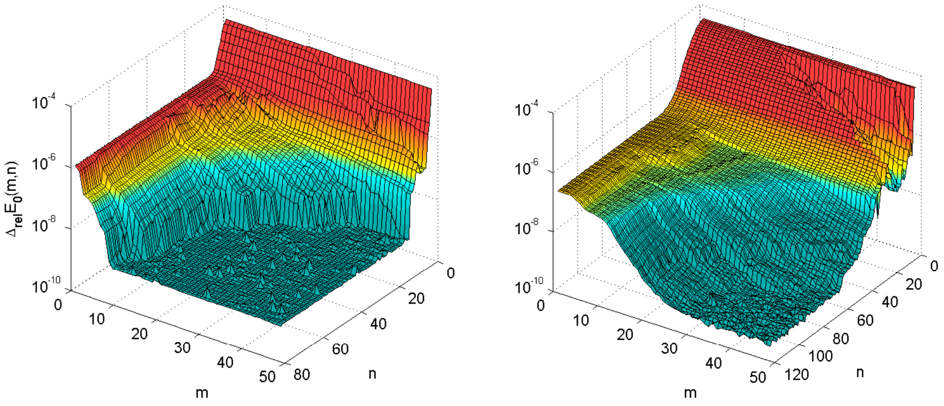

Figure 2.4: (Color online). Critical Quantum Ising chain with $N = 100$: Relative precision of the MPS ground state energy as compared to the analytical result as a function of the parameters (m, n) for $D = 16$ (left) and $D = 32$ (right).

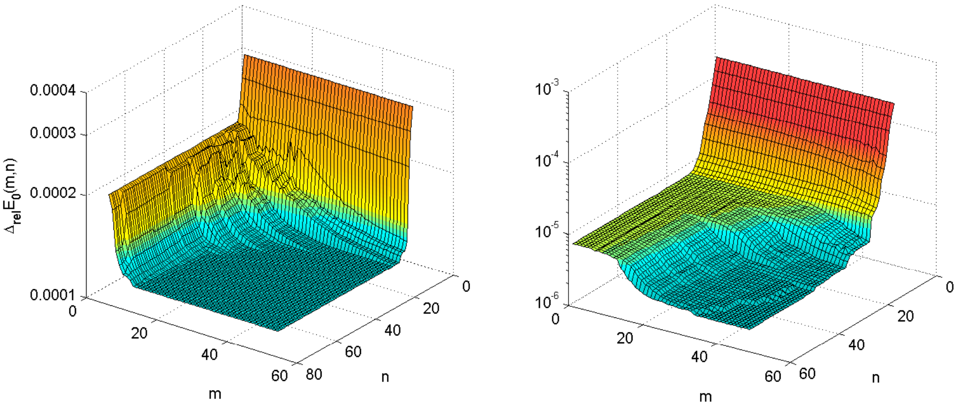

Figure 2.5: (Color online). Critical Heisenberg chain with $N = 100$: Relative precision of the MPS ground state energy as compared to the analytical result as a function of the parameters (m, n) for $D = 16$ (left) and $D = 32$ (right).

The plots reveal a further detail: if we are not very pedantic about the optimal $\{m, n\}$-pair, it is not necessary to scan the entire plane, which is computationally very expensive. If we are willing to settle for any pair $\{m, n\}$ that yields maximal precision, we can scan along any line $n = km$ and we can be sure that at some point we will hit $\mathcal{P}$. This pair is quasi-optimal in the sense that we have found the optimal n for the corresponding m and vice versa. This is due to the fact that for any point of $\mathcal{P}$, especially for its boundary, walking along lines with increasing m or n does not take us out of $\mathcal{P}$. As one can see in figure 2.4 and 2.5, $\mathcal{P}$ is roughly symmetric in m and n, so a sensible line to scan along would be given by $n = m$. In practice it might be better to choose $k < 1$ since there are parts of the algorithm with the scaling $O(nD^3)$ multiplied by a big constant factor. In our simulations we have used $k = 1/5$. As we have mentioned before, our algorithm allows us to increase m only up to $(N-2)/2$. If until then, the results obtained along $n = m$ have not converged yet, we must continue the scan along the line given by the constant maximal m towards larger n.

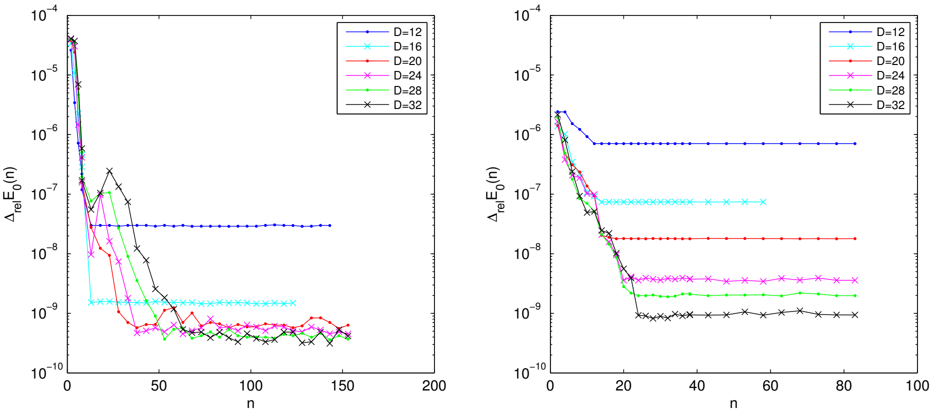

Figure 2.6: (Color online). Critical Quantum Ising chain with $N = 100$ (left) and $N = 400$ (right): Relative precision of the MPS ground state energy as a function of the parameter n for different bond dimensions D. The scan has been performed along the line $m = 5n$ up to the maximal value of m and then along the line with constant $m = (N-2)/2$.

The relative precision of the MPS ground state energy for such line scans is plotted in figure 2.6. We notice that with increasing D the maximally reachable precision gets better in concordance to what one would expect. The fact that m_{opt} and n_{opt} increase with D is also intuitive. What is a bit surprising is that for small n the results obtained for small bond dimensions are either similar or even better than the ones obtained for higher bond dimensions. This means that if one is not willing to go to larger values of n, there is no point in increasing D!

Another interesting point is that for fixed D, as we increase N, the plateau $\mathcal{P}$ is reached sooner and sooner (i.e. for smaller values of n and implicitly of m). This behaviour is due to the fact that with increasing N the weight that we loose in our contracted tensor network by choosing $n < D^2$ becomes negligible at smaller n.

2.4.2 Observables - energy and correlation functions

As the computational cost of our algorithm actually decreases if we increase the number of sites N while keeping D constant, we can investigate PBC chains of arbitrary size. Nevertheless, if we want to maintain the same level precision for very long chains, we must also increase D while going up with N. Figure 2.7 and figure 2.8 show the relative precision of the ground state energy for the critical Quantum Ising respectively Heisenberg model as a function of the MPS bond dimension D. We can see that generally the relative error is decreasing as a polynomial

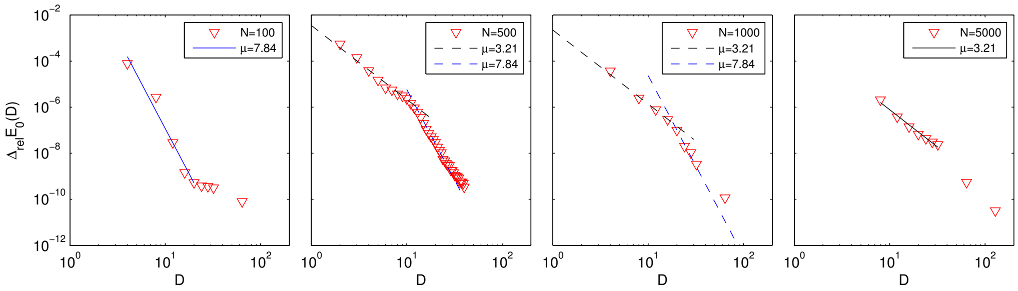

Figure 2.7: (Color online). Critical Quantum Ising model: relative precision of the MPS ground state energy for different N as a function of D.

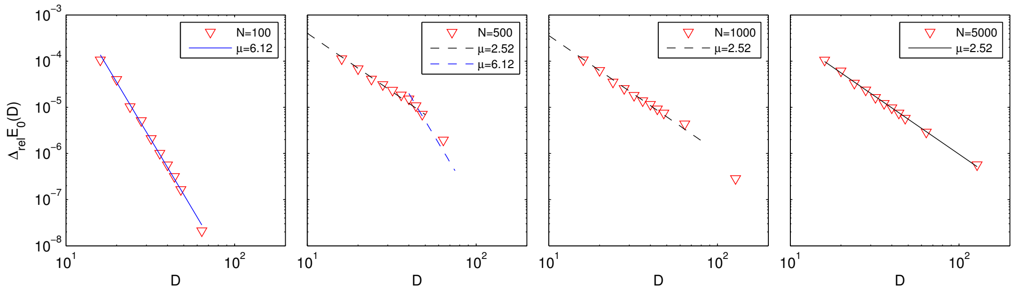

Figure 2.8: (Color online). Critical Heisenberg model: relative precision of the MPS ground state energy for different N as a function of D.

of D i.e. $\Delta_{rel}E_0(D) \propto D^{-\mu}$. We have fitted straight lines through the reliable [1] data of the $N = 100$ and $N = 5000$ plots and have obtained for the exponent μ the values 7.84 and 3.21 (6.12 and 2.52) for the critical Quantum Ising (Heisenberg) model. In the central plots (i.e. $N = 500$ and $N = 1000$) one can distinguish between two regions where the relative precision is decaying polynomially with the exponents obtained from the outer plots (i.e. $N = 100$ and $N = 5000$). We have emphasized this by drawing dashed lines through the data points in the central plots. Note that the dashed lines are not fitted, they have merely the same slope as the full lines in the outer plots. This behaviour can be best understood if one looks at correlation functions.

Let us first consider the critical Quantum Ising model. In figure 2.9 we have plotted the ZZ and the XX correlation functions i.e.

---

[1] If D is too large for a given chain length N, the optimal parameter n can get close to its maximal value i.e. $n \approx D^2$. In these cases the line scan described in section 2.4.1 converges at moderate n only due to finite machine precision. However, the precision of the MPS that is obtained in this way is not the one that is theoretically maximally achievable with an MPS of bond dimension D. We emphasize that with infinite machine precision the line scan with converge only close to $n = D^2$ and also the large D points in figure 2.7 and figure 2.8 would lie roughly on the line corresponding to polynomial decay.

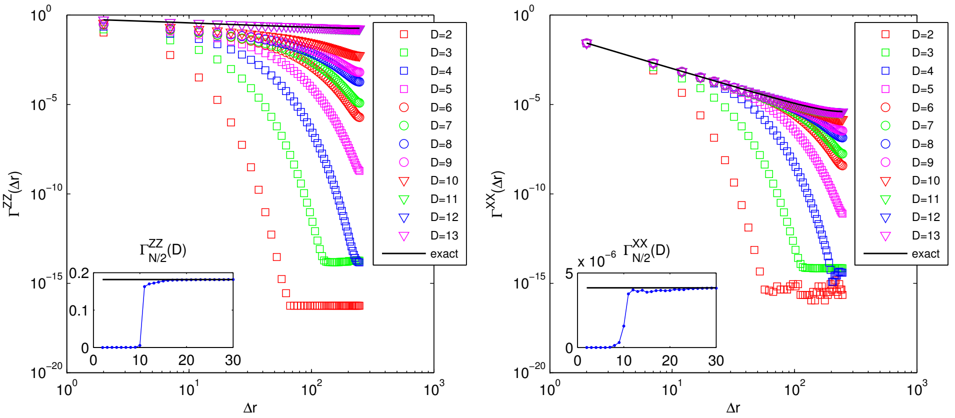

Figure 2.9: (Color online). Correlation functions for a critical Quantum Ising chain with $N = 500$. Left: order parameter correlator $\Gamma^{ZZ}(\Delta r)$ and as inset the half-chain correlator as a function of D. Right: correlator $\Gamma^{XX}(\Delta r)$ and as inset the half-chain correlator as a function of D.

$$\begin{aligned}\Gamma^{ZZ}(\Delta r) &= \langle \sigma_r^z \sigma_{r+\Delta r}^z \rangle - \langle \sigma_r^z \rangle \langle \sigma_{r+\Delta r}^z \rangle \\ \Gamma^{XX}(\Delta r) &= \langle \sigma_r^x \sigma_{r+\Delta r}^x \rangle - \langle \sigma_r^x \rangle \langle \sigma_{r+\Delta r}^x \rangle\end{aligned} \tag{2.14}$$

in the MPS ground state of a chain with $N = 500$ sites. The solid line represents the exact solution obtained by applying the programme of [18] to the Quantum Ising model with PBC. One can clearly see that with increasing D the MPS correlations become more and more accurate, just as one would expect. Note that we have only plotted the correlation functions for separations $\Delta r \leq N/2$. This is because due to the periodic boundary conditions $\Gamma(\Delta r)$ is symmetric around $\Delta r = N/2$, i.e. $\Gamma(N/2 - i) = \Gamma(N/2 + i)$ for integer $i < N/2$. Strictly speaking this holds only for even N. In the case of odd N we have the slightly different relation $\Gamma((N - i)/2) = \Gamma((N + i)/2), \forall i \in \{1, 3, 5, \ldots, N - 2\}$. We would like to point out that while the exact $\Gamma(\Delta r)$ is linear for small Δr thus implying polynomial decay of correlations in that regime, it flattens out towards $\Delta r \approx N/2$. This behaviour is consistent with the physical requirement that the correlation function is smooth at $\Delta r = N/2$. The insets show the value of the half-chain correlators $\Gamma_{N/2}(D) := \Gamma(\Delta r = N/2, D)$ as a function of D. One can clearly see a jump in $\Gamma_{N/2}(D)$ at some D'. This means that in this model, if one wants to obtain good approximations for long range correlations in the ground state, one must use MPS with bond dimension $D \geq D'(N)$. Note that the jump in the inset of figure 2.9 occurs roughly in the same region as the change of the slope in the second plot of figure 2.7. This allows us to understand why in figure 2.7 the slope for large D is steeper than the one for small D: if D is not large enough such that correlations are faithfully reproduced throughout the entire chain, this represents a further source of error besides the inherent error of MPS with non-exponential bond dimension (i.e. $D \ll d^{N/2}$).

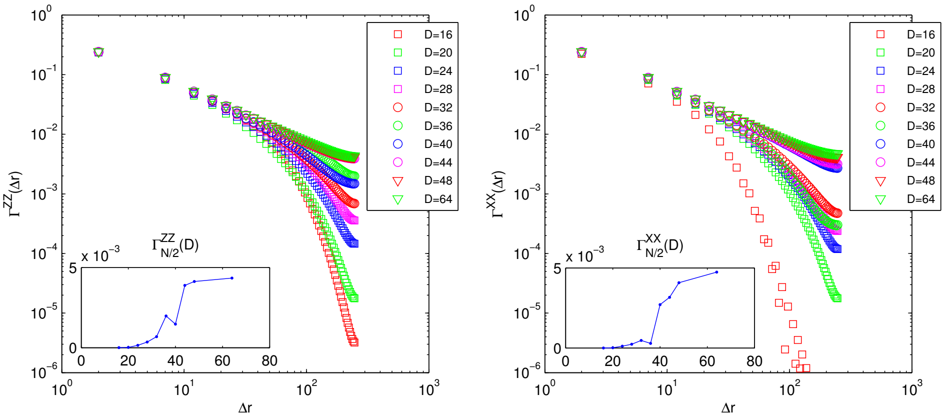

Figure 2.10: (Color online). Absolute value of the correlation functions for a critical Heisenberg chain with $N = 500$. Left: correlator $\Gamma^{ZZ}(\Delta r)$ and as inset the half-chain correlator as a function of D. Right: correlator $\Gamma^{XX}(\Delta r)$ and as inset the half-chain correlator as a function of D.

The absolute value of the correlation functions for the critical Heisenberg chain with $N = 500$ sites can be found in figure 2.10. We have taken the absolute value since due to the anti-ferromagnetic nature of the Heisenberg model the groundstate correlation function is changing its sign from site to site. Note that these plots only contain the simulation data since we do not have analytical expressions for the long range correlations. Qualitatively figure 2.10 shows the same behaviour as figure 2.9. Quantitatively we can see that correlation functions converge at much larger D than in the case of the critical Quantum Ising model, which is exactly what we would expect. The half-chain correlators $\Gamma_{N/2}(D)$ exhibit a more or less continuous transition to the region where correlations are faithfully reproduced.

We would like to make an interesting final remark regarding the error in the correlation functions as a function of Δr. In the left part of figure 2.11 we have plotted $\Gamma^{ZZ}_{MPS}(\Delta r) - \Gamma^{ZZ}_{exact}(\Delta r)$ for different D in the regime where the half-chain correlators have well converged (i.e. $D > 25$). The surprising thing is that the error does not grow monotonically as a function of Δr as one would expect, but that it rather oscillates around zero. Nevertheless the amplitude of the oscillations is growing monotonically with Δr. The right part of figure 2.11 reveals that similary to the relative error of the ground state energy, the relative error of the half-chain correlators $\Delta_{rel}\Gamma_{N/2}(D)$ obeys power-law decay as a function of D in the large D regime.

Our numerical analysis thus indicates that for each N there is a minimum value of $D = D'(N)$ such that correlations throughout the entire chain are properly captured. As investigated in [29], for critical systems this minimum value of $D'(N)$ is seen to be given by a small negative power of N that depends on the conformal field theory associated with the investigated model. For the moment we can not specify precisely the scaling of the overall computational cost as a function of N, D and the central charge [1], thus we will settle to write it down as

---

[1] I.e. the central charge of the associated conformal field theory (CFT). Note that this approch is only available

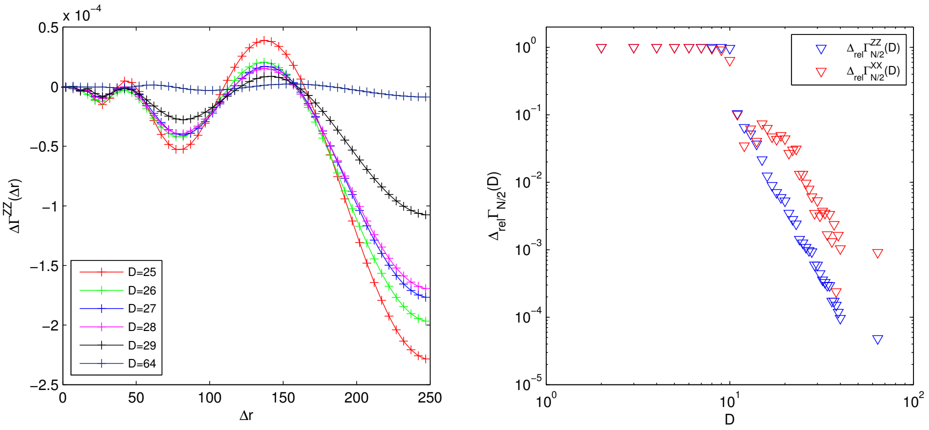

Figure 2.11: (Color online). Relative precision of correlation functions in the MPS ground state of the Quantum Ising model with $N = 500$. Left: error of the order parameter correlation function $\Gamma^{ZZ}(\Delta r)$ for several different D in the high precision regime. Right: relative precision of the half-chain correlators $\Gamma^{ZZ}_{N/2}$ and $\Gamma^{XX}_{N/2}$ as a function of the MPS bond dimension D.

$O(g(D, \xi/N)D^3)$ where $g(D, \xi/N)$ will be seen to become trivial only for non-critical systems.

2.4.3 Non-critical systems

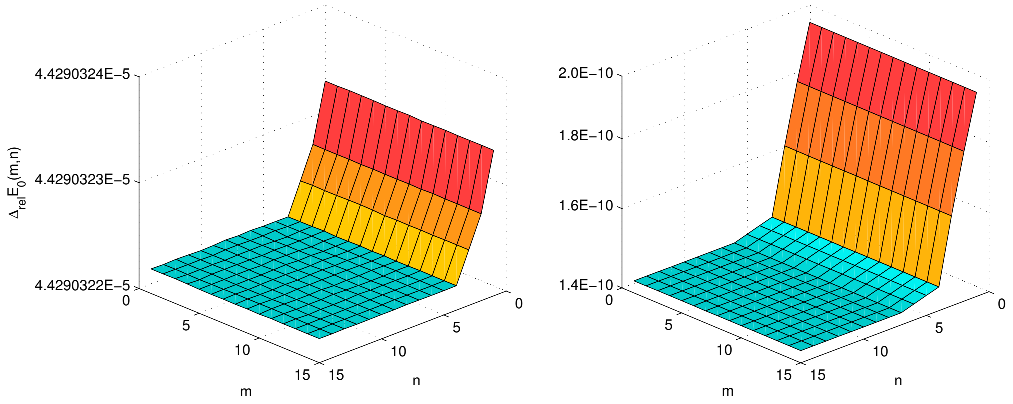

Figure 2.12: (Color online). Spin-1 Heisenberg chain with $N = 100$: Relative precision of the MPS ground state energy as compared to the best numerical approximation as a function of the parameters (m, n) for $D = 16$ (left) and $D = 100$ (right).

We have seen that for critical systems it is quite involved to predict the computational cost of MPS algorithms that find the optimal approximation of the ground state within the manifold

---

for critical models with an associated CFT.

defined by MPS with fixed bond dimension D. This turns out to be much easier for non-critical systems where the correlation length ξ is much smaller than the chain length N. We have studied the spin-1 Heisenberg chain as the prototype of a non-critical quantum spin chain in order to be able to compare our results with the ones presented in Ref. [15]. As pictured in figure 2.12, for $N = 100$ and D that is not too big, $n = 4$ is sufficient in order to obtain the optimal MPS approximation to the ground state. This is in agreement with the predictions of Ref. [15]. However for D as big as 100, we would have to choose $n = 7$ if we are not willing to loose any precision. This indicates a dependence of n on D which is much weaker than in the case of critical systems. Since due to finite computer memory we cannot increase D arbitrarily, it is safe to say that for systems where $\xi \ll N$, n is given by a small constant. This is exactly what happens for a spin-1 Heisenberg chain with 100 sites since as shown in Ref. [48] the correlation length is roughly $\xi \approx 6$ s.t. $\xi \ll N$. It is obvious from figure 2.12 that m can be chosen arbitrarily so we can fix it to $m = 1$. Thus in this case the cost of our algorithm scales like $O(D^3)$ which is indeed by a factor N less than the cost from [15]. Nevertheless we must emphasize that for systems where the condition $\xi \ll N$ is not fulfilled anymore, the picture of a small constant n breaks down and the characterization of the computational cost becomes non-trivial.

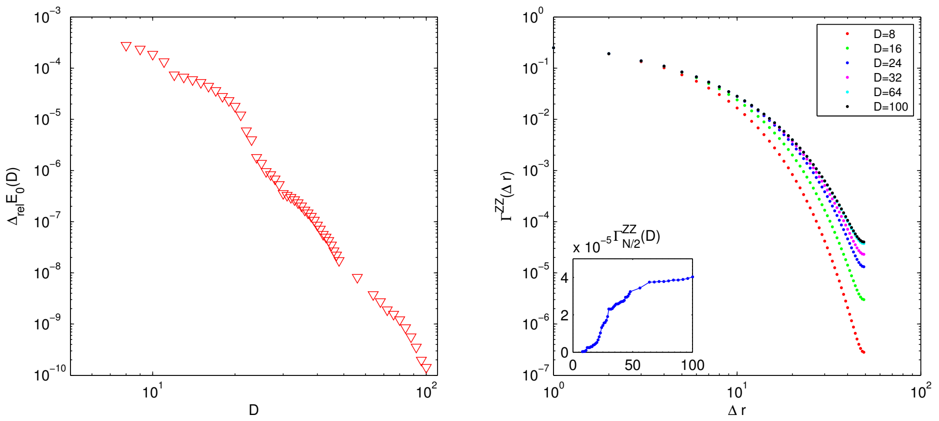

Figure 2.13: (Color online). Spin-1 Heisenberg chain with $N = 100$: Left: relative precision of the MPS ground state energy as a function of D. Right: absolute value of the correlation functions $\Gamma^{ZZ}(\Delta r)$ and as inset the half-chain correlator as a function of D.

In figure 2.13 we have plotted the relative energy precision and the correlation functions as functions of D. Note that for the "exact" ground state energy density we have used $E_0 = -1.401484039$ which is the value obtained by an extrapolation of our own finite D results to infinite D. We have done this since the ground state energy that we obtain for $D = 100$ is smaller than any other value we have found in the literature, and in particular slightly smaller than the one used as the "exact" ground state energy in Ref. [15].

The correlation functions plotted in figure 2.13 show non-trivial behaviour around $\Delta r \approx$

$N/2$ where they clearly deviate from exponential decay. The half-chain correlator plotted in the inset seems to converge as a function of D but we do not have compelling evidence for that.

2.5 Conclusions and outlook

We have demonstrated the performance of a gradient based algorithm for the simulation of TI spin chains with PBC both for critical and non-critical systems. For critical systems where the correlation length is of the order of the system size, the overall scaling of the computational cost is $O(mnD^3) + O(n^2D^3)$ and we have given an analysis of the parameter space $\{m, n\}$ with a prescription of how to obtain a quasi-optimal pair $\{m_{opt}, n_{opt}\}$. In the special case of a critical system that is simulated by MPS with comparatively small D, such that $\xi_D \ll N$ holds for the induced correlation length, the overall scaling is given by $O(mD^3)+O(nD^3)$. For non-critical systems with a correlation length that is much smaller than the system size, increasing D barely affects the parameters m and n and we can write for the overall scaling $O(D^3)$. In the last two cases the cost is one factor N less than the one of the algorithm presented in Ref. [15]. However, for critical systems in the large-D regime, the cost of Ref. [15] is improved merely by a factor N/n due to the appearence of n^2 in the scaling of our algorithm.

The different types of scaling of the computational cost are directly related to the entanglement entropy of the studied ground states. For critical systems, the exact dependence of m and n on the universality class is an open question and will be treated in future work.

With a TI MPS approximation of the ground state of a system with PBC at hand it is possible to develop efficient MPS algorithms for the approximation of excited states [49]. The preliminary results we have obtained using the MPS computed in this work as the backbone for an ansatz for momentum eigenstates are very promising.

In higher dimensions, one can use a gradient based approach to obtain tensor network approximations of the ground state too. However a straightforward generalization of the present algorithm to higher dimensional systems with PBC e.g. in the context of projected entangled pair states is not obvious due to the fact that the dimension of the transfer matrix grows exponentially with the system size in that case.

2.6 Appendix

2.6.1 Computation of $H_{eff}(\mathbf{A})$

Let us introduce a shorthand notation for the building blocks of $H_{eff}(\mathbf{A})$ that will allow us to express it in a very compact way. From the graphical representation (see figure 2.14) it should be obvious what the objects H^{AA}_{AA}, $H_{AA}{}^{\!A}$, $H^{A}{}_{AA}$, $T = T^{A}_{A}$ and T_A mean; note that T denotes the MPS transfer matrix that has been repeatedly mentioned in the previous sections. For the sake of completeness we also give the definition of the tensor H^{AA}_{AA} explicitly in terms of its components:

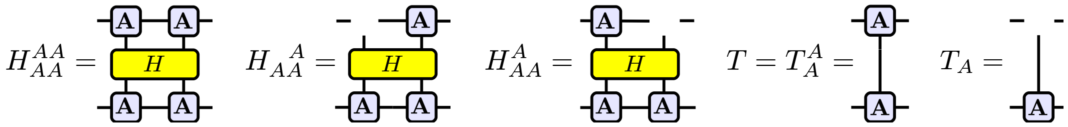

Figure 2.14: (Color online). Graphical representation of H^{AA}_{AA}, H_{AA}^{A}, H^{A}_{AA}, $T = T^{A}_{A}$ and T_A.

$$(H^{AA}_{AA})^{\alpha}{}_{\alpha'}{}^{\gamma}{}_{\gamma'} = A_i{}^{\alpha}{}_{\beta} A_j{}^{\beta}{}_{\gamma} (H_{s,s+1})^{ij}{}_{i'j'} A^{i'}{}_{\alpha'}{}^{\beta'} A^{j'}{}_{\beta'}{}^{\gamma'} \quad . \tag{2.15}$$

Here we have used greek letters to label the virtual bonds, latin ones for the physical bonds and Einstein summation convention to denote contracted indices. If one combines the left-hand side indices α and α' into one big index and does the same for the right-hand side indices γ and γ', it is clear that H^{AA}_{AA} represents a $D^2 \times D^2$-matrix. The other objects defined in figure 2.14 have similar explicit definitions. $H_{eff}(\mathbf{A})$ now reads

$$H_{eff}(\mathbf{A}) = 2 \cdot \mathrm{Tr}^* \Big[H_{AA}^{A} T^{N-2} + H^{A}_{AA} T^{N-2} + \sum_{s=0}^{N-3} H^{AA}_{AA} T^s T_A T^{N-3-s} \Big] \tag{2.16}$$

where Tr$^*[\dots]$ indicates that the trace is taken only with respect to the matrix multiplication of the ”outer” indices of the ”big” $D^2 \times D^2$-matrices. These ”big” matrices may have internal open indices that survive the Tr$^*[\dots]$-operation and make sure that $H_{eff}(\mathbf{A})$ is left with its tensor structure s.t. it can be later reexpressed as a vector.

The computation of (2.16) is the bottleneck of our method. If we would compute it by straightforward matrix multiplication, even using the sparseness, the computational cost would scale as $O(ND^5)$. In order to improve this scaling, the crucial point is to realize that for large N most terms in (2.16) will contain high powers of T which means that they can be very well approximated within the subspace spanned by the dominant eigenvectors [1] of T. This can be easily seen if we write such factors in their eigenbasis

$$T^s = \sum_{\alpha=1}^{D^2} \lambda_\alpha^s \left|\lambda_\alpha\right\rangle \left\langle\lambda_\alpha\right| = \lambda_1^s \Bigg[\left|\lambda_1\right\rangle \left\langle\lambda_1\right| + \sum_{\alpha=2}^{D^2} \left(\frac{\lambda_\alpha}{\lambda_1}\right)^s \left|\lambda_\alpha\right\rangle \left\langle\lambda_\alpha\right| \Bigg] \tag{2.17}$$

where $|\lambda_1| \geq |\lambda_2| \cdots \geq |\lambda_{D^2}|$. Obtaining the eigenbasis does not spoil the overall computational cost since due to the sparse structure of T, one can obtain its n dominant eigenvectors with $O(nD^3)$ operations. Obviously the subspace corresponding to the small magnitude eigenvalues is suppressed exponentially with s and thus can be neglected for powers s that are large enough (e.g. for $s = 20$ and $|\frac{\lambda_\alpha}{\lambda_1}| \approx 0.1$, $|\frac{\lambda_\alpha}{\lambda_1}|^s \approx 10^{-20} < 10^{-16}$ which is the machine precision of double precision floating point numbers). In these cases it is perfectly fine to restrict ourselves to the subspace spanned by say n dominant eigenvectors, with the parameter n yet to be determined. In fact, we will perform the entire computation a few times, starting with a rather small n and increasing it until the result does not improve any more. When this happens, we know that we have found the optimal n beyond which, when all other parameters are fixed, the precision does not get any better. Thus we will approximate large powers of the transfer matrix as

---

[1] Normally one denotes the eigenvector corresponding to the eigenvalue with the largest magnitude as the *dominant eigenvector*. Accordingly, the obvious meaning of the plural (i.e. *dominant eigenvectors*) would be to denote the eigenvectors of a degenerated dominant eigenvalue. However, we rather use the term *dominant eigenvectors* in order to refer to a set of eigenvectors whose corresponding eigenvalues have the largest magnitude among all eigenvalues.

$$T^s \approx \sum_{\alpha=1}^{n} \lambda_\alpha^s \left|\lambda_\alpha\right\rangle \left\langle\lambda_\alpha\right| \quad . \tag{2.18}$$

At this point we must remark that this approximation only works if the moduli of the transfer matrix eigenvalues $|\lambda_\alpha|$ are not concentrated around a certain point (i.e. T is not approximately proportional to unity). In that case, any increment of n will improve the precision and we will end up with very bad overall scaling. In the extremal case of optimal $n = D^2$ the overall scaling becomes $O(D^7)$. For models where this behaviour occurs the algorithm presented here may be worse than contracting the tensor networks explicitly, where the scaling is $O(ND^5)$. In these cases the chain length N ultimately decides which method is preferable. Fortunately for the models treated by us, this undesirable behaviour does not occur and we end up with relatively small n beyond which the precision does not improve any more.

Let us now return to (2.16). There are two different types of terms which must be treated differently. The first and the second term under our somewhat unorthodoxly defined trace can be considered as "easy". They are approximated by

$$\langle H_{1,2}\rangle_{\mathbf{A}}^{[1]} = \mathrm{Tr}^*\left[H_{AA}^{\;A} T^{N-2}\right] \approx \sum_{\alpha=1}^{n} \left\langle\lambda_\alpha\right| H_{AA}^{\;A} \left|\lambda_\alpha\right\rangle \lambda_\alpha^{N-2} \tag{2.19}$$

which is computed within $O(nD^3)$ operations. This is because each contraction $\left\langle\lambda_\alpha\right| H_{AA}^{\;A} \left|\lambda_\alpha\right\rangle$ can be performed with cost $O(D^3)$ and this has to be done n times.

The computationally more expensive terms are the ones under the sum over s, where two different powers of T are involved. We will call these terms "hard". They are approximated by

$$\langle H_{1,2}\rangle_{\mathbf{A}}^{[3+s]} = \mathrm{Tr}^*\left[H_{AA}^{AA} T^s T_A T^{N-3-s}\right] \approx \sum_{\alpha,\beta=1}^{n} \left\langle\lambda_\beta\right| H_{AA}^{AA} \left|\lambda_\alpha\right\rangle \left\langle\lambda_\alpha\right| T_A \left|\lambda_\beta\right\rangle \lambda_\alpha^s \lambda_\beta^{N-3-s} \quad . \tag{2.20}$$

Here we must remark two things: *i)* it is not necessary to let the second index β run over the same range as α. It would be possible to choose as an upper bound a further parameter n' and also vary this one until the precision does not improve any more. However, since expression (2.20) has obviously left-right symmetry, it is sensible to assume that the optimal result would yield $n = n'$. Even if this would not be the case, due to the fact that we scan along n, convergence will be reached only for some $n_{\text{optimal}} \geq \sup\{n, n'\}$, so we will find the lowest achievable energy anyway; *ii)* for very small or very large s either the left or the right transfer matrix segments in (2.20) can not be well approximated by a little number of eigenvalues n since the lower λ_α are not sufficiently suppressed by the small exponent. In the worst case we would have to take all D^2 eigenvalues into account, which dramatically increases the computational cost. In order to solve this issue we will compute these terms by exact contraction of segments of length m, which introduces this further parameter into our algorithm. This will be explained in more detail further below. For the moment let us note that depending on the magnitude of s, we can further separate the sum in (2.16) over the "hard" terms into

$$\sum_{s=0}^{N-3} \equiv \sum_{s=0}^{m-1} + \sum_{s=m}^{N-3-m} + \sum_{s=N-2-m}^{N-3} \quad . \tag{2.21}$$

We call the terms over which the second sum is taken "medium-s" terms and will treat them differently from the "extremal-s" terms that appear in the first respectively third sum. Thus $H_{eff}(\mathbf{A})$ can be divided into

$$H_{eff}(\mathbf{A}) = 2 \cdot \left(H_{eff}^{easy}(\mathbf{A}) + H_{eff}^{hard,extr}(\mathbf{A}) + H_{eff}^{hard,med}(\mathbf{A}) \right) \quad . \tag{2.22}$$

Computation of "extremal-s" terms

In this section we treat the terms with small respectively large s. The first thing to remark is that for large N, if T^s can not be well approximated within some low-dimensional subspace because s is too small, it is very likely that for T^{N-3-s} the approximation will work due to $N - 3 - s \gg s$. The same observation holds in the other direction if s is too large. Secondly, depending on the MPS bond dimension D and the ammount of entanglement present in the MPS (i.e. depending on the model one is treating), there is a certain m above which T^s with $s \geq m$ can be faithfully approximated within the $n < D^2$-dimensional subspace spanned by n dominant eigenvectors. As we don't know anything about m a priori, we introduce it as a further parameter into our algorithm. We will scan m within its range $[1, 1/2(N-2)]$ and in the end we will obtain some optimal pair (m, n). The reason why m does not go all the way up to $N - 3$ is that in order for our algorithm to scale effectively as D^3, we must employ the dominant eigenvector approximation on the other half of the chain. Without it we would get the undesirable scaling $O(ND^5)$. The contraction (see figure 2.15) we must perform for each term with small s thus reads

$$\langle H_{1,2}\rangle_{\mathbf{A}}^{[3+s]} = \mathrm{Tr}^*\left[H_{AA}^{AA}T^sT_AT^{N-3-s}\right] \approx \sum_{\alpha=1}^{n} \langle\lambda_\alpha|\, H_{AA}^{AA}T^sT_A\,|\lambda_\alpha\rangle\, \lambda_\alpha^{N-3-s} \quad , \ \forall s < m \tag{2.23}$$

and can be done with computational cost $O(nD^3)$ using a sparse matrix contraction scheme. As we have to repeat this procedure m times, the total cost scales as $O(mnD^3)$.

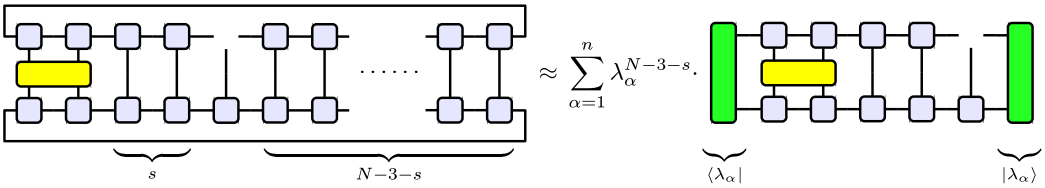

Figure 2.15: (Color online). Graphical representation of a term with small s and its approximation within the subspace spanned by n dominant eigenvectors of T.

The large s terms (i.e. when $N-3-m < s \leq N-3$) can be easily obtained by making use of the left-right symmetry of the tensor network around the point with $s = (N-2)/2$. The sum over all these s turns out to be related to the sum over the small s terms by taking the transpose with respect to the open virtual bond indices at the empty site where T_A sits. Thus the computational cost remains unchanged $O(mnD^3)$.

Computation of ”medium-s” terms

For terms where s is neither too small nor too large, both powers of the transfer matrix (i.e. T^s and T^{N-3-s}) can be well approximated whithin the subspace spanned by n dominant eigenvectors. The good news is that in this case the sum over s can be performed analitically in contrast to the ”extremal-s” case where we had to compute each of the m terms separately. However, there is also bad news, namely that we now have an additional sum over the eigenvalue index stemming from the approximation of T^{N-3-s}. Explicitly the sum over all ”medium-s” reads

$$\begin{aligned} H_{eff}^{hard,med}(\mathbf{A}) &= \mathrm{Tr}^*\Big[\sum_{s=m}^{N-3-m} H_{AA}^{AA}T^sT_AT^{N-3-s}\Big] \\ &\approx \mathrm{Tr}^*\Big[\sum_{s=0}^{N-3-2m}\ \sum_{\alpha,\beta=1}^{n} H_{AA}^{AA}T^m\,|\lambda_\alpha\rangle\, \lambda_\alpha^s\, \langle\lambda_\alpha|\, T_A\, |\lambda_\beta\rangle\, \lambda_\beta^{N-3-2m-s}\, \langle\lambda_\beta|\, T^m\Big] \\ &= \sum_{\alpha,\beta=1}^{n} \langle\lambda_\beta|\, H_{AA}^{AA}\,|\lambda_\alpha\rangle\, \langle\lambda_\alpha|\, T_A\,|\lambda_\beta\rangle\, \lambda_\alpha^m\lambda_\beta^m \frac{\lambda_\beta^{N-2-2m} - \lambda_\alpha^{N-2-2m}}{\lambda_\beta - \lambda_\alpha} \quad . \end{aligned} \tag{2.24}$$

In the first step we have shifted the summation variable s and have written the matrices T in their eigenbasis. To arrive from the second to the third line we have used the cyclic property of the trace to write the entire expression as a sum over products of scalars (actually the factor containing T_A is only a scalar with respect to our specially defined trace since it contains internal free indices). Furthermore we have performed the s-sum straightforwardly.

The computational cost scales here as $O(n^2D^3)$. This is because we have two sums going from 1 to n over terms that are contracted within $O(D^3)$ operations.

2.6.2 Computation of $N_{eff}(\mathbf{A})$

Our prescription for the computation of $N_{eff}(\mathbf{A})$ is also based on the observation that big powers of the transfer matrix T can be very well approximated within the subspace spanned by the dominant eigenvectors. However here things are much easier than for $H_{eff}(\mathbf{A})$. This is because the translational invariance is not broken by the 2-site Hamiltonian (see figure 2.3) and we can write

$$N_{eff}(\mathbf{A}) = 2N \cdot \langle I \rangle_{\mathbf{A}}^{\boxed{1}} \ . \tag{2.25}$$

Similarly to $\langle H_{1,2} \rangle_{\mathbf{A}}^{\boxed{1}}$ in (2.19), $\langle I \rangle_{\mathbf{A}}^{\boxed{1}}$ is approximated by

$$\langle I \rangle_{\mathbf{A}}^{\boxed{1}} = \mathrm{Tr}^* \left[T_A T^{N-1} \right] \approx \sum_{\alpha=1}^{n} \langle \lambda_\alpha | \, T_A \, | \lambda_\alpha \rangle \, \lambda_\alpha^{N-1} \tag{2.26}$$

which is computed within $O(nD^3)$ operations.

Chapter 3

Finite Size Scaling versus Finite Entanglement Scaling

Synopsis:

We investigate the use of matrix product states (MPS) to approximate ground states of critical quantum spin chains with periodic boundary conditions (PBC). We identify two regimes in the (N, D) parameter plane, where N is the size of the spin chain and D is the dimension of the MPS matrices. In the first regime MPS can be used to perform finite size scaling (FSS). In the complementary regime the MPS simulations show instead the clear signature of finite entanglement scaling (FES). In the thermodynamic limit (or large N limit), only MPS in the FSS regime maintain a finite overlap with the exact ground state. This observation has implications on how to correctly perform FSS with MPS, as well as on the performance of recent MPS algorithms for systems with PBC. It also gives clear evidence that critical models can actually be simulated very well with MPS by using the right scaling relations; in the appendix, we give an alternative derivation of the result of Pollmann et al. [Phys. Rev. Lett. 102, 255701 (2009)] relating the bond dimension of the MPS to an effective correlation length.

Based on:
B. Pirvu, G.Vidal, F. Verstraete and L.Tagliacozzo,
Phys. Rev. B **86**, 075117 (2012)

Changes compared to published version: minor corrections.

3.1 Introduction

Quantum many body systems are very hard to study due to the exponential growth of their Hilbert space with the number of constituents. One possible cure to this issue for one dimensional systems is to describe their ground states as matrix product states (MPS) [7, 50, 51]. This family of states is known to be well suited to study gapped 1D phases [6] where for generic systems almost exact results can be obtained with matrices whose size does not depend on the size of the system. Even more, for several gapped 1D systems the exact ground state can be expressed in terms of translationally invariant MPS with very small bond dimension [4, 6]. Gapless 1D phases are harder to simulate with MPS since the size of the matrices necessary to obtain good approximations of their ground states increases polynomially with the size of the system. This is particularly unfortunate since the universal low energy information encoded in the gapless phase becomes apparent only for large systems.

Luckily such universal information is also encoded in the way a state approaches the thermodynamic limit and one can extract it by using the celebrated finite size scaling (FSS) technique [52]. This technique amounts to study larger and larger systems in a gapless phase (that due to the finite size of the system becomes gapped) and extract universal properties through the dependence of the observables on the system size.

In the context of MPS, one can use an alternative approach to study gapless phases. It is called finite entanglement scaling (FES) [46] and amounts to study the scaling of the expectation value of observables in the ground state of infinite chains described by MPS with fixed bond dimension and thus finite entanglement [1].

Both the existence of FSS and FES close to a conformal fixed point are a direct consequence of conformal invariance [54, 16]. If N is the chain length and D the MPS bond dimension, then FSS corresponds to taking $D \to \infty$ first and then taking $N \to \infty$, whereas FES consists in taking $N \to \infty$ first and then $D \to \infty$.

An important question to ask is whether FSS and FES provide the same universal information. Since the proposal of FES for simulations with MPS [46] it has been shown that indeed quantities such as critical exponents related to local observables or the central charge of the model can be extracted with the help of this technique [55, 56, 57, 58, 42, 59, 60], in a similar way as it is normally done with FSS techniques. Here we will show, however, that some care is required in order to differentiate between the effects of FES and those of FSS.

Specifically, we consider critical systems with periodic boundary conditions (PBC), and describe their translationally invariant ground states using translationally invariant MPS. In order to properly perform FSS one should obtain for each considered system size N a sequence of increasingly accurate MPS approximations with growing bond dimension D, which for large enough D converges to the exact ground state for that size N. Importantly, we find that for an intermediate range of values of D, for which local observables are already reproduced with high accuracy and show some clearly visible scaling with D, the MPS approximation is almost completely orthogonal to the exact ground state. This is the reason why in this D-range the MPS fails to reproduce long-range correlation functions (e.g. $\Gamma_{N/2}$), as previously illustrated in the inset of Fig. 9 and 10 of Ref. [28]. In other words, reasonably converged values of local observables including the ground state energy (or emergence of clearly visible D-scaling behavior therefor), are not sufficient criteria to establish that some MPS is a good approximation to the ground state of a critical PBC system. Instead, in order to properly apply FSS, for each system size N one should consider MPS with a bond dimension D larger than some threshold value D_0, where D_0 depends both on N and on the simulated model.

---

[1] Additionally, one can also deform the system by describing it on curved geometries where the curvature induces a gap, and then study the approach to the flat limit in the same way one would study the approach to an infinite system [53].

Our results have important consequences for the design of algorithms that simulate PBC chains with MPS. Simulating PBC systems with MPS is computationally much more expensive [11] than simulating the same system with open boundary conditions (OBC). Nonetheless, when performing FSS in order to study critical ground states, systems with PBC are known to approach the thermodynamic limit much faster ($\propto N^{-2}$) than systems with OBC ($\propto N^{-1}$). For this reason, substantial effort [15, 17, 28, 61] has been made to try to lower the computational cost of MPS simulations with PBC. Two types of approaches have been pursued. One consists in building a MPS for a finite system with PBC by using the translationally invariant MPS tensor that has been optimized in an infinite chain with OBC [17]. This approach is equivalent to a crude approximation of the MPS transfer matrix: the $D^2 \times D^2$ matrix is approximated only by its dominant eigenvector [1]. The second approach [15, 28, 61] accounts for PBC by retaining more than one eigenvector in the approximation of the transfer matrix. We show in this work that the first approach fails to provide an accurate ground state approximation for critical PBC systems. A detailed comparison of these algorithms can be found in Appendix 3.6.

We will build our arguments by studying two paradigmatic critical spin models: the quantum Ising model (IS) and the quantum Heisenberg (HB) model, for chains with PBC and linear size N. The ground states are approximated by MPS of a given bond dimension D. Even if the Hamiltonian is critical, both the finite size of the chain and the finite bond dimension of the MPS induce a gap [2]

$$\Delta E_N = \xi_N^{-1} = \frac{2\pi\, x_1}{N} \tag{3.1}$$

$$\Delta E_D = \xi_D^{-1} \propto D^{-\kappa} \tag{3.2}$$

---

[1] Eigenvector corresponding to the eigenvalue with the largest magnitude.

[2] Note that in contrast to the rest of the paper where *the energy* always denotes an energy density (i.e. intensive energy measure), in this case the gap is an extensive quantity since it refers to the difference between the ground state energy and the first excited state of the entire system.

where x_1 is the smallest critical exponent of the theory [62] and κ is the exponent for the scaling of the effective correlation length of MPS simulations with finite bond dimension [16, 46]. Depending on which of the two gaps dominates, the system is in one of the two regimes

$$\xi_D \gg \xi_N : \text{FSS regime} \tag{3.3}$$

$$\xi_N \gg \xi_D : \text{FES regime} \tag{3.4}$$

The presence of two regimes in the PBC chain can be intuitively understood in the following way: in the FES regime defined by equation (3.4) the small dimension of the MPS matrices implies that the system is not aware of its geometry. Thus the boundaries do not play any role. In the FSS regime, defined by equation (3.3) on the other hand, the size of the matrices is big enough to notice the presence of the boundaries and thus different choices of boundary conditions lead to different MPS.

For simulations where

$$\xi_N \simeq \xi_D \tag{3.5}$$

we find for all values of N and D that are accessible numerically the presence of an abrupt transition between the FSS and FES regimes (for a related work see also Ref. [63]). One way to observe this transition is by looking at the difference between the exact ground state energy in the thermodynamic limit and the energy of MPS approximations with different N and D (see Fig.3.2). For fixed D these plots show a steep transition between the FSS regime where the difference scales like $\propto N^{-2}$ to the FES regime where the difference does not depend on N. Another way is to look at the overlap between MPS with different D for fixed chain length N (see Fig.3.3): starting off with a MPS with some big D_{max}, we look at its overlap with MPS with decreasing D. We then observe how the initially smoothly decreasing overlap abruptly drops towards lower values at some D_r, unambiguously showing the transition to the FES regime. Now the overlap is a global variable and as such indeed aware of the boundary conditions. The main finding of this paper is that states in the FES regime, while possessing the same local universal properties [46] like those in the FSS regime, turn out to have vanishing overlap with them.

We also present a possible technique to determine if a given bond dimension is sufficient to enter the FSS regime, so that we can give the computationally most favorable recipe to access global universal properties that depend on the boundaries (for a discussion of these properties see e.g. [64]).

The paper is organized as follows. We start by introducing the IS and HB models as well as the technique used to simulate them in section 3.2. In section 3.2.1 we present numerical evidence for the presence of the FSS and FES regimes in MPS simulations of PBC chains by

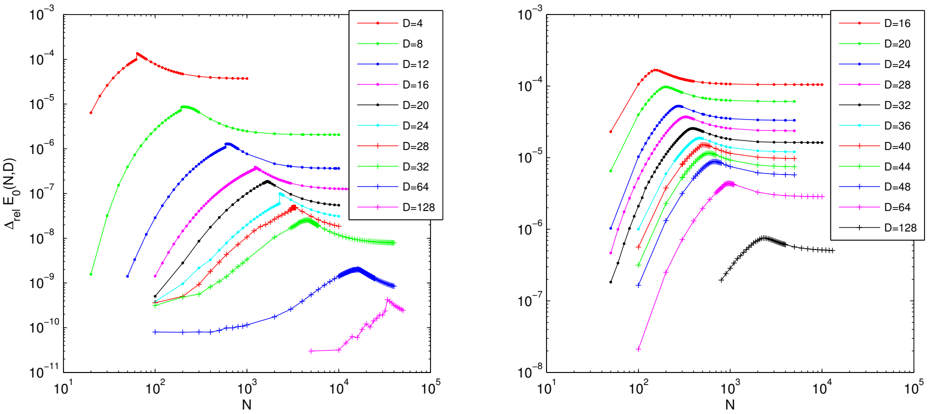

Figure 3.1: (Color online). Quantum Ising (left) and Heisenberg model (right): Relative precision of the optimal MPS ground state energy for different D as a function of N. The position of the *hump* that can be observed between the small and big N limits of each curve turns out to be proportional to the effective correlation length ξ_D of MPS with finite bond dimension.

looking at the ground state energy. In section 3.2.2 we discuss how to identify the sharp transition between the two regimes by looking at the overlap of very accurate MPS approximations of the ground state ($D = 64$) with less accurate MPS approximations ($D \leq 50$). The appearance of this transition together with several different methods for locating it accurately is one of the the main results of this paper. In section 3.2.2, we give a more detailed view on the transition between the two scaling regimes and explain that simulations of finite chains always contain a mixture of FSS and FES effects. Depending on which signature is stronger, the MPS can be assigned to either regime. Section 3.2.3 gives a recipe for obtaining the minimal bond dimension needed to capture global universal properties of critical systems. This recipe has a direct impact on future algorithm design. In section 3.2.4 we perform a numerical study of the transition and for the IS model we can provide evidence for its persistence in the thermodynamic limit. For the HB model we are not able to do the same due to the coarser precision of our simulations for this model. The evidence obtained for the IS model (see Appendix 3.5) suggests that any FSS analysis based on MPS must be performed in such a way that the studied points $\{N, D\}$ do not accidentally leave the FSS regime. In section 3.2.5 we provide a numerical analysis of the scaling function for the energy difference that reveals a two-parameter scaling analogous to the one found in the context of critical 2D classical systems by Nishino in Ref. [44]. We conclude with a discussion of the implications of our results and with a brief outline of future developments.

All technical details are contained in the appendices. There we first provide an alternative way to derive the analytical result for the scaling exponent κ in $\xi_D \propto D^{\kappa}$, which we find more intuitive than the one given in [16]. Then we show how our algorithm can be used in order to extract κ from the numerical results for the ground state energy. For the IS model, we are able to provide a numerical confirmation for the persistence of the transition between the FSS and the FES regime in the thermodynamical limit.

We would like to mention that throughout this work we always refer to the energy per site (i.e. energy density) as *the energy* unless explicitly stated otherwise.

3.2 Numerical results

We will use throughout this work the algorithm presented in [28]. That algorithm exploits the translational invariance of the models we study by using an ansatz based on translationally invariant MPS. This means that the MPS tensors at each site of the chain are identical thus reducing the cost of the simulation by a factor N. The energy is minimized by means of a conjugate gradient method in the subspace spanned by real and symmetric MPS with bond dimension D. The computational cost scales like $O(mnD^3) + O(n^2 D^3)$. m and n are parameters whose magnitude depends on the entanglement of the ground state of the model under consideration. For more details on the method we refer the reader to that work. The two paradigmatic models that we have considered are the critical quantum Ising model described by the Hamiltonian

$$H_{IS} = -\sum_{i=1}^{N} \sigma_i^z \sigma_{i+1}^z - \sum_{i=1}^{N} \sigma_i^x \ , \tag{3.6}$$

and the Heisenberg model described by the Hamiltonian

$$H_{HB} = \sum_{i=1}^{N} \vec{S}_i \vec{S}_{i+1} = \frac{1}{4} \sum_{i=1}^{N} (\sigma_i^x \sigma_{i+1}^x + \sigma_i^y \sigma_{i+1}^y + \sigma_i^z \sigma_{i+1}^z) \tag{3.7}$$

where the 1D lattice is chosen to be periodic. Both Hamiltonians are critical which means that their gap between the ground state and the first excited state closes as an inverse power of N as described in Eq. 3.1.

As a matter of fact the analysis in this work was triggered by a comprehensive study of the precision of the algorithm presented in [28]. We originally wanted to assess the usability of that method and to this end we simulated a plethora of different configurations $\{N, D\}$ for the IS and the HB models. A selection of these simulation results is shown in Figure 3.1 where we plot the relative precision of the ground state energy per site for simulations with different D and many different chain lengths N.

The shape of curves with constant D is very surprising since it shows a fundamental deviation from what we would have expected. Our expectation was that for short chains the precision will be generally better than for long chains and that as N gets bigger and bigger, the precision will eventually saturate from below to the value obtained with the corresponding D when simulating the chain in the thermodynamic limit. Obviously the small N and the big N regimes are in accordance with our expectation. However at some point between these limits we see the emergence of a *hump* which indicates that something interesting is happening in that region.

A detailed explanation for the surprising fact that the precision on the right side of the *hump* gets better with increasins N is given in the Appendix 3.4.2. In short, the reason for this behavior is the fact that *all* tensors of the ground state MPS for *any* chain length $N > \xi_D$ are basically the same. This happens because for any finite $N > \xi_D$ the simulated system looks for the MPS algorithm like an infinite system. Thus even though the MPS tensors remain unchanged for all $N > \xi_D$, the precision of the ground state energy (per site) gets better in Figure 3.1 because as N increases, the exact ground state energy also increases, i.e. it approaches the thermodynamic limit from below. We can nicely see in Figure 3.7 of Appendix 3.4.2 that on the left side of the *hump* our PBC algorithm yields a significant reduction of the energy as compared to the starting point of the algorithm, which in this case is our best MPS approximation of the ground state in the thermodynamic limit. On the right side, i.e. for $N > \xi_D$ the algorithm basically does not change the energy at all as compared to its starting point.

As a matter of fact we can show that if we interpret the position of the *hump* as an indicator for the effective correlation length ξ_D of MPS with finite D, we can reproduce the theoretically predicted result for the scaling of ξ_D [16] with very good accuracy (details in Appendix 3.4). The results presented in this work provide the general framework to understand the emergence of the *hump* and to explain what is happening when moving from the left to the right side of Fig. 3.1.

3.2.1 Two different regimes for MPS simulations

As already mentioned in the introduction a MPS simulation close to the critical point is an example of a two scale problem. This is not something unexpected as it has been pointed out in the context of 2D classical systems studied with the corner transfer matrix by Nishino and coworkers [44] and in the context of quantum phase transitions in 1D quantum chains with open boundaries by one of the authors (section IIIG of Ref. [46]). In the scenario we are considering, the two scales appearing are i) the correlation length induced by the finite size of the system N of Eq. 3.1 and ii) the correlation length induced by the size of the matrices D of Eq. 3.2. Depending on the relation among the two stated in Eqs. 3.3 and 3.4, the system will be in one of the two different regimes, respectively the FSS regime or the FES regime.

The approach to the thermodynamic limit of the ground state energy, as function of the relevant parameter N or D, is very different in the two regimes so that we can use it as a footprint for them. In the FSS regime it obeys the celebrated result by Cardy and Affleck [54, 65] from conformal field theory (CFT),

$$E_0(N) - E_0(\infty) = -\frac{v_f \pi c}{6N^2} \ , \tag{3.8}$$

where $E_0(\infty)$ is the thermodynamic limit, v_f is the Fermi velocity and c is the central charge of the considered model. In the thermodynamic limit, several authors have reported that [46, 36, 16]

$$E_0(D) - E_0(\infty) \propto \frac{\Delta}{D^{\omega}} \ . \tag{3.9}$$

where $\omega = 2\kappa$, κ is the same exponent of Eq. 3.2 and Δ is a positive non-universal constant. We show below that the same scaling holds also for MPS simulations of finite chains if N is big enough for a certain D. This happens exactly in the FES regime defined by (3.4).

The two regimes can be clearly distinguished in Fig. 3.2 where we present plots of the absolute value of the difference of the ground state energy obtained with MPS simulations and the exact value in the thermodynamic limit

$$\delta E_{N,D} = E_0(N,D) - E_0(\infty) \tag{3.10}$$

as a function of N in a log-log scale. Note that in Fig. 3.2 we make an abuse of notation by using $\delta E_N = (\delta E_{N,D})_{D=const.}$ and $\delta E_D = (\delta E_{N,D})_{N=const.}$, which can be only done as long as we specify what the constant value of D or N is. The data is collected from several simulations of the critical IS with PBC for chain lengths in the range $20 \leq N \leq 4{\cdot}10^4$ (panel a) and of the HB with PBC in the range $10^2 \leq N \leq 5 \cdot 10^3$ (panel b). D is going in both cases up to $D = 64$. Each line in the main plot represents simulations performed for different N at fixed D. The FSS predictions of Eq. 3.8 are straight lines plotted in black. For small N, each set of data follows the prediction of Eq. 3.8, which is a clear signal of the FSS regime. The maximal N for which the FSS prediction holds increases with growing D as expected. However, each set deviates at some big enough N from the FSS prediction to eventually stabilize to a value of the energy difference that only depends on D. This is a clear footprint of the FES regime scaling, as described in Eq. 3.9. In order to confirm this we have added to both panels insets where we have plotted several values of δE_D for large fixed N as a function of D in a log-log scale. Similar plots in the thermodynamic limit can be found in [36]. The linear fits (red lines) in the insets yield $\kappa_{IS} \approx 1.9776$ for $N = 10^4$ respectively $\kappa_{HB} \approx 1.3025$ for $N = 3000$. These values are compatible with the analytical values obtained for $N \to \infty$ in [16], namely $\kappa_{IS}^{anal} \approx 2.03425$ and $\kappa_{HB}^{anal} \approx 1.34405$ and thereby confirm the scaling of Eq. 3.9.

Note that we are able to obtain a much better precision for the IS than for the HB model at at the same computational cost . This is visible by comparing the panel a) to the panel b) and observing that for fixed D, the curves for the HB model deviate from the FSS at much lower values of N than the corresponding ones for the IS model.

3.2.2 The transition between the two regimes

In Figure 3.2 we can observe that for each line with constant D, the FSS region is separated from the FES region by a well distinguishable peak in the absolute value of δE_N. We would

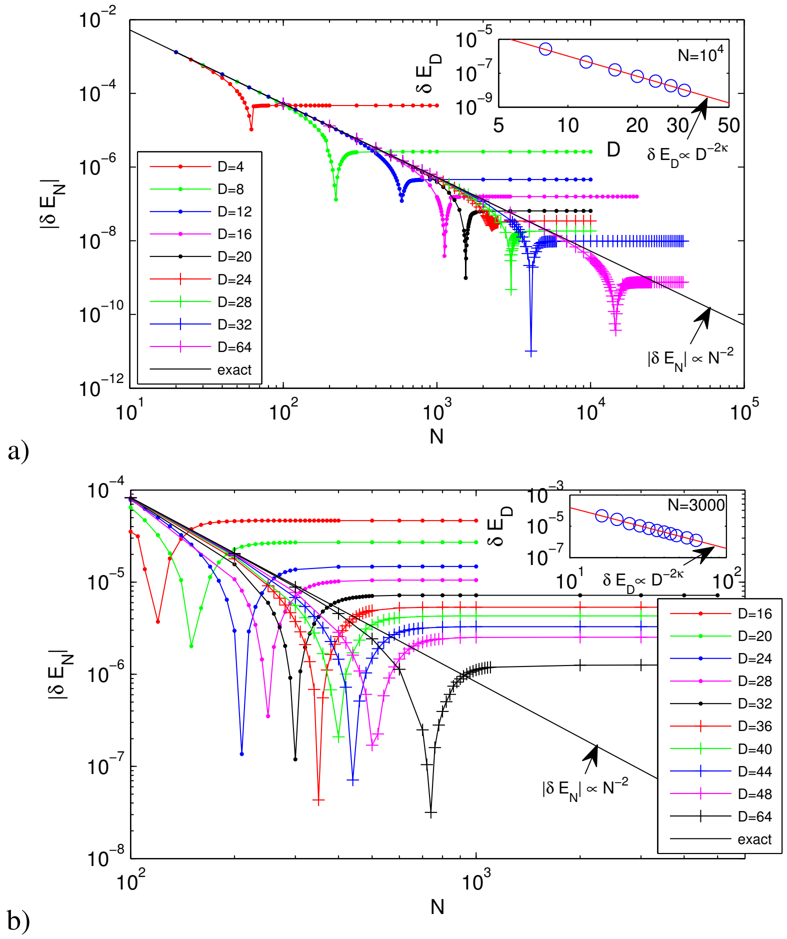

Figure 3.2: (Color online). a) Quantum Ising model, two regimes for simulations of PBC chains with lengths in the range $20 \leq N \leq 4 \cdot 10^4$, and D in the range $4 \leq D \leq 64$. Each line represents simulations performed at fixed D and different N. The plots show the absolute value of the difference $\delta E_N = E_0(N, D = const.) - E_0^{\infty}$. The FSS is represented by a diagonal black line following the scaling from Eq. 3.8. All data sets initially follow this line. The FES regime corresponds to the various horizontal lines, where δE_N saturates for different D to different values δE_D that do not depend on N. In the inset we collect these values to show that they reproduce the expected behavior of the FES. The two regimes are separated by the appearance of a pronounced peak. Since we plot an absolute value, the peak is nothing more than the change of sign in the difference $E_0(N, D) - E_0^{\infty}$ when moving from the FSS regime (3.8) to the FES regime (3.9). b) The same plot for the HB model tells us that here the FSS is much more difficult to study, since all data-sets deviate very soon from the pure FSS prediction.

now like to show that this transition does not depend on the choice of the observable but that it indicates a global change in the wave function.

To this end we can investigate the trace distance between the exact ground state of a chain with N sites and the MPS obtained from a series of simulations with different D. We have chosen the step size in D as small as possible, i.e. $\Delta D = 1$. Since the exact ground state wave function is only available for very small systems due to the exponential scaling of the number of parameters, we use as a *reference state* a MPS approximation of the ground state with very big D. For the N range in question, the biggest available bond dimension is $D = 64$. Note that the energy difference between the exact ground states and the *reference states* is much smaller than the difference to the MPS we want to compare to (see Fig. 3.1).

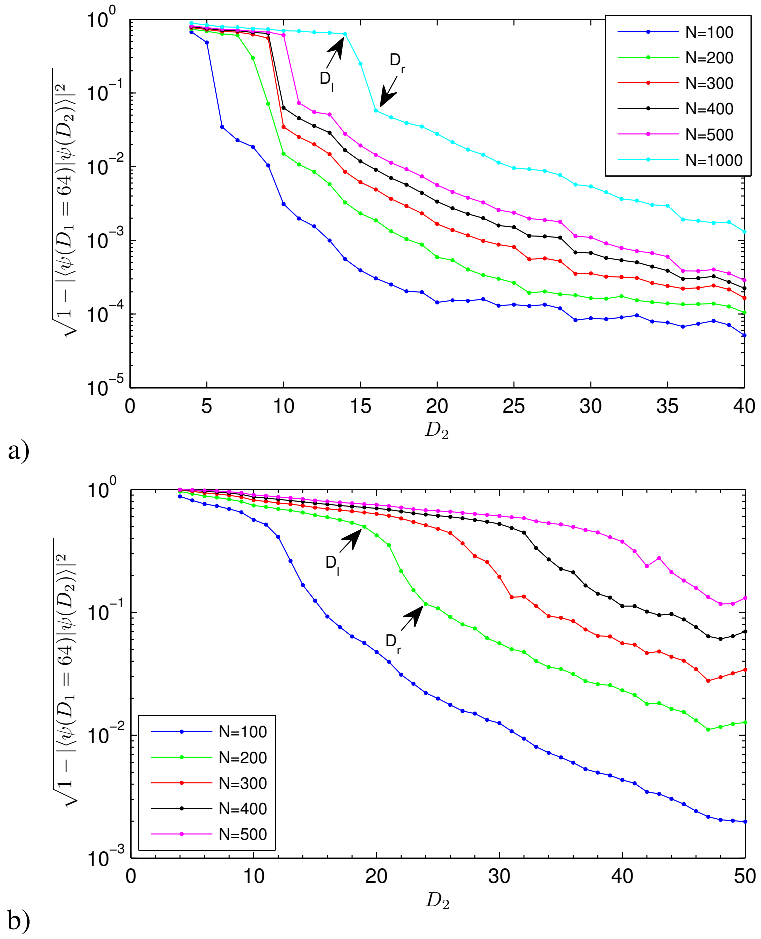

Figure 3.3: (Color online). a) Quantum Ising model: trace distance between *reference states* with $D_1 = 64$ and ground state MPS with bond dimensions D_2 for several different chain lengths. b) Heisenberg model: trace distance between *reference states* with $D_1 = 64$ and ground state MPS with bond dimensions D_2 for several different chain lengths.

Figure 3.3 shows the trace distance between states with relatively small D and *reference states*, for several different chain lengths N for both the IS and the HB models. Note that for every N there is a jump in the trace distance between states that are very far away from the *reference state* and states that are at least one order of magnitude closer to it. For the IS model the jump is very steep and for each line of constant N we can clearly identify D_l as the biggest D in the left (FES) regime and D_r as the smallest D in the right (FSS) regime. In this case the appearance of the jump evidently indicates the transition from the FSS regime, where the trace distance is close to zero, to the FES regime, where the trace distance abruptly increases.

For the HB model the transition is much smoother and we can not unambiguously define D_l and D_r for all lines with constant N. This happens presumably due to the fact that taking MPS with $D = 64$ as *reference states* is not accurate enough in the case of the HB model.

However, at least for the IS model, we are in the position to check if our intuitive expectation, that the transition occurs precisely when the correlation length of the finite size MPS reaches the size of the chain as described in Eq. 3.5, is quantitatively correct. The correlation length of MPS with finite D reads according to Eq. 3.2 as $\xi(D) = k_c \cdot D^\kappa$ where k_c is a proportionality constant. For our numerical study we obtain the parameters k_c and κ in the appendix 3.4. We can confirm that for each line of constant N the jump in the trace distance is consistent with our assumption, i.e. $\xi(D_l) < N < \xi(D_r)$.

Furthermore we would like to mention that jumps also occur in other quantities at the same D_l, for instance in the half-chain correlation function reported in [28] (see figure 9 in that work for a plot of the jump for $N = 500$). The fact that the induced correlation length $\xi(D)$ in the FES regime is smaller than the size of the system, suggests that the state is completely unaware of the presence of the boundaries. This confirms our intuition that MPS in the FSS regime are faithful approximations of finite chains with PBC, while MPS in the FES regime do not capture properties related to the boundary conditions.

Summarizing, the main point of this section is that if one is interested in the effects of PBC, results collected for D smaller than D_r should not be taken into account. Note that due to the residual dependence on D (see the section 3.2.2 for details on this point) one still has to extrapolate the results in the limit $D \to \infty$ in order to obtain accurate results. If, on the other hand, one is interested only in local universal quantities (i.e. where boundary conditions are irrelevant), there is no point in simulating the system with PBC and one should rather perform a standard FES study [46].

The real scenario, a complex cross-over induced by corrections to the scaling

We have seen above how in the extremal regions of Figure 3.2, the simulation results follow the behavior predicted by FSS respectively FES. In the intermediate region however, the simulations display a behavior that can not be attributed to either regime. We would now like to point out that the real picture is somewhat more complex than the two-regime interpretation given above.

The leading scaling behavior given in Equations 3.8 and 3.9 represents only the first terms in a series expansion with more complex analytic corrections. Thus these terms are accompanied by higher order terms called corrections to scaling. In order to understand the scenario we must consider the general Taylor expansion of a two variable function. Let us consider two variables Δ_D and Δ_N with the property that $\lim_{D\to\infty} \Delta_D = 0$ and $\lim_{N\to\infty} \Delta_N = 0$. Obviously these variables can be identified with the gaps proportional to the inverse of the correlation length induced by the system size N and by the finite matrix dimension D as defined in

Eq. 3.1 and Eq. 3.2. Part of the scaling ansatz consists in assuming that all universal quantities are universal functions of these two variables.

Let us review the case of a one-scale problem. In this case, by neglecting higher than quadratic terms in the vanishing variable (e.g. Δ_N) we get the following series expansion for some universal function g

$$g_{\Delta_N} = g_0 + (\partial_x g_x)_{x=0}\Delta_N + \frac{1}{2}(\partial_x^2 g_x)_{x=0}\Delta_N^2 + \cdots \tag{3.11}$$

In the regime where $\Delta_N^2 \ll 1$, the first two terms are considered the leading scaling behavior while the rest provide only higher order corrections. If we now take a two scale problem

$$\begin{aligned} f_{\Delta_D,\Delta_N} = f_{0,0} &+ (\partial_x f_{x,0})_{x=0}\Delta_D + (\partial_y f_{0,y})_{y=0}\Delta_N \\ &+ \frac{1}{2}(\partial_x^2 f_{x,0})_{x=0}\Delta_D^2 + \frac{1}{2}(\partial_y^2 f_{0,y})_{y=0}\Delta_N^2 \\ &+ (\partial_x\partial_y f_{x,y})_{x=0,y=0}\Delta_D\Delta_N + \cdots \end{aligned} \tag{3.12}$$

in the regime where $\Delta_D \ll \Delta_N^2 \ll \Delta_N$ we are back to the previous situation and we can apply the one-scale ansatz of Eq. 3.11 to the function $g(\Delta_N) = f(\Delta_N, 0)$; the same thing is valid in the opposite regime $\Delta_N \ll \Delta_D^2 \ll \Delta_D$ with the obvious substitution $g(\Delta_D) = f(0, \Delta_D)$. These two limits would correspond to what we have called in the main text the FSS regime and the FES regime (see Eq. 3.3 and 3.4).

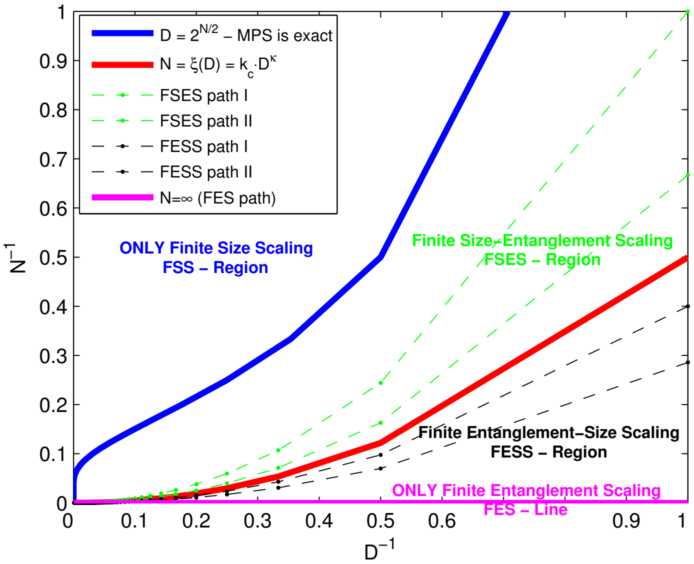

Figure 3.4: (Color online). Classification of MPS simulations of spin chains according to the simulation parameter pair $\{N, D\}$. All lines ending in the origin denote possible paths to approach the thermodynamic limit of critical systems when doing MPS simulations.

Now in general, there is a huge regime where for example $\Delta_N^2 \ll \Delta_D \leq \Delta_N$ or $\Delta_D^2 \ll \Delta_N \leq \Delta_D$. In this case the leading scaling behavior is modified by corrections that are not proportional to the next power of the relevant variable but to the ratio among the two variables. Indeed if we consider the scenario where $\Delta_D^2 \ll \Delta_N \leq \Delta_D$ in Eq. 3.12 we obtain

$$f_{\Delta_D,\Delta_N} = f_{0,0} + \Delta_D \Big[(\partial_x f_{x,0})_{x=0} + (\partial_y f_{0,y})_{y=0} \frac{\Delta_N}{\Delta_D} \Big] + \cdots \qquad (3.13)$$

How relevant the correction is clearly depends on the scale separation, i.e. on how close Δ_N/Δ_D is to one. In the following we give a sketch of how this cross-over region looks like and we introduce two new terms: *Finite Entanglement-Size Scaling* (FESS) for the region where the leading scaling is due to the finite size of the matrices and the corrections come from the size of the system and *Finite Size-Entanglement Scaling* (FSES) where the leading scaling is due to the size of the system and the corrections come from the size of the matrices.

Figure 3.4 shows a classification of MPS simulations according to the simulation parameter pair $\{N, D\}$. The thermodynamical limit can be approached by moving along any path towards the origin of the diagram $\{N^{-1} = 0, D^{-1} = 0\}$. However in order not to distort the scaling analysis by mixing the different N and D related corrections, moving from one point to the next on the path should leave the ratio Δ_N/Δ_D unchanged. This is equivalent to the requirement that any path is completely determined by the path constant $k = N/D^\kappa$.

We can distinguish three different regions and three important lines in Fig. 3.4 In the region above the *blue line* which is defined by $D = d^{N/2}$, the MPS bond dimension is large enough to represent the ground state exactly. Of course doing MPS simulations in this regime is pointless since the computational cost becomes exponential in N and there is no advantage over exact diagonalization. Thus no matter which path towards $N \to \infty$ we choose in this region, it is completely equivalent to FSS. The *magenta line* with $N^{-1} = 0$ represents the only path along which pure finite entanglement scaling (FES) holds. The *red line* represents the path along which the induced correlation length is equal to the system size, i.e. $N = \xi(D)$. We will call this line in the following the *critical line*, which can be obtained using the method described in appendix 3.4. Between this line and the *FES line*, there is a region where $N > \xi(D)$. All simulations done in this region barely registrate the boundaries of the system and the fixed point MPS is more or less the same like that of a $N = \infty$ simulation with same D. However there is a slight effect due to the finite size for points close to the $N = \xi(D)$ line as can be seen in Figure 3.1. This is why we call this region the finite entanglement-size scaling (FESS) region: the entanglement scaling predominates, but there is a small trace of finite size scaling behavior. The region between the *critical line* and the FSS-regime describes MPS simulations where $\xi(D) < N$, which turn out to reproduce faithfully the long range correlations throughout the entire chain (see figure 9 in our previous work [28]). The FSS aspect predominates in this region, however there is also the inherent error of MPS simulations with $D < d^{N/2}$, so we call it the finite size-entanglement scaling (FSES) region.

Despite the rigorous classification of regimes from Figure 3.4 we will restrict ourselves in the following to discriminate merely between the regimes on different sides of the critical line. We do this in order to improve the readability. Thus we will refer to both FSS and FSES as FSS; analogously we will denote both FES and FESS as FES.

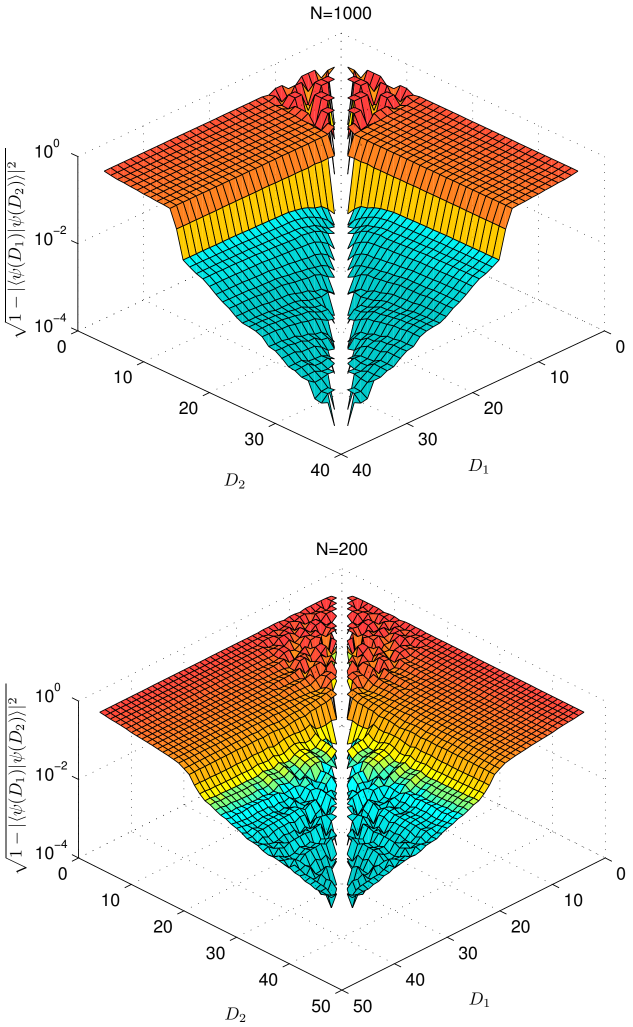

a)

b)

Figure 3.5: a) (Color online). Quantum Ising model: trace distance between ground state MPS with different bond dimensions D_1 and D_2 for a chain with $N = 1000$ sites. b) Heisenberg model: trace distance between ground state MPS with different bond dimensions D_1 and D_2 for a chain with $N = 200$ sites. By using relatively small bond dimensions we are able to localize the transition between the FES and FSS regime for each N. This can be used in case we are interested in performing a FSS analisys by providing the lower bound D_{r} such that the state we obtain is not orthogonal to the exact state.

3.2.3 Minimal D for faithful simulations

We can outline a direct application of the presence of a transition between the FSS regime and the FES regime. Suppose that we want to simulate a critical chain with PBC such that it is in the FSS regime, i.e. the properties due to the boundary conditions are faithfully reproduced since $N < \xi(D)$. In order to minimize the computational cost we would like to use the smallest possible D that captures the PBC topology. By looking at figure 3.3 it is clear that we would have to choose $D = D_r$ to this end. The problem is that in order to make that plot we had to use as *reference states* MPS with very large $D = 64$, which is exactly what we would like to avoid in this case. Fortunately it turns out that even without a large D simulation it is possible to detect the optimal $D = D_r$. This is due to the fact that all MPS with $D \geq D_r$ have a much smaller trace distance among eachother than with MPS with $D < D_r$.

The trace distance among all states with $D < 40$ for an IS chain with $N = 1000$ is shown in figure 3.5 a). The plot is of course symmetric in D_1 and D_2 and we have omitted the points on the diagonal since they are trivially 0. The transition between the FSS and the FES regime is clearly distinguishable at the same location of the jump as in figure 3.3 but in this plot we used only MPS with relatively small bond dimension. Note furthermore that if $D_1, D_2 < D_r$ the trace distance between these states is wildly oscillating. However if D_1 and D_2 are on different sides of the jump, profiles similar to figure 3.3 emerge. Now it is clear how we can find the optimal $D = D_r$ with the smallest computational cost possible: for a given N run the PBC simulations by increasing D in small steps, ideally $\Delta D = 1$. After each simulation compute the overlap with all previously obtained MPS and when the nice profile with the jump appears, we know we have reached $D = D_r$. The same strategy can be employed for the HB model, however, just like in figure 3.3, the transition is much smoother in this case.

As a side remark note that due to the fast decay of the eigenvalues of the MPS transfer matrix one can compute the overlaps with computational cost scaling like $O(nD^3)$. The meaning of n and the method how to achieve this is described in [28].

3.2.4 Thermodynamic limit of the transition

What can figure 3.3 tell us about the behavior of the transition between the FSS and FES in the limit $N \to \infty$?

For the IS model, qualitatively the height of the jump seems to remain constant for increasing N. The trace distance between MPS with bond dimensions D_l and D_r to the *reference state* also seems to remain more or less stable but this is of course not enough evidence for the persistence of the transition in the thermodynamic limit. In appendix 3.5, we present a detailed analysis that shows that for the IS model i) the $N \to \infty$ limit of the trace distance between the exact ground state (approximated by a *reference state*) and MPS obtained in the FSS regime is strictly bigger than zero, ii) the same limit for the trace distance with respect to MPS obtained in the FES regime is zero. ii) implies that states in the FES regime are globally orthogonal to the exact ground state of the PBC chain. As we already mentioned above this does not affect the possibility to extract local universal information from those states. However ii) clearly shows that MPS in the FES regime are globally not a good approximation for the ground state of the IS model with PBC.

Unfortunately we cannot obtain the same conclusions for the HB model. Presumably this is due to the fact that the *reference states* that we use are not good enough approximations of the true ground state of the model in this case. This becomes clear if we look again at figure 3.1: for the IS model the $D = 64$ states have a much better precision than the MPS we compared them to in order to prove the persistence of the transition in the thermodynamic limit (see Appendix 3.5 for details). For the HB model on the other hand, the $D = 64$ line covers almost three orders of magnitude in the relative precision plot; at its maximum it is over one order of magnitude above the points belonging to MPS that we must compare the *reference states* to in order to perform our analysis of the thermodynamic limit (e.g. the data points with $N = 100$ and $D = 48$). The $D = 128$ line in the right plot of figure 3.1 seems to fulfill similar requirements like the $D = 64$ line in the left plot. However, in that regime, for $N \ll \xi(D)$, the PBC algorithm is very inefficient and it would take unreasonably long to obtain the data points for $D = 128$.

3.2.5 The scaling function

Finally we conduct an analysis of the scaling of MPS simulations across the entire interval $N/\xi(D) \in (0, \infty)$ which covers all possible pairs $\{N, D\}$. This is very much in the spirit of the scaling analysis performed by Nishino et al. for classical 2D systems in Ref. [44]. The main differences are that in our case the energy difference $\delta E_{N,D}$ can take both positive and negative values, and that we obtain the effective correlation length $\xi(D)$ from an analysis of the *humps* in the relative precision of the energy (see Appendix 3.4 for details) instead of using the ratio between the two biggest eigenvalues of the MPS transfer matrix.

Analogously to Nishino, we first eliminate the FSS scaling from $|\delta E_{N,D}|$ and then we plot the result (in our case this is $N^2|\delta E_{N,D}|$) as a function of $N/\xi(D)$. The fact that all data (with exception of the $D = 64$ points for the IS model) collapses into a single curve justifies the assumption that

$$\delta E_{N,D} = E_0(N, D) - E_0(\infty) = \frac{f(N/\xi(D))}{N^2} \quad . \tag{3.14}$$

with some scaling function $f(x)$ that is not exactly known. What we can easily write down however is its asymptotic behavior

$$\begin{aligned} \lim_{x\to 0} f(x) &= -\frac{v_f \pi c}{6} \\ \lim_{x\to\infty} f(x) &= \Delta \cdot \left(\frac{N}{D^\kappa}\right)^2 \quad . \end{aligned} \tag{3.15}$$

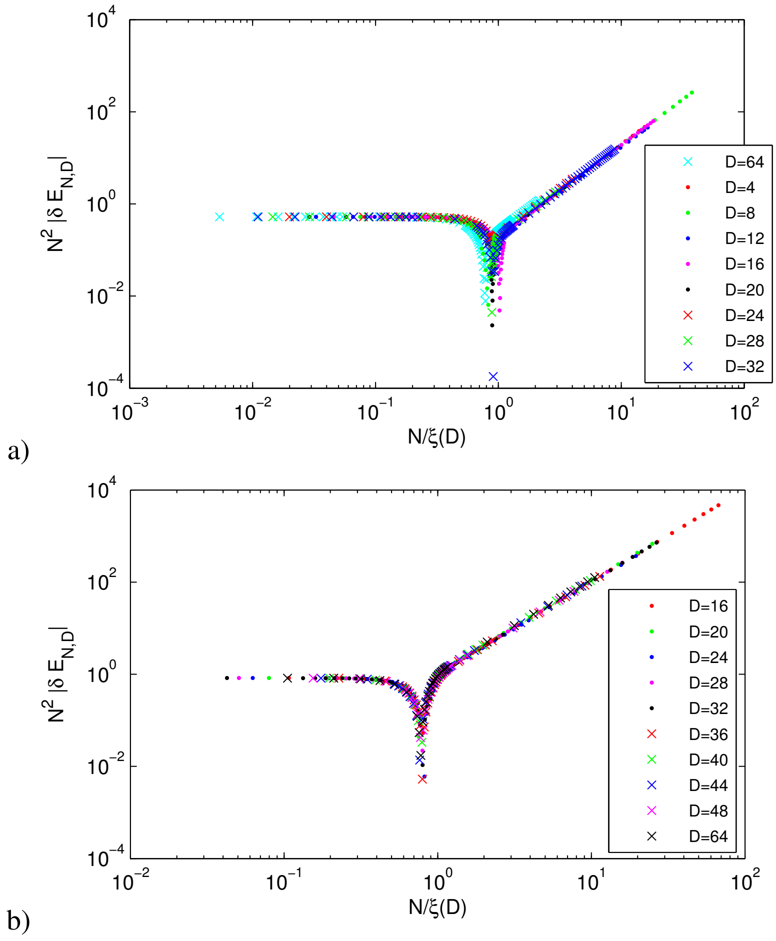

Figure 3.6: (Color online). a) Quantum Ising model: log-log plot of $N^2|\delta E_{N,D}|$ versus $N/\xi(D)$ that illustrates the collapse of the data into a single curve. The points with $D = 64$ slightly deviate from the curve traced by data points with smaller D. b) Heisenberg model: log-log plot of $N^2|\delta E_{N,D}|$ versus $N/\xi(D)$ that illustrates the collapse of the data into a single curve.

For the IS model we have used for $\xi(D)$ the expression obtained from the hyperbola fit in Fig. 3.8 of the Appendix 3.4, i.e. $\xi(D) = 3.810 \cdot D^{2.042}$. Note that in plot a) of the Fig. 3.6, the data for different D collapses almost perfectly in the extremal regimes $N \ll \xi(D)$ and $N \gg \xi(D)$. There is a slight deviation of the $D = 64$ curve that can be explained if we look at figure 1 in [36] (there the $D = 64$ data point also slightly deviates from the line that is traced by the points with $D < 64$). In the regime where $N \approx \xi(D)$ the curves do not collapse so nicely which is a manifestation of the fact that the *humps* in Fig. 3.1 are so different for the IS model.

For the HB model we have used for the effective correlation length $\xi(D) = 3.647 \cdot D^{1.338}$ as obtained from the hyperbola fit in Fig. 3.8. Plot b) of Fig. 3.6 shows an almost perfect collapse even in the region $N \approx \xi(D)$. Presumably this is due to the fact that for the HB model the *humps* in Fig. 3.1 are much more similar among each other than in the case of the IS model.

3.3 Conclusions

An accurate analysis of MPS simulations of critical spin chains with PBC reveals the appearance of two regimes. The FSS regime where the energy gap of the system is induced by the size of the system and the FES regime where an effective energy gap is induced by finite D. While in both regimes local universal quantities can be extracted by studying the scaling of the observable with respect to the relevant variable (the size of the system for the FSS or the size of the MPS matrices for the FES regime), we have shown that for the Quantum Ising model, states in the FES regime are orthogonal to the exact ground state in the thermodynamic limit. Intuitively this happens due to the fact that for MPS simulations in the in the FES regime, the induced correlation length is smaller than the system size and thus the MPS is not aware of the size of the system. Since in critical systems the boundary conditions strongly affect global properties of the system, this result seems quite natural.

Our results can be interpreted as a further benchmark for recently introduced algorithms that try to lower the computational cost of PBC simulations with MPS [15, 28, 17, 61] (see Appendix 3.6). Here we provide strong hints that in order to correctly describe the ground state of a finite chain with PBC for critical systems, these algorithms should be used with care in order not to obtain wave functions that are orthogonal to the exact ones. What one would indeed interpret as the MPS tensor for a PBC chain, in some regime could turn out to be closer to the MPS tensor of an infinite OBC system.

However, considering that in the context of FES, OBC systems approach the thermodynamic limit for expectation values of *local operators* with the same inverse power of the correlation length like the one appearing in the FSS of PBC systems (e.g. the ground state energy converges to the thermodynamic limit as a function of the corresponding correlation length as ξ^{-2}), the traditional FSS reason to prefer PBC systems instead of OBC systems does not hold in this case. In this sense our results can be also used in a constructive way. In order to extract universal information about *local operators*, one is better off by using FES rather than FSS, since simulations in the FES regime have a much better scaling of the computational cost.

Things are more complex if one is interested in *global observables*, such as e.g. two point correlation functions at half chain length. For PBC systems the scaling analysis must be performed in this case on paths with constant $k = N/D^{\kappa}$ that lie completely in the FSS regime. The computationally least expensive such path is the one where for every given N, the MPS bond dimension D is just big enough such that $\xi_D > \xi_N$. We have shown how that minimal D can be found for any N by looking at the overlap between MPS with increasing D until the discrete transition between the FES and the FSS regime is detected. Regarding the scaling exponent κ, we have been able to numerically confirm the theoretically predicted values with an accuracy of approximately 0.4% for both the Quantum Ising and the Heisenberg models. Furthermore we have shown in Appendix 3.4.1 how the analytical expression for κ, originally derived in [16], can be obtained in an alternative way.

Following Nishino's analysis for 2D classical systems [44] we have shown that also for MPS simulations of 1D quantum systems the scaling of the MPS ground state energy in simulations with finite N and D obeys a two-parameter scaling function. Finding an analytical expression for this function is something that still has to be done.

A further interesting future line of research is to understand how to extract information about the operator content of the Conformal Field Theories related to the infrared behavior of the studied critical spin systems (that strongly depend on boundary conditions [54, 64]) directly out of the MPS tensors.

3.4 Appendix A: Effective correlation length

3.4.1 Analytical results

Recently it has been shown numerically that any MPS simulation of an infinite spin chain leads to the emergence of an effective correlation length induced by the finite rank D of the MPS matrices, even if the studied system is critical [46]. In Ref. [16] the authors relate the numerical observation that $\xi(D) \propto D^{\kappa}$ from Ref. [46] to analytical results on the spectrum of the reduced density matrix of a subsystem from Ref. [66] and to well-known results from conformal field theory [54, 65] in order to derive an analytical expression for the exponent κ. Here we derive the same results in a different way.

The starting point for our argument is the same like the one in [16], namely that corrections to the exact ground state energy in the thermodynamic limit can have different origins. On one hand conformal invariance yields in the vicinity of the critical point (i.e. $\epsilon = |\lambda - \lambda_{crit}|/\lambda_{crit} \ll 1$) according to Refs. [54, 65, 16]

$$E_0(\xi_\epsilon) = E_0(\infty) + \frac{A}{\xi_\epsilon^2} \tag{3.16}$$

where A is a non-universal constant. On the other hand, MPS simulations with finite D yield according to Refs. [46, 66, 16]

$$E_0(\xi_D) = E_0(\infty) + \frac{\beta}{\xi_D} P_r(b, D) \tag{3.17}$$

where β is a non-universal constant, $P_r(b, D)$ is the residual probability due to the usage of finite D and b is related to the dominant eigenvalue of the reduced density matrix of the half-chain (see Refs. [66, 16]). Now it has been observed that the usage of finite D in MPS simulations close to the critical point leads to an effective shift of the critical point (see Fig. 2 in [46]). This observation led us to the idea of equating the corrections in Eqs. (3.16) and (3.17) and identifying ξ_ϵ with ξ_D. Together with the assumption $\xi_D = k_c \cdot D^{\kappa}$ this yields

$$P_r(b, D) = \frac{A}{\beta \cdot \xi_D} = A' \cdot D^{-\kappa} \tag{3.18}$$

where we have collected all constants into $A' = A/(k_c \cdot \beta)$.

In the large D limit (required due to our assumption of working in the scaling limit), the residual probability reads according to [16]

$$P_r(b, D) = \frac{2be^{-b}D}{\ln D - 2b} e^{-(\ln D)^2/4b} \tag{3.19}$$

where

$$b = \frac{c}{12} \ln \xi_D \approx \frac{c\kappa}{12} \ln D \tag{3.20}$$

and c denotes the central charge in the associated conformal field theory. Inserting (3.19) and (3.20) into (3.18) yields after several steps

$$\frac{c\kappa}{6 - c\kappa} D^{-\frac{c\kappa}{12} - \frac{3}{c\kappa} + 1} = A' \cdot D^{-\kappa} \ . \tag{3.21}$$

Equating the exponents in (3.21) yields a quadratic equation for κ with the solutions

$$\kappa_{\pm} = \frac{6}{c \cdot (1 \pm \sqrt{\frac{12}{c}})} \ . \tag{3.22}$$

The physical root is the one that is positive for all values of c, i.e.

$$\kappa = \frac{6}{c \cdot (1 + \sqrt{\frac{12}{c}})} \tag{3.23}$$

which is exactly the result obtained in Ref. [16].

3.4.2 Numerical results

In this appendix we show how the effective correlation length $\xi(D)$ emerges in our simulations of finite spin chains with PBC. As the scaling of the algorithm [28] is quasi-independent of the chain length N we can use it to approximate ground states of arbitrary long chains with PBC. The relative precision of the MPS ground state energy for a given D is plotted in figure 3.1 as a function of N. Each of the lines contains a *hump* which can be interpreted as the evidence for a finite correlation length $\xi(D)$. In order to see this let us have a look at how the *hump* emerges. The left part of figure 3.7 shows a comparison between the relative precision of the PBC-MPS ground state energy (i.e. the MPS towards which the algorithm in [28] has converged) and the relative precision of the energy of the MPS that we had used as a starting point for the gradient search. As explained in [28] this is the local MPS tensor obtained by imaginary time evolution [36] for a chain in the thermodynamic limit (TL) when it is used in the finite PBC geometry. One can see that for a given D, on the left side of the *hump* there is considerable improvement in the precision of the energy between starting and ending point of the gradient search. As one approaches the *hump* from the left, the improvement decreases in order to vanish

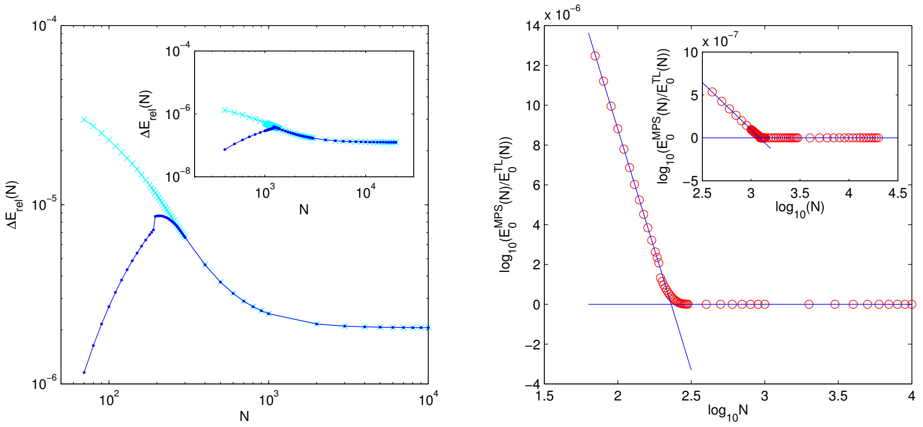

Figure 3.7: (Color online). Quantum Ising model data. Left: relative precision of the PBC-MPS ground state energy (blue/dark) and relative precision of the state used as an input for the PBC algorithm (i.e. obtained by inserting the TL-MPS, cyan/bright) as compared to the exact result for $D = 8$ and $D = 16$ (inset). Right: ratio between the PBC-MPS energy and the one of the input state (TL-MPS) for $D = 8$ and $D = 16$ (inset). Fitting a degenerate hyperbola in form of two straight lines yields a well defined point (the intersection point) whose value as a function of D is proportional to the effective correlation length.

completely on the right side. This can be interpreted as follows: if N is too large for a given D, the finite chain looks for a local MPS-tensor as if it would be infinite. Sites that lie further apart than a certain correlation length $\xi(D)$ effectively do not see each other. The transition to this region happens more or less smoothly since for growing powers of the MPS transfer matrix T, the subspace spanned by these powers gets smoothly restricted to the dominant eigenvector i.e. $T^N|_{N\gg\xi(D)} \approx \lambda_1^N |\lambda_1\rangle\langle\lambda_1|$.

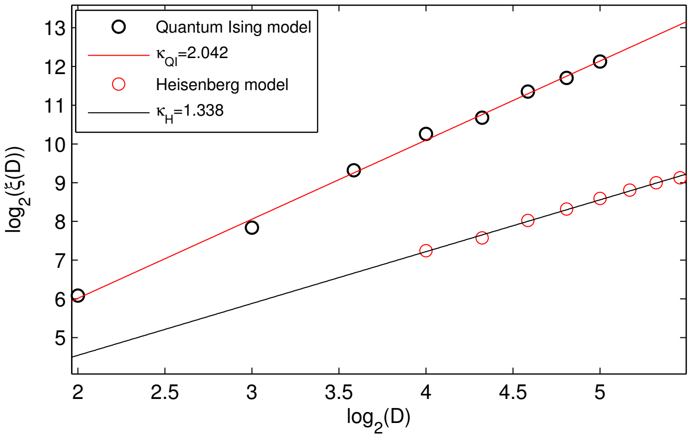

Figure 3.8: (Color online). Quantum Ising (upper) and Heisenberg model (lower): linear fit of the logarithm of the effective correlation length as a function of the bond dimension D.

Thus the *humps* must represent some evidence for the emergence of a finite correlation length, but how can we extract some reliable numbers from them, as they differ considerably in shape and width? The answer is given by the right part of figure 3.7. We have observed empirically that if we make a log-log plot of $E_0^{final}(N)/E_0^{initial}(N)$ [1] we obtain approximately two straight lines connected by a small piece that is more or less smooth. This picture is reminiscent of a rotated hyperbola. We know furthermore that in the large N limit all points have ordinate 0. This suggests to fit a hyperbola that is degenerated to two straight lines through our data. The intersection of these lines is a well defined point which should be proportional to $\xi(D)$.

Figure 3.8 shows log-log plots of the effective correlation length as defined above for both the Quantum Ising and the Heisenberg models. After fitting straight lines through each of the data sets we can read off the scaling $\xi(D) = k_c \cdot D^\kappa$ with $\{\kappa \approx 2.042, k_c \approx 3.810\}_{IS}$ and $\{\kappa \approx 1.338, k_c \approx 3.647\}_{HB}$. Comparison with the analytical results (i.e. $\kappa_{IS}^{anal} \approx 2.03425$ and $\kappa_{HB}^{anal} \approx 1.34405$) yields a difference of roughly 0.4% for the Quantum Ising model and of roughly 0.43% for the Heisenberg model. These results are the ones we refer to in Sec. 3.2.2 as the ones fulfilling $\xi(D_l) < N < \xi(D_r)$.

An alternative way to extract the effective correlation length is obtained by interpreting the abscissa of the minimum of each curve in Fig. 3.2 as a length proportional to $\xi(D)$. Fitting a straight line through these minima in a log-log plot of $N(D)$ yields for the IS model the exponent $\kappa_{\text{IS}} \approx 2.0293$ which approximates the analytical result with an accuracy of roughly 0.24%. On one hand this result is closer to the analytical value than the one obtained using the degenerated hyperbola fit. On the other hand, if we want to predict the bond dimension D for which the jump in the trace distance occurs in simulations with fixed N, it turns out that the value obtained using this fit does not always coincide with the actual values observed in figure 3.3. As mentioned above, the degenerated hyperbola fit satisfies this consistency test, which is why we prefer using that method to extract an approximation for κ. Furthermore the plots in figure 3.2 require knowledge of the exact ground state energy in the thermodynamic limit, which is not always available. The strategy with the hyperbola fit on the other hand does not require any analytical results and thus can always be used.

3.5 Appendix B: Detailed treatment of the thermodynamic limit of the transition

In this appendix we present the details we used for the conclusion drawn in section 3.2.4 of the main text. As mentioned above in section 3.2.2 a reliable analysis of the thermodynamic limit can only be made properly if we move towards it on paths of constant $k = N/D^{\kappa}$. However this analysis provides conclusive results only for the IS model which is why we skip presenting the results obtained for the HB model. As mentioned in the main text, the reason why this method fails for the HB model is that the *reference states* are in that case not precise enough.

---

[1] $E_0^{final}(N)$ is the energy of the MPS obtained as the ground state by our conjugate gradient search for the finite chain with N sites and PBC. $E_0^{initial}(N)$ is the energy obtained by plugging the MPS resulting from imaginary time evolution of the infinite chain into the finite size geometry with PBC. As mentioned in the main text, this MPS is used as the starting point of the conjugate gradient search.

As a first step let us normalize the tensors in our states such that the largest eigenvalue of the MPS transfer matrix T is equal to one (i.e. $\lambda_1 = 1$ and $\lambda_i \geq \lambda_j, \ \forall i < j$). This yields for the norm of such a state

$$\langle \Psi(D,N)|\Psi(D,N)\rangle = \mathrm{Tr}(T^N) = 1 + \sum_{i=2}^{D^2} \lambda_i^N(D,N) \ . \tag{3.24}$$

We will always use in the following lower-case greek letters to denote states that are normalized to one and upper-case letters for the corresponding state normalized according to (3.24), i.e.

$$|\psi\rangle = \frac{|\Psi\rangle}{\sqrt{\langle\Psi|\Psi\rangle}} \ . \tag{3.25}$$

For the computation of the trace distance between *reference states* and states lying on a curve with fixed k we need the absolute square of the overlap which becomes

$$\begin{aligned} &|\langle\psi(D_{k,N},N)|\psi(D_{\text{ref}},N)\rangle|^2 \\ =&\frac{|\langle\Psi(D_{k,N},N)|\Psi(D_{\text{ref}},N)\rangle|^2}{\langle\Psi(D_{k,N},N)|\Psi(D_{k,N},N)\rangle\,\langle\Psi(D_{\text{ref}},N)|\Psi(D_{\text{ref}},N)\rangle} \\ =&\frac{\left[\sum_{i=1}^{D_{\text{ref}}\cdot D_{k,N}} \mu_i^N(D_{k,N},D_{\text{ref}},N)\right]^2}{\left[1+\sum_{i=2}^{D_{k,N}^2}\lambda_i^N(D_{k,N},N)\right]\left[1+\sum_{i=2}^{D_{\text{ref}}^2}\lambda_i^N(D_{\text{ref}},N)\right]} \ . \end{aligned} \tag{3.26}$$

In the numerator we have used $\mu_i(D_{k,N}, D_{\text{ref}}, N) =: \mu_i(k,N)$ to denote the eigenvalues of the overlap transfer matrix

$$T_{\text{ovlp}}(k,N) = \sum_{i=1}^{d} A_i(D_{k,N},N) \otimes A_i^*(D_{\text{ref}},N) \ , \tag{3.27}$$

where the $A_i(D,N)$ represent as usually the matrices of a translationally invariant MPS with N sites and virtual bond dimension D. Similarly we will use for the eigenvalues of the MPS transfer matrix the notation $\lambda_i(k,N) := \lambda_i(D_{k,N},N)$ in the following. This can be done since we need only two of the quantities (D,N,k) to uniquely specify the point of the phase diagram that we want to refer to.

The crucial argument in favor of the persistence of a discrete transition between the two regimes in the thermodynamic limit will be the fact that in this limit $\mu_1(k,N)$ converges quickly to 1 in the FSS regime (i.e. for $k < k_c$), while in the FES regime (i.e. for $k > k_c$) this does not happen. In fact we will show below that in the first case $\lim_{N\to\infty}\mu_1^N(k,N) = 1$ while in the second case we have $\lim_{N\to\infty} \mu_1^N(k,N) = 0$. The other contributions in the numerator of (3.26) will turn out to be negligible for $N \to \infty$, i.e. $\lim_{N\to\infty} \mu_i^N(k,N) = 0$ for any k and all $i > 1$. Furthermore we will show that the denominator of (3.26) remains finite in all cases such that we will be able to conclude that the overlap of the *quasi-exact* [1] ground state with states in the FES regime converges to zero in the thermodynamic limit. Along the same lines we will argue that the overlap of the *quasi-exact* ground state with states in the FSS regime is always larger than zero in the thermodynamic limit, thereby concluding that a detectable transition between the two regimes persists for $N \to \infty$.

To this end we have considered three paths in the FSS regime ($k \approx 0.37, 0.54, 0.97$) and two paths in the FES regime ($k \approx 18.0, 58.7$). The exact data points (N, D) for four of these paths are listed in table 3.1. Note that since $N, D \in \mathbb{N}$ the exact value for $k = N/D^\kappa$ varies slightly within each path.

$\kappa = 2.03425$											
$k \approx 0.37 < k_c$			$k \approx 0.54 < k_c$			$k \approx 18.0 > k_c$			$k \approx 58.7 > k_c$		
k	N	D	k	N	D	k	N	D	k	N	D
0.374	122	17	0.538	118	14	17.9	300	4	58.9	1000	4
0.373	206	22	0.540	198	18	17.8	470	5	59.0	1580	5
0.371	288	26	0.540	298	22	18.3	700	6	58.7	2280	6
0.371	386	30	0.536	384	25	18.1	950	7	58.8	3130	7
0.369	526	35	0.539	560	30	18.2	1250	8	58.6	4100	8
0.369	690	40	0.537	810	36	17.7	1550	9	58.6	5210	9
0.368	1000	48	0.535	1000	40	18.0	1950	10	58.5	6450	10
						17.9	2350	11	58.4	7830	11
						17.9	2800	12	58.4	9350	12

Table 3.1: Data points constituting several of the investigated paths with roughly constant k depicted in figure 3.11.

Let us first investigate how the numerator of the ratio (3.26) behaves. We have observed that if we look at the eigenvalues $\mu_i(k,N)$ along paths with constant k, then $1 - \mu_i(k,N)$ scales polynomially in N as can be seen in the log-log plot of figure 3.9, such that we have

$$\mu_i(k,N) = 1 - \frac{\alpha_i(k)}{N^{\beta_i(k)}} \ . \tag{3.28}$$

---

[1] Quasi-exact means in this context that we use as a *reference state* a MPS with virtual bond dimension D that is *much larger* than the one of the studied points on the path of constant k. If we restrict our scaling analysis to chains of length $N \ll \xi(D_{\text{ref}})$ it is sensible to assume that the MPS with bond dimension D_{ref} is much closer to the exact ground state than it is to the states we analyze. Thus the overlap that we obtain in this way is very close to the overlap with the exact ground state.

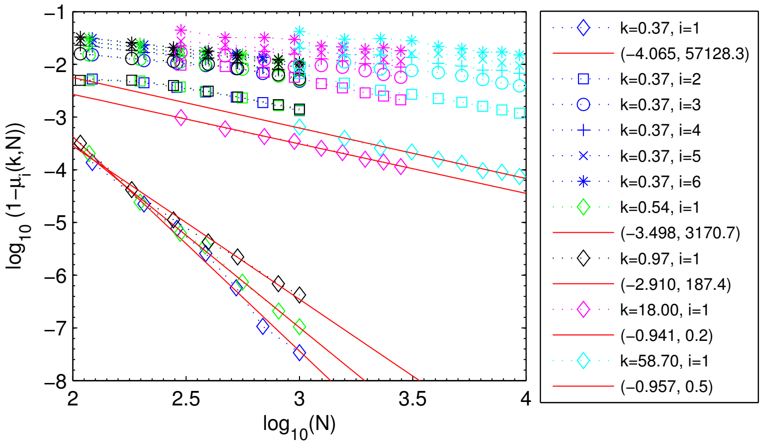

Figure 3.9: (Color online). Quantum Ising model: scaling of the eigenvalues of the overlap transfer matrix for five paths with roughly constant $k = N/D^{\kappa}$ in different regimes. The exact pairs (N, D) for the data points are given in table 3.1. In the legend we have only explained in detail what the different markers mean for the path with $k \approx 0.37$. The markers for the other paths follow the same pattern. The full red lines are linear fits through the data for each $\mu_1(k, N)$ respectively. The legend entries for these lines contain the values $(-\beta_1(k), \alpha_1(k))$.

$\kappa = 2.03425$						
	$k \approx 0.37 < k_c$		$k \approx 0.54 < k_c$		$k \approx 0.97 < k_c$	
i	β_i	α_i	β_i	α_i	β_i	α_i
1	4.06477	57128.2	3.49773	3170.6	2.90998	187.3
2	0.66454	0.14622	0.64177	0.12814	0.60463	0.10416
3	0.51554	0.19106	0.51270	0.19112	0.48326	0.16400
4	0.58048	0.37486	0.57835	0.37607	0.55326	0.33117
5	0.48173	0.26650	0.51001	0.31294	0.51875	0.32733
6	0.50660	0.35546	0.50828	0.36216	0.49502	0.33813
7	0.47451	0.31883	0.46129	0.30227	0.42975	0.26069
8	0.46673	0.35474	0.46928	0.36415	0.45436	0.33884
9	0.48042	0.42354	0.47013	0.41012	0.44586	0.37264
10	0.51091	0.55418	0.50601	0.54819	0.48431	0.49597

Table 3.2: Scaling of $\mu_i(k, N)$: parameters $\beta_i(k)$ and $\alpha_i(k)$ for the fitting of $1 - \mu_i(k, N) = \alpha_i(k)/N^{\beta_i(k)}$ for paths in the FSES regime.

Figure 3.9 shows a log-log plot of $1 - \mu_i(k, N)$ for all k and fixed $D_{ref} = 64$. The numerical values of $\alpha_i(k)$ and $\beta_i(k)$ for the 10 largest $\mu_i(k, N)$ are listed for the paths in the FSS regime in table 3.2. The equivalent data for paths in the FES regime can be found in table 3.3. We see that in the FSS regime for $i = 1$ we have $\beta_1(k) > 1$ while in all other cases we get $\beta_i(k) < 1$.

$\kappa = 2.03425$				
	$k \approx 18.0 > k_c$		$k \approx 58.7 > k_c$	
i	β_i	α_i	β_i	α_i
1	0.94079	0.20604	0.95736	0.46203
2	0.72904	0.74874	0.75036	1.14015
3	0.46762	0.25046	0.43380	0.23299
4	0.42154	0.26209	0.49195	0.62481
5	0.37208	0.23363	0.37851	0.33497
6	0.38713	0.38566	0.44232	0.87896
7	0.36770	0.38856	0.38792	0.65807
8	0.40633	0.58072	0.41378	0.94025
9	0.42088	0.80086	0.45836	1.67698
10	0.40215	0.80529	0.43306	1.58778

Table 3.3: Scaling of $\mu_i(k,N)$: parameters $\beta_i(k)$ and $\alpha_i(k)$ for the fitting of $1 - \mu_i(k,N) = \alpha_i(k)/N^{\beta_i(k)}$ for paths in the FES regime.

This means that for $N \to \infty$ the overlap (3.26) always converges to zero in the FES regime due to

$$\lim_{N\to\infty}(1 - \frac{\alpha}{N^\beta})^N = 0 \quad \forall\beta < 1, \alpha > 0 \tag{3.29}$$

and due to the fact that the denominator is always larger than zero (in fact it is always larger than one). In the FSS regime on the other hand, the $i = 1$ terms in the numerator of (3.26) survive in the thermodynamic limit due to

$$\lim_{N\to\infty}(1 - \frac{\alpha}{N^\beta})^N = 1 \quad \forall\beta > 1, \alpha > 0 \ . \tag{3.30}$$

However this is not enough in order to show that the overlap is strictly larger than zero in this regime. A diverging denominator in the limit $N \to \infty$ could spoil this line of reasoning, so we have to convince ourselves that both factors in the denominator of (3.26) remain finite in the thermodynamic limit.

Let us first treat the norm of the reference MPS since this turns out to be the easier one. Figure 3.10 shows a log-log plot of $1 - \lambda_i(k,N)$ for all k and fixed $D_{ref} = 64$. The numerical values for $i \leq 10$ are given in tables 3.4 and 3.5. For large chains with $N > 1000$ figure 3.10 clearly indicates polynomial scaling in N. Note that for small chains with $N < 1000$ the plot deviates from the nice linear behavior that we see for $N > 1000$. The reason for this are numerical errors in the computation of the ground state MPS. This effect can also be seen in figure 3.1: for $N < 1000$ the algorithm we use cannot minimze the energy beyond a relative precision of roughly $8 \cdot 10^{-11}$ even if we decrease N while keeping a constant $D = 64$. Apart

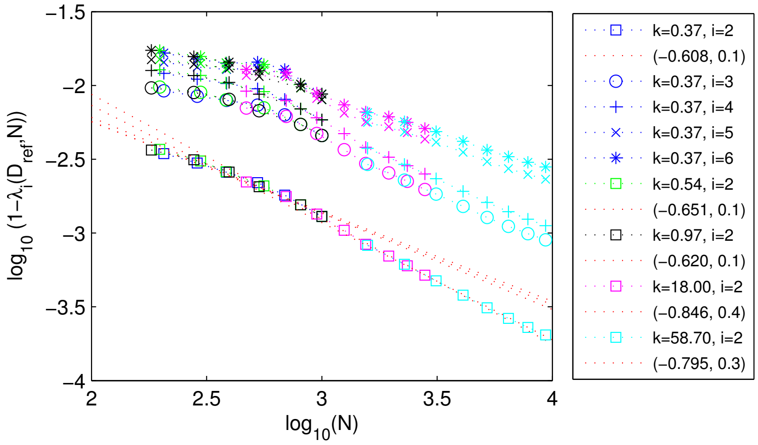

Figure 3.10: (Color online). Quantum Ising model: scaling of the eigenvalues of the MPS transfer matrix for $D_{\text{ref}} = 64$ and all N occuring in table 3.1. In the legend we have only explained in detail what the different markers mean for the N in the path with $k \approx 0.37$. The markers for the other paths follow the same pattern. The dotted red lines are linear fits through the data for each $\lambda_2(k, N)$ respectively. The legend entries for these lines contain the values $(-\beta_2(k), \alpha_2(k))$.

	$\kappa = 2.03425$					
	$k \approx 0.37 < k_c$		$k \approx 0.54 < k_c$		$k \approx 0.97 < k_c$	
i	β_i	α_i	β_i	α_i	β_i	α_i
2	0.60788	0.09304	0.65085	0.12184	0.62045	0.09914
3	0.41227	0.08847	0.46692	0.12433	0.44144	0.10401
4	0.43118	0.12846	0.48404	0.17837	0.45909	0.14987
5	0.30225	0.07647	0.36915	0.11385	0.35609	0.10226
6	0.34175	0.10783	0.40765	0.15889	0.39654	0.14462
7	0.40046	0.17074	0.44681	0.22606	0.43958	0.21126
8	0.41688	0.19910	0.46402	0.26460	0.45243	0.24089
9	0.33412	0.13003	0.36584	0.15862	0.36051	0.15116
10	0.28957	0.10620	0.34067	0.14540	0.33743	0.14045

Table 3.4: Scaling of $\lambda_i(D_{\text{ref}}, k, N)$: parameters $\beta_i(k)$ and $\alpha_i(k)$ for the fitting of $1 - \lambda_i(D_{\text{ref}}, k, N) = \alpha_i(k)/N^{\beta_i(k)}$ for paths in the FSS regime.

from that, the fitting in figure 3.10 yields all $\beta_i(k) < 1$ for $i \geq 2$ thus we can conclude that the norm $\langle \Psi(D_{ref}, N) | \Psi(D_{ref}, N) \rangle$ converges to one in the thermodynamic limit when we use the normalization prescription (3.24).

The norm of the states $|\Psi(D_{k,N}, N)\rangle$ along paths with constant k also turns out to converge to a finite value even though the argument is a bit trickier in this case. The scaling of the largest eigenvalues $\lambda_i(k, N)$ for each path is shown in figure 3.11. The numerical values for $i \leq 10$

	$\kappa = 2.03425$			
	$k \approx 18.0 > k_c$		$k \approx 58.7 > k_c$	
i	β_i	α_i	β_i	α_i
2	0.84555	0.42728	0.79472	0.28481
3	0.76096	0.82750	0.67333	0.41376
4	0.76823	1.11696	0.68922	0.59758
5	0.61161	0.54136	0.51839	0.26161
6	0.55554	0.41101	0.49502	0.25624
7	0.42416	0.19075	0.52876	0.42488
8	0.36840	0.13854	0.42626	0.21306
9	0.42172	0.22169	0.40383	0.19455
10	0.39138	0.19807	0.31502	0.10918

Table 3.5: Scaling of $\lambda_i(D_{\text{ref}}, k, N)$: parameters $\beta_i(k)$ and $\alpha_i(k)$ for the fitting of $1 - \lambda_i(D_{\text{ref}}, k, N) = \alpha_i(k)/N^{\beta_i(k)}$ for paths in the FES regime.

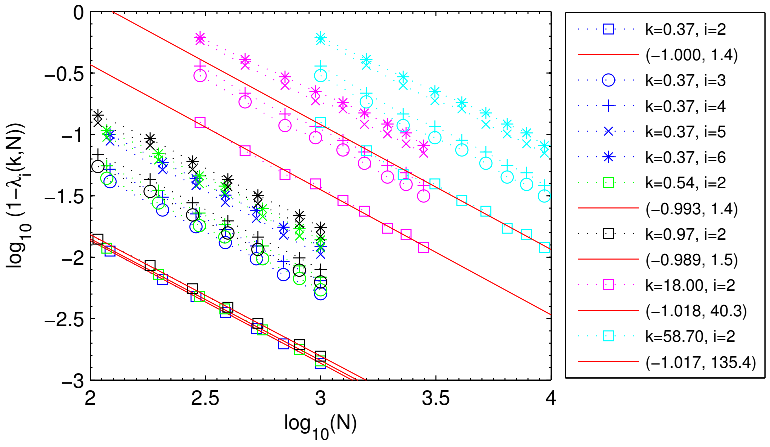

Figure 3.11: (Color online). Quantum Ising model: scaling of the eigenvalues of the MPS transfer matrix for five paths with roughly constant $k = N/D^{\kappa}$ in different regimes. The exact pairs (N, D) for the data points are given in table 3.1. In the legend we have only explained in detail what the different markers mean for the path with $k \approx 0.37$. The markers for the other paths follow the same pattern. The full red lines are linear fits through the data for each $\lambda_2(k, N)$ respectively. The legend entries for these lines contain the values $(-\beta_2(k), \alpha_2(k))$.

are given in tables 3.6 and 3.7. We see that most of the $\beta_i(k)$ are very close to one for small i in contrast to the values obtained for $\lambda_i(D_{ref}, N)$ which are all well below one. In fact some of the $\beta_i(k)$ are even bigger than one suggesting that $\lim_{N\to\infty} \lambda_i^N = 1$ in these cases. In section 3.5.1 of this appendix we give evidence for the fact that even if $\beta_i(k) > 1$ in some cases, the number of these values remains finite for any k. Furthermore we argue that in these cases

$\kappa = 2.03425$						
	$k \approx 0.37 < k_c$		$k \approx 0.54 < k_c$		$k \approx 0.97 < k_c$	
i	β_i	α_i	β_i	α_i	β_i	α_i
2	0.99979	1.36876	0.99261	1.37029	0.98869	1.45137
3	0.99838	5.00085	0.98501	4.96160	0.97751	5.42433
4	0.99397	6.19275	0.98129	6.13836	0.97395	6.67115
5	1.00992	11.36417	0.97979	10.64645	0.96439	11.79694
6	0.99749	12.14274	0.96755	11.35451	0.95325	12.79517
7	0.99290	15.20975	0.96478	14.29878	0.94933	15.72285
8	0.99385	16.84721	0.94982	14.52223	0.93257	16.11736
9	1.03853	23.13857	0.98133	19.63216	0.94593	20.59742
10	1.03720	25.64027	0.95765	19.24667	0.92658	21.15268

Table 3.6: Scaling of $\lambda_i(k,N)$: parameters $\beta_i(k)$ and $\alpha_i(k)$ for the fitting of $1-\lambda_i(k,N) = \alpha_i(k)/N^{\beta_i(k)}$ for paths in the FSS regime.

$\kappa = 2.03425$				
	$k \approx 18.0 > k_c$		$k \approx 58.7 > k_c$	
i	β_i	α_i	β_i	α_i
2	1.01831	40.25148	1.01731	135.41657
3	0.98774	81.55159	0.98683	264.69533
4	0.97128	88.78991	0.97053	282.91558
5	0.92704	111.61975	0.92647	337.75755
6	0.88126	94.42375	0.88080	270.69784
7	0.88252	104.24989	0.88232	299.97710
8	0.77072	64.57797	0.77072	162.76623
9	0.79065	82.78179	0.78996	212.48337
10	0.76184	72.53475	0.76185	180.90762

Table 3.7: Scaling of $\lambda_i(k,N)$: parameters $\beta_i(k)$ and $\alpha_i(k)$ for the fitting of $1-\lambda_i(k,N) = \alpha_i(k)/N^{\beta_i(k)}$ for paths in the FES regime.

it is reasonable to assume that we actually have $\beta_i(k) = 1$ which yields in the thermodynamic limit

$$\lim_{N\to\infty} \lambda_i^N(k,N) = \lim_{N\to\infty}(1-\frac{\alpha_i}{N})^N = \exp(-\alpha_i) \ . \tag{3.31}$$

Summing up all relevant contributions then yields for the norm of states in the different regimes

$$\begin{aligned}&\lim_{N\to\infty} \langle\Psi(k,N)|\Psi(k,N)\rangle_{k<k_c} \approx 2.2\\&\lim_{N\to\infty} \langle\Psi(k,N)|\Psi(k,N)\rangle_{k>k_c} \leq 2.0\ .\end{aligned} \tag{3.32}$$

This allows us to approximate the overlap (with a *quasi-exact* state) towards which MPS simulations in different regimes converge to (on the paths we considered) as

$$\begin{aligned}&\lim_{N\to\infty} \langle\psi(k,N)|\psi(D_{\text{ref}},N)\rangle_{k<k_c} \approx 0.45\\&\lim_{N\to\infty} \langle\psi(k,N)|\psi(D_{\text{ref}},N)\rangle_{k>k_c} = 0\ .\end{aligned} \tag{3.33}$$

Thus we can conclude that the thermodynamic limit of the overlap in the FSS regime is always greater than zero proving that there is indeed an discrete transition from the FSS regime to the FES regime where the overlap becomes zero.

3.5.1 Scaling of $\lambda_i(k,N)$

The first ten parameters α_i and β_i for the MPS transfer matrix eigenvalues $\lambda_i(k,N)$ on paths in the FSS regime are given in table 3.6, the ones for paths in the FES regime in table 3.7. In the FES regime we have $\beta_2 > 1$ which then yields a contribution of $\lim_{N\to\infty}\lambda_2^N(k) = 1$ to the norm. For $i > 2$ we clearly see how the β_i rapidly decay below one, thereby making sure that the corresponding contributions to the norm become zero in the thermodynamic limit. This means that if we approach the thermodynamic limit on paths in the FES regime and always normalize the MPS according to (3.24), i.e. $\lambda_1 = 1$, the norm of these states does not get bigger than two. In fact it is very likely that the true contribution of λ_2 is de facto zero [1]: for N as big as 10^9, using the values for α_2 and β_2 given in table 3.7, we get $\lambda_2^N(k = 18.0) \approx 2\cdot 10^{-12}$ and $\lambda_2^N(k = 58.7) \approx 4\cdot 10^{-42}$.

In the FSS regime on the other hand the β_i seem to oscillate randomly around one so we must look at the behavior of larger i in order to see if and when they decay below one, which is what we ultimately need in order to show that the norm of these states remains finite in the thermodynamic limit when the normalization prescription (3.24) is employed.

Figure 3.12 shows a log-plot of the first 200 β_i in the FSS regime and of the first 120 in the FES regime. All curves are approximately straight lines in this plot which means that the β_i decay exponentially with i. Remember that on the paths we chose to investigate in the FES regime, the MPS with the largest virtual bond dimension have $D = 12$, thus we cannot fit any parameters β_i for $i > 121$ since we have only one data point available there. For $100 < i \leq 121$ we have only two data points, namely the ones for $D = 11$ and $D = 12$ (see

---

[1] Actually it might also be that β_2 is in fact equal to one which yields in the thermodynamic limit $\lim_{N\to\infty}\lambda_2^N = \exp(-\alpha_2)$. Unfortunately, as opposed to the similar case in the FSS regime, we cannot conclude here that this must be the case.

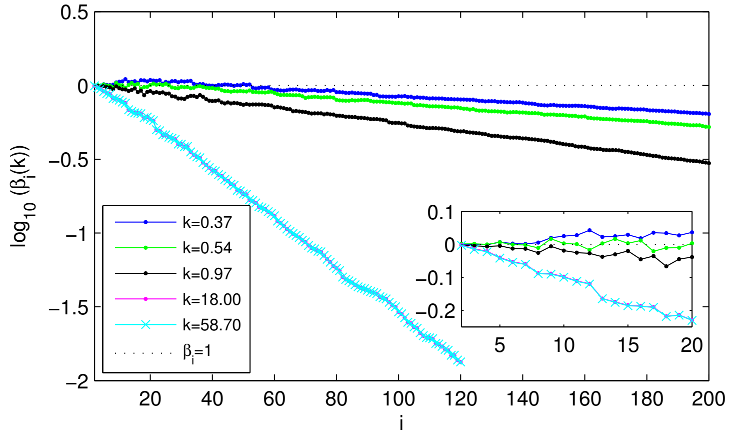

Figure 3.12: (Color online). Quantum Ising model: log-plot of the first values of $\beta_i(k)$ for $i \leq 200$. A zoomed view on the first 20 values is shown in the inset.

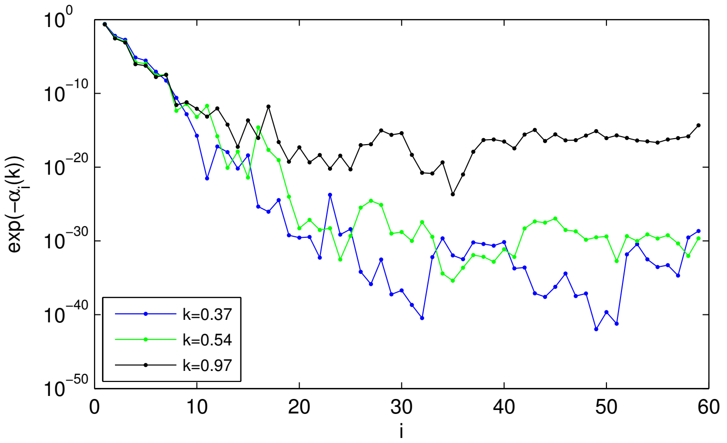

Figure 3.13: (Color online). Quantum Ising model: contribution of the eigenvalues with $\beta_i(k) \approx 1$ to the norm of the states in the thermodynamic limit, i.e. $\lim_{N\to\infty} \lambda_i^N(k) \approx \exp(-\alpha_i(k))$. Note how all contributions fall off exponentially below machine precision at $i \approx 14$.

table 3.1 in the main text) which is usually not the best premise for an accurate fit. Nonetheless the β_i fitted in this range obey the same exponential decay observed for smaller i, where more data points are available. The inset in figure 3.12 shows a zoom into the region with $i \leq 20$. While for $i \leq 8$ all β_i in the FSS regime are very close to one, we observe that for larger i, the $k = 0.37$ line is visibly above the $\beta_i = 1$ line. This would suggest that in the thermodynamic limit the eigenvalues $\lambda_{i>8}$ would each yield a contribution equal to one to the norm while the contribution from the λ_i with $i \in \{2, 3, 4, 6, 7, 8\}$ would vanish, since in these cases $\beta_i < 1$. This makes however no sense since the λ_i are decreasingly ordered, i.e. $\lambda_i > \lambda_j$ if $i < j$. This leads us to the conclusion that the oscillations around one that we observe for $i > 8$ are numerical relics and that the true value of the β_i is either one or something smaller than one.

This conclusion is based on the fact that in MPS simulations the transfer matrix eigenvalues that converge first are the dominant eigenvalues (i.e. the ones with the largest absolute value) so we can assume that the values obtained for $\beta_{i\leq 8}$ are much more accurate than the other ones.

Thus the worst case for our purpose is when all β_i that are not clearly smaller than one, are actually equal to one. Let us investigate what we would get for the norm in this case. If $\beta_i = 1$, the contribution of these eigenvalues to the norm in the thermodynamic limit solely depends on α_i due to

$$\lim_{N\to\infty} \lambda_i^N(k,N) = 1 \lim_{N\to\infty}(1-\frac{\alpha_i}{N})^N = \exp(-\alpha_i) \ . \tag{3.34}$$

Figure 3.13 shows the behavior of $\exp(-\alpha_i)$ for the paths in the FSS regime and $i < 60$, which according to figure 3.12 is the problematic i-range. We see how all contributions rapidly decay below machine precision. Note that the black line (i.e. the path with $k = 0.97$) is for $i \geq 17$ several orders of magnitude above the $k = 0.37$ and $k = 0.54$ lines, which is due to the fact that the corresponding β_i are so much smaller than one in this region, that the assumption $\beta_i \approx 1$ simply does not hold, and the actual contribution to the norm converges to zero. Note furthermore how for small i all three lines are almost on top of each other meaning that the values to which the norm converges in the thermodynamic limit for MPS on different paths in the FSS regime will be very similar. In fact we get

$$\begin{aligned}
\lim_{N\to\infty} \langle\Psi(k,N)|\Psi(k,N)\rangle_{k=0.37} &= 2.261646939734277 \\
\lim_{N\to\infty} \langle\Psi(k,N)|\Psi(k,N)\rangle_{k=0.54} &= 2.236037631274709 \\
\lim_{N\to\infty} \langle\Psi(k,N)|\Psi(k,N)\rangle_{k=0.97} &= 2.225635928039641
\end{aligned} \tag{3.35}$$

which completes our argument that the norm of the MPS remains finite on any path in the FSS regime.

3.6 Appendix C: Comparison to other PBC MPS algorithms

In this appendix we will show that the algorithm [28] that we used to obtain all results in this work is performing better than other recently presented approaches.

For the sake of completeness let us first recapitulate the result of the comparison to the algorithm presented in [15]. We have already shown in [28] that our PBC algorithm yields a better precision. Apart from several other differences in these two approaches, the crucial point is that we allow for a variable dimension n of the dominant subspace used to approximate big powers of the transfer matrix. Even though this contributes a factor n^2 to the overall computational cost $O(n^2D^3)$, we have shown in [28] that there is no way to get rid of the factor n if one wants to reproduce the correlation function throughout the entire PBC chain faithfully. If the same n-scanning strategy would be employed in [15], probably the same precision level could be achieved, however the computational cost in that algorithm would then scale like $O(NnD^3)$. There is an additional factor N in that scaling because that approach is not translationally invariant. The power of n is reduced by one due to the fact that the energy is minimized directly and not using the gradient.

Next we would like to compare our PBC algorithm to the one presented in [17]. In that work the authors simulate the critical Quantum Ising Model by using Time Evolving Block Decimation [37] to locally update a translationally invariant MPS which is then plugged into a chain with PBC geometry in order to compute the energy. The weakness of that algorithm is that the local update of the MPS tensors does not take into account the boundary conditions: the fixed point MPS is exactly the same like the one obtained when trying to approximate the ground state of an infinite chain. In spite of this, the ground state energy can be approximated quite well since the scaling of the computational cost is only $O(nD^3)$ which allows the use of very large D. Unfortunately there are no explicit plots of the precision of the ground state energy in [17] as a function of D. From the abstract and footnote 4 of that work we deduce that the simulation that yields the error $\approx 2.0 \times 10^{-10}$ for the critical Quantum Ising PBC chain with $N = 4800$ was done with a MPS with bond dimension $D = 200$. We reach the same precision with D as small as 64 as can be seen in figure 3.1. Due to the higher computational cost of our algorithm $D = 200$ is out of reach for us. Nonetheless we have computed an approximation of the ground state of the infinite chain with a translationally invariant MPS with $D = 200$ (details of this are given below) and then plugged this MPS into a PBC chain geometry with $N = 4800$. The relative precision that we obtained using this strategy was $\Delta_{rel}E_0(N = 4800, D = 200) \approx 1.39 \cdot 10^{-10}$ which is in perfect agreement with the claim made in [17]. However, if we take into account the fact that a PBC simulation with $N = 4800$ and $D = 200$ is well in the FSS regime due to $N \ll \xi(D = 200) \approx 1.910^5$, it becomes immediately clear that with $D = 200$ one can in principle reach a much better precision than $\approx 10^{-10}$. In other words, the results obtained in [17] correspond to the cyan (light) lines in the left plot of figure 3.7. While this is perfectly fine for simulations in the FES regime, if one is in the FSS regime, there is room for one or more orders of magnitude of improvement of the relative precision.

There is another point worth mentioning regarding our PBC algorithm [28]. In order to check the claims made in [17], we needed to first approximate the ground state of the infinite chain with an MPS with $D = 200$. For this we used a new method called Time-Dependent Variational Principle [67]. We did this because TDVP converges much faster than Imaginary Time Evolution based on Matrix Product Operators [36] or iTEBD [30]. The relative precision we achieved with TDVP was $\Delta_{rel}E_0(N = \infty, D = 200) \approx 7.7 \cdot 10^{-11}$. We knew that this cannot be the best precision that can be reached with $D = 200$ since in [36] we get roughly the same precision with D as small as 128. Thus we ran the PBC algorithm for a huge chain with $N = 10^6$ sites on top of the MPS obtained by TDVP. Choosing as the parameters of that algorithm $m = 1000$ and $n = 100$ we managed to reduce the relative precision to $\approx 1.3 \cdot 10^{-11}$

which is in perfect agreement with the polynomial scaling shown in figure 1 of [36]. The lesson learned from this approach is that TDVP results can be improved using our PBC algorithm well in the FES regime. We emphasize that running the PBC algorithm with small n did not yield any improvement to the TDVP result. Only with n as large as 100 we obtained the improved precision. This is quite strange as when we compute the energy density for the infinite chain, only one dominant eigenvector is used, i.e. $n = 1$. So it seems that even if additional dominant eigenvectors do not enter the final computation of the ground state energy, they do have an effect during the local optimization procedure of the translationally invariant MPS.

Chapter 4

Determining dispersion relations of PBC chains

Synopsis:

We study a matrix product state (MPS) algorithm to approximate excited states of translationally invariant quantum spin systems with periodic boundary conditions. By means of a momentum eigenstate ansatz generalizing the one of Östlund and Rommer [see S. Östlund and S. Rommer, Phys. Rev. Lett. 75, 3537 (1995); S. Rommer and S. Östlund, Phys. Rev. B 55, 2164 (1997)], we separate the Hilbert space of the system into subspaces with different momentum. This gives rise to a direct sum of effective Hamiltonians, each one corresponding to a different momentum, and we determine their spectrum by solving a generalized eigenvalue equation. Surprisingly, many branches of the dispersion relation are approximated to a very good precision. We benchmark the accuracy of the algorithm by comparison with the exact solutions and previous numerical results for the quantum Ising, the antiferromagnetic Heisenberg spin-$1/2$ and the bilinear-biquadratic spin-1 model.

Based on:
B. Pirvu, J.Haegeman and F. Verstraete,
Phys. Rev. B **85**, 035130 (2012)

Changes compared to published version: minor corrections.

4.1 Introduction

Recently we have presented an algorithm [28] for the approximation of the ground state of translationally invariant (TI) spin chains with periodic boundary conditions (PBC) by means of TI matrix product states (MPS). In this work we will use the ground states obtained in [28] as the basis of an ansatz for excited states with definite momentum. We will consider only spin chain Hamiltonians that are translationally invariant thereby fulfilling $[H, T] = 0$ where T is the translation operator that shifts the lattice by one site. Furthermore, as we will deal with finite chains in the following, it means that there is no well defined momentum operator for our systems. Nevertheless we can classify translationally invariant states by their quasi-momentum which is defined in terms of the their eigenvalue with respect to T. This definition is sensible since in the thermodynamic limit, if we keep the chain length fixed, the lattice spacing becomes infinitesimally small and the quasi-momentum becomes identical to the momentum, which is then well defined. For convenience, we will use the term *momentum* when we actually refer to the quasi-momentum. This should not cause any confusion since we will only deal with quasi-momenta throughout this work.

Since H and T commute, they can be diagonalized simultaneously. This suggests that any variational ansatz based on eigenstates of the translation operator will be well suited to define families of states within which minimization with respect to some variational parameters will yield *momentum* eigenstates with minimal energy. Formulating this observation in terms of an MPS-based ansatz has led in the past to some very interesting results about excitation spectra. The first approach in this direction has been made in [3, 35] where the main result is the celebrated insight that the fixed point of the Density Matrix Renormalization Group (DMRG) [2] can be written as an MPS. In addition to this, based on the MPS that is obtained for the ground state of the infinite Heisenberg spin-1 chain, the authors suggest a variational ansatz for excitations with definite *momentum*. Since the translationally invariant MPS they start with is an approximation of the ground state in the thermodynamic limit, their ansatz for excitations is only well suited in the limit $N \to \infty$. For finite chains, the idea of using *momentum* eigenstates for the diagonalization of TI Hamiltonians has been used in [68] in order to obtain a few of the lowest branches of excitations for the bilinear-biquadratic (BB) spin-1 chain. The resulting state is a TI superposition of a special class of tensor network states, which can be viewed as an extension of MPS with PBC [11] to states that can accommodate multipartite entanglement. Even though the multipartite entanglement is a nice feature which yields a better variational ansatz in the cases when the approximated states have that special entanglement structure (in [68] one has in addition to the usual maximally entangled virtual bonds between nearest neighbors a virtual GHZ state connecting all sites) we will not adopt it in our present ansatz. Furthermore we would like to point out that the individual MPS tensors produced by the minimization procedure in [68] are not TI, only their superposition is.

Recent results [28] on the approximation of ground states of TI PBC Hamiltonians opened up the possibility of unifying the ideas from [3] and [68] in order to obtain an algorithm for excitations with definite *momentum* in which only one local tensor has to be determined, thereby avoiding the usual sweeping procedure and the associated factor N in the computational cost. One of the main features of TI MPS is the fact that the tensor network that has to be contracted for the computation of expectation values contains big powers of a so-called transfer matrix [6]. For non-critical systems the eigenvalues of this transfer matrix usually decay rapidly enough s.t. big powers thereof can be accurately approximated by considering only a few dominant eigenvectors. In these cases the computational cost for the evaluation of expectation values for systems with PBC can be reduced significantly from $O(D^5)$ to $O(D^3)$, where D denotes the virtual bond dimension of the MPS. For critical systems however the eigenvalues of the transfer matrix decay much slower and the algorithm that must be employed in order to obtain the optimal approximation within the class of MPS with fixed D has a scaling that depends in a not yet fully understood way [28] on D, N and on the universality class of the simulated model.

The ansatz we present in this work is based on TI-MPS and thereby all computed quantities will contain big powers of the transfer matrix. We would like to emphasize that the computational cost can be reduced by a factor of D^2 only in the case of non-critical systems. For critical systems the full contraction of tensor networks (i.e. without using any approximations of the transfer matrix) will turn out to have a more favorable overall scaling of the computational cost. Details on why this is the case and on the scaling of the computational cost can be found in the next section.

4.2 Overview

Due to $T^N = \mathbb{1}$, the translation operator T that shifts a state on a PBC lattice with N sites by 1 site is the generator of the cyclic group of order N. Hence its eigenvalues τ_k must be roots of the unity i.e. $\tau_k = e^{-ik\frac{2\pi}{N}}$ with integer $k \in [0, N-1]$. An ansatz for eigenstates of T with eigenvalue $e^{-ik\frac{2\pi}{N}}$ is obviously given by

$$|\psi_k(\mathbf{B})\rangle = \sum_{n=0}^{N-1} \frac{1}{\sqrt{N}} e^{i\frac{2\pi kn}{N}} T^n \, |\phi_{\mathbf{A}}(\mathbf{B})\rangle \quad . \tag{4.1}$$

Henceforth we will refer to states of the form (4.1) as Bloch states. Note that we have used the convention that T is the operator that realizes a translation by one site to the right s.t. $T\,|\phi(i_1, i_2, \ldots, i_N)\rangle = |\phi(i_N, i_1, i_2, \ldots, i_{N-1})\rangle$. The state $|\phi_{\mathbf{A}}(\mathbf{B})\rangle$ can in principle be any arbitrary state, but in order to exploit the advantages of TI MPS, we choose

$$|\phi_{\mathbf{A}}(\mathbf{B})\rangle = \sum_{i_1,\ldots i_N=1}^{d} \mathrm{Tr}\big(B_{i_1} A_{i_2} \ldots A_{i_N}\big) \, |i_1 i_2 \ldots i_N\rangle \tag{4.2}$$

with identical matrices A_i on all sites except the first one. We will choose the A_i to be the matrices corresponding to the best TI MPS ground state approximation for a given model. We emphasize that the A_i remain fixed throughout the entire simulation. This is the reason why we have omitted them from our labeling convention for the Bloch states $|\psi_k(\mathbf{B})\rangle$. We have used bold letters in order to denote objects that are obtained if one rearranges the components of three indexed MPS tensors into vectors, i.e. $\mathbf{A} := \mathrm{vec}(A_{i\ \beta}^{\ \alpha})$. After fixing the *momentum* k, the Bloch states $|\psi_k(\mathbf{B})\rangle$ will depend only on the tensors $\mathbf{B}$ which will define the variational manifold.

Our ansatz for Bloch eigenstates differs slightly from the ones presented in Refs. [3, 68, 69] although it is conceptually very similar. An important feature of all these approaches is the reduction of the dimension of the problem by a factor N. This is reached by effectively projecting the original problem into the subspace with fixed *momentum* k and minimizing the energy within the variational manifold spanned by the free parameters in the ansatz. In our case these free parameters are the components $\mathbf{B}$ of an MPS tensor. As it is always the case with MPS algorithms, one must eliminate the ambiguities arising from the MPS representation by fixing the gauge. Here this is done by starting with certain tensors $\mathbf{A}$ in (4.2) and not changing them throughout the entire minimization procedure. This automatically fixes the gauge of the tensors $\mathbf{B}$ as they are surrounded on both sides by $\mathbf{A}$.

4.3 The algorithm

Ansatz (4.1) defines a class of variational states for the lowest energy states with fixed *momentum*. The energy is a quadratic expression in the tensor $\mathbf{B}$ and thereby, as it is usually the case in MPS based algorithms, minimizing

$$E_0(k) = \min_{\mathbf{B}\in\mathbb{C}^{dD^2}} \frac{\langle\psi_k(\mathbf{B})|\, H\, |\psi_k(\mathbf{B})\rangle}{\langle\psi_k(\mathbf{B})|\psi_k(\mathbf{B})\rangle} \quad , \tag{4.3}$$

is equivalent to solving a generalized eigenvalue equation

$$H_{eff}(k)\mathbf{B}_i(k) = E_i(k) N_{eff}(k)\mathbf{B}_i(k) \tag{4.4}$$

where $H_{eff}(k)$ is defined by

$$\mathbf{B}^\dagger H_{eff}(k)\mathbf{B} := \langle\psi_k(\mathbf{B})|\, H\, |\psi_k(\mathbf{B})\rangle \tag{4.5}$$

and $N_{eff}(k)$ by

$$\mathbf{B}^\dagger N_{eff}(k)\mathbf{B} := \langle\psi_k(\mathbf{B})|\psi_k(\mathbf{B})\rangle \quad . \tag{4.6}$$

The eigenvector corresponding to the smallest eigenvalue $E_0(k)$ yields then the tensor $\mathbf{B}_0(k)$ that when plugged into our ansatz (4.1) gives the *momentum-k* state with minimal energy. Note that the variational principle guarantees that only the Bloch state (4.1) with lowest energy is the best approximation to the exact eigenstate with that *momentum* within the subspace spanned by our ansatz states. However if the lowest energy state is approximated accurately, due to the fact that the other $\mathbf{B}_i(k)$ are orthogonal to $\mathbf{B}_0(k)$, the next solution $\mathbf{B}_1(k)$ has a good chance to be close to the next higher energy state with that momentum. In fact it will turn out that quite a few of the higher energy solutions of (4.4) are good approximations to low energy states with fixed *momentum*. Their precision is most of the time surprisingly good given the fact that the variational principle does not hold for these states. The quality of these solutions depends strongly on the bond dimension D, the chain length N and the model under consideration.

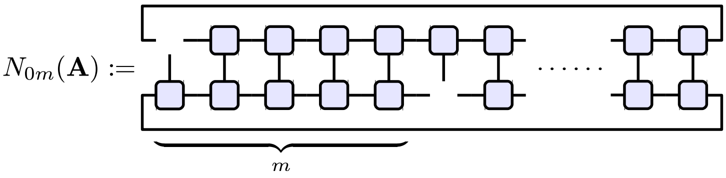

Figure 4.1: (Color online). Definition of $N_{0m}(\mathbf{A})$ as the norm of a TI MPS determined by the tensor $\mathbf{A}$.

The bottleneck of our method is the computation of the effective matrices $H_{eff}(k)$ and $N_{eff}(k)$. Let us first consider $N_{eff}(k)$ since it is the slightly simpler one. It reads

$$\begin{aligned}
&\mathbf{B}^\dagger N_{eff}(k)\mathbf{B} = \\
&= \frac{1}{N}\sum_{m,n=0}^{N-1} e^{i\frac{2\pi k(n-m)}{N}} \langle\phi_{\mathbf{A}}(\mathbf{B})|\, T^{(n-m)}\, |\phi_{\mathbf{A}}(\mathbf{B})\rangle \\
&= \sum_{\bar{n}=0}^{N-1} e^{-i\frac{2\pi k\bar{n}}{N}} \langle\phi_{\mathbf{A}}(\mathbf{B})|\, T^{-\bar{n}}\, |\phi_{\mathbf{A}}(\mathbf{B})\rangle \\
&= \mathbf{B}^\dagger \left[\sum_{m=0}^{N-1} e^{-i\frac{2\pi k m}{N}} \cdot N_{0m}(\mathbf{A})\right]\mathbf{B}
\end{aligned} \tag{4.7}$$

where $N_{0m}(\mathbf{A})$ is a tensor network resembling the norm of a TI MPS with empty slots 0 and m [see Fig. 4.1]. To get from the second to the third line we have used the fact that due to the PBC only the relative distance between n and m plays a role. In the last line we have merely renamed the summation index and introduced the quantity $N_{0m}(\mathbf{A})$. Thus in order to obtain $N_{eff}(k)$ we have to compute the contraction of the N tensor networks $N_{0m}(\mathbf{A})$ and then take the sum of these terms after weighting each one of them with the corresponding phase factor. The computational cost for the contraction of each tensor network is $O(D^6)$ s.t. the overall cost for computing $N_{eff}(k)$ is $O(ND^6)$.

$H_{eff}(k)$ is constructed very much in the same spirit. First, due to the translational invariance of the Hamiltonian we can write

$H_{0nm}(\mathbf{A}) :=$

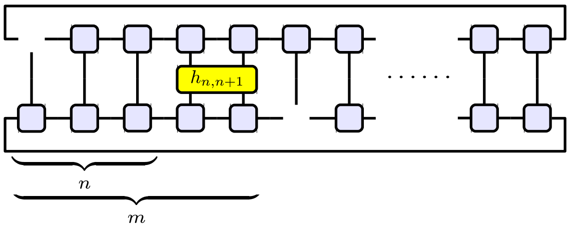

Figure 4.2: (Color online). Definition of $H_{0nm}(\mathbf{A})$ as the expectation value of a two-site operator with respect to a TI MPS determined by the tensor $\mathbf{A}$.

$$H = \sum_{l=0}^{N-1} h_{l,l+1} = \sum_{l=0}^{N-1} T^l h_{01} T^{-l} \tag{4.8}$$

where h_{01} is the term acting between the first two sites of the chain. Note that in (4.8) we have restricted ourselves to nearest neighbor Hamiltonians since this is the type of models we will treat numerically in this work. Generalizing the ideas developed here to any local Hamiltonian is straightforward. With (4.8), $H_{eff}(k)$ reads

$$\begin{aligned}
&\mathbf{B}^\dagger H_{eff}(k)\mathbf{B} = \\
&= \frac{1}{N} \sum_{l,m,n=0}^{N-1} e^{i\frac{2\pi k(n-m)}{N}} \left\langle \phi_{\mathbf{A}}(\mathbf{B})\right| T^{l-m} h_{01} T^{n-l} \left|\phi_{\mathbf{A}}(\mathbf{B})\right\rangle \\
&= \frac{1}{N} \sum_{l=0}^{N-1} \sum_{\bar{m},\bar{n}=-l}^{N-1-l} e^{i\frac{2\pi k(\bar{n}-\bar{m})}{N}} \left\langle \phi_{\mathbf{A}}(\mathbf{B})\right| T^{-\bar{m}} h_{01} T^{\bar{n}} \left|\phi_{\mathbf{A}}(\mathbf{B})\right\rangle \quad .
\end{aligned} \tag{4.9}$$

Again, due to the fact that the $\bar{m}$ and $\bar{n}$ sums run over all N sites of a PBC chain, it is irrelevant where they begin s.t. the l sum merely yields a factor N. We rename the summation indices for convenience and obtain

$$\begin{aligned}
&\mathbf{B}^\dagger H_{eff}(k)\mathbf{B} = \\
&= \sum_{m,n=0}^{N-1} e^{i\frac{2\pi k(n-m)}{N}} \left\langle \phi_{\mathbf{A}}(\mathbf{B})\right| T^{n-m} T^{-n} h_{01} T^{n} \left|\phi_{\mathbf{A}}(\mathbf{B})\right\rangle \\
&= \sum_{n=0}^{N-1} \sum_{\bar{m}=n}^{n-N+1} e^{-i\frac{2\pi k\bar{m}}{N}} \left\langle \phi_{\mathbf{A}}(\mathbf{B})\right| T^{-\bar{m}} h_{n,n+1} \left|\phi_{\mathbf{A}}(\mathbf{B})\right\rangle \\
&= \mathbf{B}^\dagger \left[\sum_{m,n=0}^{N-1} e^{-i\frac{2\pi k m}{N}} \cdot H_{0nm}(\mathbf{A}) \right] \mathbf{B}
\end{aligned} \tag{4.10}$$

where $H_{0nm}(\mathbf{A})$ is a tensor network resembling the expectation value of an operator acting on the sites n and $n+1$ with respect to a TI MPS where the slots 0 and m have been left open [see Fig. 4.2]. The computational cost for the contraction of each tensor network is again $O(D^6)$ but now we have a total of N^2 summands s.t. the overall cost for computing $H_{eff}(k)$ is $O(N^2D^6)$. Note that to obtain $H_{eff}(k)$ is computationally the most expensive part of our algorithm so we can say that the overall computational cost scales like $O(N^2D^6)$.

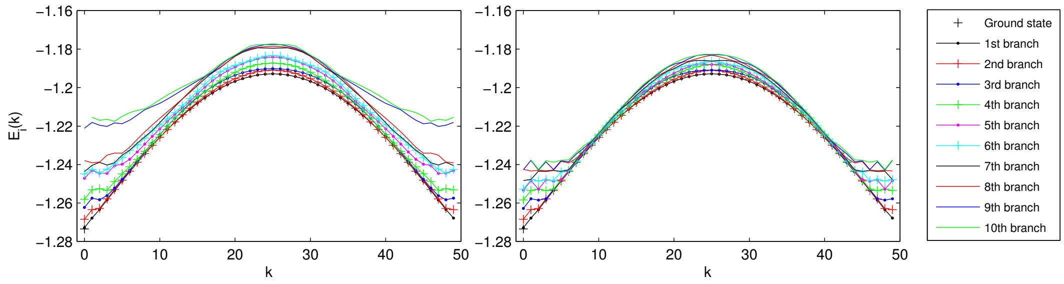

Figure 4.3: (Color online). Lowest ten branches of the excitation spectrum for a critical Ising chain with $N = 50$. Left: $D = 8$. Right: $D = 32$.

4.3.1 Overall scaling of the computational cost

At first sight the cost seems horrible for a 1D-algorithm. Let us however have a closer look at what we get for this price. First of all note that if we compute the sets of matrices $\{N_{0m}(\mathbf{A})\}$ and $\{H_{0nm}(\mathbf{A})\}$ for $n, m \in [0, N-1]$ and store these, we can obtain the $H_{eff}(k)$ and $N_{eff}(k)$ for all k trivially by just building the appropriately weighted sums. For each of these k we then have to solve the generalized eigenvalue equation (4.4). Since $H_{eff}(k)$ and $N_{eff}(k)$ are small $dD^2 \times dD^2$ matrices solving (4.4) does not represent any difficulty and can be done using any standard library eigenvalue solver. Each eigenvalue problem leads to D^2 orthonormal vectors $\mathbf{B}_i(k)$ which plugged into the ansatz (4.1) yield D^2 states. The reason why we do not get all dD^2 eigenvectors as valid solutions has something to do with the singularity of $N_{eff}(k)$ and is explained in more detail below. Thus computing the sets $\{N_{0m}(\mathbf{A})\}$ and $\{H_{0nm}(\mathbf{A})\}$ only once supplies us immediately with ND^2 states! By comparing our numerical results to exactly solvable models we will show that the low energy states obtained in this way are very accurate. This means that in terms of computational time per state our algorithm performs quite well.

The computational bottleneck at the moment is that we have to store N^2 $dD^2 \times dD^2$ matrices in the memory. With the present implementation, for a chain with $N = 100$ sites, we can go up to $D = 32$. For larger N simulations we have to settle for smaller D. It is however straightforward how this boundary can be pushed considerably towards larger D. First, instead of keeping all matrices in the memory, one can write them to the hard disk after computing each of them. Second, since the $\{N_{0m}(\mathbf{A})\}$ and $\{H_{0nm}(\mathbf{A})\}$ are independent, one can parallelize their computation.

Thus the conceptual bottleneck becomes the contraction of the tensor networks $\{N_{0m}(\mathbf{A})\}$

and $\{H_{0nm}(\mathbf{A})\}$. For non-critical systems big powers of the transfer matrix can be well approximated by a few of its dominant eigenvectors [28] and the contraction of *most* of the $\{N_{0m}(\mathbf{A})\}$ can be done with the computational cost $O(n^2D^3)$ while that of *most* of the $\{H_{0nm}(\mathbf{A})\}$ with the cost $O(n^3D^3)$. Here n represents the dimension of the subspace within which we approximate the powers of the transfer matrix [28]. This cannot be done however for critical systems where in principle n may grow as big as D^2 thereby yielding a much worse scaling than the naive $O(D^6)$. Note that since $\{N_{0m}(\mathbf{A})\}$ and $\{H_{0nm}(\mathbf{A})\}$ are *open* tensor networks the $O(D^5)$ contraction scheme [11] that works for expectation values (i.e. *closed* tensor networks) cannot be applied here. Additionally, even if we restrict ourselves to non-critical systems, not *all* of the $\{N_{0m}(\mathbf{A})\}$ and $\{H_{0nm}(\mathbf{A})\}$ can be computed with the cost that scales like D^3: if the distance between the *open* slots is not big enough, we cannot use the approximation for big powers of the transfer matrix between the slots, and we are back to exact contraction for this portion of the chain which in the case of $\{N_{0m}(\mathbf{A})\}$ leads to the overall scaling $O(nD^5)$ and in the case of $\{H_{0nm}(\mathbf{A})\}$ to the scaling $O(n^2D^5)$. Thus the very naive exact contraction procedure that we use is not so bad after all in this case even if it scales like $O(D^6)$.

There is one more subtlety we would like to point out here. It turns out that the matrix $N_{eff}(k)$ is always singular which presents a problem when we try to solve the generalized eigenvalue equation (4.4) since the solution involves the inverse $N_{eff}^{-1}(k)$. We can circumvent this problem by solving (4.4) within the nonsingular subspace like it has been done in [3]. Eigenvectors associated to the zero eigenspace of $N_{eff}(k)$ will result in physical states $|\psi_k(\mathbf{B})\rangle = 0$, i.e. these are states of zero length in the Hilbert space. Any physical operator will produce a zero when acting on these states. In particular, the effective Hamiltonian $H_{eff}(k)$ will also have zero eigenvalues for the same eigenvectors, and we do not loose any information by restricting to the nonsingular subspace. The dimension of the zero eigenspace can be shown to be $D^2(d-1)$ for $k \neq 0$ and $D^2(d-1)+1$ for $k=0$ as we demonstrate in [70]. The tricky point is that for some models the strictly non-zero eigenvalues of $N_{eff}(k)$ become so small that they yield the generalized eigenvalue problem ill conditioned. In general this behavior does not occur for small D. For big D or in certain regions of the phase diagram however the nonsingular eigenvalues become so small that it is hard to distinguish numerically between the singular subspace and the nonsingular one. This issue might be the source of the mysterious negative gap that appears in [3] in the vicinity of the critical point.

We have employed a slightly different method for the regularization of $N_{eff}(k)$. Instead of projecting the problem into the strictly non-singular subspace, we restrict ourselves to the subspace in which the eigenvalues of $N_{eff}(k)$ are larger than some ϵ. There is a tradeoff between loss in precision due to this projection and loss in precision due to the bad conditioned generalized eigenvalue problem. In the end we have settled for a seemingly optimal $\epsilon = 10^{-11}$.

4.4 Numerical results

We have applied the algorithm presented above to three nearest neighbour interaction spin models in order to benchmark its accuracy: the quantum Ising model, the antiferromagnetic Heisenberg spin-$1/2$ model and the bilinear-biquadratic spin-1 model. The quantum Ising model is exactly solvable and its entire energy spectrum can be easily computed [18].

The Heisenberg model is in principle also exactly solvable by means of Bethe ansatz, in practice however it is much harder to obtain its entire low-energy spectrum. This is due to the fact that the elementary excitations are two-spinon states, and among these, the solution of the Bethe ansatz equations for the two-spinon singlet states are computationally very challenging [71]. Thus for long chains we have restricted ourselves to check only the precision of the lowest two-spinon triplets. For small chains that are accessible via exact diagonalization on the other hand, we compare not only the entire low-energy spectrum but also the fidelity of the states themselves.

For the bilinear-biquadratic model we have studied only two special points out of the available range of the model parameter $\theta \in [0, 2\pi)$. The *first*, $\theta = 0$ is not exactly solvable and here we can only compare our simulations with other numerical results. The *second*, $\theta = -\pi/2$, is in principle exactly solvable [72], but only very few of its excitations are easily computable, so we settle for comparison only with the states explicitly given in [72].

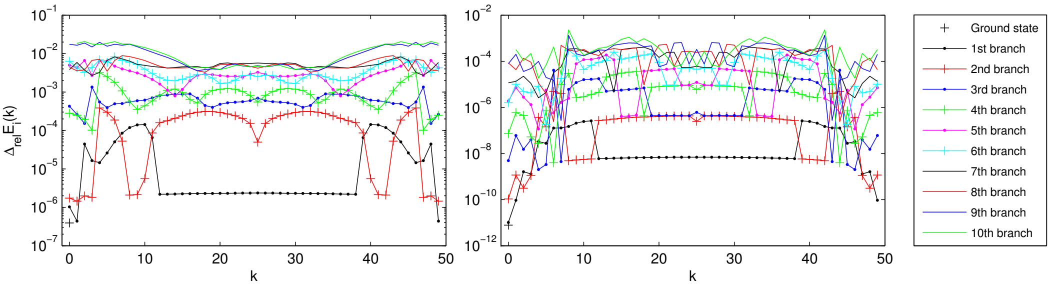

Figure 4.4: (Color online). Relative precision of the low excitation spectrum for a critical Ising chain with $N = 50$. Left: $D = 8$. Right: $D = 32$.

4.4.1 Quantum Ising model

The Hamiltonian we have used in our simulations of the quantum Ising model is given by

$$H_{IS} = -\sum_{i=1}^{N} \sigma_i^z \sigma_{i+1}^z - g \sum_{i=1}^{N} \sigma_i^x \quad . \tag{4.11}$$

We have used this version rather than

# \ k	0	1	2	3	4	5	6	7	8	9	10	11	12
1	$\|0\rangle$	$\|1\rangle$	$\|\frac{3}{2},\frac{1}{2}\rangle$	$\|\frac{5}{2},\frac{1}{2}\rangle$	$\|\frac{7}{2},\frac{1}{2}\rangle$	$\|\frac{9}{2},\frac{1}{2}\rangle$	$\|\frac{11}{2},\frac{1}{2}\rangle$	$\|\frac{13}{2},\frac{1}{2}\rangle$	$\|\frac{15}{2},\frac{1}{2}\rangle$	$\|\frac{17}{2},\frac{1}{2}\rangle$	$\|\frac{19}{2},\frac{1}{2}\rangle$	$\|\frac{21}{2},\frac{1}{2}\rangle$	$\|12\rangle$
2	$\|\frac{1}{2},-\frac{1}{2}\rangle$	$\|\frac{3}{2},-\frac{1}{2}\rangle$	$\|2\rangle$	$\|3\rangle$	$\|\frac{5}{2},\frac{3}{2}\rangle$	$\|\frac{7}{2},\frac{3}{2}\rangle$	$\|\frac{9}{2},\frac{3}{2}\rangle$	$\|\frac{11}{2},\frac{3}{2}\rangle$	$\|8\rangle$	$\|9\rangle$	$\|10\rangle$	$\|11\rangle$	$\|\frac{23}{2},\frac{1}{2}\rangle$
3	$\|1,-1,0\rangle$	$\|2,-1,0\rangle$	$\|\frac{5}{2},-\frac{1}{2}\rangle$	$\|2,1,0\rangle$	$\|4\rangle$	$\|5\rangle$	$\|\frac{7}{2},\frac{5}{2}\rangle$	$\|7\rangle$	$\|\frac{13}{2},\frac{3}{2}\rangle$	$\|\frac{15}{2},\frac{3}{2}\rangle$	$\|\frac{17}{2},\frac{3}{2}\rangle$	$\|\frac{19}{2},\frac{3}{2}\rangle$	$\|\frac{21}{2},\frac{3}{2}\rangle$
4	$\|\frac{3}{2},-\frac{3}{2}\rangle$	$\|\frac{5}{2},-\frac{3}{2}\rangle$	$\|3,-1,0\rangle$	$\|\frac{7}{2},-\frac{1}{2}\rangle$	$\|3,1,0\rangle$	$\|4,1,0\rangle$	$\|6\rangle$	$\|\frac{9}{2},\frac{5}{2}\rangle$	$\|\frac{11}{2},\frac{5}{2}\rangle$	$\|8,1,0\rangle$	$\|9,1,0\rangle$	$\|10,1,0\rangle$	$\|11,1,0\rangle$

# \ k	13	14	15	16	17	18	19	20	21	22	23	24	25
1	$\|13\rangle$	$\|14\rangle$	$\|15\rangle$	$\|16\rangle$	$\|17\rangle$	$\|18\rangle$	$\|19\rangle$	$\|20\rangle$	$\|21\rangle$	$\|22\rangle$	$\|23\rangle$	$\|24\rangle$	$\|25\rangle$
2	$\|\frac{25}{2},\frac{1}{2}\rangle$	$\|\frac{27}{2},\frac{1}{2}\rangle$	$\|\frac{29}{2},\frac{1}{2}\rangle$	$\|\frac{31}{2},\frac{1}{2}\rangle$	$\|\frac{33}{2},\frac{1}{2}\rangle$	$\|\frac{35}{2},\frac{1}{2}\rangle$	$\|\frac{37}{2},\frac{1}{2}\rangle$	$\|\frac{39}{2},\frac{1}{2}\rangle$	$\|\frac{41}{2},\frac{1}{2}\rangle$	$\|\frac{43}{2},\frac{1}{2}\rangle$	$\|\frac{45}{2},\frac{1}{2}\rangle$	$\|\frac{47}{2},\frac{1}{2}\rangle$	$\|\frac{49}{2},\frac{1}{2}\rangle$
3	$\|12,1,0\rangle$	$\|13,1,0\rangle$	$\|14,1,0\rangle$	$\|15,1,0\rangle$	$\|16,1,0\rangle$	$\|17,1,0\rangle$	$\|\frac{39}{2},-\frac{1}{2}\rangle$	$\|\frac{41}{2},-\frac{1}{2}\rangle$	$\|\frac{43}{2},-\frac{1}{2}\rangle$	$\|\frac{45}{2},-\frac{1}{2}\rangle$	$\|\frac{47}{2},-\frac{1}{2}\rangle$	$\|\frac{49}{2},-\frac{1}{2}\rangle$	$\|\frac{-49}{2},\frac{-1}{2}\rangle$
4	$\|\frac{23}{2},\frac{3}{2}\rangle$	$\|\frac{25}{2},\frac{3}{2}\rangle$	$\|\frac{27}{2},\frac{3}{2}\rangle$	$\|\frac{29}{2},\frac{3}{2}\rangle$	$\|\frac{31}{2},\frac{3}{2}\rangle$	$\|\frac{37}{2},-\frac{1}{2}\rangle$	$\|18,1,0\rangle$	$\|19,1,0\rangle$	$\|20,1,0\rangle$	$\|21,1,0\rangle$	$\|22,1,0\rangle$	$\|23,1,0\rangle$	$\|24,1,0\rangle$

Table 4.1: (Color online). Quasi-particle structure of the lowest four branches for $g = 1$. The red/blue (grayscale: dark/light) boxes highlight states from the odd parity subspace respectively from the even parity subspace. The quantum numbers by which the states are labeled denote the momentum of the elementary Bogoliubov modes: modes from the odd parity subspace have integer momentum while modes from the even parity subspace have half-integer momentum. The ground state which is not shown in the table is the fermionic vacuum in the even parity subspace i.e. $|GS\rangle = |\Omega\rangle_{even}$.

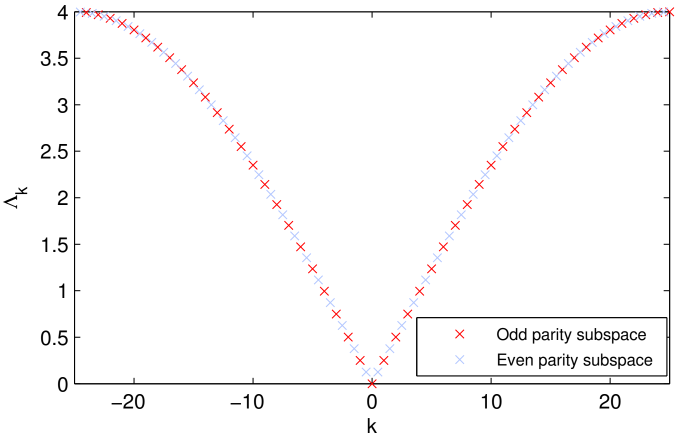

Figure 4.5: (Color online). Exact solution for the dispersion relation of the Bogoliubov modes at criticality (i.e., $g = 1$).

$$H'_{IS} = -\sum_{i=1}^{N} \sigma_i^x \sigma_{i+1}^x - g \sum_{i=1}^{N} \sigma_i^z \tag{4.12}$$

due to the fact that having a diagonal interaction term is more convenient for the numerics. Of course both versions are equivalent since they can be transformed into each other by means of the unitary transformation $U = \bigotimes_{i=1}^{N} H_i$ where the H_i are 1-qubit Hadamard gates.

The exact diagonalization of (4.12) for PBC in the limit of an infinite number of sites is straightforward [73]. The first thing one has to do is to map the spin Hamiltonian to a fermionic one via a Jordan-Wigner transformation. Now the Jordan-Wigner transformation is non-local due to the fact that it transforms local spin operators into fermionic ones that anticommute if they act on different sites. Luckily for almost all terms in the Hamiltonian the non-localities cancel except for the term representing the interaction between the last and the first site. This term ends up containing a global parity operator acting on all sites and thus breaking the translational invariance with respect to the fermionic modes.

Now, if we are interested in the thermodynamic limit, we will eventually take the limit $N \to \infty$ at some point, and in this limit the contribution of one interaction term to the energy can be neglected. We thus have the freedom to alter this term as we please in order to simplify things. One very convenient choice are the so-called Jordan-Wigner boundary conditions which are nothing more than simply neglecting the global parity operator in the last term thereby yielding the fermionic Hamiltonian translationally invariant. Note that the Jordan-Wigner boundary conditions cannot be expressed in a trivial way in terms of spin operators. The fermionic Hamiltonian obtained in this way is quadratic and translationally invariant, but it is not particle conserving. This can be fixed by a canonical transformation [18] to non-interacting Bogoliubov fermions. The ground state of the system is then given by the new fermionic vacuum while excited states can be obtained by sequentially filling the fermionic modes. Ordering the eigenstates of the original spin model by momentum and energy, it turns out that the lowest energy branch coincides with the dispersion relation of the Bogoliubov fermions. This happens because for a given momentum, the lowest energy state is always a state where precisely one fermionic mode is occupied.

For finite systems with periodic boundary conditions, the Hamiltonian after the Jordan-Wigner transformation presents a difficulty: due to the fact that in this case we cannot choose the boundary conditions freely, there is one term that contains a global parity operator as prefactor (see Eq. 2.11' in [18]). At first sight, this term makes the Bogoliubov transformation impossible. However, if we project the Hamiltonian onto the subspaces with either odd or even parity, we can replace the parity operator by its eigenvalue in that subspace s.t. it becomes ± 1, and we can apply the Bogoliubov transformation in each subspace separately. The spectrum of the original Hamiltonian can then be constructed by picking from each subspace the states with the correct parity. It turns out that we can arbitrarily choose the sign of the Bogoliubov parity by shifting the Fermi surface. For example, if we choose the fermionic vacuum to be the state with lowest energy, all excited states are particle excitations [1] and it turns out that the parity operator changes its sign under the Bogoliubov transformation for fields below the critical point i.e. $g < 1$. For $g \geq 1$ this choice of the vacuum state leaves the parity operator invariant. Thus for $g < 1$, in principle we can switch the sign of the parity operator by shifting the Fermi surface and thereby we could always define the Bogoliubov modes such that the parity operator remains invariant. We will however give numerical evidence for the fact that choosing the Fermi surface to be the fermionic vacuum state is the physical choice. All details of the exact solution of the finite system with PBC can be found in Appendix A.

---

[1] If the fermionic vacuum is not the lowest energy state there also exist hole and particle-hole excitations. If we choose the vaccum in such a way that there exists exactly one hole-mode we effecively switch the sign of the parity operator opposed to choosing no hole-modes at all.

Critical field $g = 1$

Let us first present the results obtained for the critical field strength $g = 1$. In Fig. 4.3 we have plotted the energy of the lowest ten branches of excitations of a chain with 50 spins obtained for MPS bond dimensions $D = 8$ and $D = 32$. The results for $D = 32$ are so close to the exact spectrum that it makes much more sense to look at plots of the relative energy precision rather than at plots of the energy itself. This is shown in Fig. 4.4.

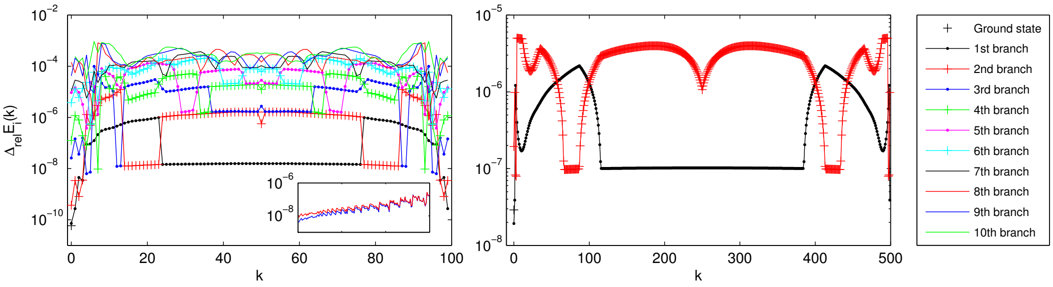

Figure 4.6: (Color online). Relative precision of the low excitation spectrum for the critical Ising chain with different chain lengths. Left: $N = 100$, $D = 32$. Right: $N = 500$, $D = 20$. The inset in the left plot shows the relative precision of the low energy spectrum (150 states) of a Quantum Ising chain with $N = 100$ and OBC when approximated using DMRG (red) respectively vNRG (blue) with $D = 150$. The data for the inset is courtesy I. Pizorn [74].

At first sight the crossing of the precision line for the first branch of excitations with the one for the second branch seems a little unusual. How can it be that states with higher energy are approximated by roughly two orders of magnitude better than states with lower energy? The answer to this question is obvious if one looks at how the eigenstates emerge from the elementary Bogoliubov modes. Table 4.1 shows which Bogoliubov modes contribute to each individual eigenstate in the first four branches of excitations. Modes from the even parity subspace have half-integer momentum while the ones from the odd parity subspace have integer momentum. Note that since only excitations with an even number of particles are allowed in the even-parity subspace, the resulting states always have integer momentum. Henceforth $|\Omega\rangle_{even}$ shall denote the vacuum in the even parity subspace and $|\Omega\rangle_{odd}$ the vacuum in the odd parity one. The ground state of the critical chain is the Bogoliubov vacuum in the even parity subspace i.e. $|GS\rangle = |\Omega\rangle_{even}$. The first excited state is the zero momentum state from the first branch and is given by a Bogoliubov mode with zero momentum from the odd parity subspace [1]. It is sufficient to show in Table 4.1 how the spectrum emerges from elementary excitations for momenta $0 \leq k \leq N/2$ since the dispersion relation of the Bogoliubov fermions is symmetric around $k = 0$ as can be seen in Fig. 4.5. The important thing to notice in Table 4.1 is that the lowest branch of excitations does not contain solely one-particle excitations as it does in the case of the infinite chain. Looking back at the right plot in Fig. 4.4 we see immediately that the one-particle excitations from the first two branches are approximated with roughly the same accuracy between 10^{-11} and 10^{-9} with the lower value for small momentum states. One can easily check that the states with the same order of accuracy from higher branches are precisely one-particle excitations. On the other hand it is obvious that two-particle excitations from any branch where one of the particles has fixed momentum $k = 1/2$ can be found in the plateau with relative precision of roughly 10^{-7}. The other plateaus of similar precision in the $D = 32$ plot of Fig. 4.4 represent either two-particle states where each particle has higher momentum or three and more particle excitations.

---

[1] Actually at $g = 1$ the zero momentum mode has energy zero so the states $|\Omega\rangle_{odd}$ and $|0\rangle$ have exactly the same energy. However this happens only at the critical point $g = 1$. In general $|\Omega\rangle_{odd}$ and $|0\rangle$ have different energy.

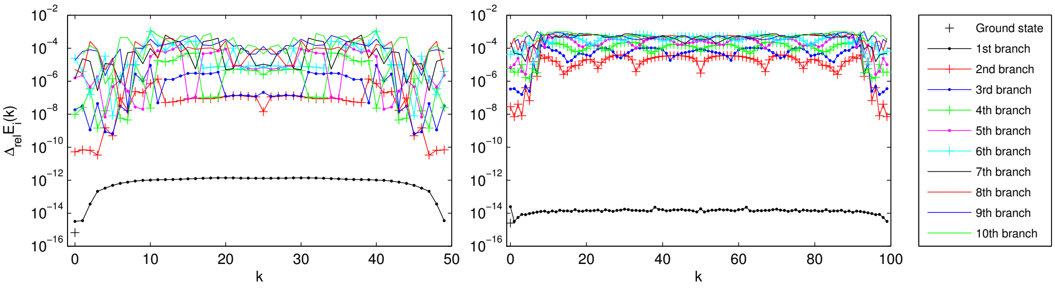

Figure 4.7: (Color online). Relative precision of the low excitation spectrum for the Ising chain at $g = 1.1$ for different chain lengths. Left: $N = 50$, $D = 32$. Right: $N = 100$, $D = 32$.

# \ k	0	1	2	3	4	5	6	7	8	9	10	11	12	13	14	15	16	17	18	19	20	21	22	23	24	25
1	$\vert 0\rangle$	$\vert 1\rangle$	$\vert 2\rangle$	$\vert 3\rangle$	$\vert 4\rangle$	$\vert 5\rangle$	$\vert 6\rangle$	$\vert 7\rangle$	$\vert 8\rangle$	$\vert 9\rangle$	$\vert 10\rangle$	$\vert 11\rangle$	$\vert 12\rangle$	$\vert 13\rangle$	$\vert 14\rangle$	$\vert 15\rangle$	$\vert 16\rangle$	$\vert 17\rangle$	$\vert 18\rangle$	$\vert 19\rangle$	$\vert 20\rangle$	$\vert 21\rangle$	$\vert 22\rangle$	$\vert 23\rangle$	$\vert 24\rangle$	$\vert 25\rangle$
2	$\vert\frac{1}{2},-\frac{1}{2}\rangle$	$\vert\frac{3}{2},-\frac{1}{2}\rangle$	$\vert\frac{3}{2},\frac{1}{2}\rangle$	$\vert\frac{5}{2},\frac{1}{2}\rangle$	$\vert\frac{5}{2},\frac{3}{2}\rangle$	$\vert\frac{7}{2},\frac{3}{2}\rangle$	$\vert\frac{7}{2},\frac{5}{2}\rangle$	$\vert\frac{9}{2},\frac{5}{2}\rangle$	$\vert\frac{13}{2},\frac{3}{2}\rangle$	$\vert\frac{15}{2},\frac{3}{2}\rangle$	$\vert\frac{17}{2},\frac{3}{2}\rangle$	$\vert\frac{19}{2},\frac{3}{2}\rangle$	$\vert\frac{23}{2},\frac{1}{2}\rangle$	$\vert\frac{25}{2},\frac{1}{2}\rangle$	$\vert\frac{27}{2},\frac{1}{2}\rangle$	$\vert\frac{29}{2},\frac{1}{2}\rangle$	$\vert\frac{31}{2},\frac{1}{2}\rangle$	$\vert\frac{33}{2},\frac{1}{2}\rangle$	$\vert\frac{35}{2},\frac{1}{2}\rangle$	$\vert\frac{37}{2},\frac{1}{2}\rangle$	$\vert\frac{39}{2},\frac{1}{2}\rangle$	$\vert\frac{41}{2},\frac{1}{2}\rangle$	$\vert\frac{43}{2},\frac{1}{2}\rangle$	$\vert\frac{45}{2},\frac{1}{2}\rangle$	$\vert\frac{47}{2},\frac{1}{2}\rangle$	$\vert\frac{49}{2},\frac{1}{2}\rangle$
3	$\vert 1,-1,0\rangle$	$\vert 2,-1,0\rangle$	$\vert\frac{5}{2},-\frac{1}{2}\rangle$	$\vert 2,1,0\rangle$	$\vert\frac{7}{2},\frac{1}{2}\rangle$	$\vert\frac{9}{2},\frac{1}{2}\rangle$	$\vert\frac{9}{2},\frac{3}{2}\rangle$	$\vert\frac{11}{2},\frac{3}{2}\rangle$	$\vert\frac{11}{2},\frac{5}{2}\rangle$	$\vert\frac{13}{2},\frac{5}{2}\rangle$	$\vert\frac{15}{2},\frac{5}{2}\rangle$	$\vert\frac{21}{2},\frac{1}{2}\rangle$	$\vert\frac{21}{2},\frac{3}{2}\rangle$	$\vert\frac{23}{2},\frac{3}{2}\rangle$	$\vert\frac{25}{2},\frac{3}{2}\rangle$	$\vert\frac{27}{2},\frac{3}{2}\rangle$	$\vert\frac{29}{2},\frac{3}{2}\rangle$	$\vert\frac{31}{2},\frac{3}{2}\rangle$	$\vert\frac{33}{2},\frac{3}{2}\rangle$	$\vert\frac{35}{2},\frac{3}{2}\rangle$	$\vert\frac{41}{2},-\frac{1}{2}\rangle$	$\vert\frac{43}{2},-\frac{1}{2}\rangle$	$\vert\frac{45}{2},-\frac{1}{2}\rangle$	$\vert\frac{47}{2},-\frac{1}{2}\rangle$	$\vert\frac{49}{2},-\frac{1}{2}\rangle$	$\vert\frac{-49}{2},\frac{-1}{2}\rangle$

Table 4.2: (Color online). Quasi-particle structure of the lowest three branches for $g = 1.1$. The red/blue (grayscale: dark/light) boxes highlight states from the odd parity subspace respectively from the even parity subspace. The quantum numbers by which the states are labeled denote the momentum of the elementary Bogoliubov modes: modes from the odd parity subspace have integer momentum while modes from the even parity subspace have half-integer momentum. The ground state which is not shown in the table is the fermionic vacuum in the even parity subspace i.e. $|GS\rangle = |\Omega\rangle_{even}$.

This interpretation of the branch crossings in Fig. 4.4 is strong evidence for the fact that (4.1) is a very good ansatz for one-particle excitations. However it turns out that if D is large enough, (4.1) is also a fairly good ansatz for many-particle excitations. The reason for this is that the large bond dimension compensates for the localization of excitations inherent in ansatz (4.1) by spreading the effect of the optimized tensor $\mathbf{B}$ to a region around it whose size is of the order of the induced correlation length of the MPS we start with. This is exactly why for the Ising chain with $g = 1$, $N = 50$ and $D = 32$ even states from tenth branch are approximated with an accuracy of roughly 10^{-4}.

Now let us have a closer look at the region of the ”level-crossing” between the lowest two-fermion branch from the even parity subspace and the lowest one-fermion branch from the odd parity subspace. In the case of $g = 1$ this crossing turns out to be at approximately $N/4$. In the immediate neighborhood of the crossing the energy difference between states with identical momentum becomes very small. Now if the bond dimension D is chosen such that the precision of the MPS is of the same order like the interlevel spacing, these two levels cannot be discriminated properly by the MPS algorithm and thus there is no clear interpretation we can give to these MPS states in terms of one or two-particle states. As can be seen in the $D = 8$ plot of Fig. 4.4, in this region the first and second MPS branch interpolate between the one and the two-particle states which we can safely discriminate. Note that this observation holds only on the side of the level crossing where the one-particle state has higher energy than the two-particle state (e.g. at $k \approx N/4$ on the left side of the crossing). On the other side, the one-particle excitation has lower energy and our one-particle MPS ansatz is perfectly suited to discriminate between the first and the second branch even if the precision is smaller than the actual gap between the levels.

The last thing we would like point out about Fig. 4.4 is the gap in accuracy between the states from the second and third branch at momentum $k = N/2$. It turns out that this is a doubly degenerate state since it can be created by two different superpositions of elementary excitations with the same energy namely $|\frac{49}{2}, \frac{1}{2}\rangle$ and $|-\frac{49}{2}, -\frac{1}{2}\rangle$. This is the reason why the precision of the $k = N/2$ state in the second branch is better than that of the surrounding two-particle states which are not degenerated: variational algorithms are more precise if they try to approximate the energy of an entire subspace of the Hilbert space rather than that of a single state. However since all states generated by our algorithm are orthogonal, the price we have to pay for the improved precision in the second branch, is a slightly worse precision of the $k = N/2$ state in the third branch.

With this said, we can present the results we have obtained for different chain lengths N. Fig. 4.6 shows the accuracy of the algorithm for chains with 100 and 500 sites at $g = 1$. The plot for $N = 100$ is very similar to the $D = 32$ plot from Fig. 4.4. At small momenta $6 \leq k \leq 11$ the one-particle excitations lie in the branches 4 to 6. These states are not reliably reproduced by our algorithm within the precision that is otherwise reached for one-particle excitations. Presumably this would be fixed by increasing the bond dimension D beyond 32. However at the moment we cannot go to larger D for $N = 100$. For $N = 500$ the maximally accessible bond dimension is $D = 20$. The corresponding plot from Fig. 4.6 is very similar to the small D plot for $N = 50$. Again in the region of the ”level-crossing” between one-particle and two-particle excitations around $k = N/4$ our algorithm has difficulties obtaining the maximally reachable precision for the one-particle states.

We would like to conclude this section with a comparison of the accuracy of our results with other numerical computations of the excitation spectrum of the Quantum Ising model.

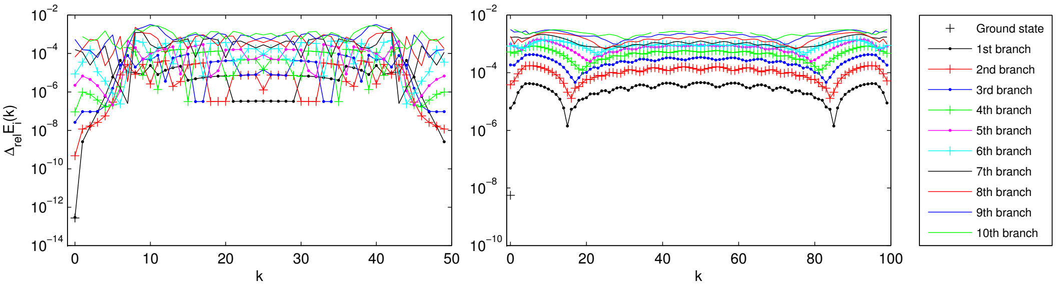

Figure 4.8: (Color online). Relative precision of the low excitation spectrum for the Ising chain at $g = 0.9$ for different chain lengths. Left: $N = 50$, $D = 32$. Right: $N = 100$, $D = 32$.

# \ k	0	1	2	3	4	5	6	7	8	9	10	11	12	13	14	15	16	17	18	19	20	21	22	23	24	25
1	$\lvert\Omega\rangle_{odd}$	$\lvert 1,0\rangle$	$\lvert\frac{3}{2},\frac{1}{2}\rangle$	$\lvert 2,1\rangle$	$\lvert\frac{5}{2},\frac{3}{2}\rangle$	$\lvert 3,2\rangle$	$\lvert\frac{7}{2},\frac{5}{2}\rangle$	$\lvert 4,3\rangle$	$\lvert\frac{11}{2},\frac{5}{2}\rangle$	$\lvert\frac{15}{2},\frac{3}{2}\rangle$	$\lvert\frac{17}{2},\frac{3}{2}\rangle$	$\lvert 10,1\rangle$	$\lvert 11,1\rangle$	$\lvert 12,1\rangle$	$\lvert 13,1\rangle$	$\lvert\frac{29}{2},\frac{1}{2}\rangle$	$\lvert\frac{31}{2},\frac{1}{2}\rangle$	$\lvert\frac{33}{2},\frac{1}{2}\rangle$	$\lvert\frac{35}{2},\frac{1}{2}\rangle$	$\lvert\frac{37}{2},\frac{1}{2}\rangle$	$\lvert\frac{39}{2},\frac{1}{2}\rangle$	$\lvert 21,0\rangle$	$\lvert 22,0\rangle$	$\lvert 23,0\rangle$	$\lvert 24,0\rangle$	$\lvert 25,0\rangle$
2	$\lvert\frac{1}{2},-\frac{1}{2}\rangle$	$\lvert\frac{3}{2},-\frac{1}{2}\rangle$	$\lvert 2,0\rangle$	$\lvert\frac{5}{2},\frac{1}{2}\rangle$	$\lvert 3,1\rangle$	$\lvert\frac{7}{2},\frac{3}{2}\rangle$	$\lvert 4,2\rangle$	$\lvert\frac{9}{2},\frac{5}{2}\rangle$	$\lvert 6,2\rangle$	$\lvert 7,2\rangle$	$\lvert 9,1\rangle$	$\lvert\frac{19}{2},\frac{3}{2}\rangle$	$\lvert\frac{21}{2},\frac{3}{2}\rangle$	$\lvert\frac{25}{2},\frac{1}{2}\rangle$	$\lvert\frac{27}{2},\frac{1}{2}\rangle$	$\lvert 14,1\rangle$	$\lvert 15,1\rangle$	$\lvert 16,1\rangle$	$\lvert 18,0\rangle$	$\lvert 19,0\rangle$	$\lvert 20,0\rangle$	$\lvert\frac{41}{2},\frac{1}{2}\rangle$	$\lvert\frac{43}{2},\frac{1}{2}\rangle$	$\lvert\frac{45}{2},\frac{1}{2}\rangle$	$\lvert\frac{47}{2},\frac{1}{2}\rangle$	$\lvert\frac{49}{2},\frac{1}{2}\rangle$
3	$\lvert 1,-1\rangle$	$\lvert 2,-1\rangle$	$\lvert\frac{5}{2},-\frac{1}{2}\rangle$	$\lvert 3,0\rangle$	$\lvert\frac{7}{2},\frac{1}{2}\rangle$	$\lvert 4,1\rangle$	$\lvert\frac{9}{2},\frac{3}{2}\rangle$	$\lvert 5,2\rangle$	$\lvert 5,3\rangle$	$\lvert\frac{13}{2},\frac{5}{2}\rangle$	$\lvert 8,2\rangle$	$\lvert 9,2\rangle$	$\lvert\frac{23}{2},\frac{1}{2}\rangle$	$\lvert\frac{23}{2},\frac{3}{2}\rangle$	$\lvert\frac{25}{2},\frac{3}{2}\rangle$	$\lvert\frac{27}{2},\frac{3}{2}\rangle$	$\lvert 16,0\rangle$	$\lvert 17,0\rangle$	$\lvert 17,1\rangle$	$\lvert 18,1\rangle$	$\lvert 19,1\rangle$	$\lvert 20,0\rangle$	$\lvert\frac{45}{2},-\frac{1}{2}\rangle$	$\lvert\frac{47}{2},-\frac{1}{2}\rangle$	$\lvert\frac{49}{2},-\frac{1}{2}\rangle$	$\lvert\frac{-49}{2},\frac{-1}{2}\rangle$

Table 4.3: (Color online). Quasi-particle structure of the lowest three branches for $g = 0.9$. The red/blue (grayscale: dark/light) boxes highlight states from the odd parity subspace respectively from the even parity subspace. The quantum numbers by which the states are labeled denote the momentum of the elementary Bogoliubov modes: modes from the odd parity subspace have integer momentum while modes from the even parity subspace have half-integer momentum. $|\Omega\rangle_{odd}$ denotes the fermionic vacuum in the odd parity subspace. The ground state which is not shown in the table is the fermionic vacuum in the even parity subspace i.e. $|GS\rangle = |\Omega\rangle_{even}$.

Unfortunately we are not aware of any results for chains with PBC. For chains with OBC however DMRG [2] and the recently presented variational Numerical Renormalization Group (vNRG) [74] methods were used in order to approximate the low energy spectrum. The inset in Fig. 4.6 shows the relative precision of the energy of the lowest lying 150 states when approximated using DMRG (red line) respectively vNRG (blue line). We can see that the precision for the most states shown there is roughly of the same order like the one we obtain for one-particle excitations with large momentum, i.e. $\approx 10^{-8}$. For the one and two-particle excitations with very small momentum our precision is up to two orders of magnitude better than the one obtained for the lowest excited states in [74]. Based on this analysis it might seem feasible that our method and vNRG can be used in a complementary way: many-particle states with small energy may in some cases be better accessible via vNRG. For chains with PBC however both DMRG and vNRG must use a much bigger ($\approx D^2$) bond dimension in order achieve the same precision like for OBC, so from today's point of view these methods are computationally far too expensive to tackle PBC problems. Our method on the other hand cannot be used for finite chains with OBC.

Non-critical field $g > 1$

Now let us look at how the algorithm performs when we move away from the critical point. Fig. 4.7 shows the relative energy difference of the MPS approximation for $g = 1.1$ i.e. above the critical point. The most striking feature in this regime is the clear separation of the lowest branch of excitations from the higher ones. This happens due to the fact that in this case the lowest branch contains only one-particle states as can be seen in Table 4.2. Again if D is large enough (e.g. $D = 32$ for $N = 50$), the different plateaus of similar precision become clearly visible. The first one at roughly $\Delta_{rel} E_i(k) \approx 10^{-8}$ contains two-particle excitations from the second and third branch where one of the fermionic modes has momentum $k = 1/2$. The second one with precision around 10^{-6} consists of states where one of the fermionic modes has momentum $k = 3/2$. Note that in the plot for $N = 100$ the lowest branch has slightly better precision than the one in the $N = 50$ plot even though the virtual bond dimension is the same. This happens presumably because in this case the chain is long enough such that the running particle cannot "feel its own tail" due to the PBC. This is another piece of evidence that ansatz (4.1) is very well suited to describe one-particle excitations. Whether many-particle excitations are faithfully reproduced depends strongly on the magnitude of D with respect to N.

Non-critical field $g < 1$

For $g < 1$ the picture changes dramatically. We can see in Fig. 4.8 that at $g = 0.9$ the best precision for states from the lowest branch is five to seven orders of magnitude worse than for $g = 1.1$. Without any knowledge of the quasi-particle structure of the spectrum this huge difference might look a bit surprising. Even more surprising is the fact that the best precision at $g = 0.9$ is one order of magnitude worse than at the critical point $g = 1$. However looking at the quasi-particle structure in Table 4.3 clarifies the situation. As already mentioned above the parity of the Bogoliubov fermions in the odd-parity subspace can in principle be arbitrarily chosen by shifting the Fermi surface. Throughout this work, we have made the most natural choice of choosing all modes to have positive energy i.e. none of the quasi-particle excitations are hole modes. For $g < 1$ this choice switches the sign of the Bogoliubov parity operator such that we must pick states with an even number of excitations from the odd-parity subspace. One might argue against this convention and claim that it would be much more natural to pick the Fermi surface s.t. the zero-momentum mode is a hole excitation which yields the Bogoliubov parity operator identical to the spin parity operator. In this case we would have to construct all states from this subspace using an odd number of quasi-particles. On the other hand Fig. 4.8 clearly shows that our one-particle excitation ansatz (4.1) is a poor approximation to all states in this regime thereby indicating that indeed for $g < 1$ there exist no one-particle excitations. Thus our choice of the Fermi surface is justified and we have to construct the spectrum by picking the even quasi-particle excitations from the odd-parity subspace.

We can understand this behavior from another point of view if we consider an infinite chain with open boundary conditions. It is well known that in the region of the phase diagram where the ground state is doubly degenerated, the elementary excitations are kink excitations. If we would however impose periodic boundary conditions on the infinite chain, the single kink states would not be eigenstates any more since the existence of one domain wall would automatically imply the existence of a second one. In finite systems with PBC, the situation is a bit more complicated since the ground state degeneracy is not exact (the energy difference decays exponentially with N), but we can still argue along similar lines that localized perturbations, that interpolate between the states of the almost degenerated ground state manifold, must always come in pairs.

4.4.2 Heisenberg model

The second model we have studied is the antiferromagnetic (AF) Heisenberg spin-$1/2$ chain. The Hamiltonian reads

$$H_{HB} = \sum_{i=1}^{N} \vec{S}_i \vec{S}_{i+1} = \frac{1}{4}\sum_{i=1}^{N} (\sigma_i^x \sigma_{i+1}^x + \sigma_i^y \sigma_{i+1}^y + \sigma_i^z \sigma_{i+1}^z) \tag{4.13}$$

where $S^\alpha = \sigma^\alpha/2$ and σ^α denote as usually the Pauli operators. As we already mentioned, the tensors $\mathbf{A}$ that constitute the backbone of ansatz (4.1) are the results of the simulations presented in [28]. In that work we have obtained a TI MPS approximation of ground states for finite spin chains with PBC using matrices A_i that were real and symmetric. These results themselves were based on previous work [36] where we have approximated the ground state of infinite OBC chains by TI MPS with real symmetric matrices. Thus the starting point in the entire procedure that leads ultimately to the excited states presented here is the imaginary time evolution for an infinite chain with a set of real symmetric matrix product operators (MPO). As we explained in [36] it is not possible to construct these directly from the the Hamiltonian (4.13). However, by means of the unitary transformation $U = U^\dagger = \prod_{j=1}^{N/2} \sigma_{2j-1}^y$ (i.e. acting with a σ^y-gate on every second site) we obtain

$$H'_{HB} = U^\dagger H_{HB} U = \frac{1}{4}\sum_{i=1}^{N} (-\sigma_i^x \sigma_{i+1}^x + \sigma_i^y \sigma_{i+1}^y - \sigma_i^z \sigma_{i+1}^z) \tag{4.14}$$

which allows us to express the imaginary time evolution in terms of real symmetric MPO. Note that in order for this procedure to work we have to restrict ourselves to chains with an even number of sites. In this case it does not matter if we apply the σ^y-gates on sites with an odd or an even index, so without loss of generality we will apply them on the odd ones. Now H_{HB} and H'_{HB} have the same spectrum and since their eigenstates are simply related to eachother by

$$|\psi_i\rangle = \prod_{j=1}^{N/2} \sigma_{2j-1}^y \, |\psi_i'\rangle \tag{4.15}$$

we can digonalize H'_{HB} first and obtain the eigenstates of H_{HB} subsequently with very little effort.

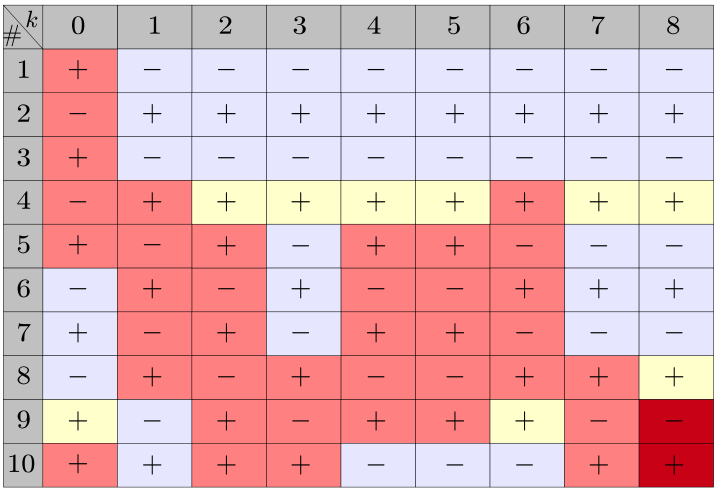

# \ k	0	1	2	3	4	5	6	7	8
1	$+$	$-$	$-$	$-$	$-$	$-$	$-$	$-$	$-$
2	$-$	$+$	$+$	$+$	$+$	$+$	$+$	$+$	$+$
3	$+$	$-$	$-$	$-$	$-$	$-$	$-$	$-$	$-$
4	$-$	$+$	$+$	$+$	$+$	$+$	$+$	$+$	$+$
5	$+$	$-$	$+$	$-$	$+$	$+$	$-$	$-$	$-$
6	$-$	$+$	$-$	$+$	$-$	$-$	$+$	$+$	$+$
7	$+$	$-$	$+$	$-$	$+$	$+$	$-$	$-$	$-$
8	$-$	$+$	$-$	$+$	$-$	$-$	$+$	$+$	$+$
9	$+$	$-$	$+$	$-$	$+$	$+$	$+$	$-$	$-$
10	$+$	$+$	$+$	$+$	$-$	$-$	$-$	$+$	$+$

Table 4.4: (Color online). Multiplet structure of the lowest ten branches of excitations for a Heisenberg 16-site chain with Hamiltonian (4.13). The colors encode the multiplet information: yellow-singlet, blue-triplet, red-quintuplet, dark red-septuplet (grayscale: darker colors encode higher multiplets). The states within each multiplet are ordered according to their total spin projection quantum number. The sign denotes the parity of a state.

We will show below that the momentum of a state is not always invariant under the transformation (4.14). The easiest way to obtain the momentum for any given state is by computing the expectation value of the translation operator T with respect to that state. H_{HB} and H'_{HB} are both translationally invariant thus all their eigenstates have well defined momentum so we can be sure that the reverse transformation $|\psi'_i(k')\rangle \to |\psi_i(k)\rangle$ will map momentum eigenstates to momentum eigenstates albeit k will generally differ from k'. The relation between the momenta follows easily from

$$\begin{aligned} e^{-i\frac{2\pi k}{N}} &= \langle\psi_i(k)|T|\psi_i(k)\rangle = \\ &= \langle\psi'_i(k')|\Big(\prod_{j=1}^{N/2}\sigma^y_{2j-1}\Big)T\Big(\prod_{j=1}^{N/2}\sigma^y_{2j-1}\Big)|\psi'_i(k')\rangle \\ &= \langle\psi'_i(k')|\Big(\prod_{j=1}^{N/2}\sigma^y_{2j-1}\Big)\Big(\prod_{j=1}^{N/2}\sigma^y_{2j}\Big)T|\psi'_i(k')\rangle \\ &= e^{-i\frac{2\pi k'}{N}}\,\langle\psi'_i(k')|\prod_{j=1}^{N}\sigma^y_j\,|\psi'_i(k')\rangle = e^{-i\frac{2\pi k'}{N}}\,\langle P_y\rangle_{i',k'} \end{aligned} \tag{4.16}$$

where we have used $T\big(\prod_j O_j\big)T^{-1} = \prod_j O_{j+1}$ and $T\,|\psi'_i(k')\rangle = e^{-i\frac{2\pi k'}{N}}\,|\psi'_i(k')\rangle$. Thus the

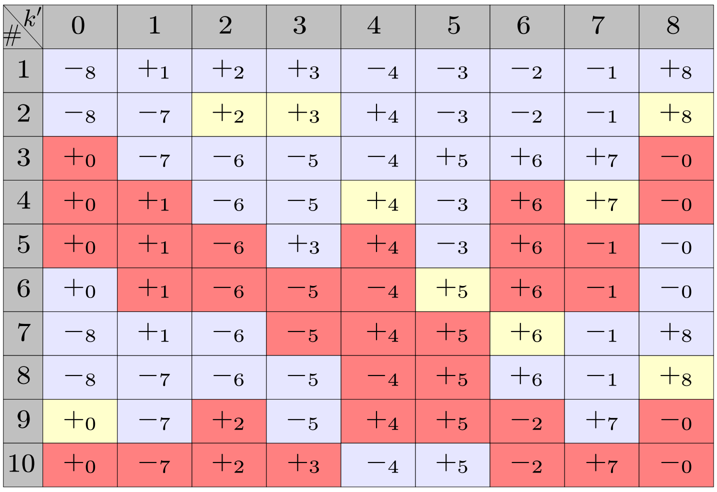

$\#$ k'	0	1	2	3	4	5	6	7	8
1	$-_8$	$+_1$	$+_2$	$+_3$	$-_4$	$-_3$	$-_2$	$-_1$	$+_8$
2	$-_8$	$-_7$	$+_2$	$+_3$	$+_4$	$-_3$	$-_2$	$-_1$	$+_8$
3	$+_0$	$-_7$	$-_6$	$-_5$	$-_4$	$+_5$	$+_6$	$+_7$	$-_0$
4	$+_0$	$+_1$	$-_6$	$-_5$	$+_4$	$-_3$	$+_6$	$+_7$	$-_0$
5	$+_0$	$+_1$	$-_6$	$+_3$	$+_4$	$-_3$	$+_6$	$-_1$	$-_0$
6	$+_0$	$+_1$	$-_6$	$-_5$	$-_4$	$+_5$	$+_6$	$-_1$	$-_0$
7	$-_8$	$+_1$	$-_6$	$-_5$	$+_4$	$+_5$	$+_6$	$-_1$	$+_8$
8	$-_8$	$-_7$	$-_6$	$-_5$	$-_4$	$+_5$	$+_6$	$-_1$	$+_8$
9	$+_0$	$-_7$	$+_2$	$-_5$	$+_4$	$+_5$	$-_2$	$+_7$	$-_0$
10	$+_0$	$-_7$	$+_2$	$+_3$	$-_4$	$+_5$	$-_2$	$+_7$	$-_0$

Table 4.5: (Color online). Multiplet structure of the lowest ten branches of excitations for a Heisenberg 16-site chain with Hamiltonian (4.14). The colors encode the multiplet information: yellow-singlet, blue-triplet, red-quintuplet (grayscale: darker colors encode higher multiplets). The sign denotes the parity of a state and the index denotes the momentum k if we apply the transformation (4.15) to an eigenstate with momentum k'.

change in momentum depends solely on the expectation value of the operator $P_y = \prod_{j=1}^{N} \sigma_j^y$ which in the following we will call the *parity* operator. This naming convention makes sense since $P_y = i^N \exp(i\pi S_T^y)$ where $S_T^y = \sum_{j=1}^{N} S_j^y$ thus P_y measures the parity of the total spin along the y-direction. Note that due to the factor i^N the meaning of positive and negative parity is interchanged for chains with $N = 0(\mod 4)$ and chains with $N = 2(\mod 4)$. The parity is a good quantum number for both H_{HB} and H'_{HB} so there exist eigenstates $|\psi'_i(k')\rangle$ that have well defined parity plus or minus one. If $\langle P_y \rangle_{i',k'} = +1$ the momentum remains unchanged i.e. $k = k'$, if $\langle P_y \rangle_{i',k'} = -1 = e^{\pm i\pi}$ we have $k = k' \oplus_N N/2$ where $\oplus_N$ denotes addition modulo N. Note that the parity itself is invariant under the mapping between H_{HB} and H'_{HB} since $U^\dagger P_y U = P_y$.

Now the generators of the $SU(2)$ symmetry for H'_{HB} do not commute with the translation operator thus we cannot classify the momentum eigenstates in terms of irreducible representations of $SU(2)$. For H_{HB} however we can do this, so we know exactly the degeneracy structure of the spectrum in each subspace with fixed momentum. Thus if we encounter for instance a threefold degenerated eigenstate of H'_{HB}, we know this is mapped to a spin triplet with well defined momentum in the original Hamiltonian. Accordingly it must contain a two-dimensional subspace with negative parity corresponding to total spin along the y-direction ± 1 and a one-dimensional subspace corresponding to total spin 0. Since the spin triplet in the original Hamiltonian has well defined momentum, according to the rules for the mapping $k \leftrightarrow k'$, we will have one eigenstate of H'_{HB} with momentum k and a two-dimensional subspace with

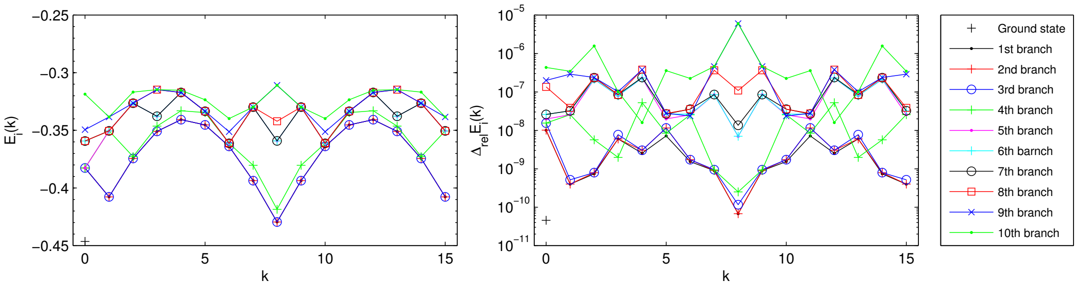

Figure 4.9: (Color online). Results for the low excitation spectrum (left) and the corresponding relative precision (right) for the Heisenberg spin-$1/2$ chain with $N = 16$ sites.

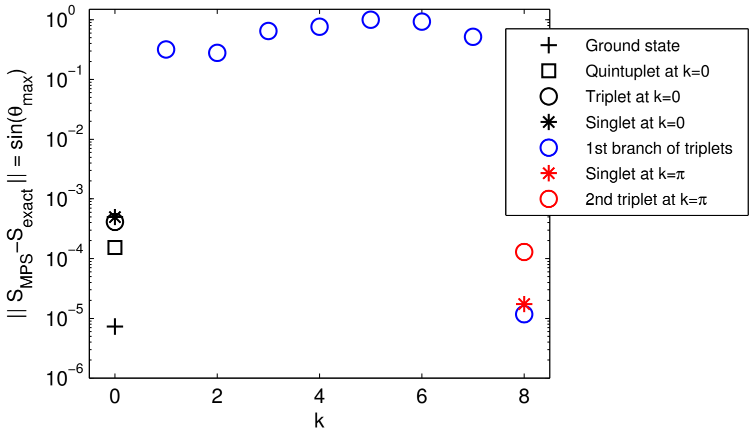

Figure 4.10: (Color online). Distance between several degenerated subspaces obtained by our algorithm to the corresponding degenerated subspaces obtained by exact diagonalization. As a measure for the distance we have used the sine of the canonical angle with the largest magnitude as defined in [75].

the same energy but different momentum $k' = k \ominus_N N/2$. In this way [1], after approximating the spectrum of H'_{HB} and labeling all energies with the corresponding momentum we can obtain the spectrum of H_{HB} by mere inspection of the degeneracy structure. Table 4.4 and Table 4.5 illustrate how the multiplets of H_{HB} and H'_{HB} are related to eachother.

This procedure works very well for the lower branches of the dispersion relation where the precision of our simulation is good enough to discriminate unambigously between different multiplets. For higher branches, on one hand the precision gets worse and on the other hand the density of states increases such that multiplets with similar energy become effectively undistiguishable for our algorithm. In this case the eigenstates with well defined momentum

---

[1] A singlet state would have parity $+1$ and thus there would be no momentum shift in this case. A quintuplet would contain a three-dimensional subspace with parity $+1$ and a two-dimensional subspace with parity -1. Thus in this case we would observe three states with no momentum shift and two states with a π-shift. The generalization to higher multiplets is obvious.

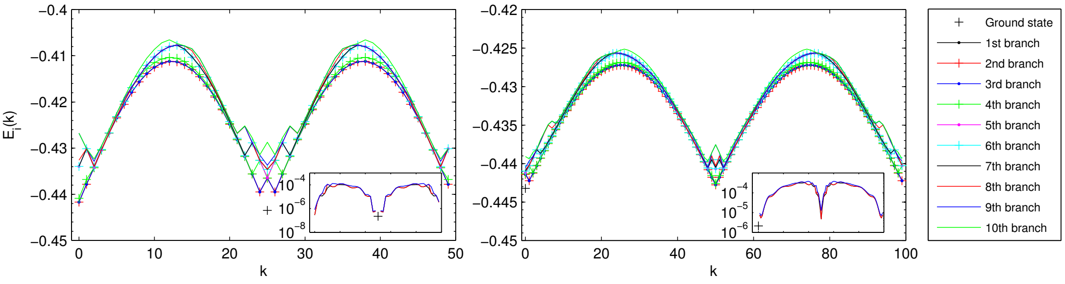

Figure 4.11: (Color online). Results for the low excitation spectrum and the corresponding relative precision of the lowest triplet (insets) for the Heisenberg spin-$1/2$ chain with $N = 50$ (left) and $N = 100$ (right) sites.

that we obtain for the Hamiltonian H'_{HB} do not have well defined parity i.e. they mix parity eigenstates with different parity. Since states with same momentum and different parity are mapped by (4.15) to states with different momentum, if we start with such a momentum eigenstate we obtain after the transformation a superposition of states with different momenta which is clearly not a momentum eigenstate. There are however two ways to overcome this issue and obtain approximations of the eigenstates of H_{HB} that are at the same time exact momentum eigenstates.

The *first* one amounts to computing the matrix elements of the translation operator T in the subspace spanned by the transformed states $\{M^y_{odd} \, |\psi'_i(k)'\rangle\}$ where $M^y_{odd} := \prod_{j=1}^{N/2} \sigma^y_{2j-1}$ and then diagonalize this matrix. It is not difficult to check that this can be done for each momentum k' separately since $M^y_{odd} T \, M^y_{odd} = M^y_{odd} \, M^y_{even} \, T = P_y T$ which is a translationally invariant operator and thus it does not mix states with different momentum. Diagonalizing each of the $T(k')_{ij} = U^\dagger(k')_{il} D(k')_{lm} U(k')_{mj}$ yields for each k' a unitary $U(k')$ that is nothing more than the transformation that we need to obtain the desired momentum eigenstates via $|\psi_i(k_i)\rangle = U(k')_{ij} \, |\psi'_j(k')\rangle$. The new momentum k_i can be read off the diagonal matrix $D(k')$. There are two drawbacks that come with this procedure. The first one is that we must compute the matrix elements $T(k')_{ij}$ each of which is done with the computational cost $O(ND^5)$. Since there are Nb^2 of these where b is the number of branches, we obtain the overall cost $O(N^2 b^2 D^5)$. Usually we compute enough branches such that $b^2 > D$ holds, thus the cost for this procedure ends up being higher than the one for the diagonalization of H'_{HB}. The second drawback is that the superpositions $U(k')_{ij} \, |\psi'_j(k')\rangle$ mix the original approximations of the energy levels thereby slightly lowering the energy of higher excitations but increasing the energy of lower excitations, which are usually the ones we are most interested in.

The *second* way to approximate the eigenstates of the original Hamiltonian H_{HB} such that they are at the same time exact momentum eigenstates is to add to H'_{HB} a perturbation that splits degenerated levels with different parity. This is easily achieved by taking $H^{\pm}_{HB} :=$

$H'_{HB} \pm \lambda P_y$ where λ must be chosen such that it is big enough for our algorithm to deliver only states with a single parity, but as small as possible in order to avoid numerical inaccuracies caused by altering the Hamiltonian. In the case of the Heisenberg model, if we choose to compute $b = 10$ branches, $\lambda = 0.1 \cdot N$ fulfills these requirements. In practice we first apply our algorithm to H^{-}_{HB} which yields for each momentum k' b states with positive parity. These states do not change their momentum under the transformation (4.15). Subsequently we apply the algorithm to H^{+}_{HB} which yields states with negative parity that change their momentum after the transformation according to $k = k' \oplus_N N/2$. In this way we end up with $2b$ branches of states that approximate the spectrum of H_{HB} and that are at the same time exact momentum eigenstates. The computational cost per state is thus exactly the same like diagonalizing only H'_{HB}.

Let us first look at the results we have obtained for a small chain with 16 sites. We have chosen to look at such a small system first for two reasons: *First*, even though the Heisenberg model is exactly solvable via Bethe ansatz, obtaining *all* energy levels can be quite involved. Choosing N as small as 16 allows us to compute the spectrum of this small chain by means of exact diagonalization. *Second*, even for the energy levels that are easily computable with the Bethe ansatz (i.e., the triplet states in the subspace of two-spinon excitations [71]) it is not possible to obtain the eigenstates themselves. Exact diagonalization of a small chain on the other hand allows us to compute and store the exact eigenstates in order to check the fidelity of our MPS approximation.

Fig. 4.9 shows the energy of the first ten branches of excitations and the corresponding relative precision. Note how states belonging to the same multiplet have very similar precision even though they have different parity and thus correspond to eigenstates of H'_{HB} with different momentum. Since there are no one-particle excitations in the low-energy spectrum of the AF Heisenberg model, we do not obtain such a good precision like in the case of the quantum Ising model. Nevertheless we get a very good approximation of the first excited level, namely the triplet excitation at $k = N/2$. We have also tested the accuracy of the states themselves: for non-degenerated states, the absolute value of the overlap is a perfect measure for this, and for reasons that will become clear immediately, we have looked at the sine of the fidelity. For degenerated states, in order to compare the subspace spanned by our MPS to the one spanned by the exact eigenstates, we have used as a measure for the distance the definition given in chapter 7 of [75]: the sine of the largest canonical angle between the two subspaces. The canonical angles can be easily computed from the matrix that has as its entries the overlaps between all states of the subspaces that we want to compare. The results are plotted in Fig. 4.10. We see that only the MPS with momentum $k = 0$ and $k = N/2$ are extremely accurate. All other states, especially those around $k = N/4$, are much further away from the exact solutions, which is a bit surprising given the fact that the energy precision for these states is comparable to the one obtained for $k = 0$.

The spectrum that we obtain for longer chains is plotted in Fig. 4.11. In this regime we have only looked at the precision of the lowest two-spinon triplet for which the exact results were obtained following [71]. Again we see that the states at momentum $k = k_0 \oplus N/2$ have the best accuracy. We would like to make two more remarks concerning the chain with $N = 50$. First, note that the ground state has momentum $k_0 = N/2$ in this case. Second, unlike in the case of $N = 100$, where for all momenta $k \neq k_0$ the lowest excitation is a triplet, we observe that for $N = 50$ this does not happen. Our simulations reveal that at $k \in \{2, 3, 47, 48\}$ the quintuplet excitation lies below the triplet while at $k \in \{23, 27\}$ it is a singlet that is the lowest lying excitation.

Let us conclude this section by comparing the performance of our algorithm to other methods from literature when applied to the Heisenberg spin-$1/2$ chain. The only published result for excitations of this model that we are aware of is given in [69]. There the authors simulate a chain with $N = 512$ sites and claim to have reached a precision of 1% when compared to the exact solution. We have applied our algorithm to a chain with $N = 500$ sites using the bond dimension $D = 20$. For the low energy states at $k = 0$ respectively $k = \pi$ we obtain an absolute precision of $\approx 1 \cdot 10^{-5}$ which is by three orders of magnitude better than the result reported in [69]. For high energy states with $k \approx 2\pi/3$ the absolute precision is around $\approx 1 \cdot 10^{-4}$ which is still two orders of magnitude better the one from [69].

4.4.3 Bilinear-Biquadratic spin-1 chain

We will finish our numerical analysis with results obtained for two very special points in the phase diagram of the bilinear-biquadratic spin-1 model. This is the most general $SU(2)$ invariant three-state model with nearest-neighbor interaction. The PBC Hamiltonian reads

$$H_{BB} = \sum_{i=1}^{N} \cos\theta \cdot \vec{S}_i \vec{S}_{i+1} + \sin\theta \cdot (\vec{S}_i \vec{S}_{i+1})^2 \tag{4.17}$$

where S_i^α are the spin-1 operators acting on site i. In the past decades there has been a considerable amount of numerical and analytical work on H_{BB} which has led to some of the most exciting results (e.g. [4, 5]) obtained in the field of spin systems. Even though nowadays there is broad consensus on almost the entire phase diagram of this model, there are still some regions thereof that are not fully explored yet. We will not attempt to clarify any of the open questions here, but rather illustrate that ansatz (4.1) is well suited as a numerical tool to study the excitation spectrum of H_{BB} in cases where no analytical solution is available. To this end we will look at two very special points, namely $\theta = 0$ and $\theta = -\pi/2$.

Bilinear chain $\theta = 0$

The Hamiltonian of the bilinear chain (also known as antiferromagnetic Heisenberg spin-1 model) reads

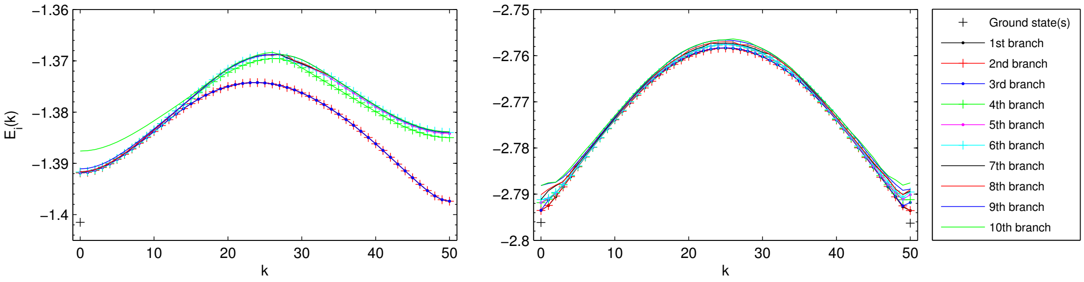

Figure 4.12: (Color online). Results for the low excitation spectrum for two selected configurations of the Bilinear-Biquadratic spin-1 chain with $N = 100$ sites. Left: $\theta = 0$, i.e. Bilinear chain. Right: $\theta = -\pi/2$, i.e. Biquadratic chain. Note that here we have given the dispersion relation only in the interval $k \in [0, \pi]$ for better clarity of the plots.

$$H_{BL} = \sum_{i=1}^{N} \vec{S}_i \vec{S}_{i+1} \quad . \tag{4.18}$$

There exist extensive numerical studies on H_{BL} in the literature [48, 3, 76, 69]. The lowest 10 branches of the dispersion relation obtained with our algorithm for a PBC chain with $N = 100$ sites are presented in the left plot of Fig. 4.12. Our result for the Haldane gap reads $\Delta_{100} = 0.41047276$ which is in good agreement with the most precise results obtained until now for PBC chains in [76], namely $\Delta_{400} = 0.41047925$. There the authors use DMRG with bond dimension $D = 500$ in order to simulate a chain with $N = 400$ sites. Unfortunately the current implementation of our PBC algorithm cannot deal with bond dimensions large enough to achieve the precision of [76] for such long chains. However the generalization of our method to infinite OBC chains [70] delivers as far as we know the most precise approximation that can be found in literature for the Haldane gap in the thermodynamic limit.

Biquadratic chain $\theta = -\pi/2$

The Hamiltonian of the biquadratic chain with PBC reads

$$H_{BQ} = -\sum_{i=1}^{N} (\vec{S}_i \vec{S}_{i+1})^2 \tag{4.19}$$

and can be solved analytically via mapping to the spin-$1/2$ XXZ model with twisted boundary conditions and subsequent Bethe Ansatz [72]. The lowest 10 branches of the dispersion relation obtained with our algorithm for a PBC chain with $N = 100$ sites are presented in the right plot of Fig. 4.12. Note that the ground state of this model is degenerated in the thermodynamic limit. Finite geometry however induces a gap that closes exponentially with increasing N. A comparison of our numerical results with the analytical values from [72] yields relative precisions of $\Delta_{rel}E_0 \approx 2.29 \cdot 10^{-4}$, $\Delta_{rel}E_1 \approx 2.31 \cdot 10^{-4}$ and $\Delta_{rel}E_2 \approx 2.55 \cdot 10^{-4}$ for the lowest energy states. These values are one order of magnitude better than the results previously obtained in [68].

4.5 Conclusions and Outlook

Inspired by previous approaches [3, 68] we have introduced a method for the simulation of translationally invariant spin chains with periodic boundary conditions. We have used an MPS based ansatz that corresponds to a particle-like excitation with well defined momentum in order to obtain extremely accurate results for models where the spectrum contains precisely one-particle states. For states that can be expressed in terms of many quasi-particle excitations, we still obtain useful results if the MPS bond dimension is chosen to be big enough. In the case of the quantum Ising model, our results indicate that for $g < 1$ the spectrum is built up entirely out of excitations with an even number of quasi-particles.

Generalizations of our approach can go in two directions: First, it is possible to adjust ansatz (4.1) in order to treat infinite systems with open boundary condition, which we are addressing in [70]. Second, it seems feasible to generalize our approach to a many-particle ansatz by using more than one MPS tensor in (4.1) in order to define the variational manifold.

Conclusions and Outlook

In conclusion, we have presented several novel MPS based algorithms for the simulation of translationally invariant systems in one spatial dimension. During the development of these algorithms our main emphasis was on improving both the precision of the approximations and the scaling of the computational cost as compared to previously known methods. We believe we can safely claim to have achieved this goals as we have shown in the main text. Furthermore, during our investigations of the applicability of these new algorithms, we have learned important lessons about general properties and restrictions of MPS simulations.

In chapter 1 we have introduced a new method for expressing time evolution operators as real and symmetric translationally invariant Matrix Product Operators and then used these MPO in order to approximate ground states of infinite chains as translationally invariant MPS. The thusly obtained ground state MPS are crucial for the following chapters, as they must be used as a starting point for the gradient descent algorithm in chapter 2, which itself is the starting point for the investigations in chapter 3 and chapter 4. The methods for constructing the MPO can furthermore be applied to many other models both in one or more spatial dimensions.

In chapter 2 we have introduced a gradient-based algorithm for the simulation of translationally invariant chains with PBC which seemingly achieves unprecedented precision for the ground states of the studied models. Apart from the pure algorithmic aspects, we show in this chapter that the computational cost for simulating critical models must contain a previously unnoticed factor if one wants to faithfully reproduce long-range correlations. As a generalization and further development of the results of this chapter we can highlight the so-called Time-Dependent Variational Principle [67] which represents a gradient-descent in the full Hilbert space, as opposed to the gradient descent in parameter space.

In chapter 3 we have used the methods of chapter 2 for an extensive study of critical chains with PBC. Our investigations then led to the introduction of two different regimes for MPS simulations of critical PBC chains: the *Finite Size Scaling* and the *Finite Entanglement Scaling* regime. We have observed that in order to faithfully reproduce expectation values of global operators, one must ensure that the MPS simulations stay within the FSS regime. The lessons learned in this context have the potential to be very useful in the future whenever MPS are used for the scaling analysis of unknown systems. Furthermore they might also be useful in the context of MPS-related investigations such as cMPS for continuous 1D systems [14] or higher dimensional systems when treated within the corresponding framework of MPS generalizations (e.g. PEPS [12]).

In chapter 4 we have introduced a MPS-based ansatz for momentum eigenstates that uses the ground state MPS obtained in chapter 2 as its backbone. We then applied this ansatz in order to obtain a big part of the excitation spectrum of several one-dimensional models with unprecedented precision. The numerical results also helped to draw some conclusions about an ambiguity that emerges during the exact diagonalization of the Quantum Ising model with PBC[1] . One generalization of the results of this chapter for infinite systems with OBC has already been presented in [70]. Further possible generalizations would be for instance similar approaches for many-particle excitations as well as applying these ideas in the new field of cMPS [14].

---

[1] More details about this ambiguity can be found in Appendix A.

Bibliography

[1] K.G. Wilson. The renormalization group: Critical phenomena and the kondo problem. *Reviews of Modern Physics*, 47(4):773, 1975.

[2] Steven R. White. Density matrix formulation for quantum renormalization groups. *Phys. Rev. Lett.*, 69(19):2863–2866, Nov 1992.

[3] Stellan Östlund and Stefan Rommer. Thermodynamic limit of density matrix renormalization. *Phys. Rev. Lett.*, 75(19):3537–3540, Nov 1995.

[4] Ian Affleck, Tom Kennedy, Elliott H. Lieb, and Hal Tasaki. Rigorous results on valence-bond ground states in antiferromagnets. *Phys. Rev. Lett.*, 59(7):799–802, Aug 1987.

[5] Ian Affleck, Tom Kennedy, Elliott H. Lieb, and Hal Tasaki. Valence bond ground states in isotropic quantum antiferromagnets. *Communications in Mathematical Physics*, 115:477–528, 1988. 10.1007/BF01218021.

[6] M. Fannes, B. Nachtergaele, and R. Werner. Finitely correlated states on quantum spin chains. *Communications in Mathematical Physics*, 144:443–490, 1992. 10.1007/BF02099178.

[7] A. Klümper, A. Schadschneider, and J. Zittartz. Matrix product ground states for one-dimensional spin-1 quantum antiferromagnets. *EPL (Europhysics Letters)*, 24(4):293, 1993.

[8] Tobias J. Osborne and Michael A. Nielsen. Entanglement in a simple quantum phase transition. *Phys. Rev. A*, 66:032110, Sep 2002.

[9] G. Vidal, J. I. Latorre, E. Rico, and A. Kitaev. Entanglement in quantum critical phenomena. *Phys. Rev. Lett.*, 90(22):227902, Jun 2003.

[10] Guifré Vidal. Efficient classical simulation of slightly entangled quantum computations. *Phys. Rev. Lett.*, 91:147902, Oct 2003.

[11] Frank Verstraete, Diego Porras, and Juan I. Cirac. Density matrix renormalization group and periodic boundary conditions: A quantum information perspective. *Phys. Rev. Lett.*, 93(22):227205, Nov 2004.

[12] Frank Verstraete and Juan I. Cirac. Renormalization algorithms for Quantum-Many Boday Systems in two and higher dimensions. *arXiv:cond-mat/0407066*, 2004.

[13] G. Vidal. Class of quantum many-body states that can be efficiently simulated. *Physical Review Letters*, 101(11):110501, 2008.

[14] F. Verstraete and J.I. Cirac. Continuous matrix product states for quantum fields. *Physical Review Letters*, 104(19):190405, 2010.

[15] Peter Pippan, Steven R. White, and Hans Gerd Evertz. Efficient matrix-product state method for periodic boundary conditions. *Phys. Rev. B*, 81(8):081103, Feb 2010.

[16] Frank Pollmann, Subroto Mukerjee, Ari M. Turner, and Joel E. Moore. Theory of finite-entanglement scaling at one-dimensional quantum critical points. *Phys. Rev. Lett.*, 102(25):255701, Jun 2009.

[17] Qian-Qian Shi and Huan-Qiang Zhou. An efficient algorithm for translationally invariant finite-size periodic lattice systems in one spatial dimension. *Journal of Physics A: Mathematical and Theoretical*, 42(27):272002, 2009.

[18] Elliott Lieb, Theodore Schultz, and Daniel Mattis. Two soluble models of an antiferromagnetic chain. *Annals of Physics*, 16(3):407 – 466, Dec 1961.

[19] U. Schollwöck. The density-matrix renormalization group. *Rev. Mod. Phys.*, 77:259–315, Apr 2005.

[20] A. J. Daley, C. Kollath, U. Schollwöck, and G. Vidal. Time-dependent density-matrix renormalization-group using adaptive effective hilbert spaces. *Journal of Statistical Mechanics: Theory and Experiment*, 2004(04):P04005, 2004.

[21] Steven R. White and Adrian E. Feiguin. Real-time evolution using the density matrix renormalization group. *Phys. Rev. Lett.*, 93:076401, Aug 2004.

[22] F. Verstraete, J. J. García-Ripoll, and J. I. Cirac. Matrix product density operators: Simulation of finite-temperature and dissipative systems. *Phys. Rev. Lett.*, 93:207204, Nov 2004.

[23] Michael Zwolak and Guifré Vidal. Mixed-state dynamics in one-dimensional quantum lattice systems: A time-dependent superoperator renormalization algorithm. *Phys. Rev. Lett.*, 93:207205, Nov 2004.

[24] F. Verstraete, M. M. Wolf, D. Perez-Garcia, and J. I. Cirac. Criticality, the area law, and the computational power of projected entangled pair states. *Phys. Rev. Lett.*, 96:220601, Jun 2006.

[25] Gregory M. Crosswhite and Dave Bacon. Finite automata for caching in matrix product algorithms. *Phys. Rev. A*, 78:012356, Jul 2008.

[26] Ian P. McCulloch. From density-matrix renormalization group to matrix product states. *Journal of Statistical Mechanics: Theory and Experiment*, 2007(10):P10014, 2007.

[27] Gregory M. Crosswhite, A. C. Doherty, and Guifré Vidal. Applying matrix product operators to model systems with long-range interactions. *Phys. Rev. B*, 78:035116, Jul 2008.

[28] B. Pirvu, F. Verstraete, and G. Vidal. Exploiting translational invariance in matrix product state simulations of spin chains with periodic boundary conditions. *Phys. Rev. B*, 83(12):125104, Mar 2011.

[29] B. Pirvu, G. Vidal, F. Verstraete, and L. Tagliacozzo. Matrix product states for critical spin chains: Finite-size versus finite-entanglement scaling. *Phys. Rev. B*, 86:075117, Aug 2012.

[30] Guifré Vidal. Classical simulation of infinite-size quantum lattice systems in one spatial dimension. *Phys. Rev. Lett.*, 98(7):070201, Feb 2007.

[31] F. Verstraete, J. I. Cirac, J. I. Latorre, E. Rico, and M. M. Wolf. Renormalization-group transformations on quantum states. *Phys. Rev. Lett.*, 94:140601, Apr 2005.

[32] F. Fröwis, V. Nebendahl, and W. Dür. Tensor operators: Constructions and applications for long-range interaction systems. *Phys. Rev. A*, 81:062337, Jun 2010.

[33] David E. Evans and Raphael Hoegh-Krohn. Spectral properties of positive maps on c*-algebras. *Journal of the London Mathematical Society*, s2-17(2):345–355, 1978.

[34] Roger A. Horn and Charles R. Johnson. *Matrix Analysis*. Cambridge University Press, 2006.

[35] Stefan Rommer and Stellan Östlund. Class of ansatz wave functions for one-dimensional spin systems and their relation to the density matrix renormalization group. *Phys. Rev. B*, 55(4):2164–2181, Jan 1997.

[36] B. Pirvu, V. Murg, J. I. Cirac, and F. Verstraete. Matrix product operator representations. *New J. Phys.*, 12(2):025012, 2010.

[37] Guifré Vidal. Efficient simulation of one-dimensional quantum many-body systems. *Phys. Rev. Lett.*, 93(4):040502, Jul 2004.

[38] Frank Verstraete, Valentin Murg, and Juan I. Cirac. Matrix product states, projected entangled pair states, and variational renormalization group methods for quantum spin systems. *Advances in Physics*, 57(2):143, 2008.

[39] A. W. Sandvik and G. Vidal. Variational quantum monte carlo simulations with tensor-network states. *Phys. Rev. Lett.*, 99(22):220602, Nov 2007.

[40] John Cardy. *Scaling and renormalization in statistical physics*. Cambridge University Press, 1996.

[41] Tomotoshi Nishino and Kouichi Okunishi. Product wave function renormalization group. *Journal of the Physical Society of Japan*, 64(11):4084–4087, 1995.

[42] Ian P. McCulloch. Infinite size density matrix renormalization group, revisited. *arXiv:0804.2509*, Apr 2008.

[43] R. Orús and G. Vidal. Infinite time-evolving block decimation algorithm beyond unitary evolution. *Phys. Rev. B*, 78(15):155117, Oct 2008.

[44] T. Nishino, K. Okunishi, and M. Kikuchi. Numerical renormalization group at criticality. *Physics Letters A*, 213(1-2):69 – 72, 1996.

[45] Martin Andersson, Magnus Boman, and Stellan Östlund. Density-matrix renormalization group for a gapless system of free fermions. *Phys. Rev. B*, 59(16):10493–10503, Apr 1999.

[46] L. Tagliacozzo, Thiago R. de Oliveira, S. Iblisdir, and J. I. Latorre. Scaling of entanglement support for matrix product states. *Phys. Rev. B*, 78(2):024410, 2008.

[47] W. H. Press, S. A. Teukolsky, W. T. Vetterling, and Brian P. Flannery. *Numerical Recipes: The Art of Scientific Computing*. Cambridge University Press, 2007.

[48] Steven R. White and David A. Huse. Numerical renormalization-group study of low-lying eigenstates of the antiferromagnetic s=1 heisenberg chain. *Phys. Rev. B*, 48(6):3844–3852, Aug 1993.

[49] B. Pirvu, J. Haegeman, and F. Verstraete. Matrix product state based algorithm for determining dispersion relations of quantum spin chains with periodic boundary conditions. *Phys. Rev. B*, 85:035130, Jan 2012.

[50] F. Verstraete, V. Murg, and J.I. Cirac. Matrix product states, projected entangled pair states, and variational renormalization group methods for quantum spin systems. *Advances in Physics*, 57(2):143–224, 2008.

[51] U. Schollwöck. The density-matrix renormalization group in the age of matrix product states. *Annals of Physics*, 326(1):96 – 192, 2011.

[52] M. N. Barber. *Phase Transitions and Critical Phenomena edited by C. Domb and J. L. Lebowitz Vol. 8.* Academic, New York, 1983.

[53] Hiroshi Ueda and Tomotoshi Nishino. Hyperbolic deformation on quantum lattice hamiltonians. *Journal of the Physical Society of Japan*, 78:014001, 2009.

[54] H. W. J. Blöte, John L. Cardy, and M. P. Nightingale. Conformal invariance, the central charge, and universal finite-size amplitudes at criticality. *Phys. Rev. Lett.*, 56(7):742–745, Feb 1986.

[55] D. Zheng, G.H. Zhang, T. Xiang, and D.H. Lee. Continuous quantum phase transition between two topologically distinct valence bond solid states associated with the same spin value. *Physical Review B*, 83(1):014409, January 2011.

[56] K. Rodriguez, A. Arguelles, A. K. Kolezhuk, L. Santos, and T. Vekua. Field-Induced phase transitions of repulsive spin-1 bosons in optical lattices. *Physical Review Letters*, 106(10):105302, March 2011.

[57] Yan-Wei Dai, Bing-Quan Hu, Jian-Hui Zhao, and Huan-Qiang Zhou. Ground-state fidelity and entanglement entropy for the quantum three-state potts model in one spatial dimension. *Journal of Physics A: Mathematical and Theoretical*, 43(37):372001, September 2010.

[58] Roman Orus and Tzu-Chieh Wei. Geometric entanglement of one-dimensional systems: bounds and scalings in the thermodynamic limit. *arXiv:1006.5584*, June 2010.

[59] F. Heidrich-Meisner, I. P. McCulloch, and A. K. Kolezhuk. Phase diagram of an anisotropic frustrated ferromagnetic spin-1/2 chain in a magnetic field: A density matrix renormalization group study. *Physical Review B*, 80(14):144417, October 2009.

[60] J.H. Zhao, H.L. Wang, B. Li, and H.Q. Zhou. Spontaneous symmetry breaking and bifurcations in ground-state fidelity for quantum lattice systems. *Physical Review E*, 82(6):061127, December 2010.

[61] Davide Rossini, Vittorio Giovannetti, and Rosario Fazio. Stiffness in 1d matrix product states with periodic boundary conditions. *Journal of Statistical Mechanics: Theory and Experiment*, 2011(05):P05021, 2011.

[62] John L. Cardy. Operator content of two-dimensional conformally invariant theories. *Nuclear Physics B*, 270:186–204, 1986.

[63] Chen Liu, Ling Wang, Anders W. Sandvik, Yu-Cheng Su, and Ying-Jer Kao. Symmetry breaking and criticality in tensor-product states. *Phys. Rev. B*, 82:060410, Aug 2010.

[64] G. Evenbly, R. N. C. Pfeifer, V. Picó, S. Iblisdir, L. Tagliacozzo, I. P. McCulloch, and G. Vidal. Boundary quantum critical phenomena with entanglement renormalization. *Phys. Rev. B*, 82:161107, Oct 2010.

[65] I. Affleck. Universal term in the free energy at a critical point and the conformal anomaly. *Phys. Rev. Lett.*, 56:746–748, Feb 1986.

[66] Pasquale Calabrese and Alexandre Lefevre. Entanglement spectrum in one-dimensional systems. *Phys. Rev. A*, 78:032329, Sep 2008.

[67] Jutho Haegeman, J. Ignacio Cirac, Tobias J. Osborne, Iztok Pizorn, Henri Verschelde, and Frank Verstraete. Time-dependent variational principle for quantum lattices. *Phys. Rev. Lett.*, 107:070601, Aug 2011.

[68] D. Porras, F. Verstraete, and J. I. Cirac. Renormalization algorithm for the calculation of spectra of interacting quantum systems. *Phys. Rev. B*, 73(1):014410, Jan 2006.

[69] Sung Gong Chung and Lihua Wang. Entanglement perturbation theory for the elementary excitation in one dimension. *Physics Letters A*, 373(26):2277 – 2280, 2009.

[70] J. Haegeman, B. Pirvu, D. J. Weir, J. I. Cirac, T. J. Osborne, H. Verschelde, and F. Verstraete. Variational matrix product ansatz for dispersion relations. *Phys. Rev. B*, 85:100408, Mar 2012.

[71] Michael Karbach, Kun Hu, and Müller Gerhard. Introduction to the bethe ansatz ii. *Comp. in Phys.*, 12:565, 1998.

[72] E. S. Sørensen and A. P. Young. Correlation length of the biquadratic spin-1 chain. *Phys. Rev. B*, 42:754–759, Jul 1990.

[73] Pierre Pfeuty. The one-dimensional ising model with a transverse field. *Annals of Physics*, 57(1):79 – 90, 1970.

[74] Iztok Pizorn and Frank Verstraete. Variational numerical renormalization group: Bridging the gap between nrg and density matrix renormalization group. *arXiv:1102.1401*, 2011.

[75] Rajendra Bhatia. *Matrix analysis*. Springer-Verlag, 1997.

[76] S. R. White and I. Affleck. Spectral function for the $s = 1$ heisenberg antiferromagetic chain. *Phys. Rev. B*, 77:134437, Apr 2008.

[77] P. Jordan and E. Wigner. über das paulische äquivalenzverbot. *Z. Physik*, 47(9-10):631 – 651, 1928.

[78] C.W. Gear. A simple set of test matrices for eigenvalue programs. *Math. Comp.*, 23(105):119–125, Jan 1969.

Appendix A

Analytical solution of the Quantum Ising model with PBC

The Quantum Ising Hamiltonian used throughout the main text reads

$$H_{IS} = -\sum_{i=1}^{N} Z_i Z_{i+1} - g \sum_{i=1}^{N} X_i \ , \tag{A.1}$$

where again $X := \sigma^x$, $Y := \sigma^y$ $Z := \sigma^z$ denote the Pauli spin-1/2 matrices. The periodic boundary conditions are as usually realized by identifying site $N+1$ with site 1. Note that H_{IS} has a $\mathbb{Z}_2$-symmetry generated by

$$S = \prod_{i=1}^{N} X_i \ , \tag{A.2}$$

i.e. $[H_{IS}, S] = 0$. This can be easily seen due to the special properties of the Pauli spin-1/2 matrices: we have $S^\dagger H_{IS} S = H_{IS}$ due to $XZX = -Z$ and $XXX = X$.

It turns out to be much easier to continue in the basis obtained by applying a Hadamard gate to each site, i.e.

$$H'_{IS} = \left[\bigotimes_{i=1}^{N} G_i\right] \cdot H_{IS} \cdot \left[\bigotimes_{i=1}^{N} G_i\right] \ , \tag{A.3}$$

where G reads

$$G = \frac{1}{\sqrt{2}} \begin{pmatrix} 1 & 1 \\ 1 & -1 \end{pmatrix} \ . \tag{A.4}$$

Due to the identities

$$\begin{aligned} GXG &= Z \\ GZG &= X \\ GYG &= -Y \end{aligned} \tag{A.5}$$

we get

$$H'_{IS} = -\sum_{i=1}^{N} X_i X_{i+1} - g \sum_{i=1}^{N} Z_i \ . \tag{A.6}$$

Of course the generator of the $\mathbb{Z}_2$-symmetry for H'_{IS} reads $S' = \prod_i Z_i$. Since for the rest of this appendix we will treat only the Hamiltonian (A.6) we will use in the following the shorter notation $\mathcal{H} := H'_{IS}$.

For the diagonalization of $\mathcal{H}$ we will follow closely the procedure described by Lieb, Schultz and Mattis in their seminal paper from 1961 [18]. Even though in that work the authors treat the XY model, their approach can be used almost identically for the Quantum Ising model. The only significant difference appears when one performs the Bogoliubov transformation: it turns out that in a certain region of the phase diagram of the Quantum Ising model, *the parity operator flips its sign under the Bogoliubov transformation*, a behavior that does not occur for the XY model.

A.1 Jordan-Wigner transformation

The first step towards the diagonalization of $\mathcal{H}$ is the intuition that there must exist a simple mapping between the Hilbert space of a system with a spin-1/2 degree of freedom per site and that of spinless fermions hopping between sites with single orbitals. This intuition is due to the similarity between the spin raising and lowering operators and the fermion creation and annihilation operators acting on a single site. The straightforward definition

$$\begin{aligned} a_i &:= \sigma_i^- = \frac{1}{2}(X_i - iY_i) \\ a_i^\dagger &:= \sigma_i^+ = \frac{1}{2}(X_i + iY_i) \end{aligned} \tag{A.7}$$

yields for the Pauli matrices

$$\begin{aligned} X_i &= a_i^\dagger + a_i \\ Y_i &= (-i) \cdot [a_i^\dagger - a_i] \\ Z_i &= 2a_i^\dagger a_i - 1 \ . \end{aligned} \tag{A.8}$$

Then the Hamiltonian (A.6) reads

$$\mathcal{H} = -\sum_{i=1}^{N}(a_i^\dagger a_{i+1}^\dagger + a_i^\dagger a_{i+1} + a_i a_{i+1}^\dagger + a_i a_{i+1} + g \cdot 2a_i^\dagger a_i - g) \ . \tag{A.9}$$

The commutation relations between the new operators partially resemble fermionic anticommutation relations

$$\{a_i, a_i^\dagger\} = \mathbb{1},\ \ a_i^2 = (a_i^\dagger)^2 = 0 \tag{A.10}$$

and partially resemble bosonic commutation relations

$$[a_i^\dagger, a_j] = [a_i^\dagger, a_j^\dagger] = [a_i, a_j] = 0, \quad i \neq j. \tag{A.11}$$

However note that the operators (A.7) are not proper fermionic operators since $\{a_i, a_j^\dagger\} \neq 0$ for $i \neq j$. In order to obtain the correct anticommutation relations for $i \neq j$ we must use following non-local transformation which was first introduced by Jordan and Wigner in [77] in 1928

$$\begin{aligned} c_i &= \exp\Big[i\pi \sum_{j=1}^{i-1} a_j^\dagger a_j\Big] \cdot a_i \\ c_i^\dagger &= a_i^\dagger \cdot \exp\Big[- i\pi \sum_{j=1}^{i-1} a_j^\dagger a_j\Big] \end{aligned} \tag{A.12}$$

where the a_i and $a_i^\dagger$ are defined as in (A.7). It is straightforward to show that the operators c_i and $c_i^\dagger$ satisfy now the canonical fermionic anticommutation relations properly

$$\{c_i, c_j^\dagger\} = \delta_{ij} \cdot \mathbb{1},\ \ \{c_i, c_j\} = \{c_i^\dagger, c_j^\dagger\} = 0 \ . \tag{A.13}$$

We will call in the following the modes created and annihilated by c_i and $c_i^\dagger$ *Jordan-Wigner fermions*. With the inverse transformation

$$\begin{aligned} a_i &= \exp\Big[- i\pi \sum_{j=1}^{i-1} c_j^\dagger c_j\Big] \cdot c_i \\ a_i^\dagger &= c_i^\dagger \cdot \exp\Big[i\pi \sum_{j=1}^{i-1} c_j^\dagger c_j\Big] \end{aligned} \tag{A.14}$$

one can express all terms in the Hamiltonian (A.9) in terms of Jordan-Winger fermions. For the terms with $i \leq N-1$ we get similarly looking expressions up to a sign

$$\begin{aligned} a_i^\dagger a_{i+1}^\dagger &= \ \ c_i^\dagger c_{i+1}^\dagger \\ a_i^\dagger a_{i+1} &= \ \ c_i^\dagger c_{i+1} \\ a_i a_{i+1}^\dagger &= -c_i c_{i+1}^\dagger \\ a_i a_{i+1} &= -c_i c_{i+1} \ . \end{aligned} \tag{A.15}$$

The interaction terms that connect the last to the first site read

$$\begin{aligned} a_N^\dagger a_1^\dagger &= -c_N^\dagger c_1^\dagger \cdot \exp(i\pi\mathcal{N}) \\ a_N^\dagger a_1 &= -c_N^\dagger c_1 \cdot \exp(i\pi\mathcal{N}) \\ a_N a_1^\dagger &= \quad c_N c_1^\dagger \cdot \exp(i\pi\mathcal{N}) \\ a_N a_1 &= \quad c_N c_1 \cdot \exp(i\pi\mathcal{N}) \ . \end{aligned} \tag{A.16}$$

where $\mathcal{N}$ denotes the global number operator for Jordan-Wigner fermions

$$\mathcal{N} = \sum_{i=1}^{N} c_i^\dagger c_i \ . \tag{A.17}$$

Note that in order to derive the above relations we have used following useful identities

$$\begin{aligned} \exp(i\pi\mathcal{N}_j) &= \exp(-i\pi\mathcal{N}_j) \\ c_j^\dagger &= c_j^\dagger \cdot \exp(\pm i\pi\mathcal{N}_j) \\ c_j &= \exp(\pm i\pi\mathcal{N}_j) \cdot c_j \ . \end{aligned} \tag{A.18}$$

where $\mathcal{N}_j = c_j^\dagger c_j = a_j^\dagger a_j$ denotes the local number operator for Jordan-Wigner fermions at site j. This allows us to reformulate the Hamiltonian (A.9) as

$$\begin{aligned} \mathcal{H} = gN \cdot \mathbb{1} - 2g \sum_{i=1}^{N} c_i^\dagger c_i - \sum_{i=1}^{N} (c_i^\dagger c_{i+1}^\dagger + c_i^\dagger c_{i+1} - c_i c_{i+1}^\dagger - c_i c_{i+1}) \\ - (-c_N^\dagger c_1^\dagger - c_N^\dagger c_1 + c_N c_1^\dagger + c_N c_1) \cdot (e^{i\pi\mathcal{N}} + \mathbb{1}) \ . \end{aligned} \tag{A.19}$$

The Hamiltonian (A.19) is a quadratic expression in Fermi operators which turns out to be digonalizable by means of a so-called Bogoliubov transformation which we explain in detail in the next chapter.

A.2 Bogoliubov transformation - Diagonalization of a general quadratic form in Fermi operators

This chapter is a brief overview of the method presented in Appendix A of [18]. We give this overview for consistency reasons in order to enable the reader to understand Section A.3 without having to go to the original reference.

Consider the following Hermitian operator

$$H = \sum_{i,j} [c_i^\dagger A_{ij} c_j + \frac{1}{2}(c_i^\dagger B_{ij} c_j^\dagger + c_j B_{ij} c_i)] \ . \tag{A.20}$$

which is a pure quadratic expression in Fermi operators. Since we want H to be Hermitian, due to the anticommutation rules of the fermionic operators c_i, we can derive following necessary properties of the coefficient matrices

$$\begin{aligned} A &= A^\dagger \\ B &= -B^T \ . \end{aligned} \tag{A.21}$$

In the following we will consider only cases where A and B are real, thus the first condition becomes $A = A^T$. We will now try to find a linear transformation of the form

$$\begin{aligned} \eta_k &= \sum_i (g_{ki} c_i + h_{ki} c_i^\dagger) \\ \eta_k^\dagger &= \sum_i (g_{ki} c_i^\dagger + h_{ki} c_i) \end{aligned} \tag{A.22}$$

with real g_{ki} and h_{ki}, which is canonical (i.e. the new operators η_k and $\eta_k^\dagger$ fulfill fermionic anticommutation rules) and which diagonalizes the original operator such that

$$H = \sum_k \Lambda_k \eta_k^\dagger \eta_k + \text{const.} \ . \tag{A.23}$$

It is an easy exercise to show that the requirement of a canonical transformation leads to a set of necessary and sufficient conditions for the transformation coefficients. More explicitly, $\{\eta_i, \eta_j^\dagger\} = \delta_{ij} \cdot \mathbb{1}$ leads to

$$GG^T + HH^T = \mathbb{1} \tag{A.24}$$

while $\{\eta_i, \eta_j\} = 0$ leads to

$$GH^T + HG^T = 0 \ , \tag{A.25}$$

where G and H are the matrices of coefficients $\{g_{ij}\}$ respectively $\{h_{ij}\}$. For the moment we will not need these conditions as it is enough to simply assume that there exists a valid canonical transformation that diagonalizes H. This assumption together with the properties (A.21) turns out to automatically yield a transformation which fulfills (A.24) and (A.25). To this end we first compute the commutator $[\eta_k, H]$ assuming that the η_k are indeed fermionic modes that diagonalize H according to (A.23)

$$[\eta_k, H] = \Lambda_k \eta_k \ . \tag{A.26}$$

Plugging (A.20) and (A.22) into (A.26) yields after a tedious but straightforward calculation the following equations for the g_{ij} and h_{ij}

$$\begin{aligned} \Lambda_k g_{kj} &= \sum_i (g_{ki}A_{ij} - h_{ki}B_{ij}) \\ \Lambda_k h_{kj} &= \sum_i (g_{ki}B_{ij} - h_{ki}A_{ij}) \ . \end{aligned} \tag{A.27}$$

Adding and subtracting equations (A.27) yields the following set of coupled equations

$$\begin{aligned} \Lambda_k \phi_{kj} &= \sum_i \psi_{ki}(A_{ij} + B_{ij}) \\ \Lambda_k \psi_{kj} &= \sum_i \phi_{ki}(A_{ij} - B_{ij}) \ , \end{aligned} \tag{A.28}$$

where we have used

$$\begin{aligned} \phi_{kj} &= g_{ki} + h_{ki} \\ \psi_{kj} &= g_{ki} - h_{ki} \ . \end{aligned} \tag{A.29}$$

Expressing the coefficients ϕ_{kj} and ψ_{kj} as row vectors $\vec{\phi}_k$ and $\vec{\psi}_k$ yields

$$\begin{aligned} \Lambda_k \vec{\phi}_k &= \vec{\psi}_k(A + B) \\ \Lambda_k \vec{\psi}_k &= \vec{\phi}_k(A - B) \ , \end{aligned} \tag{A.30}$$

where via substitution we can eliminate either $\vec{\phi}_k$ or $\vec{\psi}_k$ in order to get

$$\begin{aligned} \vec{\psi}_k(A + B)(A - B) &= \Lambda_k^2 \vec{\psi}_k \\ \vec{\phi}_k(A - B)(A + B) &= \Lambda_k^2 \vec{\phi}_k \ . \end{aligned} \tag{A.31}$$

Now since $A = A^T$ and $B = -B^T$ we have $(A + B)^T = A - B$ which means that both operators $(A + B)(A - B)$ and $(A - B)(A + B)$ are symmetric and positive semi-definite since they are of the form MM^T where M is any arbitrary real matrix. This further implies that they possess a complete orthonormal eigenbasis which means that we can chose the $\vec{\phi}_k$ and $\vec{\psi}_k$ such that they obey

$$\begin{aligned} \langle \vec{\phi}_k, \vec{\phi}_l \rangle &= \delta_{kl} \\ \langle \vec{\psi}_k, \vec{\psi}_l \rangle &= \delta_{kl} \ , \end{aligned} \tag{A.32}$$

where $\langle \cdot \, , \cdot \rangle$ denotes the scalar product in the vector space spanned by $\{\vec{\phi}_i\}$ respectively $\{\vec{\psi}_i\}$. One now can easily check that plugging (A.29) into the sum and difference of (A.32) yields exactly (A.24) respectively (A.25) which proves that our assumption that there exists a canonical transformation (A.22) that diagonalizes (A.20) was indeed justified.

Finally the constant from (A.23) can be computed by substituting (A.23) in (A.20) or from the invariance of Tr(H) under (A.22). The original operator then reads in terms of the new Bogoliubov fermions as

$$H = \sum_k \Lambda_k \eta_k^\dagger \eta_k + \frac{1}{2}\Big(\sum_i A_{ii} - \sum_k \Lambda_k\Big) \ . \tag{A.33}$$

A.3 Bogoliubov transformation - Applied

Now we are in the position to diagonalize the Quantum Ising Hamiltonian expressed in terms of Jordan-Wigner fermions A.19 relatively easily. Note however that A.19 contains a term that spoils the general quadratic form we assumed in A.20 of the previous section: that is the term containing the global fermionic number operator $\mathcal{N}$ in the exponent, namely

$$(-c_N^\dagger c_1^\dagger - c_N^\dagger c_1 + c_N c_1^\dagger + c_N c_1) \cdot (e^{i\pi\mathcal{N}} + \mathbb{1}) \ . \tag{A.34}$$

Now since the Jordan-Wigner parity operator

$$\mathcal{P} = e^{i\pi\mathcal{N}} \tag{A.35}$$

commutes with the Hamiltonian A.19

$$[\mathcal{H}, e^{i\pi\mathcal{N}}] = 0 \ , \tag{A.36}$$

the Jordan-Wigner parity is a good quantum number and we can diagonalize $\mathcal{H}$ in the subspaces with different parity separately. To this end we write the Hamiltonian as

$$\mathcal{H} = \mathcal{H}_{odd} + \mathcal{H}_{even} = P_{odd} \cdot \mathcal{H} \cdot P_{odd} + P_{even} \cdot \mathcal{H} \cdot P_{even} \tag{A.37}$$

where P_{odd} and P_{even} are projection operators onto the subspaces with odd respectively even Jordan-Wigner parity. Of course they fulfill $P_{odd} + P_{even} = \mathbb{1}$. The parity operator can now be replaced by its eigenvalue in each subspace with well defined parity

$$\begin{aligned} \langle e^{i\pi\mathcal{N}} \rangle_{even} &= 1 \\ \langle e^{i\pi\mathcal{N}} \rangle_{odd} &= -1 \ , \end{aligned} \tag{A.38}$$

where the expectation value is taken with respect to any element of the *even* respectively *odd* parity subspace. Thus we obtain for A.19 in the even parity subspace

$$\begin{aligned} \mathcal{H}_{even} = gN \cdot \mathbb{1} - 2g \sum_{i=1}^N c_i^\dagger c_i - \sum_{i=1}^N (c_i^\dagger c_{i+1}^\dagger + c_i^\dagger c_{i+1} - c_i c_{i+1}^\dagger - c_i c_{i+1}) \\ - 2(-c_N^\dagger c_1^\dagger - c_N^\dagger c_1 + c_N c_1^\dagger + c_N c_1) \ , \end{aligned} \tag{A.39}$$

respectively in the odd parity subspace [1]

$$\mathcal{H}_{odd} = gN \cdot \mathbb{1} - 2g \sum_{i=1}^{N} c_i^\dagger c_i - \sum_{i=1}^{N} (c_i^\dagger c_{i+1}^\dagger + c_i^\dagger c_{i+1} - c_i c_{i+1}^\dagger - c_i c_{i+1}) \ . \tag{A.40}$$

A.3.1 Diagonalization of $\mathcal{H}_{odd}$ - Jordan-Wigner boundary conditions

Using the anticommutation relations (A.13) we can rearrange the terms in (A.40) in order to read off the matrices A and B from (A.20) more easily

$$\mathcal{H}_{odd} = gN \cdot \mathbb{1} - \left\{ \sum_{i=1}^{N} 2g(c_i^\dagger c_i) + c_i^\dagger c_{i+1} + c_{i+1}^\dagger c_i + \frac{1}{2} \left[c_i^\dagger c_{i+1}^\dagger - c_{i+1}^\dagger c_i^\dagger - c_i c_{i+1} + c_{i+1} c_i \right] \right\} \ . \tag{A.41}$$

For the moment let us discard the first term proportional to the identity and diagonalize the quadratic form $\left[\mathcal{H}_{odd} - gN \cdot \mathbb{1}\right]$ using the procedure described in section A.2. The matrices A and B then read

$$A = (-1) \cdot \begin{pmatrix} 2g & 1 & 0 & \dots & 0 & 1 \\ 1 & 2g & 1 & & & 0 \\ 0 & 1 & \ddots & \ddots & & \vdots \\ \vdots & & \ddots & \ddots & 1 & 0 \\ 0 & & & 1 & 2g & 1 \\ 1 & 0 & \dots & 0 & 1 & 2g \end{pmatrix} , \quad B = (-1) \cdot \begin{pmatrix} 0 & 1 & 0 & \dots & 0 & -1 \\ -1 & 0 & 1 & & & 0 \\ 0 & -1 & \ddots & \ddots & & \vdots \\ \vdots & & \ddots & \ddots & 1 & 0 \\ 0 & & & -1 & 0 & 1 \\ 1 & 0 & \dots & 0 & -1 & 0 \end{pmatrix} , \tag{A.42}$$

which yields for the matrix we must diagonalize

$$(A-B)(A+B) = 4 \cdot \left[(g^2+1) \cdot \mathbb{1} + g \cdot \begin{pmatrix} 0 & 1 & 0 & \dots & 0 & 1 \\ 1 & 0 & 1 & & & 0 \\ 0 & 1 & \ddots & \ddots & & \vdots \\ \vdots & & \ddots & \ddots & 1 & 0 \\ 0 & & & 1 & 0 & 1 \\ 1 & 0 & \dots & 0 & 1 & 0 \end{pmatrix} \right] \ . \tag{A.43}$$

Note that the non-trivial part of (A.43) is a circulant matrix for which we can immediately write down the eigenvectors

---

[1] We would like to emphasize that the Hamiltonian A.40 is the one that is usually used when solving the problem in the thermodynamic limit (see Ref. [73]). If one is directly considering A.40 in the full Hilbert space, this Hamiltonian is also known under the name of Quantum Ising model with *Jordan-Wigner Boundary Conditions*. Note that Jordan-Wigner Boundary Conditions cannot be trivially expressed in terms of the original spin operators.

$$\vec{\phi}_k = \begin{pmatrix} 1 \\ \omega_k \\ \omega_k^2 \\ \vdots \\ \omega_k^{N-1} \end{pmatrix} , \quad \omega_k = \exp \frac{2\pi i}{N} k \tag{A.44}$$

and the eigenvalues

$$\lambda_k = 2\cos\left(\frac{2\pi k}{N}\right) \ . \tag{A.45}$$

Combining this with the trivial part of (A.43) yields for the energy of the Bogoliubov modes according to (A.23) and (A.31)

$$\Lambda_k = \pm 2 \cdot \sqrt{1 + g^2 + 2g \cdot \cos\left(\frac{2\pi k}{N}\right)} \ . \tag{A.46}$$

The eigenvectors $\vec{\psi}_k$ can be then obtained by plugging $\vec{\psi}_k$ and Λ_k into (A.30). Now it is a simple exercise to compute the coefficients $\{g_{ij}\}$ and $\{h_{ij}\}$ using (A.29) and then to write down the creation and annihilation operators $\eta_k^\dagger$ and η_k for the Bogoliubov modes using (A.22).

Finally, according to (A.33), $\mathcal{H}_{odd}$ reads in terms of Bogoliubov fermions as

$$\begin{aligned} \mathcal{H}_{odd} &= gN + \sum_k \Lambda_k \eta_k^\dagger \eta_k + \frac{1}{2}\Big(\sum_i A_{ii} - \sum_k \Lambda_k\Big) \\ &= \sum_k \Lambda_k \eta_k^\dagger \eta_k - \frac{1}{2}\sum_k \Lambda_k \ , \end{aligned} \tag{A.47}$$

with Λ_k as defined in (A.46). Note how the trace over A exactly cancels the first term gN.

A.3.2 Diagonalization of $\mathcal{H}_{even}$

Again we rearrange the terms in (A.39) in order to read off the matrices A and B more easily

$$\begin{aligned} \mathcal{H}_{even} = gN \cdot \mathbb{1} - \Bigg\{ \sum_{i=1}^{N} 2g(c_i^\dagger c_i) + c_i^\dagger c_{i+1} + c_{i+1}^\dagger c_i + \frac{1}{2}\Big[c_i^\dagger c_{i+1}^\dagger - c_{i+1}^\dagger c_i^\dagger - c_i c_{i+1} + c_{i+1} c_i\Big]\Bigg\} \\ + 2\Big\{c_N^\dagger c_1 + c_1^\dagger c_N + \frac{1}{2}\Big[c_N^\dagger c_1^\dagger - c_1^\dagger c_N^\dagger - c_N c_1 + c_1 c_N\Big]\Big\} \ . \end{aligned} \tag{A.48}$$

Again we discard the first term and diagonalize only $\big[\mathcal{H}_{even} - gN \cdot \mathbb{1}\big]$. The matrices A and B read now

$$A = (-1) \cdot \begin{pmatrix} 2g & 1 & 0 & \dots & 0 & -1 \\ 1 & 2g & 1 & & & 0 \\ 0 & 1 & \ddots & \ddots & & \vdots \\ \vdots & & \ddots & \ddots & 1 & 0 \\ 0 & & & 1 & 2g & 1 \\ -1 & 0 & \dots & 0 & 1 & 2g \end{pmatrix}, \quad B = (-1) \cdot \begin{pmatrix} 0 & 1 & 0 & \dots & 0 & 1 \\ -1 & 0 & 1 & & & 0 \\ 0 & -1 & \ddots & \ddots & & \vdots \\ \vdots & & \ddots & \ddots & 1 & 0 \\ 0 & & & -1 & 0 & 1 \\ -1 & 0 & \dots & 0 & -1 & 0 \end{pmatrix}, \tag{A.49}$$

such that we obtain for $(A-B)(A+B)$ the expression

$$(A-B)(A+B) = 4 \cdot \left[(g^2+1) \cdot \mathbb{1} + g \cdot \begin{pmatrix} 0 & 1 & 0 & \dots & 0 & -1 \\ 1 & 0 & 1 & & & 0 \\ 0 & 1 & \ddots & \ddots & & \vdots \\ \vdots & & \ddots & \ddots & 1 & 0 \\ 0 & & & 1 & 0 & 1 \\ -1 & 0 & \dots & 0 & 1 & 0 \end{pmatrix} \right] . \tag{A.50}$$

Note that now the non-trivial part of (A.50) is not a circulant matrix, but a so-called *Gear matrix*. This type of matrices has been studied in [78] where the explicit formulas for the eigenvalues and eigenectors of such a matrix can be found. Specifically we get for the λ_k

$$\lambda_k = 2\cos\left[\frac{2\pi}{N}\left(k+\frac{1}{2}\right)\right] , \tag{A.51}$$

which then yields for the single mode energies

$$\Lambda_k = \pm 2 \cdot \sqrt{1+g^2+2g\cdot\cos\left[\frac{2\pi}{N}\left(k+\frac{1}{2}\right)\right]} . \tag{A.52}$$

Similarly to (A.47), $\mathcal{H}_{even}$ reads now

$$\mathcal{H}_{even} = \sum_k \Lambda_k \chi_k^\dagger \chi_k - \frac{1}{2}\sum_k \Lambda_k , \tag{A.53}$$

where the Λ_k are now defined according to (A.52) and we have used $\chi_k^\dagger$ and χ_k to denote the Bogoliubov modes.

A.3.3 The parity anomaly

Now we would like to emphasize a very important point: depending on how the sign of Λ_k is chosen in (A.46) or (A.52), the Bogoliubov fermions are either particle or hole modes. If one wants the ground state of $\mathcal{H}_{odd/even}$ to be the Bogoliubov vacuum, i.e. $|\Omega\rangle_{odd/even}$, then one must choose all $\Lambda_k > 0$ such that when fermions are added to the system, the energy grows.

With this choice all excitations of the model are particle modes, as opposed to the hole modes that one would have for the choice $\Lambda_k < 0$. Note that the spectrum of the model is in both cases exactly the same; the only difference is the interpretation one gives to the states. Especially the ground state has for any choice of the sign of the Λ_k the same energy

$$E_0^{odd/even} = \frac{1}{2} \sum_k -|\Lambda_k| \ . \tag{A.54}$$

Note furthermore that only the eigenstates of $\mathcal{H}_{odd/even}$ that have the correct parity are also eigenstates of the original Quantum Ising Hamiltonian $\mathcal{H}$ (A.37). This means that in order to obtain the full spectrum of $\mathcal{H}$ we must pick from the spectrum of $\mathcal{H}_{odd}$ the eigenstates with odd Jordan-Wigner parity (A.35) while from the spectrum of $\mathcal{H}_{even}$ we must pick the ones with even Jordan-Wigner parity.

The crucial point now is to realize that the Jordan-Wigner parity $\mathcal{P}_{JW}$ and the Bogoliubov parities $\mathcal{P}_{odd}$ and $\mathcal{P}_{even}$ which are defined as

$$\begin{aligned} \mathcal{P}_{odd} &= e^{i\pi\mathcal{N}_{odd}} \ , \ \mathcal{N}_{odd} = \sum_{i=1}^{N} \eta_i^\dagger \eta_i \\ \mathcal{P}_{even} &= e^{i\pi\mathcal{N}_{even}} \ , \ \mathcal{N}_{even} = \sum_{i=1}^{N} \chi_i^\dagger \chi_i \ . \end{aligned} \tag{A.55}$$

with the creation and annihilation operators defined as in (A.47) and (A.53), are not necessarily the same under all circumstances. Specifically, it turns out that for $g \geq 1$ we indeed have $\langle \mathcal{P}_{JW} \rangle = \langle \mathcal{P}_{odd} \rangle = \langle \mathcal{P}_{even} \rangle$ and we can construct the spectrum of the original Hamiltonian $\mathcal{H}$ simply as

$$\{ |\Omega\rangle_{even} , \eta_i^\dagger |\Omega\rangle_{odd} , \chi_i^\dagger \chi_j^\dagger |\Omega\rangle_{even} , \eta_i^\dagger \eta_j^\dagger \eta_k^\dagger |\Omega\rangle_{odd} , \dots \} \ . \tag{A.56}$$

However, for $g < 1$, we find $\langle \mathcal{P}_{JW} \rangle = -\langle \mathcal{P}_{odd} \rangle = \langle \mathcal{P}_{even} \rangle$ which means that in order to correctly construct the spectrum of $\mathcal{H}$ we must pick from the spectrum of $\mathcal{H}_{odd}$ the excitations with even parity. Explicitly this means that the spectrum reads in this case

$$\{ |\Omega\rangle_{even} , |\Omega\rangle_{odd} , \chi_i^\dagger \chi_j^\dagger |\Omega\rangle_{even} , \eta_i^\dagger \eta_j^\dagger |\Omega\rangle_{odd} , \dots \} \ . \tag{A.57}$$

Note that due to the ambiguity in the sign of Λ_k we could in principle decide to define the quasi-particles in such way that one mode is is a hole mode (e.g. by picking $\Lambda_0 < 0$) while all the others are particle modes with positive energy. This obviously flips the sign of the parity such that also for $g < 1$ we have $\langle \mathcal{P}_{JW} \rangle = \langle \mathcal{P}_{odd} \rangle = \langle \mathcal{P}_{even} \rangle$ and the spectrum would again read as (A.56). However we have seen in section 4.4.1 how our MPS ansatz (4.1) for one-particle excitations only manages to reproduce the low-energy spectrum with relatively bad precision in the regime where $g < 1$. This is a strong hint for the fact that when $g < 1$

the spectrum of the Quantum Ising model with PBC does not contain any one-particle states indeed. This means that the ambiguity in the choice of the sign of Λ_k can be raised with a physical argument by demandig that the choice of the sign must be made in such a way that all Bogoliubov modes are indeed particle modes with positive energy $\Lambda_k \geq 0$.

Lebenslauf

Persönliche Daten

Name:	Bogdan Corneliu Pirvu
Geburtsdatum:	14. Mai 1980
Geburtsort:	Bukarest, Rumänien
Nationalität:	Österreichisch

Ausbildung und Tätigkeiten

07 / 1998	Reifeprüfung am Christian Doppler Gymnasium, Salzburg
10 / 1998 – 05 / 2006	Studium der Technischen Physik an der Technischen Universität Wien
07 / 2006 – 03 / 2007	Zivildienst bei Jugend am Werk, Wien
05 / 2007 – 06 / 2011	Assistent in Ausbildung (Dissertation) an der Universität Wien
07 / 2011 – heute	Systemanalytiker, F&E, Austrian Gaming Industries GmbH

Publikationsliste

- E. Rico, R. Hübener, S. Montangero, N. Moran, B. Pirvu, J. Vala and H.J. Briegel,
  "Valence-bond states: Link models", *Annals of Physics* **324**, 1875-1896 (2009)
- B. Pirvu, V. Murg, J.I. Cirac and F. Verstraete,
  "Matrix product operator representations", *New J. Phys.* **12**, 025012 (2010)
- B. Pirvu, F. Verstraete and G.Vidal,
  "Exploiting translational invariance in matrix product state simulations of spin chains with periodic boundary conditions", *Phys. Rev. B* **83**, 125104 (2011)
- B. Pirvu, J.Haegeman and F. Verstraete,
  "Matrix product state based algorithm for determining dispersion relations of quantum spin chains with periodic boundary conditions", *Phys. Rev. B* **85**, 035130 (2012)
- J. Haegeman, B. Pirvu, D.J. Weir, J.I. Cirac, T.J. Osborne, H. Verschelde, and F. Verstraete,
  "Variational matrix product ansatz for dispersion relations", *Phys. Rev. B* **85**, 100408(R) (2012)
- B. Pirvu, G.Vidal, F. Verstraete and L.Tagliacozzo,
  "Matrix product states for critical spin chains: Finite-size versus finite-entanglement scaling", *Phys. Rev. B* **86**, 075117 (2012)